KU LEUVEN

ARENBERG DOCTORAL SCHOOL
FACULTY OF ENGINEERING

NUMERICAL MODELLING OF NEAR-BOTTOM SEDIMENT TRANSPORT: TURBULENCE MODULATION, NEW PROCESS MODELS AND APPLICATION TO THE SCHELDT & THE BELGIAN COAST

Qilong **BI**

Supervisor:
Prof. Dr. Erik A. Toorman

Examination Committee:
Prof. Dr. Y. Willems (Chairman)
Prof. Dr. Jean Berlamont
Prof. Dr. Eric Deleersnijder (UCL and TU Delft)
Prof. Dr. Gerard Govers
Prof. Dr. Jean-Michel Hervouet (EDF R&D)
Prof. Dr. Jaak Monbaliu

A Dissertation Submitted in Partial Fulfilment of the Requirements
for the Degree of Doctor of Philosophy in Engineering Science

Department of Civil Engineering
Faculty of Engineering Science

November 2015

Uitgegeven in eigen beheer, Qilong Bi, Kasteelpark Arenberg 40 - box 2448, B-3001 Heverlee (Belgium)

Acknowledgements

First of all, I would like to thank my supervisor, Professor Erik Toorman, for introducing me to the world of sediment. It was only due to his inspiration, guidance and encouragement that I was able to complete my Ph.D. study in a respectable manner. Whenever I had questions in my research, I walked to his office and he always had time for me, guiding me with his knowledge and patience. He showed me how to be a good researcher: dig into the fundamentals and remain critical to each step I took in the research process. I am also very thankful to him for allowing me some extra time to finish my work and offering me the opportunity to continue my research with him in this field.

I am also very thankful to Professor Jaak Monbaliu. In all these years, I received much help from him. He always came from the next door and shared his valuable insight with me on my research work. Although his expertise is a little different from my topic, he still showed me how to see the research problems from a different angle and reminded me of what I did not notice before.

I wish to express my gratitude to Professor Jean Berlamont and Professor Gerard Govers. They are members of my Supervisory Committee and they have always given me valuable advice. They have been in my presentations since the beginning of my Ph.D. study. They provided me with many suggestions on how to find the right path to tackle the research problems and how to improve my work from different aspects.

My special thanks to Dr. Jean-Michel Hervouet (EDF R&D). Dr. Jean-Michel Hervouet is the father of TELEMAC, an advanced integrated suite of solvers for use in the field of free-surface flow. In all these years, especially in the beginning of using TELEMAC for my research, I asked countless questions on the user forum and he always answered with detailed explanations. Sometimes he even spent his time in my specific model for helping me to figure out where the problem was. I really appreciate for his support.

I am also grateful to Professor Eric Deleersnijder (UCL and TU Delft) for helping me to improve my thesis during the last four months. He inspired me with his knowledge and experience in numerical modelling. I learned many things and I am thankful that he has been spending his precious time to read my manuscript and giving me valuable comments.

I would like to thank my friends and colleagues who were/are in KU Leuven. Pursuing a Ph.D. is not only a truly intellectual challenge, but also a spiritual journey. Like someone said, the journey of Ph.D. is solitary and intensely personal, but there are others who we encounter on the way who share the same quest, have the same desire for knowledge of universally understood insights, self-understanding, and seek to achieve a major goal. I think I am lucky to have all of you here, making my journey well accompanied and joyful.

Finally yet importantly, I would like to express my sincere gratitude to my family. They are always being there for me. Without their support and encouragement I could not make it this far.

Qilong Bi

November 20th, 2015

English summary

Sediment transport due to fluid motion is a crucial process in many environmental and engineered systems. Therefore, understanding sediment transport is critical for predicting sediment movements and evaluating the short and/or long-term influence to the surface water systems. Despite the importance of sediment transport, the fundamental aspects involved are far from being completely understood. At the core of the problem is the complex interaction between a turbulent flow field and sediment particles. In this sense, for sediment transport modelling, how to account for as many turbulence generation or destruction mechanisms as possible is one of the keys to improving the accuracy of prediction. The most widely used and validated model for turbulence is two-equation k-ε model. However, the traditional k-ε model cannot provide accurate predictions when considering the presence of sediment in water due to missing the terms in the equations that can account for energy transfer between sediments and turbulence, as well as the terms for inter-particle interactions. Moreover, the standard k-ε model is only valid for fully developed turbulent flow, so it often has difficulties to deal with near-bottom layer (e.g. low-Reynolds effects and high sediment concentrations). Therefore, an alternative approach to overcome these difficulties is two-phase flow theory. In the first part of this study, a modified two-equation k-ε model with additional turbulence modulation terms, accounting for the influence of particles on the turbulent flow field, has been proposed. These extra terms are derived using a two-phase flow approach. In the numerical tests, the modified two-phase k-ε model reproduces the features of turbulence modulation observed in the experiments on sediment-laden flow.

Another important aspect in sediment transport is the treatment of the near-bottom layer. It has been hypothesized for more than a decade that currently used sediment transport models for morphodynamic studies (e.g., harbour siltation, system response to dredging or structures) can be improved considerably in their predicting capacity when the near-bottom high-concentration effects in the last few centimetres above the bed can be accounted for with a physics-based model. Indeed, experimental observations and theoretical considerations (partially based on two-phase micro-scale models) show that the flow and suspension capacity of the water column are strongly affected by the processes of particle-fluid interactions in the benthic layer. Hence, the second part of this study focusses on the efficient modelling of near-

bottom sediment transport in morphodynamic modelling codes through an innovative methodology. In this part, the performance of a few new physics-based process models has been investigated by implementation into a numerical model for the simulation of the flow and morphodynamics in the Western Scheldt estuary. In order to deal with the complexity within the research domain, and improve the prediction accuracy, a two-dimensional (2D) depth-averaged model has been set up as realistic as possible, *i.e.* including two-way hydrodynamic-sediment transport coupling, mixed sand–mud sediment transport (bedload transport as well as suspended load in the water column) and a dynamic non-uniform bed composition. A newly developed bottom friction law, based on a generalised mixing-length (GML) theory, is implemented, with which the new bed shear stress closure is constructed as the superposition of the turbulent and the laminar contribution. It allows the simulation of all turbulence conditions (fully developed turbulence, from hydraulic rough to hydraulic smooth, transient and laminar), and the drying and wetting of intertidal flats can now be modelled without specifying an inundation threshold. Erosion and deposition in these areas can now be estimated with much higher accuracy, as well as their contribution to the overall net fluxes. Furthermore, Krone's deposition law has been adapted to sand–mud mixtures, and the critical stresses for deposition are computed from suspension capacity theory, instead of being tuned. The model has been calibrated and the results show considerable differences in sediment fluxes, compared to a traditional approach and the analysis reveals that the concentration effects play a very important role. The new bottom friction law with concentration effects can considerably alter the total sediment flux in the estuary, not only in terms of magnitude, but also in terms of erosion and deposition patterns.

Nederlandse samenvatting

Sedimenttransport door vloeistofbeweging is een cruciaal proces in veel milieu- en technische systemen. Daarom is het begrijpen van sedimenttransport essentieel voor het voorspellen van sedimentbewegingen en het evalueren van de korte en / of lange-termijn invloed op oppervlaktewatersystemen. Ondanks het belang van sedimenttransport, zijn de betrokken fundamentele aspecten verre van volledig begrepen. De kern van het probleem is de complexe wisselwerking tussen een turbulent stromingsveld en sedimentdeeltjes. Daarom is één van de sleutels tot de nauwkeurige voorspelling van sedimenttransport het beschrijven van zoveel mogelijk processen voor generatie en destructie van turbulentie. Het meest gebruikte en gevalideerde model voor turbulentie is het twee-vergelijkingen k-ε-model. Echter, het traditionele k-ε-model geeft geen nauwkeurige voorspellingen bij de evaluatie van de aanwezigheid van sediment in water als gevolg van het ontbreken van de termen in de vergelijkingen die rekening houden met de energieoverdracht tussen sedimenten en turbulentie en de interacties tussen de deeltjes onderling. Bovendien is het standaard k-ε-model alleen geldig voor volledig ontwikkelde turbulente stroming, en geeft het dus –problemen in de onderste laag tegen de bodem (met name laag-Reynolds effecten en hoge sedimentconcentraties). Daarom biedt twee-fasenstromingstheorie een alternatieve benadering om deze problemen te aan te pakken. In het eerste deel van deze studie werd een aangepast twee-vergelijkingen k-ε-model met extra turbulentiemodulatietermen, die de invloed van deeltjes op het turbulente stromingsveld beschrijven, voorgesteld. Deze extra termen worden verkregen door een twee-fasenstroombenadering. In de numerieke simulaties reproduceert dit gewijzigde tweefasige k-ε-model de kenmerken van turbulentiemodulatie waargenomen in experimenten op een sediment-beladen stroom.

Een ander belangrijk aspect in sedimenttransport is de behandeling van de laag tegen de bodem. Het wordt al meer dan tien jaar gehypothetiseerd dat de voorspelling met de huidig gebruikte sedimenttransportmodellen voor morfodynamische studies (bijvoorbeeld voor de aanslibbing van een haven, of systeemrespons op baggeren of nieuwe waterbouwkundige structuren aanzienlijk verbeterd kunnen worden wanneer de hoge-concentratie-effecten in de laatste centimeters boven de bodem kunnen worden beschrevenmet een fysisch-gebaseerd model. Inderdaad, uit experimentele waarnemingen en theoretische

overwegingen (mede op basis van tweefasen-microschaalmodellen) blijkt dat de stroming en de suspensiecapaciteit van de waterkolom sterk beïnvloed worden door de processen van deeltjes-vloeistofinteractie in de benthische laag. Vandaar dat het tweede deel van de studie de nadruk legt op de efficiënte studie van benthisch sedimenttransport in morfodynamische numerieke modellen door een innovatieve methodologie. In dit deel zijn de prestaties van enkele nieuwe fysisch-gebaseerde procesmodellen onderzocht door toepassing in een numeriek model voor de simulatie van de stroming en morfodynamica in de Westerschelde. Om rekening te houden met de complexiteit binnen het onderzoeksdomein, en te streven naar het verbeteren van de nauwkeurigheid van voorspellingen, is een twee-dimensioneel (2D) diepte-gemiddelde model opgezet, dat zo realistisch mogelijk is, waarbij: de koppeling tussen hydrodynamica en sedimenttransport in de twee richtingen gebeurt, gemengd zand-slibtransport beschouwd wordt (zowel bodemtransport als suspensietransport in de waterkolom) en een dynamische, niet-uniforme bodemsamenstelling. Een nieuw ontwikkelde bodemwrijvingsmodel, gebaseerd op een veralgemeende menglengtetheorie, werd geïmplementeerd, waarbij de bodemschuifspanning wordt berekend als de superpositie van de turbulente en laminaire bijdrage. Het laat de simulatie toe van alle turbulente stromingsregimes (van volledig ontwikkelde turbulentie, van hydraulische ruw tot hydraulische glad, over transiënte condities naar laminaire) en het drogen en nat worden van intergetijdengebieden kan nu nauwkeuriger worden gemodelleerd zonder gebruik te moeten maken van een overstromingsdrempel. Erosie en depositie op deze gebieden kunnen nu worden geschat met een veel hogere nauwkeurigheid, evenals hun bijdrage aan de totale netto fluxen. Verder werd Krones empirische bezinkingswet aangepast aan zand-slib mengsels en de kritische schuifspanning voor depositie wordt nu berekend uit een suspensiecapaciteittheorie, in plaats van afgestemd. Het model is gekalibreerd en de resultaten vertonen grote verschillen in sedimentstromingen, vergeleken met een traditionele aanpak. Uit de analyse blijkt dat de concentratie-effecten een zeer belangrijke rol spelen. De nieuwe bodemwrijvingswet, die hiermee rekening houdt, kan de totale sedimentflux in het estuarium aanzienlijk veranderen, niet alleen in termen van grootte, maar ook in termen van erosie- en depositiepatronen.

Table of contents

List of symbols

A_+	the empirical parameter in the damping function f_A
B_+	the parameter in the generalized mixing-length model
b_1, b_2, b_3	the empirical constants for curve-fitting of the lag velocity
C	the mass concentration of sediment
c_a	the reference concentration
C_{cr}	the critical volumetric concentration of sediment for modified k-ε model
C_s	the volumetric concentration of sediment
C_{total}	the mass concentration of total suspended sediment
C_μ	the closure constants for standard k-ε model
$C_{\varepsilon1}$, $C_{\varepsilon2}$, $C_{\varepsilon3}$	the closure constants for standard k-ε model
$C_{\varepsilon4}$	the closure constant for the modified k-ε model
D	the deposition flux
D_*	the particle parameter related to D_{50}
D_{50}	the characteristic diameter of sediment particle
D_m	the deposition flux of mud
D_s	the deposition flux of sand
D_T	the mass diffusivity coefficient
E	the erosion flux
E_{0m}	the erosion constant for cohesive regime
E_{0s}	the erosion constant for non-cohesive regime
E_m	the erosion rate for mud

E_s	the erosion rate for sand
f, $\bar{f}$, f'	the interaction force between fluid and particle phase
f_A	the damping function in the generalized mixing-length model
f_c	the auxiliary function defined in the modified k-ε model
f_m	the mud fraction
$f_{m,crit}$, $f_{m,crit^*}$	the lower and upper bounds of critical mud fraction
g	the gravitational acceleration
G	the buoyancy term in standard k-ε model
h	the water depth
i, j	the indices of coordinates
J	the Jacobian matrix
k	the turbulence kinetic energy
k_s	the Nikuradse roughness length scale
N_i	the shape functions in a quadratic line element
P	the production term in standard k-ε model
p, $\bar{p}$, p'	the pressure, the Reynolds-averaged pressure and its fluctuation
p_m	the deposition probabilities of mud
p_s	the deposition probabilities of sand
Rf_m	the flux Richardson number for mud at suspension capacity
Rf_s	the flux Richardson number for sand at suspension capacity
s	the strain rate of suspension

t	the time
T	is the transport stage parameter
U	the Reynolds-averaged related velocity of fluid phase
u_*	the shear velocity
$u_{*,cr}$	the critical shear velocity for erosion
u_{*lam}	the shear velocity for laminar open-channel flow
u_{*turb}	the shear velocity for fully-developed turbulent open-channel flow
u, $\bar{u}$, u'	the fluid velocity, the Reynolds-averaged fluid velocity and its fluctuations
U_D	the fluid drift velocity
u_{lag}	the lag velocity
u_m	the suspension velocity
V	the Reynolds-averaged related velocity of particle phase
v, $\bar{v}$, v'	the particle velocity, the Reynolds-averaged particle velocity and its fluctuations
V_D	the particle drift velocity
W	the Reynolds-averaged related slip velocity
w, $\bar{w}$, w'	the slip velocity, the Reynolds-averaged slip velocity and its fluctuations
w_n	the weighting factor at n^{th} Gauss points
w_s	the sediment settling velocity
x, y, z	the coordinate
x_1	the empirical constant in the erosion model for mixed-sediment transport
z	the water level

z_+	the distance from the bottom z non-dimensionalized by the length-scale ν/u_*
z_0	the equivalent roughness height
Z_{ref}	the reference level between bedload and suspended load
Z_s	the free surface
z_u, z_l	the upper and lower bounds in a quadratic line element
β	the suspension friction (or apparent roughness) coefficient
γ	the inverse of the turbulent time scale
δ	the Kronecker delta
ε	the turbulence dissipation rate
η	the non-dimensionalized water level
κ	the von Kármán constant
μ	the molecular viscosity of fluid
μ_e	the effective viscosity of suspension
μ_m	the molecular viscosity of suspension
μ_{mt}	the eddy viscosity of fluid
μ_t	the eddy viscosity of fluid
ν	the kinematic viscosity of fluid
ν_a	the artificial viscosity for numerical stability
ν_{SGS}	the subgrid-scale turbulence viscosity generated by vortex shedding in the wake of bed roughness elements and/or of suspended particles
ν_t	the kinematic eddy viscosity of fluid
ξ	the local coordinate in a quadratic line element

Π_k, Π_ε	the extra terms for turbulence modulation in modified k-ε model
ρ	the density of suspension
ρ_f	the density of fluid (water)
ρ_p	the density of sediment particle
σ	the viscous stress tensor of suspension
σ_D	the drift diffusion stress tensor
σ_f	the viscous stress tensor of fluid phase
σ_k, σ_ε	the closure constants for modified k-ε model
σ_p	the viscous stress tensor of particle phase
σ_T	the Reynolds stress tensor of suspension
σ_t	the turbulent Prandtl-Schmidt number
τ_b	the bed shear stress
$\tau_{cd,m}$	the critical shear stress for mud deposition
$\tau_{cd,s}$	the critical shear stress for sand deposition
τ_{ce}	the critical shear stress for sand-mud mixture
$\tau_{ce,m}$	the critical shear stress for mud
$\tau_{ce,s}$	the critical shear stress for sand
ϕ, $\bar{\phi}$, ϕ'	the volume fraction of particle phase
ω, $\bar{\omega}$, ω'	the interaction force density, the Reynolds-averaged interaction force density and its fluctuations

Chapter 1

INTRODUCTION

1.1. Problem identification

Problems involving the erosion, transport and deposition of sediment as well as the mixing of those sediments within the active upper layer of the sediment column are, fundamentally, problems of the near-bottom layer. This near-bottom layer can be characterized as the inner boundary layer where turbulence is not fully developed, i.e. where other stresses than the shear-flow induced turbulent Reynolds stress cannot be neglected.

It has been hypothesized for more than a decade that currently used sediment transport models for morphodynamic studies (e.g., harbour siltation, system response to dredging or structures) can be improved considerably in their predicting capacity when the near-bottom high-concentration effects in the last few centimetres above the bed can be accounted for with a physics-based model (Toorman, 2010).

The traditional sediment transport models cannot provide accurate prediction when considering the existence of this high-concentrated near-bottom layer, where interactions between sediments and turbulence and inter-particle interactions occur at any time and location.

Indeed, the physics in this high-concentration near-bottom layer is complex (Elghobashi, 1994). The interactions between sediment and turbulent flow as well as inter-particle collisions become important when concentration is high. For very dilute sediment-laden flows, the influence of the sediment particles on the fluid can be neglected, which results in a one-way coupling, where the sediment motion is entirely driven by the continuous carrier flow. With growing volume fraction, the modification of the turbulent flow by the dispersed sediment particles has to be taken into account by means of a two-way coupling. For the high-concentration near-bottom layer, momentum and energy will be transferred between sediment particles as well as between particles and fluid, leading to a so-called four-way coupling approach. Experimental observations and theoretical considerations (partially based on two-phase micro-scale models) show that the flow and suspension capacity of the water column

are strongly affected by the processes of particle-fluid interactions and inter-particle collisions in the high-concentration near-bottom layer. This is further elaborated in Section 3.2.

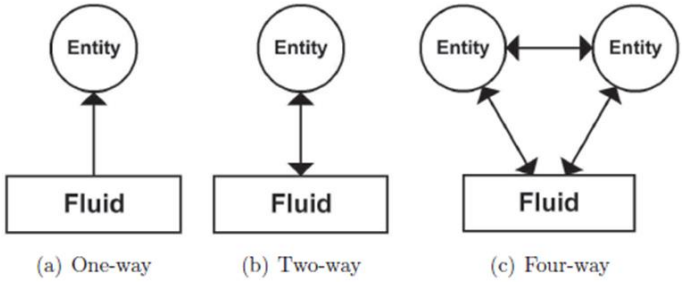

Figure 1.1. Types of interactions between fluid and particle phases: (a) one-way coupling; (b) two-way coupling; (c) four-way coupling.

Therefore, this study aims to develop a new numerical model for the simulation of near-bottom sediment transport by considering the physics of sediment transport processes in the near-bottom high-concentrated layer.

1.2. Objective of the research

The overall objective of this research is to obtain a better understanding on the near-bottom sediment transport mechanism. It includes investigation of the turbulence modulation due to fluid-particle interactions, the low-Reynolds effects in the near bed region, and the bottom roughness corrections due to flow conditions and high concentration effects in the coastal and estuarine areas, especially in the intertidal areas in the transitional period between high water and low water. In this context, the following research questions are identified:

- How does the presence of sediment particles affect the turbulence in the flow? In addition, what are the key factors contributing to turbulence modulation due to particles especially in the near-bottom region?
- Can those extra turbulence modulation terms be described mathematically from a two-phase perspective? Moreover, how to model those terms numerically based on a two-equation turbulence model?

- In terms of large-scale hydrodynamic and morphological simulations, how can the bottom effects, including high-concentration effects in the near-bottom layer, be taken into consideration? What can be improved by including these physical processes?
- What can be learnt if applying above findings to the Scheldt estuary? How to assess the influence of sediment transport in the estuary?

To answer these research questions, the following activities were conducted:

- Several two-phase fluid-particle experiments were reviewed and the impact of the presence of sediment particles on the turbulent flow was studied qualitatively. By looking at the behaviour of particle-fluid interactions, a better understanding of the physical processes of turbulence modulation due to sediments in the flow was obtained.
- Two-phase flow theory was carefully studied. Following Toorman's (2010) ensemble-averaged governing equations for two-phase/mixture sediment-laden flow, a modified two-equation k-ε turbulence model with extra turbulence modulation terms was developed. The cause of these extra terms was analysed and the closures were proposed for modelling them.
- For investigating the effects of turbulence modulation terms, a one-dimensional horizontally homogeneous (1-DV) finite-element sediment-turbulence model was developed. The experimental data from Muste *et al.* (2005) was used for model validation. The performance of the modified k-ε model with different combinations of extra terms was compared and evaluated.
- A new physics-based process model for mixed-sediment transport was developed. It consists of a newly developed bottom friction law based on a generalized mixing-length (GML) theory (Toorman, 2010) for improving the bed shear stress calculation under all turbulence conditions, and a new deposition criterion for sand–mud mixtures that is derived from suspension capacity theory.
- For the case study, a numerical model for the simulation of the flow and morphodynamics in the Western Scheldt estuary was

built. In order to deal with the complexity within the research domain, and improve the prediction accuracy, a 2D depth-averaged model has been set up as realistic as possible. Besides the implementations of the physics-based process model mentioned above, it also includes two-way hydrodynamic-sediment transport coupling, mixed sand–mud sediment transport and a dynamic non-uniform bed composition.

- The Western Scheldt model was calibrated and validated. The results were analysed and the sediment movements and distribution patterns were examined. The sediment fluxes at several cross-sections were calculated and the sediment balance in the estuary was studied. Finally, a preliminary analysis of the wave effects on coastal sediment transport was performed.

1.3. Outline of the thesis

There are seven chapters in this dissertation. Chapter 1 presents the motivation, the importance of the research, its objectives and the outline of the thesis.

Chapter 2 describes the current state of the research on sediment transport modelling. It has two parts. The first part summarises the state-of-the-art approaches for numerical modelling of sediment transport with a comprehensive literature review. The second part aims to explain the theoretical background of hydrodynamic and morphological modelling in openTELEMAC (an integrated suite of solvers for use in the field of free-surface flow), which was used for the development of the Western Scheldt model at a later stage of this study.

In Chapter 3, the related concepts and definitions are clarified in the beginning, followed by the literature review on the two-phase flow experiments. The conclusions from those experimental studies and the descriptions of the physical processes regarding the sediment-turbulence interactions were presented. After that, the two-phase/mixture theory and the governing equations proposed by Toorman (2008) is described. Based on this, the following sections give the details on the derivation of a modified two-phase k-ε turbulence model, together with the discussion on the extra turbulence modulation terms.

Chapter 4 describes the 1-DV model from a mathematical point of view. It contains a section about the theoretical background. The discretization

procedures with the Finite Element Method (FEM) are discussed as well. In the last part, the model was firstly validated against the experimental data from Muste *et al.* (2005) using a standard k-ε turbulence model. Then the turbulence modulation terms were added to the model. Their influences on the flow field and sediment transport are evaluated through the analysis of the results.

Chapter 5 focuses on the new physics-based process model for mixed-sediment transport. The generalized mixing length (GML) theory (Toorman, 2010) is briefly described in the first section. Then the new bottom roughness law based on GML theory is introduced and its improvements on the computation of bed shear stress on intertidal flats are demonstrated. The second section deals with the erosion and deposition of mixed-sediment. A unified way of computing erosion of sand-mud mixtures and a new deposition criterion derived from suspension capacity condition are presented.

In Chapter 6, the development of the Western Scheldt model is addressed. The research area is firstly introduced. Then the model set-ups are described in detail. It also covers the model calibration and validation. Finally, the results are processed and analysed. The movements of turbidity maximum areas, the sediment fluxes and the wave effects on sediment balance in the estuary are discussed.

The last chapter, Chapter 7 summarizes the findings of the research, draws the conclusions and recommends future research areas.

Chapter 2

SEDIMENT TRANSPORT MODELLING

2.1. State-of-the-art

Sediment transport due to fluid motion occurs in rivers, estuaries, seas and other bodies of water due to currents and tides. It is a crucial process in many environmental and engineered systems (Johnson *et al.* 1993). Many ecosystems benefit from sediment transport, whether directly or indirectly. Sediment builds aquatic habitats for spawning and benthic organisms. It is also responsible for providing nutrients in nearshore ecosystems such as floodplains and marshes. In addition to that, without sediment deposition, coastal zones can become eroded or non-existent (Czuba *et al.*, 2011). However, too much or too little sediment can easily cause ecosystem and safety issues. Whether the concerns are caused by scour, erosion, build up, or simply excessive turbidity, the sediment transport rate is an important factor (Zaimes & Emanuel, 2006). In addition to the problems caused by load quantity, sediment can easily introduce pollution and other contaminants into a waterway, spreading the pollutants downstream (Palermo *et al.*, 2008).

For engineering projects involving aquatic systems, an understanding of sediment-related issues is usually required before implementing important decisions, *e.g.* regarding construction or restoration. This especially includes dredging of shipping channels, construction of piers, breakwaters, and harbours, and restoration of eutrophic lakes and estuaries (James *et al.*, 2010). Therefore, understanding sediment transport is critical for predicting sediment movements and evaluating the short and/or long-term influence to surface water systems.

Numerical simulations are often the most efficient and practical methods for understanding and predicting sediment transport in complex hydrodynamic systems. Numerical modelling requires descriptions of the individual processes involved in sediment transport, specifically erosion, deposition, and movement of sediments in the water column. Erosion is the flux of particles from a sediment bed into the overlying water column, and deposition is the flux of particles back to the sediment bed. The movement of sediment particles in a water column is due to advection,

turbulent dispersion, and settling. An accurate treatment of the interaction between these processes leads to improved predictions of sediment transport in aquatic systems.

From a theoretical perspective, the traditional sediment transport modelling usually consists of the following aspects:

1. Modelling hydrodynamics

The hydrodynamics is usually modelled with the Reynolds-averaged Navier–Stokes equations that describe the motion of viscous fluids. This is fundamental to the sediment transport modelling since it solves the flow field and sediment movement depends on the flow conditions.

2. Modelling sediment movements

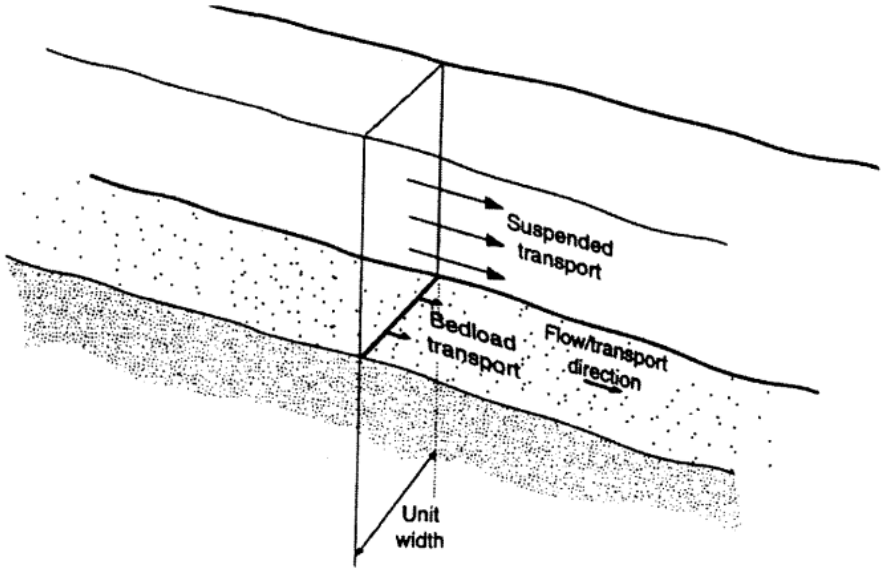

Figure 2.1. Bedload- and suspended transport (Soulsby, 1997)

Usually two kinds of sediment movements are considered. One is called suspended load, which means that the sediment particles are carried by the fluid and kept in suspension by the turbulent flow. In this case, turbulence plays an essential role. The suspended load is often modelled by the advection-diffusion equation. It describes physical phenomena where particles are transported within a physical system due to two processes: diffusion and advection. The diffusion is mainly caused by the turbulent dispersion and the concentration gradient while the advection

describes the process, which is that the concentration changes due to the flow motion.

The other kind of sediment motion is bedload. It describes particles in a flowing fluid that are transported along the bed. Bedload moves by traction (rolling and sliding), and/or saltation. There are many (semi) empirical formulas for solving the bedload transport. The commonly used ones are from Meyer-Peter & Müller (1948), Einstein (1950), Engelund & Hansen (1967), Van Rijn (1984), *etc*.

3. Modelling erosion/deposition processes

Erosion and deposition provide respectively a source or sink flux as the bottom boundary conditions for the advection-diffusion equation of sediment transport. Moreover, they also provide an important source term in the equation for the bed-level elevation for the morphology.

4. Modelling turbulence

Turbulence modelling is crucial to sediment transport modelling, not only because it can affect the sediment movements in the water column, but also because it can be altered by the sediment particles and further influence the flow field. The most widely used and validated model for wall-bounded turbulence is the two-equation k-ε model. For sediment transport modelling, it can be modified in order to account for the two-way coupling effects between sediment and fluid.

Because the above governing equations are highly nonlinear and it is impossible to solve analytically, numerical methods should be applied in order to find the best approximations to the problem. In general, the process of obtaining computational solutions consists of two stages: conversion of partial differential equations and auxiliary conditions into a system of discrete algebraic equations, and then implementation of numerical method to solving the system of linear equations.

In computational fluid dynamics, there are two modern approaches for discretization, Finite Volume Method (FVM) and Finite Element Method (FEM).

The FVM uses the integral form of the conservation equations as its starting point. The solution domain is subdivided into a finite number of contiguous control volumes (CVs), and the conservation equations are applied to each CV. At the centroid of each CV lies a computational node at which the variable values are to be calculated. Interpolation is used to express variable values at the CV surface in terms of the nodal (CV-centre) values. Surface and volume integrals are approximated using suitable

quadrature formulae. As a result, one obtains an algebraic equation for each CV, in which a number of neighbour nodal values appear. The FVM can accommodate any type of grid, so it is suitable for complex geometries. The grid defines only the control volume boundaries and need not be related to a coordinate system. The method is conservative by construction, so long as surface integrals (which represent convective and diffusive fluxes) are the same for the CVs sharing the boundary. The disadvantage of FVM is that methods of order higher than second are more difficult to develop in 3D. This is due to the fact that the FV approach requires three levels of approximation: interpolation, differentiation, and integration (Ferziger & Peric, 2002).

The FEM is similar to the FV method in many ways. The domain is broken into a set of discrete volumes or finite elements that are generally unstructured; in 2D, they are usually triangles or quadrilaterals, while in 3D tetrahedra or hexahedra are most often used. The distinguishing feature of FE methods is that the equations are multiplied by a weight function before they are integrated over the entire domain. In the simplest FE methods, the solution is approximated by a linear shape function within each element in a way that guarantees continuity of the solution across element boundaries. Such a function can be constructed from its values at the corners of the elements. The weight function is usually of the same form. This approximation is then substituted into the weighted integral of the conservation law and the equations to be solved are derived by requiring the derivative of the integral with respect to each nodal value to be zero; this corresponds to selecting the best solution within the set of allowed functions (the one with minimum residual). The result is a set of non-linear algebraic equations. An important advantage of finite element methods is the ability to deal with arbitrary geometries; there is an extensive literature devoted to the construction of grids for finite element methods. The grids are easily refined; each element is simply subdivided. Finite element methods are relatively easy to analyse mathematically and can be shown to have optimality properties for certain types of equations. The principal drawback, which is shared by any method that uses unstructured grids, is that the matrices of the linearized equations are not as well structured as those for regular grids making it more difficult to find efficient solution methods (Ferziger & Peric, 2002). The order of accuracy of FEM increases by raising the approximation order within elements. The basic steps of solving a problem using FEM are as follows:

- Discretization of the problem by selection of elements interconnected at nodal points.
- Evaluation of the matrices of the element by applying the governing equations.
- Formulation of the complete matrix of the continuum.
- Application of the boundary conditions.
- Solution of the resulting system of equations.
- Calculations of any other functions based on nodal unknowns.

For solving the system of linear equations, the commonly used numerical methods are Gaussian Elimination, Conjugate Gradient Method and Generalised Minimum Residual Method.

2.2. TELEMAC-SISYPHE

2.2.1. Overview

The openTELEMAC system consists of a complete processing chain for the calculation of water, solute and sediment motions in the fluvial, coastal, estuarine and lacustrine domains. It comprises pre-processors for digitizing the data and describing the problem, simulation programmes and post-processors for displaying and analysing the results. One of the key assets of the system is the use of the finite element theory that comprises a rigorous theoretical framework and a flexibility for describing complex geometries (Hervouet *et al.* 2000).

There are several modules in the openTELEMAC system and the most commonly used modules are as follows:

- TELEMAC-2D is a horizontal depth-averaged hydrodynamics solver. It solves the Saint-Venant (or shallow water) equations in two dimensions.
- TELEMAC-3D solves the three-dimensional Navier-Stokes equations with a free surface.
- SYSIPHE uses the results of the TELEMAC-2D and TELEMAC-3D to undertake simulation of bedload and suspended sediment transport. It offers various sediment transport formulas and multi-layer consolidation model.

- TOMAWAC models the changes of the power spectrum of wind-driven waves and wave agitation for applications in the oceanic domain, in the intracontinental seas as well as in the coastal zone.

All the physical phenomena treated by modules in the openTELEMAC system generally interact, *e.g.* the hydrodynamics may generate sediment transport, which modifies the topography and hence has an influence on the hydrodynamics. This is called two-way coupling.

2.2.2. TELEMAC-2D

In TELEMAC-2D, the Navier-Stokes equations for incompressible flow are averaged vertically by integration from the bottom to the surface, taking into account the impermeability conditions of the bottom and surface. They are solved simultaneously using the finite-element method, as well as the equation for tracer conservation (Hervouet, 2007). To be more specific, it solves the following equations.

Continuity equation:

$$\frac{\partial h}{\partial t}+\frac{\partial (hu)}{\partial x}+\frac{\partial (hv)}{\partial y}=0 \qquad (2.1)$$

Momentum along x:

$$\frac{\partial (hu)}{\partial t}+\frac{\partial (huu)}{\partial x}+\frac{\partial (huv)}{\partial y}=-gh\frac{\partial Z_s}{\partial x}+S_x+\nabla\cdot\left[h(\nu+\nu_t)\nabla u\right] \qquad (2.2)$$

Momentum along y:

$$\frac{\partial (hv)}{\partial t}+\frac{\partial (huv)}{\partial x}+\frac{\partial (hvv)}{\partial y}=-gh\frac{\partial Z_s}{\partial y}+S_y+\nabla\cdot\left[h(\nu+\nu_t)\nabla v\right] \qquad (2.3)$$

Tracer conservation:

$$\frac{\partial (hT)}{\partial t}+\frac{\partial (hTu)}{\partial x}+\frac{\partial (hTv)}{\partial y}=S_T+\nabla\cdot(h\nu_T\nabla T) \qquad (2.4)$$

in which: h = water depth [m], u and v = velocity components [m/s], T = passive (non-buoyant) tracer, g = the gravity acceleration [m/s^2], ν_t = turbulent viscosity [m^2/s] and ν = kinematic water viscosity [m^2/s], ν_T = the tracer diffusivity coefficient, Z_s = free surface elevation (positive upwards) [m], t = time [s], x and y = horizontal space coordinates [m], S_x

and S_y = source terms representing the wind, Coriolis force, bottom friction, a source or a sink of momentum within the domain, S_T = the tracer source or sink term.

The turbulent viscosity may be given by the user. In this case, a constant viscosity is imposed and it is sufficient when flow is governed by the pressure gradient and by advection, for example the tide-driven flow, and especially for modelling oceanic circulation on a large scale (Hervouet, 2007). However, there are also several other approaches provided in TELEMAC-2D for modelling turbulent viscosity: zero-equation models, such as the Elder model and the Smagorinsky model, and the most commonly used two-equation model, k-ε model (vertical averaged in TELEMAC-2D).

As a module in the openTELEMAC system, TELEMAC-2D is able to take into account the following phenomena thanks to the integration with other modules (TELEMAC-2D software release 7.0 user manual, 2014):

- Propagation of long waves, including non-linear effects,
- Friction on the bed,
- The effect of the Coriolis force,
- The effects of meteorological phenomena such as atmospheric pressure and wind,
- Turbulence,
- Supercritical and subcritical flows,
- Influence of horizontal temperature and salinity gradients on density,
- Cartesian or spherical coordinates for large domains,
- Dry areas in the computational field: tidal flats and flood-plains,
- Entrainment and diffusion of a tracer by currents, including creation and decay terms,
- Particle tracking and computation of Lagrangian drifts,
- Treatment of singularities: weirs, dikes, culverts, etc.,
- Dyke breaching,
- Drag forces created by vertical structures,
- Porosity phenomena,

- Wave-induced currents,
- Coupling with sediment transport,
- Coupling with water quality tools.

2.2.3. SISYPHE

SISYPHE is a module of the openTELEMAC system for modelling sediment transport and morphodynamics. In SISYPHE, sediment transport rates, split into bedload and suspended load, are calculated at each node as a function of various flow (velocity, water depth, wave height, etc.) and sediment (grain diameter, relative density, settling velocity, etc.) parameters.

The bedload is calculated by using a classical sediment transport formula from the literature. SISYPHE provides a variety of bedload transport formulas. The commonly used formulas in SISYPHE are listed below.

Table 2.1. Validity range of some of the bedload transport formulas.

Formula	**Meyer-Peter & Müller (1948)**	**Einstein–Brown (1950)**	**Engelund-Hansen (1967)**	**van Rijn (1984)**
Mode of transport	bedload	bedload	bedload + suspended load	bedload
Validity range (d_{50})	0.4-29mm	0.25-32mm	0.19-0.93mm	0.2-2.0mm

The suspended load is determined by solving an advection-diffusion equation for the depth-averaged suspended sediment concentration. It is obtained by integrating the 3D advection-diffusion equation over the suspended-load zone. By applying the Leibniz integral rule, adopting suitable boundary conditions and assuming that the bedload zone is very thin, the depth-integrated suspended-load transport equation is obtained:

$$\frac{\partial(hC)}{\partial t}+\frac{\partial(hUC)}{\partial x}+\frac{\partial(hVC)}{\partial y}=\frac{\partial}{\partial x}\left(h\varepsilon_s\frac{\partial C}{\partial x}\right)+\frac{\partial}{\partial y}\left(h\varepsilon_s\frac{\partial C}{\partial y}\right)+E-D \tag{2.5}$$

with h = water depth [m], assuming that the bedload layer thickness is very thin, U and V = depth-averaged velocity components [m/s], C = depth-averaged suspension concentration [kg/m^3], E = erosion flux [kg·m^{-2}·s^{-1}], D = deposition flux [kg·m^{-2}·s^{-1}], and ε_s = diffusivity coefficient for sediment particles [m^2/s].

For the non-cohesive sediment, the net sediment flux E-D is determined based on the concept of equilibrium concentration:

$$(E-D)_{Z_{ref}}=w_s\left(C_{eq}-C_{ref}\right) \tag{2.6}$$

where w_s is the settling velocity of particle [m/s], C_{eq} is the equilibrium near-bed concentration [kg/m^3] and C_{ref} is the near-bed reference concentration [kg/m^3], calculated at the interface between the bed-load and the suspended load. The reference elevation Z_{ref} [m] corresponds to the interface between bedload and suspended load.

The equilibrium near-bed concentration C_{eq} can be determined by different fomulas, e.g. Zyserman and Fredsøe formula (1994), Bijker formula (1992) and van Rijn formula (1984).

Take the Zyserman and Fredsøe formula for example. The equilibrium near-bed concentration C_{eq} is given by:

$$C_{eq}=\frac{0.331\left(\theta'-\theta_c\right)^{1.75}}{1+0.72\left(\theta'-\theta_c\right)^{1.75}} \tag{2.7}$$

with θc is the critical Shields parameter, $\theta' = \mu\theta$, the non-dimensional skin friction which is related to the Shields parameter, μ is the dynamic viscosity of water.

The near-bed reference concentration C_{ref} is calculated using the relation established between the depth-averaged concentration and the near-bed reference concentration C_{ref}:

$$C_{ref}=FC \tag{2.8}$$

In SISYPHE, the ratio F can be approximated by the expression:

$$F^{-1} = \begin{cases} \dfrac{1}{1-Z}\left(\dfrac{Z_{ref}}{h}\right)^{R}\left(1-\left(\dfrac{Z_{ref}}{h}\right)^{1-R}\right), & \text{for } R \neq 1 \\ -\dfrac{Z_{ref}}{h}\log\left(\dfrac{Z_{ref}}{h}\right), & \text{for } R = 1 \end{cases} \tag{2.9}$$

in which, C is the depth-averaged concentration, Z is the water level, h is the water depth, and R is the rouse number.

For the cohesive sediment, the classical Partheniades formula is applied for computing the erosion flux:

$$E = \begin{cases} M\left(\left(\dfrac{u_*}{u_{*e}}\right)^2 - 1\right), & \text{if } u_* > u_{*e} \\ 0, & \text{otherwise} \end{cases} \tag{2.10}$$

The deposition flux is calculated as a function of the near bed concentration:

$$D = \begin{cases} 0, & \text{if } u_* > u_{*d} \\ w_s C\left(1-\left(\dfrac{u_*}{u_{*d}}\right)^2\right), & \text{otherwise} \end{cases} \tag{2.11}$$

where u^* is the friction velocity, u_{*e} is the critical erosion shear velocity, M is the Partheniades coefficient, C is the depth-averaged concentration, w_s is the settling velocity, and u_{*d} is the critical deposition. For the computation of deposition flux, it assumes that the bed concentration is approximately equal to the depth-averaged concentration in SISYPHE,

The bed evolution can be calculated by solving the Exner equation:

$$\left(1-n_b\right)\frac{\partial Z_f}{\partial t} + \nabla \cdot Q_b + \left(E - D\right) = 0 \tag{2.12}$$

where n_b is the non-cohesive bed porosity, Z_f the bottom elevation [m], t is the time [s], and Q_b the solid volume transport (bedload) per unit width [m^2/s].

SISYPHE is applicable to non-cohesive sediments (uniform or graded), cohesive sediments as well as sand-mud mixtures. The sediment

composition is represented by a finite number of classes, each characterized by its mean diameter, grain density and settling velocity. Sediment transport processes can also include the effect of bottom slope, rigid beds, secondary currents (bedload movement direction deviates from the main flow direction due to helical flow effect) and slope failure. For cohesive sediments, the effect of bed consolidation can be accounted for.

SISYPHE can be applied to a large variety of hydrodynamic flow conditions including rivers, estuaries and coastal applications. For the latter, the effects of waves superimposed to a tidal current can be included. The bed shear stress, decomposed into skin friction and form drag, can be calculated either by imposing a friction coefficient (Strickler, Nikuradse, Manning, Chézy or user defined) or by a bed-roughness predictor.

In SISYPHE, the relevant hydrodynamic variables can be either imposed in the model (chaining method) or calculated by a hydrodynamic computation (internal two-way coupling) by using one of the hydrodynamic modules of the openTELEMAC system (modules TELEMAC-2D or TELEMAC -3D) or an external hydrodynamic model.

Chapter 3

LESSONS FROM TWO-PHASE FLOW THEORY

3.1. Introduction

In the last two decades, many numerical models of suspended sediment transport in estuaries and coastal zones have been made. Most of the existing numerical models, which are single-phase, are based on the hypothesis that solid particles move at the same velocity as fluid particles, with the exception of their falling velocity. This is known as the ‘‘passive scalar” hypothesis. However, there remain a number of flaws regarding the physical concept. The impact of particle motion upon fluid flows, for example, is ignored. Nor are particle–particle interactions, which can be very strong in dense flows, taken into account. Consequently, the single-phase models are likely to lose predictive capacity. In order to correct the flaws mentioned above, another approach, two-phase flow (fluid and solid particles), has been developed.

In a two-phase sediment transport model, the computational domain is extended to the ‘‘true” non-erodible bottom (to incorporate bedload which is no longer computed separately), while the governing equations are the same for both high and low concentration areas of the domain. Fluid flows are free surface and considered as non-hydrostatic. The main physical processes for sediment transport such as fluid-solid particles, particle-particle interactions, particle-wall collision, and fluid-bottom exchanges are integrated into the equations of motion and treated as momentum exchanges between phases. Fluid mud is handled as a non-Newtonian fluid. In the physical sense, this approach is more complex, but more realistic than the single-phase modelling (Nguyen et al., 2009).

Models for the flow of a fluid with dispersed particles or flocs can be formulated with two kinds of two-phase flow models. In the case of a dilute suspension there are only a few particles suspended in the liquid. If the interaction between the particles is weak, a Lagrangian model for the particulate phase can be used. By solving Newton’s law of motion, each particle is kept track of in the flow of the continuous phase. In a high concentration benthic suspension, the interactions between the particles and between the phases have to be considered. A Lagrangian model

would not be practical since the effort to keep track of every particle would be computationally expensive.

To model the behaviour of high concentration benthic suspension mathematically an Eulerian two-phase fluid model or two-fluid model should be used. The suspension is then treated as a two-constituent mixture of solid particles and a fluid. Both phases are described as incompressible continua assumed to satisfy averaged equations of motion. This means, for each phase, conservation of mass and of momentum is formulated as partial differential equations. The phases are coupled through the inter-phase momentum transfer. A scalar volume fraction field is introduced for the proportion of the total volume occupied by particles.

Because the length scales related to the flow process are much larger than the microscopic length scales related to the suspension, e.g. a typical particle size, it is sufficient to describe each phase as a continuous medium. The local instantaneous conservation equations for mass, momentum and energy supplemented with jump conditions at the interfaces between the fluid and particles are averaged over each field to produce a two-fluid model.

3.2. Concepts and related Work

Suspended sediment concentration above 0.1% is common near the bed in nature and it falls within the range of four-way coupling from Elghobashi's (1994) classification for multiphase flow. Thus, from a physical point of view, significant interactions between flow and particles are expected, as well as inter-particle interactions. The way to account for these effects properly is to implement two-phase flow theory.

Toorman (2008) made some further interpretations on the multiphase processes in the sediment-laden flows from the aspect of momentum transfer. For very small volumetric concentrations ($\phi<10^{-6}$) the particle motion is determined by the fluid, while the momentum transfer from the particles to the turbulence has a negligible effect on the flow. This is called one-way coupling. For higher concentrations, the momentum transfer from the particles is large enough to alter the turbulence. When heavier than the fluid, particles will respond slower to sudden accelerations than the fluid and energy is dissipated by friction between the two phases (inertia effect). Furthermore, gravity opposes upward and favours downward fluctuations of the suspended particles (buoyancy or

stratification effect). These phenomena are called two-way coupling. The effects of mutual hindrance and inter-particle friction and collisions, referred to as four-way coupling (*i.e.*, particle fluctuations are affected not only by the fluid, but also by the particles themselves, while fluid fluctuations are affected by particle movements), become increasingly important with higher concentrations (ϕ>10^{-3}).

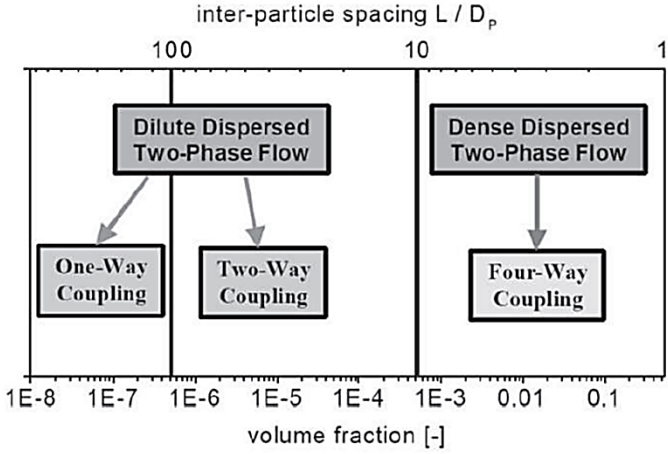

Figure 3.1. Quantification of momentum coupling approaches in terms of entity spacing and volume fraction

Recent measurements indeed have demonstrated that the turbulent fluctuations of solid particles and fluid are not the same (Rashidi *et al.*, 1990; Best *et al.*, 1997). Furthermore, experiments on turbulent suspension flows show that turbulence can be enhanced or damped and the maximum suspension capacity is governed by the auto-suspension capacity of the high-concentrated near-bed layer where four-way particle-fluid interactions are very important. Therefore, for the high-concentration near-bottom layer, the particle-turbulence interactions as well as particle-particle interactions should be considered.

Many studies have suggested that the existence of sediment particles in water can change the turbulence characteristics in suspended sediment-laden flows. This phenomenon becomes more notable when the sediment concentration is high. Tsuji and Morikawa (1982) showed that small particles with diameter of about 200 μm attenuated the turbulence outside the viscous sublayer, while larger particles with diameter in the range of 3-4 mm lead to augmentation of turbulence fluctuations.

Gore and Crowe (1989) have first reviewed the earlier research on particle-fluid interactions, *i.e.*, the two-way coupling, in particle-laden air jets and pipe flows, and proposed a noticeable criterion that smaller size particles than the scale of energy-containing eddies suppress the turbulence, whereas larger size particles enhance it. Further, Hetsroni (1989) re-examined the particle-turbulence interactions on the basis of available experimental data of mainly gas-solid flows (some liquid-solid and gas-liquid flows were also examined) including data of Gore and Crowe (1989) and found that the presence of smaller particles with a low particle Reynolds number tended to suppress the turbulence of the carrier fluid. In contrast, he concluded that larger particles with high particle Reynolds number (based on relative velocity and particle size), larger than about 400, tended to enhance the turbulence most likely due to vortex shedding by particles.

Lyn (1991) has first conducted the simultaneous measurements of particle phase and fluid phase in sediment-laden open channel flows by laser Doppler anemometer (LDA), and pointed out that the fluid velocity of sediment-laden flow became slower than that of sediment-free flow (*i.e.*, clear-water flow) as the particle concentration increased. Lyn (1992) also found that turbulence characteristics in sediment-laden open-channel flows might be changed significantly by particle-turbulence interaction as compared with those in clear-water flows. Yarin and Hetsroni (1994) also studied particle-turbulence interactions. They showed that finer particles damped the turbulence, while coarser particles enhanced it. They found that the level of turbulence modulation was affected by four parameters: the particle mass loading, the particle-fluid density ratio, the particle Reynolds number, and the ratio of the particle diameter to the characteristic eddy diameter. Furthermore, Song *et al.* (1994) measured the bed-load flow in the near-bed region by acoustic Doppler velocimetry (ADV), and pointed out that the turbulence intensity and Reynolds stress became weaker than those of the fixed-bed clear-water flow due to the existence of bed-load materials. These earlier experimental results of turbulence modulation in sediment-laden open-channel flows might be similar to those of gas-solid two-phase flows, and thus it is further necessary to investigate the mechanism of such particle-turbulence interaction based on recent turbulence theory.

It is well known that the coherent structure of ejections and sweeps occurs intermittently and periodically near the wall in boundary layers and open-channel flows. This so-called bursting phenomenon is quite important in particle entrainment and transport mechanism, as pointed

out by Rashidi *et al.* (1990), Ninõ and García (1998), and others. They suggested that the ejections and sweeps in the near-wall region might govern the interaction between particles and fluid. The transport mechanism of suspended sediment is also one of the most important and challenging topics in river engineering, because it has a complicated interaction among turbulent flow, particle motion and bed configuration. Therefore, many efforts have been devoted to the understanding and predictive capability of the closely coupled phenomena of sediment-laden flow and sediment transport in open-channel flows. Rashidi *et al.* (1990) and Ninõ and Garcia (1998) have measured the suspended particle motion in sediment-laden flows by flow-visualization techniques, and pointed out that the fluid velocities are faster than those of particles in the outer layer of open-channel flow. However, the velocities of particles and fluid were not measured simultaneously in their research. Yamamoto *et al.* (2001) studied the interaction between turbulence and solid particles in a fully developed channel flow using LES; they also considered the inter-particle collisions that were important for flows with high mass loading of particles.

Recently, simultaneous measurements of both fluid velocity and particle velocity in sediment-laden open-channel flows have been feasible with non-intrusive measurement techniques. Best *et al.* (1997) and Righetti & Romano (2004) have conducted simultaneous velocity measurements of water and glass beads using a phase Doppler anemometer (PDA). PDA is an epoch-making system for the simultaneous measurements of particle-laden flows although particles must be exact sphere. They suggested that the enhancement and suppression of turbulence intensity due to particles were distinguished by the Stokes number of particle-laden flow. Muste and Patel (1997) have developed LDA system incorporated with a unit for particle-size discrimination and measured the particle velocity U_p and fluid velocity U_f simultaneously in the outer layer of open-channel flow. Kulick *et al.* (1994) conducted similar measurements in duct flow and pointed out an existence of the relative velocity between particles and fluid. That is to say, the values of ($U_p - U_f$) did not become equal to zero, and thus the particle Reynolds number had a finite value, which inferred an occurrence of turbulence modulation on the basis of Hetsroni's (1989) criterion. To reveal the momentum exchanges between particles and fluid, Kaftori *et al.* (1995) have measured the relative velocity by using LDA even in the near-wall region although the particle specific density ρ_p was near-neutrally buoyant solid particles, i.e., the density ratio of particle to fluid ρ_p/ρ_f = 1.05. They pointed out that the averaged velocity of particles was larger than that of carrier fluid in the near-wall region. This feature of the

relative velocity is opposite to that of the outer region. They explained then that the result of $U_p > U_f$ very near the wall might be caused by the following two factors, *i.e.*, one is the deceleration of fluid velocity due to viscous effect and the other is due to the high speed particles which inrush into the viscous sublayer. These surprising results of Kaftori *et al.* (1995) that the particle velocity might become larger than the carrier water velocity very near the wall have recently been verified using innovative PIV/PTV measurements by Nezu and Azuma (2004), Muste *et al.* (2009) and others, who all pointed out the importance of simultaneous measurements of particles and fluid in open channel flows.

Such simultaneous measurements of particles and fluid have first been conducted by LDA and PDA as mentioned above, although these measurement systems have some difficult limitations. For example, the size of suspended particles have to be small enough in order to avoid the blocking of laser beams due to particles. Only spherical particles are feasible in PDA measurements. Moreover, because LDA and PDA are point measurement systems, it is rather difficult to examine the relation among the coherent structure, particle-fluid interaction and particle concentration in sediment-laden open-channel flows. To overcome such difficulties, Nezu and Azuma (2004) have measured both the fluid and particle velocities simultaneously in sediment-laden open-channel flows by using a discriminator Particle Tracking Velocimetry (D-PTV), in which sediment particles were separated from fluid tracers by the occupied area of particles in camera images. With this technique of PTV, the relative velocity between particles and fluid was examined in the inner layer as well as in the outer layer. Recently, Bigillon *et al.* (2006), Breugem and Uijttewaal (2006), Le Louvetel-Poilly *et al.* (2007), Noguchi *et al.* (2008) and Muste *et al.* (2009) have conducted simultaneous measurements of particles and fluid velocities in sediment-laden open-channel flows by using a combination of PTV and PIV, the techniques of which are almost similar to those developed by Nezu and Azuma (2004). All of them found an essential importance of particle-turbulence interaction as well as significant contributions of ejection and sweep motions to suspended sediment transport.

Noguchi and Nezu (2009) conducted an experiment to investigate the particle-turbulence interaction and relation with local particle concentration in sediment-laden open-channel flows. The result showed that very near the bed, the velocities of sediment-laden flows were faster than those of clear-water flow. These tendencies are in good agreement with recent data of Muste et al (2009). It is considered that the existence

of particles cannot be disregarded in the viscous layer when dimensionless distance from the bottom $y^+ \leq 10$. In the near-wall region of $y^+ \leq 15$, the particle velocity U_p is faster than the fluid velocity U_f, whereas in the region of $15 \leq y^+ \leq 100$, the particles are transported slower than the carrier fluid. In the outer region of $y^+ \geq 100$, the value of U_p approaches to the U_f distribution because of the good following of suspended particles to the carrier flow. From these tendencies of $U_p - U_f$ the sediment-laden turbulence structure can be classified into three sub-regions, (i) the viscous region of $y^+ \leq 15$, (ii) the inner region of $15 \leq y^+ \leq 100$, and (iii) the outer region of $y^+ \geq 100$. The particle-fluid interaction in the inner region should be distinguished from that in the outer region. In the inner region, the particle concentration is much larger than the volume-averaged one. Therefore, the particle-fluid interaction (two-way coupling) would be also influenced by the particle-particle interaction (four-way coupling) in the inner region. On the other hand, in the outer region, the particle concentration is much smaller than the volume-averaged one, and consequently, the four-way coupling effects may be negligibly small. It is also found that the heavier particles of $\rho_p/\rho_f = 1.5$ have slightly larger relative velocity than the light particles of $\rho_p/\rho_f = 1.2$, which infers an effect of particle inertia. The turbulence enhancement and suppression by particles in water flows might depend on the particle size d_p rather than the particle density ρ_p. The critical diameter d_c of turbulence modulation, in which turbulence is enhanced at $d_p > d_c$ whereas it is suppressed at $d_p < d_c$, was evaluated as $d_c = 0.44$ mm. This value of d_c was in good agreement with the zone-averaged Kolmogoroff microscale. However, this criterion found are only valid for smooth bottoms, as found in laboratory flumes, which are not representative for non-flat and rough natural sediment beds. Furthermore, one would expect also adapted criteria depending on the relative particle size.

In the study of Noguchi and Nezu (2009), they also investigated the properties of turbulent motions. There are four types of turbulent motions which can be observed by employing the quadrant analysis (Corino and Brodkey, 1969). These motions are identified as low-speed fluid moving away from the wall called ejections ($u' < 0, v' > 0$), high-speed fluid moving toward the wall called sweep ($u' > 0, v' < 0$), high-speed fluid from the sweep motion reflected back as outward interaction ($u' > 0, v' > 0$), and low-speed fluid being pushed back toward the wall as inward interaction ($u' < 0, v' < 0$). Ejections and sweeps are most energetic and together account for about 70% of the turbulent shear stress in boundary layers (Bridge, 2009). In Noguchi and Nezu's (2009) experiment, the counted number of ejections and sweeps are not changed significantly by

the existence of suspended sediment. The local particle concentration increased when the ejections occurred, whereas it decreased when the sweeps occurred. The stronger ejections increase the local particle concentration, whereas the stronger sweeps decrease it. This suggests that the stronger and more violent ejections contribute to sediment transport more significantly. The largest contribution to the sediment flux is from the ejection events. The second largest contribution is from the sweeps. The outward and the inward interactions are negligibly small. This means that the ejection and sweep events play an important role in sediment transport.

Zaichik *et al.* (2008) developed statistical models for predicting the transport, dispersion, and deposition of colliding particles in the framework of the Eulerian continuum approach. The models start from a kinetic equation for the probability density function (PDF) of the particle velocity distribution in anisotropic turbulent flow. The particle–turbulence interaction is modelled by a second-order operator of the Fokker–Planck type, while the particle–particle interaction is described by an integral operator of the Boltzmann type. The models are able to capture the main features of transport, deposition, and preferential concentration of non-colliding and colliding particles in turbulent channel flows. The main predicted effects of collisions on the particulate phase consist of a decrease in the average streamwise velocity, increasing the transverse fluctuating velocity, and decreasing the preferential accumulation in the near-wall region of the flow as well as in enhancing the deposition rate. However, their models are only valid for small volume fractions.

3.3. Governing equations for two-phase/mixture model

In order to describe the physical processes in the two-phase flow, the following basic governing equations are employed (Toorman, 2008):

Conservation of mass

In the case of non-cohesive sediments (like sand), the solids mass conservation is:

$$\frac{\partial \phi}{\partial t} + \frac{\partial (v_j \phi)}{\partial x_j} = 0 \tag{3.1}$$

And fluid mass conservation:

$$\frac{\partial(1-\phi)}{\partial t}+\frac{\partial(u_j(1-\phi))}{\partial x_j}=0 \tag{3.2}$$

Conservation of momentum

The volume-averaged momentum conservation equation for particle phase is written as:

$$\frac{\partial(\rho_p\phi v_i)}{\partial t}+\frac{\partial(\rho_p\phi v_i v_j)}{\partial x_j}=-\phi\frac{\partial p}{\partial x_i}+\rho_p\phi g\delta_{iz}+f_i+\phi\frac{\partial\sigma_{pij}}{\partial x_j} \tag{3.3}$$

or, using mass conservation equation

$$\rho_p\frac{\partial v_i}{\partial t}+\rho_p v_j\frac{\partial v_i}{\partial x_j}=-\frac{\partial p}{\partial x_i}+\rho_p g\delta_{iz}+\frac{f_i}{\phi}+\frac{\partial\sigma_{pij}}{\partial x_j} \tag{3.4}$$

For the fluid phase, one can write the equivalent:

$$\begin{aligned}\frac{\partial(\rho_f(1-\phi)u_i)}{\partial t}+\frac{\partial(\rho_f(1-\phi)u_i u_j)}{\partial x_j}\\ =-(1-\phi)\frac{\partial p}{\partial x_i}+\rho_f(1-\phi)g\delta_{iz}-f_i+(1-\phi)\frac{\partial\sigma_{fij}}{\partial x_j}\end{aligned} \tag{3.5}$$

or, using mass conservation equation

$$\rho_f\frac{\partial u_i}{\partial t}+\rho_f u_j\frac{\partial u_i}{\partial x_j}=-\frac{\partial p}{\partial x_i}+\rho_f g\delta_{iz}-\frac{f_i}{1-\phi}+\frac{\partial\sigma_{fij}}{\partial x_j} \tag{3.6}$$

In the above equations, ϕ = the volume fraction of the particle phase, t = time [s], x = the location of Cartesian coordinate [m], i and j = the indices of the coordinate, v = the particle velocity [m/s] and u = the fluid velocity [m/s], ρ_p = the density of particles [kg/m^3], ρ_f = the density of fluid [kg/m^3], p = the pressure [Pa], g = the gravity constant [m/s^2], δ = the Kronecker delta, σ_p = the viscous stress of particle phase [kg·m^{-1}·s^{-2}], σ_f = the viscous stress of fluid phase [kg·m^{-1}·s^{-2}], f = the interaction forces between the two phases.

The basic governing equations are able to describe the fundamental physical processes and interactions in the two-phase flow, however, they cannot be directly implemented to engineering applications since they require unacceptable small time scale and mesh size. The commonly used Reynolds-averaging procedure is also not ideal for these equations

because it will add many extra terms that cannot be easily modelled. To overcome this issue, a different kind of Reynolds-averaged related velocities is introduced. It consists of a Reynolds-averaged part and a so-called drift velocity in addition to that. The advantage using this form is that it can reduce the extra terms in the averaged governing equations and thus reduce the complexity. However, its disadvantage is also obvious: the drift velocities cannot be directly measured from the physical models.

The most elegant form of equations is obtained in terms of representative fluid velocity U_i and solids velocity V_i related to Reynolds-averaged properties (Toorman, 2008):

$$U_i = \overline{u_i} + \frac{-\overline{u_i'\phi'}}{1-\overline{\phi}} = \overline{u_i} + U_{Di} \quad \text{and} \quad V_i = \overline{v_i} + \frac{\overline{v_i'\phi'}}{\overline{\phi}} = \overline{v_i} + V_{Di} \tag{3.7}$$

where: $\overline{u_i}$ and $\overline{v_i}$ = the respective Reynolds-averaged fluid and solids velocities [m/s], U_{Di} and V_{Di} are the respective fluid and solids drift velocities [m/s], $\overline{\phi}$ = the Reynolds-averaged solids volume fraction, $-\overline{u_i'\phi'}$ and $\overline{v_i'\phi'}$ = the respective Reynolds averaged fluid and solids turbulent flux. Substitution of (3.7) into the Reynolds-averaged equations leads to the following equations (for the details of the derivation please refer to Appendix I).

The suspension continuity equation reads:

$$\frac{\partial(U_j + W_j\overline{\phi})}{\partial x_j} = 0 \tag{3.8}$$

where: x_j = the location coordinate [m], and $W_j=V_j-U_j$ = the (Reynolds-averaged related) slip velocity [m/s]. The exact suspension momentum equation becomes:

$$\begin{aligned}\rho\left(\frac{\partial U_i}{\partial t} + U_j\frac{\partial U_i}{\partial x_j}\right) = &-\frac{\partial \overline{p}}{\partial x_i} + \rho g\delta_{iz} + \frac{\partial \overline{\sigma_{ij}}}{\partial x_j} + \frac{\partial(\sigma_{Tij}+\sigma_{Dij})}{\partial x_j} \\ &- \rho_p\overline{\phi}\left(\frac{\partial W_i}{\partial t} + U_j\frac{\partial W_i}{\partial x_j} + W_j\frac{\partial(U_i+W_i)}{\partial x_j}\right)\end{aligned} \tag{3.9}$$

with: $\rho = \rho_p\overline{\phi} + \rho_f(1-\overline{\phi})$ = the suspension bulk density [kg/m^3], p = pressure [Pa], g = gravity constant [m/s^2], σ_T = the turbulent Reynolds

stress [kg·m^{-1}·s^{-2}] and σ_D = the drift diffusion stress [kg·m^{-1}·s^{-2}], respectively given by:

$$\sigma_{Tij} = \rho_p \bar{\phi}(-\overline{v_i' v_j'}) + \rho_f (1-\bar{\phi})(-\overline{u_i' u_j'}) \tag{3.10}$$

$$\sigma_{Dij} = \rho_p \bar{\phi}(V_{Di} V_{Dj}) + \rho_f (1-\bar{\phi})(U_{Di} U_{Dj}) \tag{3.11}$$

The suspension Reynolds stress can be approximated by $\sigma_{Tij} \approx -\rho\overline{u_i' u_j'}$. The drift velocities can be closed using a gradient diffusion hypothesis (Combest *et al.*, 2011):

$$U_{Di} = \frac{-\overline{u_i'\phi'}}{1-\bar{\phi}} = \frac{1}{1-\bar{\phi}} \frac{\nu_t}{\sigma_t} \frac{\partial \bar{\phi}}{\partial x_i} \quad \text{and} \quad V_{Di} = \frac{\overline{v_i'\phi'}}{\bar{\phi}} = \frac{1}{\bar{\phi}} \frac{\nu_t}{\sigma_t} \frac{\partial \bar{\phi}}{\partial x_i} \tag{3.12}$$

with: turbulent eddy viscosity $\nu_t = c_\mu k^2/\varepsilon$ [m^2/s], σ_t = the turbulent Schmidt number and the constant $c_\mu = 0.09$.

The slip velocity W_i can be solved using a so-called drift flux model. Drift flux modelling tries to avoid the solution of the particle momentum equation, by computing the slip velocity from a steady state force balance, which is either obtained from the local relative particle force balance (a local approach) (Maxey and Riley, 1983), or by subtracting the momentum equations for the two phases (*e.g.* a macroscopic approach) (Brethour, 2009). Inertia terms are assumed to be negligible and usually only drag is retained as the dominant interaction force. This results in an algebraic equation for the velocity lag. Toorman (2008) has argued that different particle time scales have to be applied to the drag from respectively the mean particle flow and the particle drift.

3.4. *k-ε* turbulence model for two-phase/mixture model

Turbulence is a key element in the flow of fluid-particle mixtures. It is responsible for the mixing of suspended sediment and the shear stresses (Reynolds stress) in the continuous phase. The influence of the presence of particles or a second phase on the turbulence of the continuous phase is known as turbulence modulation (Crowe, 2000).

Therefore, another important perspective on investigating fluid-particle interactions is the turbulence modelling. Hence, the next step is to derive the corresponding equation for conservation of turbulent kinetic energy (TKE), since the *k-ε* model remains the most popular turbulence closure for large-scale applications (at least for the vertical mixing of sediments).

This results in the determination of the extra terms resulting from the presence of the particle phase.

The derivation of k-ε turbulence model is based on the two-phase/mixture flow equations described in the section 3.3. The momentum conservation equation for the fluid phase are used in the derivation. The detailed derivation is shown in Appendix II.

The turbulent kinetic energy k [m²/s²] and its dissipation rate ε [m²/s³] are defined as:

$$k = \frac{1}{2}\overline{u_i' u_i'} \quad \text{and} \quad \varepsilon = \nu \overline{\frac{\partial u_i'}{\partial x_k}\frac{\partial u_i'}{\partial x_k}} \tag{3.13}$$

in which u_i' is the fluctuating part of the fluid velocity from Reynolds-averaging procedure, ν is the kinematic viscosity of fluid.

Then we have the conservation of turbulent kinetic energy (TKE):

$$\rho_f \frac{\partial k}{\partial t} + \rho_f \overline{u}_j \frac{\partial k}{\partial x_j} = \tau_{ij}\frac{\partial \overline{u_i}}{\partial x_j} - \rho_f \epsilon + \frac{\partial}{\partial x_j}((\mu + \frac{\mu_t}{\sigma_k})\frac{\partial k}{\partial x_j}) + \Pi_k \tag{3.14}$$

with the extra term which is due to the interaction between two phases:

$$\Pi_k = \overline{p'\frac{\partial u_i'}{\partial x_i}} + \frac{1}{2}\overline{\rho_f u_i' u_i' \frac{\partial u_j'}{\partial x_j}} - \overline{u_i'\omega_i'} \tag{3.15}$$

Notice here, instead of using the interaction force f_i in the equation (3.6) for the derivation, the relation $\omega_i = f_i/(1\text{-}\phi)$ is adopted to reduce the complexity.

The conservation of turbulent dissipation rate (TDR):

$$\begin{aligned}\rho_f \frac{\partial \epsilon}{\partial t} + \rho_f \overline{u}_j \frac{\partial \epsilon}{\partial x_j} \\ = C_{\epsilon 1}\frac{\epsilon}{k}\tau_{ij}\frac{\partial \overline{u_i}}{\partial x_j} - C_{\epsilon 2}\rho_f \frac{\epsilon^2}{k} + \frac{\partial}{\partial x_j}((\mu + \frac{\mu_t}{\sigma_\epsilon})\frac{\partial \epsilon}{\partial x_j}) + \Pi_\varepsilon\end{aligned} \tag{3.16}$$

with the extra term*:*

$$\Pi_\varepsilon = \mu\overline{\frac{\partial u_k'}{\partial x_k}\frac{\partial u_i'}{\partial x_j}\frac{\partial u_i'}{\partial x_j}} + 2\nu\overline{\frac{\partial p'}{\partial x_i}\frac{\partial^2 u_i'}{\partial x_j \partial x_j}} - 2\nu\overline{\frac{\partial u_i'}{\partial x_j}\frac{\partial \omega_i'}{\partial x_j}} \tag{3.17}$$

where τ = the viscous stress tensor of fluid [kg·m^{-1}·s^{-2}], μ = fluid dynamic viscosity [N·s/m2], ν = fluid kinematic viscosity [m^2/s], μ_t = turbulent eddy viscosity [N·s/m2], f = the interaction forces between fluid and particle phase [N·m^{-2}·s^{-1}], ϕ = the volume fraction of particle phase, $C_{\varepsilon 1}$, $C_{\varepsilon 2}$, σ_k and σ_ε = the closure coefficients as in the standard k-ε model, which are usually determined semi-empirically and are commonly taken as σ_k = 1.0, σ_ε = 1.3, $C_{\varepsilon 1}$ = 1.44, $C_{\varepsilon 2}$ = 1.92 and C_μ = 0.09 for turbulent shear flows (Rodi, 1980; Chen and Jaw, 1998).

Analysing the extra terms in Π_k and Π_ε suggests that there are two main reasons for these extra terms emerging from the equations:

- the interactions between fluid and particle phases (including forces such as drag force, lift force, virtual mass force and Basset force);
- the presence of the second phases (the quantities such as $\nabla \cdot u$ and $\nabla \cdot v$ are no longer zero due to phase replacing in the control volume).

3.5. Turbulence modulation due to particle phase

In this section, we examine the extra terms appearing in the derived two-phase k-ε model. These extra terms are responsible for the turbulence modulation due to the particle phase. Through the analysis of the experimental data from Muste *et al.* (2005), the turbulence is affected significantly by the presence of the particles in the lower part of the water column near the bottom.

The extra terms in TKE equation are written as:

$$\Pi_k = \overline{p' \frac{\partial u_i'}{\partial x_i}} + \frac{1}{2} \overline{\rho_f u_i' u_i' \frac{\partial u_j'}{\partial x_j}} - \overline{u_i' \omega_i'}$$

The standard approximation made to represent turbulent transport of scalar quantities in a turbulent flow is that of gradient-diffusion (Wilcox, 1994). In analogy to molecular transport processes, the diffusion of a scalar quantity is expressed as:

$$\overline{u_i' \phi'} = -\frac{\nu_t}{\sigma_\phi} \frac{\partial \bar{\phi}}{\partial x_i} \tag{3.18}$$

in which ν_t is the turbulent eddy viscosity [m²/s], σ_ϕ is the turbulent Schmidt number of ϕ, u' is the fluctuating velocity [m/s], ϕ' is the fluctuating part of the quantity ϕ and $\overline{\phi}$ is its Reynolds-averaged mean value.

In the derivation of standard k-ε model, the turbulent transport term $\frac{1}{2}\rho_f \overline{u_i' u_i' u_j'}$ and the pressure diffusion term $\overline{p' u_j'}$ are usually grouped together and the sum assumed to behave as a gradient-transport process (Wilcox, 1994). There is no corresponding straightforward analogy for the pressure diffusion term. Fortunately, recent DNS results (Mansour, Kim and Moin, 1988) indicate that the term is quite small for simple flows. Thus, in the standard k-ε model we have:

$$\frac{1}{2}\overline{\rho_f u_i' u_i' u_j'} + \overline{p' u_j'} = -\frac{\mu_t}{\sigma_k}\frac{\partial k}{\partial x_j} \tag{3.19}$$

where σ_k is a closure coefficient and normally equals to 1. The scalar quantity in equation (3.19) is considered as the TKE:

$$k = \frac{1}{2}\overline{u_i' u_i'}\,.$$

Comparing to the first two terms in Π_k with the turbulent transport term and the pressure diffusion term in equation (3.19), the similarity can be found, which is that the quantity u_j' in the left hand side of (3.19) is replaced by its gradient $\partial u_j'/\partial x_j$.

The second term on the right hand side of equation (3.15) can be written as:

$$\frac{1}{2}\overline{\rho_f u_i' u_i' \frac{\partial u_j'}{\partial x_j}} = \frac{1}{2}\rho_f \left(\frac{\partial(\overline{u_i' u_i' u_j'})}{\partial x_j} - \overline{u_j' \frac{\partial u_i' u_i'}{\partial x_j}} \right) \tag{3.20}$$

Following the similar procedure in equation (3.19) and applying gradient transport theorem to the first term on the right hand side of (3.20) we have:

$$\frac{\partial(\overline{u_i' u_i' u_j'})}{\partial x_j} = \frac{\partial}{\partial x_j}\left(-2\frac{\nu_t}{\sigma_k}\frac{\partial k}{\partial x_j}\right) = -2\left[\frac{\partial}{\partial x_j}\left(\frac{\nu_t}{\sigma_k}\right)\frac{\partial k}{\partial x_j} + \frac{\nu_t}{\sigma_k}\frac{\partial}{\partial x_j}\left(\frac{\partial k}{\partial x_j}\right)\right] \tag{3.21}$$

The second term on right side of equation (3.20) also appears in Elghobashi and Abou-Arab's derivation of two-phase turbulence model (1983). They did not present a closure for this term directly. However, they grouped several diffusion terms of *k* together and obtained the total contribution without detailed discussion. Through the analysis of his derivation, it is evident that he neglected the second term on right side of equation (3.20). However, we can investigate this term in the following way.

Firstly, define the term:

$$k' = \frac{1}{2}u_i' u_i' \tag{3.22}$$

$$\frac{\partial k'}{\partial x_j} = \lim_{\Delta x_j \to 0}\frac{k'(x_j + \Delta x_j) - k'(x_j)}{\Delta x_j} \tag{3.23}$$

Thus, the following relation can be established:

$$-\overline{u_j'\frac{\partial u_i' u_i'}{\partial x_j}} = -2\overline{u_j'\frac{\partial k'}{\partial x_j}} = -2\lim_{\Delta x_j \to 0}\frac{\overline{u_j' k'(x_j + \Delta x_j) - u_j' k'(x_j)}}{\Delta x_j} \tag{3.24}$$

If considering Δx_j is smaller enough and applying the equation (3.18), equation (3.24) can be rewritten as:

$$
\begin{aligned}
-\overline{u_j' \frac{\partial u_i' u_i'}{\partial x_j}} &= -2 \lim_{\Delta x_j \to 0} \frac{\overline{u_j' k'(x_j + \Delta x_j) - u_j' k'(x_j)}}{\Delta x_j} \\
&= 2 \lim_{\Delta x_j \to 0} \frac{1}{\Delta x_j} \left[\frac{\nu_t(x_j)}{\sigma_k} \frac{\partial k(x_j + \Delta x_j)}{\partial x_j} - \frac{\nu_t(x_j)}{\sigma_k} \frac{\partial k(x_j)}{\partial x_j} \right] \\
&= 2 \frac{\nu_t(x_j)}{\sigma_k} \frac{\partial}{\partial x_j} \left(\frac{\partial k(x_j)}{\partial x_j} \right) \\
&= 2 \frac{\nu_t}{\sigma_k} \frac{\partial}{\partial x_j} \left(\frac{\partial k}{\partial x_j} \right)
\end{aligned}
\tag{3.25}
$$

Substituting equations (3.21) and (3.25) into (3.20) gives:

$$
\frac{1}{2} \overline{\rho_f u_i' u_i' \frac{\partial u_j'}{\partial x_j}} = -\rho_f \frac{\partial}{\partial x_j} \left(\frac{\nu_t}{\sigma_k} \right) \frac{\partial k}{\partial x_j} \tag{3.26}
$$

Elghobashi and Abou-Arab (1983) argued that the contribution to the diffusion of turbulence energy due to the pressure interaction $\partial(\overline{u_i' p'})/\partial x_i$ could be neglected, as it is of relatively small magnitude in two-phase flow. Hence,

$$
\frac{\partial \left(\overline{u_i' p'} \right)}{\partial x_i} = \overline{p' \frac{\partial u_i'}{\partial x_i}} + \overline{u_i' \frac{\partial p'}{\partial x_i}} \approx 0 \tag{3.27}
$$

If we consider a simple flow driven by the constant pressure gradient, the second term in right hand side of (3.27) is also negligible, which means that the first term in Π_k is of small magnitude too. It is worth mentioning that the above Elghobashi's assumption is also consistent with the assumption used in the derivation of standard k-ε model by Wilcox (1994).

Finally, we group the first and second terms in Π_k together and get:

$$
\overline{p' \frac{\partial u_i'}{\partial x_i}} + \frac{1}{2} \overline{\rho_f u_i' u_i' \frac{\partial u_j'}{\partial x_j}} = -\rho_f \frac{\partial}{\partial x_j} \left(\frac{\nu_t}{\sigma_k} \right) \frac{\partial k}{\partial x_j} \tag{3.28}
$$

In the framework of two-phase flow theory, the fluctuating velocity-divergence $\partial u_j'/\partial x_j$ does not vanish (Elghobashi, 1982). The reason is

that the mass of fluid phase in a moving control volume does not remain the same amount due to the non-uniform distributed particle phase. However, the fluctuating velocity-divergence indeed becomes very small in the upper water column in the sediment-laden flow since the volumetric concentration of particle is very low and its gradient also does not change much. This may indicate that the closure coefficient σ_k is not constant over the water column and can be linked with the sediment concentration.

Now the interaction term in Π_k in the TKE equation derived in section 3.4 is examined. Based on the relation

$$(1-\phi)\omega_i = f_i \tag{3.29}$$

and performing Reynold decomposition results in:

$$(1-\bar{\phi}-\phi')(\overline{\omega_i}+\omega_i') = \overline{f_i} + f_i' \tag{3.30}$$

$$\overline{\omega_i} + \omega_i' - (\bar{\phi}\overline{\omega_i} + \phi'\overline{\omega_i} + \bar{\phi}\omega_i' + \phi'\omega_i') = \overline{f_i} + f_i' \tag{3.31}$$

Applying Reynolds-averaging to the above equation gives:

$$\overline{\overline{f_i} + f_i'} = \overline{f_i} = \overline{\omega_i} - \bar{\phi}\overline{\omega_i} - \overline{\phi'\omega_i'} \tag{3.32}$$

$$f_i' = \omega_i' - \phi'\overline{\omega_i} - \bar{\phi}\omega_i' - \phi'\omega_i' + \overline{\phi'\omega_i'} \tag{3.33}$$

The following also can be written;

$$\overline{\omega_i} = \frac{\overline{f_i} + \overline{\phi'\omega_i'}}{1-\bar{\phi}} \tag{3.34}$$

$$\omega_i' = \frac{f_i' + \phi'\overline{\omega_i} + \phi'\omega_i' - \overline{\phi'\omega_i'}}{1-\bar{\phi}} \tag{3.35}$$

Finally, the interaction term can be interpreted as:

$$\overline{u_i'\omega_i'} = \frac{\overline{u_i' f_i'} + \overline{u_i'\phi'}\,\overline{\omega_i} + \overline{u_i'\phi'\omega_i'}}{1-\bar{\phi}} \tag{3.36}$$

Analysis of the interaction term in equation (3.15) shows that, the complexity is always hidden in this term (given by equation 3.36)

although the whole equation appears simpler. An approximation will be presented in next chapter.

The extra terms in TDR equation are written as:

$$\Pi_\varepsilon = \mu\overline{\frac{\partial u_k'}{\partial x_k}\frac{\partial u_i'}{\partial x_j}\frac{\partial u_i'}{\partial x_j}} + 2\nu\overline{\frac{\partial p'}{\partial x_i}\frac{\partial^2 u_i'}{\partial x_j \partial x_j}} - 2\nu\overline{\frac{\partial u_i'}{\partial x_j}\frac{\partial \omega_i'}{\partial x_j}}$$

It is usually difficult to model. Comparing to the extra term Π_k in the TKE equation, the similarity can be observed. Using the similar approach of modelling the shear production term in the TDR equation, the extra term Π_ε can be approximated by:

$$\Pi_\varepsilon = C_{\varepsilon 4}\frac{\varepsilon}{k}\Pi_k \tag{3.37}$$

where k = turbulence kinetic energy, ε = turbulence dissipation rate and $C_{\varepsilon 4}$ is a constant included in the interaction terms for dissipation. It is usually determined empirically (Elghobashi and Abou-Arab, 1983) and a discussion is presented in Section 4.5.1.

Chapter 4

1DV MODEL

4.1. Introduction

In previous chapter, the two-phase/mixture governing equations and the modified *k-ε* turbulence model derived from the two-phase approach were presented. In order to test the assumptions and extra terms in the new equations, it is necessary to develop a 1DV model and perform validation against experimental data.

The finite element method is used for the discretization of the governing equations. For achieving higher accuracy, the quadratic element is adopted in the model. The momentum conservation of fluid, modified *k-ε* model and the advection-diffusion equation are coupled and solved iteratively.

4.2. Theoretical background

4.2.1. Two-phase/mixture theory

For the sake of convenience, the overbar in the Reynolds-averaged terms has been dropped, resulting in the following governing equations:

The suspension continuity equation:

$$\frac{\partial\left(U_j + W_j\phi\right)}{\partial x_j} = 0 \tag{4.1}$$

It can be written as

$$\frac{\partial\left(U_x + W_x\phi\right)}{\partial x} + \frac{\partial\left(U_y + W_y\phi\right)}{\partial y} + \frac{\partial\left(U_z + W_z\phi\right)}{\partial z} = 0 \tag{4.2}$$

The suspension momentum equation reads:

$$\rho\left(\frac{\partial U_i}{\partial t}+U_j\frac{\partial U_i}{\partial x_j}\right)=-\frac{\partial p}{\partial x_i}+\rho g\delta_{iz}+\frac{\partial \sigma_{ij}}{\partial x_j}+\frac{\partial\left(\sigma_{Tij}+\sigma_{Dij}\right)}{\partial x_j}$$
$$-\rho_p\phi\left(\frac{\partial W_i}{\partial t}+U_j\frac{\partial W_i}{\partial x_j}+W_J\frac{\partial(U_i+W_i)}{\partial x_j}\right) \tag{4.3}$$

in which U_j is the ensemble-averaged velocity of fluid phase [m/s], W_j is the slip velocity [m/s], ϕ is the particle volume fraction, p is the pressure [Pa], ρ, ρ_f and ρ_p are the suspension density, the fluid density and the particle density respectively [kg/m^3] and $\rho = \rho_p\overline{\phi} + \rho_f(1-\overline{\phi})$, σ_{ij} is the viscous shear stress [kg·m^{-1}·s^{-2}], σ_{Tij} is the turbulent Reynolds stress [kg·m^{-1}·s^{-2}] and σ_{Dij} is the drift diffusion stress [kg·m^{-1}·s^{-2}].

The shear stress term σ_{ij} here represents the viscous stress of the mixture. We still consider the mixture as a Newtonian fluid and the viscous stress term can be derived as follows.

$$\sigma_{ij}=2\mu_m\mathbf{E}-\frac{2}{3}\mu_m\left(\nabla\cdot\mathbf{u_m}\right)\mathbf{I}=2\mu_m\left(s_{ij}-\frac{1}{3}s_{kk}\delta_{ij}\right) \tag{4.4}$$

It is noteworthy that the mixture viscosity μ_m should be variable (i.e. concentration dependent) in space. In equation (4.4):

$$s_{ij}=\frac{1}{2}\left(\frac{\partial u_{mi}}{\partial x_j}+\frac{\partial u_{mj}}{\partial x_i}\right),\ s_{kk}=\frac{\partial u_{mk}}{\partial x_k}=\nabla\cdot\mathbf{u_m} \tag{4.5}$$

Defining the phase-averaged mixture velocity $u_{mi} = u_i(1-\phi)+v_i\phi$, in which u_i is the fluid velocity and v_i is the particle velocity, we obtain from the basic governing equations that its divergence $\nabla\cdot\mathbf{u_m}=0$. Hence, the viscous stress is obtained:

$$\frac{\partial\sigma_{ij}}{\partial x_j}=\frac{\partial}{\partial x_j}\left(\mu_m\left(\frac{\partial u_{mi}}{\partial x_j}+\frac{\partial u_{mj}}{\partial x_i}\right)\right)=\mu_m\frac{\partial}{\partial x_j}\left(\frac{\partial u_{mi}}{\partial x_j}\right)+\frac{\partial\mu_m}{\partial x_j}\left(\frac{\partial u_{mi}}{\partial x_j}+\frac{\partial u_{mj}}{\partial x_i}\right) \tag{4.6}$$

The second part can be neglected only if considering μ_m is assumed constant over the water column. By substituting equation (3.10) and (3.11) in equation (4.3), the complex suite of equations is written for the x direction as

$$
\begin{aligned}
&\rho\left(\frac{\partial U_x}{\partial t}+U_x\frac{\partial U_x}{\partial x}+U_y\frac{\partial U_x}{\partial y}+U_z\frac{\partial U_x}{\partial z}\right)\\
&\quad=-\frac{\partial p}{\partial x}+\mu_m\left(\frac{\partial^2 u_{mx}}{\partial x^2}+\frac{\partial^2 u_{mx}}{\partial y^2}+\frac{\partial^2 u_{mx}}{\partial z^2}\right)\\
&\quad+\frac{\partial}{\partial x}\left(-\rho\overline{u_x'u_x'}+\rho_p\phi\left(V_{Dx}V_{Dx}\right)+\rho_f\left(1-\phi\right)\left(U_{Dx}U_{Dx}\right)\right)\\
&\quad+\frac{\partial}{\partial y}\left(-\rho\overline{u_x'u_y'}+\rho_p\phi\left(V_{Dx}V_{Dy}\right)+\rho_f\left(1-\phi\right)\left(U_{Dx}U_{Dy}\right)\right)\\
&\quad+\frac{\partial}{\partial z}\left(-\rho\overline{u_x'u_z'}+\rho_p\phi\left(V_{Dx}V_{Dz}\right)+\rho_f\left(1-\phi\right)\left(U_{Dx}U_{Dz}\right)\right)\\
&\quad-\rho_p\phi\left(\frac{\partial W_x}{\partial t}+U_x\frac{\partial W_x}{\partial x}+U_y\frac{\partial W_x}{\partial y}+U_z\frac{\partial W_x}{\partial z}\right.\\
&\quad\left.+W_x\frac{\partial(U_x+W_x)}{\partial x}+W_y\frac{\partial(U_x+W_x)}{\partial y}+W_z\frac{\partial(U_x+W_x)}{\partial z}\right)
\end{aligned}
\tag{4.7}
$$

The complex suite of equations is written for the y direction as

$$
\begin{aligned}
&\rho\left(\frac{\partial U_y}{\partial t}+U_x\frac{\partial U_y}{\partial x}+U_y\frac{\partial U_y}{\partial y}+U_z\frac{\partial U_y}{\partial z}\right)\\
&\quad=-\frac{\partial p}{\partial y}+\mu_m\left(\frac{\partial^2 u_{my}}{\partial x^2}+\frac{\partial^2 u_{my}}{\partial y^2}+\frac{\partial^2 u_{my}}{\partial z^2}\right)\\
&\quad+\frac{\partial}{\partial x}\left(-\rho\overline{u_y'u_x'}+\rho_p\phi\left(V_{Dy}V_{Dx}\right)+\rho_f\left(1-\phi\right)\left(U_{Dy}U_{Dx}\right)\right)\\
&\quad+\frac{\partial}{\partial y}\left(-\rho\overline{u_y'u_y'}+\rho_p\phi\left(V_{Dy}V_{Dy}\right)+\rho_f\left(1-\phi\right)\left(U_{Dy}U_{Dy}\right)\right)\\
&\quad+\frac{\partial}{\partial z}\left(-\rho\overline{u_y'u_z'}+\rho_p\phi\left(V_{Dy}V_{Dz}\right)+\rho_f\left(1-\phi\right)\left(U_{Dy}U_{Dz}\right)\right)\\
&\quad-\rho_p\phi\left(\frac{\partial W_y}{\partial t}+U_x\frac{\partial W_y}{\partial x}+U_y\frac{\partial W_y}{\partial y}+U_z\frac{\partial W_y}{\partial z}\right.\\
&\quad\left.+W_x\frac{\partial(U_y+W_y)}{\partial x}+W_y\frac{\partial(U_y+W_y)}{\partial y}+W_z\frac{\partial(U_y+W_y)}{\partial z}\right)
\end{aligned}
\tag{4.8}
$$

The complex suite of equations is written for the z direction as

$$\rho\left(\frac{\partial U_z}{\partial t}+U_x\frac{\partial U_z}{\partial x}+U_y\frac{\partial U_z}{\partial y}+U_z\frac{\partial U_z}{\partial z}\right)$$
$$=-\frac{\partial p}{\partial z}+\left(\phi\rho_p+(1-\phi)\rho_f\right)g$$
$$+\mu_m\left(\frac{\partial^2 u_{mz}}{\partial x^2}+\frac{\partial^2 u_{mz}}{\partial y^2}+\frac{\partial^2 u_{mz}}{\partial z^2}\right)$$
$$+\frac{\partial}{\partial x}\left(-\rho\overline{u_z'u_x'}+\rho_p\phi\left(V_{Dz}V_{Dx}\right)+\rho_f(1-\phi)\left(U_{Dz}U_{Dx}\right)\right)$$
$$+\frac{\partial}{\partial y}\left(-\rho\overline{u_z'u_y'}+\rho_p\phi\left(V_{Dz}V_{Dy}\right)+\rho_f(1-\phi)\left(U_{Dz}U_{Dy}\right)\right)$$
$$+\frac{\partial}{\partial z}\left(-\rho\overline{u_z'u_z'}+\rho_p\phi\left(V_{Dz}V_{Dz}\right)+\rho_f(1-\phi)\left(U_{Dz}U_{Dz}\right)\right)$$
$$-\rho_p\phi\left(\frac{\partial W_z}{\partial t}+U_x\frac{\partial W_z}{\partial x}+U_y\frac{\partial W_z}{\partial y}+U_z\frac{\partial W_z}{\partial z}\right.$$
$$\left.+W_x\frac{\partial(U_z+W_z)}{\partial x}+W_y\frac{\partial(U_z+W_z)}{\partial y}+W_z\frac{\partial(U_z+W_z)}{\partial z}\right) \qquad (4.9)$$

4.2.2. Advection-diffusion of suspended sediment

In nature, sediment transport occurs in fluids through the combination of advection and diffusion. Conservation of sediment is expressed by the sediment transport equation:

$$\frac{\partial C}{\partial t}+U_j\frac{\partial C}{\partial x_j}=\frac{\partial}{\partial x_i}\left(\frac{\nu_t}{\sigma_t}\frac{\partial C}{\partial x_i}+w_s C\delta_{i3}\right) \qquad (4.10)$$

In this equation the following notations are used: U = the mean velocity [m/s], t = time [s], x_j = the components of the coordinate vector [m], ν_t = the eddy viscosity [m^2/s], σ_t = the turbulent Prandtl-Schmidt number (the ratio of ν_t to the eddy diffusivity of the sediment particles), C = sediment concentration, w_s = the representative mean settling velocity [m/s], δ_{ij}= the Kronecker delta.

In summary, the equation reflects two transport mechanisms: advective transport with the mean flow; and diffusive transport due to concentrations gradients. Equation (4.10) also considers the molecular diffusion, but this is usually negligible compared to the turbulent diffusion.

4.2.3. Modified *k-ε* turbulence model

The above set of equations requires a turbulence closure. In this study, the standard *k-ε* model is firstly adopted, where the turbulent eddy viscosity is defined as:

$$\nu_t = C_\mu \frac{k^2}{\varepsilon} \tag{4.11}$$

The *k-ε* model solves the conservation of turbulent kinetic energy *k*:

$$\frac{\partial k}{\partial t} + U_j \frac{\partial k}{\partial x_j} = \frac{\partial}{\partial x_j}\left[\left(\nu + \frac{\nu_t}{\sigma_k}\right)\frac{\partial k}{\partial x_j}\right] + P + G - \varepsilon + \Pi_k \tag{4.12}$$

and its dissipation rate ε:

$$\frac{\partial \varepsilon}{\partial t} + U_j \frac{\partial \varepsilon}{\partial x_j} = \frac{\partial}{\partial x_j}\left[\left(\nu + \frac{\nu_t}{\sigma_\varepsilon}\right)\frac{\partial \varepsilon}{\partial x_j}\right] + \frac{\varepsilon}{k}\left(C_{\varepsilon 1}P + C_{\varepsilon 3}G - C_{\varepsilon 2}\varepsilon\right) + \Pi_\varepsilon \tag{4.13}$$

The turbulence production term due to viscous forces *P* is modelled as:

$$P = \nu_t\left(\frac{\partial U_i}{\partial x_j} + \frac{\partial U_j}{\partial x_i}\right)\frac{\partial U_i}{\partial x_j} - \frac{2}{3}\frac{\partial U_k}{\partial x_k}\left(3\nu_t \frac{\partial U_k}{\partial x_k} + k\right) \tag{4.14}$$

In case of a vertical density gradient, turbulent kinetic energy *k* is transformed into potential energy when the stratification is weakened by turbulence, the so-called buoyancy destruction. The buoyancy term *G* is defined as:

$$G = \frac{g}{\rho}\frac{\nu_t}{\sigma_t}\frac{\partial \rho}{\partial z} \tag{4.15}$$

$$\rho = \rho_f + \left(1 - \frac{\rho_f}{\rho_s}\right)\cdot C \tag{4.16}$$

with k the turbulent kinetic energy [m^2/s^2] and its dissipation rate ε [m^2/s^3], g the gravity constant [m/s^2] and z the vertical coordinate [m], ρ is the bulk fluid density [kg/m^3]. ρ_f and ρ_s are the water and sediment densities respectively [kg/m^3], C is the sediment concentration by mass [kg/m^3]. The remaining coefficients have been determined semi-empirically and are taken as $\sigma_t = 0.7$, $\sigma_k = 1.0$, $\sigma_\varepsilon = 1.3$, $\sigma_\rho = 1$, $C_{\varepsilon 1} = 1.44$, $C_{\varepsilon 2} = 1.92$ and $C_\mu = 0.09$ which are commonly used values for turbulent shear flows (Rodi, 1980; Chen and Jaw, 1998). The value of $C_{\varepsilon 3}$ in stable stratified shear flows is generally somewhere in the range 0-0.3 (Rodi, 1980). Uittenbogaard *et al.* (1992) argue that the Richardson number effect is negligible for the scales where ε is important. Hence, they suggest $C_{\varepsilon 3} = 0$, which is chosen here also. It is computationally advantageous and seems to perform satisfactorily (Toorman, 2002). The semi-empirical constants like C_μ and many others can be dependent on the flow properties and sediment concentration in a buoyancy extended k-ε model. In many studies, even for the k-ε model with buoyancy term, the constant values are used, as well as in this study.

4.3. Discretization using FEM for 1DV steady state

In the finite element method, continuous models are approximated using information at a finite number of discrete locations. Dividing the structure into discrete elements is called discretization. Interpolation within the elements is achieved through shape functions.

The finite element technique relies on identifying functions that represent, approximately, the exact solution. It does not attempt to make this residual equal to zero. Rather, the finite element technique tries to make the weighted, average residual equal to zero.

In this chapter, the Galerkin weighted residual method is employed. The weighting functions are the same as the shape functions.

In order to obtain better approximations, 3-node quadratic line element is used in discretization, of which the shape functions are defined as follows:

$$N_1 = \frac{1}{2}\xi(\xi - 1)$$
$$N_2 = -(\xi + 1)(\xi - 1) \qquad (4.17)$$
$$N_3 = \frac{1}{2}\xi(\xi + 1)$$

in which: ξ = the local coordinate ranging from -1 to 1. The shape of the three functions is shown in Figure 4.1.

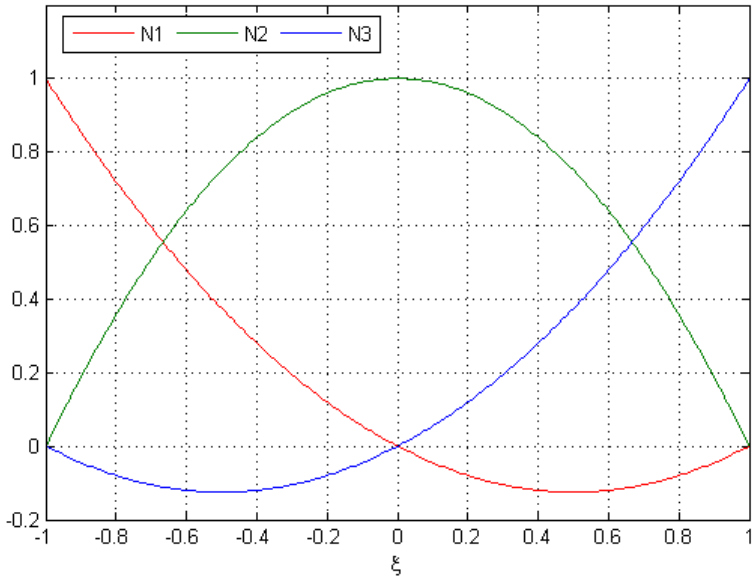

Figure 4.1. Shape functions of quadratic line element

4.3.1. Conservation of momentum of suspension

The governing equations for the 1DV model in steady state have been reduced to (gradient in x and y = 0, U_z = 0, slip velocities W_x = 0):

The mixture momentum balance in x:

$$-\frac{\partial p}{\partial x} + \mu_m \frac{\partial^2 u_{mx}}{\partial z^2} + \frac{\partial}{\partial z}\left(-\rho\overline{u_x' u_z'}\right) - \rho_p \phi W_z \frac{\partial (U_x + W_x)}{\partial z} = 0 \qquad (4.18)$$

The Reynolds stress is expressed using the Boussinesq approximation:

$$-\rho\overline{u_x'u_z'} = \mu_{mt}\left(\frac{\partial u_x}{\partial z} + \frac{\partial u_z}{\partial x}\right) \tag{4.19}$$

in which u_x and u_z are Reynolds-averaged velocity components and the gradient of u_z in x is zero in the 1DV case. Until now, one of the problems occurring in equation (4.18) is that the mixture velocity u_{mx} requires an additional closure. In order to simplify the model, we assume $u_{mx} \approx u_x$ due to the small magnitude of particle fraction (if we consider a near bottom concentration of 100 g/l, the corresponding volume fraction is only about 0.038 and it does not affect the mixture velocity very much). Moreover, using the gradient transport theorem, the ensemble averaged velocity U_x can be written as:

$$U_x = u_x - \frac{\overline{u_i'\phi'}}{1-\phi} = u_x - \frac{1}{1-\phi}\frac{\nu_t}{\sigma_\phi}\frac{\partial \phi}{\partial x} \tag{4.20}$$

However, in 1DV case, the gradient of ϕ in x direction is zero. Hence, equation (4.18) can be rewritten as

$$-\frac{\partial p}{\partial x} + \frac{\partial}{\partial z}\left(\mu_e \frac{\partial u_x}{\partial z}\right) - \rho_p \phi W_z \frac{\partial u_x}{\partial z} = 0 \tag{4.21}$$

where p is the pressure, u_x is the Reynolds-averaged velocity in x direction, ρ_p is the particle density, ϕ is the particle fraction, W_z is the slip velocity in vertical and can be considered as the particle settling velocity, and the effective viscosity can be written as the superposition of dynamic viscosity and eddy viscosity of the mixture:

$$\mu_e = \mu_m + \mu_{mt} \tag{4.22}$$

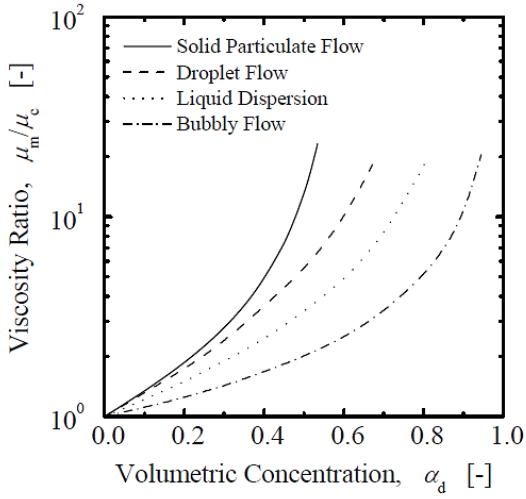

Figure 4.2. Mixture viscosity for various two-phase flow systems (Ishii and Chawla, 1979)

Ishii and Chawla (1979) studied the influence of volumetric concentration on the mixture viscosity for various two-phase flow systems (Figure 4.2). It can be seen that, for solid particulate flow, even in the near bottom region with the volumetric concentration of 0.1 (265 g/l), the ratio of mixture viscosity to the water viscosity is still less than 1.1, not to mention the ratio in the rest of the water column. Furthermore, the mixture viscosity has a relatively smaller magnitude compared to the turbulent eddy viscosity. Thus, we consider the μ_m as constant here and equal to the water dynamic viscosity.

The last term on the right hand side of equation (4.21) represents the momentum transfer to the particle phase from the fluid. It is obvious that this term is negligible in the dilute suspension due to the small particle fraction. However, it may become complex in the near bottom layer since the particle fraction is increased and the gradient of u_x in the z direction becomes larger, whereas the settling of particles may be hindered, which leads to smaller W_z.

In order to account for the hindered settling (induced by return flow and wake formation, viscosity change and particle collisions, etc.), we employ the empirical equation proposed by Richardson & Zaki (1954):

$$W_z = w_s \cdot (1-c)^n \tag{4.23}$$

where w_s is the free falling velocity of an individual particle, c is the fractional volumetric concentration of particles in the suspension. The value of the index n had a constant value of about 4.65 for particle Reynolds numbers less than about 0.2 (Stokes' law region), but for high Reynolds numbers became progressively less until it reached a second constant value of about 2.3 at Reynolds numbers exceeding about 500 (Newton's law region) (Richardson & Zaki, 1954).

The hindered settling velocity can be accurately predicted by the equation (4.23), provided an appropriate value for the exponent n is available for the particular material (Baldock *et al*., 2003).

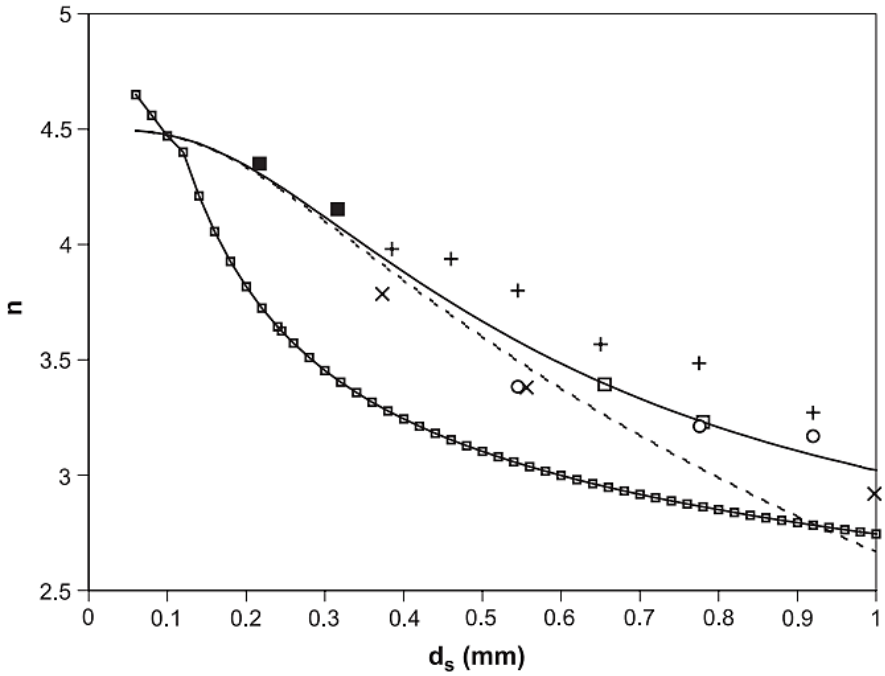

Figure 4.3. Predicted relationships between n and sieve grain size for sands, together with present experimental data and data extracted from cited sources: — non-Darcy flow; –– Darcy flow; –□– Richardson and Zaki (spherical particles); ■ natural beach sand (present data); × Wilhelm and Kwauk (1948) beach sand; □ filter sand (present data); ○ Cleasby and Fan (1981) filter sand; + Cleasby and Woods (1975) filter sand (from Baldock *et al*., 2003).

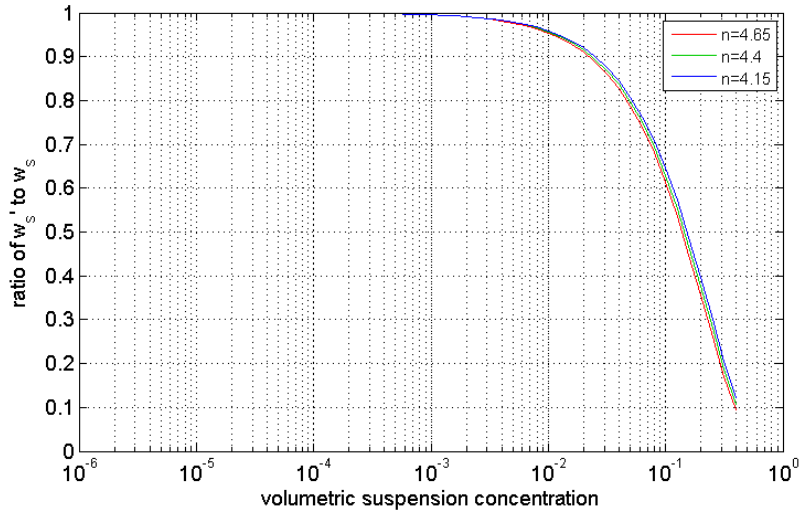

Figure 4.4. Influence of volumetric suspension concentration on particle settling velocity according to the equation (4.23).

As indicated in the Figure 4.3, the appropriate value of *n* for fine sand (0.1-0.3mm) can vary between 4.15 and 4.65. Here, we plot the settling velocities for different *n* values based on equation (4.23) in the Figure 4.4. It can be seen that the hindered settling only becomes obvious when volumetric concentration exceeds 0.01. It can be expected that the settling velocity at the high volumetric concentration (with the magnitude of 0.1), which usually occurs in the bottom layer, can easily have a reduction of 50% - 70% compared with the free falling velocity of an individual particle in clear water. Nevertheless, the differences between different *n* values within this range are not significant.

The mixture momentum balance in the *z* direction is reduced to:

$$\frac{\partial}{\partial z}\left(-\rho\overline{u_z'u_z'}\right)=-\frac{\partial}{\partial z}\left(\rho_p\phi\left(V_{Dz}V_{Dz}\right)+\rho_f\left(1-\phi\right)\left(U_{Dz}U_{Dz}\right)\right)-\rho_p\phi W_z\frac{\partial W_z}{\partial z} \tag{4.24}$$

which means the drift diffusion stress equals to the turbulent Reynolds stress in steady state if the slip velocity gradient in *z* is negligible (settling velocity is constant).

In this study, the Galerkin weighted residual method is employed to discretize the governing equations. In the Galerkin method, the same

approximating functions N_i are used for the weighting and trial functions. Hence, discretization of momentum equation in x gives:

$$\begin{aligned}
&\int_{z_l}^{z_u} N_i \frac{\partial}{\partial z}\left(\mu_e \frac{\partial u_x}{\partial z}\right) dz - \int_{z_l}^{z_u} N_i \rho_p W_z \phi \frac{\partial u_x}{\partial z} dz \\
&= \int_{z_l}^{z_u} \left[\frac{\partial}{\partial z}\left(N_i \mu_e \frac{\partial u_x}{\partial z}\right) - \frac{\partial N_i}{\partial z} \mu_e \frac{\partial u_x}{\partial z} - N_i \rho_p W_z \phi \frac{\partial u_x}{\partial z} \right] dz \\
&= -\int_{z_l}^{z_u} \left(\mu_e \frac{\partial N_i}{\partial z} \frac{\partial u_x}{\partial z} + \rho_p W_z N_i \phi \frac{\partial u_x}{\partial z} \right) dz + \mu_e N_i \frac{\partial u_x}{\partial z}\Bigg|_{z_l}^{z_u}
\end{aligned} \tag{4.25}$$

$$\begin{aligned}
&= \int_{z_l}^{z_u} N_i \frac{\partial p}{\partial x} dz \\
&-\int_{z_l}^{z_u} \left(\mu_e \frac{\partial N_i}{\partial z} \sum_{j=1}^{n} \frac{\partial N_j}{\partial z} u_{xj} + \rho_p W_z N_i \phi \sum_{j=1}^{n} \frac{\partial N_j}{\partial z} u_{xj} \right) dz \\
&= \int_{z_l}^{z_u} N_i \frac{\partial p}{\partial x} dz - \mu_e N_i \frac{\partial u_x}{\partial z}\Bigg|_{z_l}^{z_u}
\end{aligned} \tag{4.26}$$

where: z_u and z_l are the upper bound and lower bound in a line element, N is the shape function, the subscript i and j =1, 2, …, n, representing the number of different nodes in an element. In this study, a three-node quadratic line element is used, therefore, n = 3.

Using Gauss integration (3 Gauss points) the following matrix form is obtained:

$$a_{ij} = -\sum_{n=1}^{3} \mu_e^{(n)} \frac{\partial N_i^{(n)}}{\partial z} \frac{\partial N_j^{(n)}}{\partial z} \left|\mathrm{J}\right| w_n - \rho_p \sum_{n=1}^{3} W_z^{(n)} N_i^{(n)} \phi^{(n)} \frac{\partial N_j^{(n)}}{\partial z} \left|\mathrm{J}\right| w_n \tag{4.27}$$

$$b_i = \sum_{n=1}^{3} N_i^{(n)} \frac{\partial p}{\partial x} \left|\mathrm{J}\right| w_n - \mu_e N_i \frac{\partial u_x}{\partial z}\Bigg|_{z_l}^{z_u} \tag{4.28}$$

where: a_{ij} is the element at line i column j in the left-hand-side matrix, b_i is the element at line i in the right-hand-side vector, n is the number of Gauss point, J is the Jacobian matrix, and w_n is the weighting factor at Gauss point n in Gaussian integration.

Regarding the boundary conditions for solving momentum balance equation, a Dirichlet condition (specifying the value of the solution) is

imposed at the bottom and a Neumann condition imposed at the free surface, which is that the flux across the upper boundary is zero.

4.3.2. Sediment transport in 1DV

The advection-diffusion equation in 1DV is used to solve the vertical concentration profile.

$$\frac{\partial C}{\partial t}-\frac{\partial}{\partial z}\left(w_s C\right)-\frac{\partial}{\partial z}\left(D_T\frac{\partial C}{\partial z}\right)=0 \tag{4.29}$$

in which D_T is diffusivity coefficient of sediment particles and has the following form

$$D_T=\frac{\nu_t}{\sigma_t} \tag{4.30}$$

Discretization of advection-diffusion equations using the Galerkin weighted residual method gives:

$$\begin{aligned}
&\int_{z_l}^{z_u}\left[N_i\frac{\partial C}{\partial t}-N_i\frac{\partial}{\partial z}\left(w_s C+D_T\frac{\partial C}{\partial z}\right)\right]dz\\
&=\int_{z_l}^{z_u}N_i\frac{C-C_{t-1}}{\Delta t}dz\\
&-\int_{z_l}^{z_u}\left[\frac{\partial}{\partial z}\left(N_i w_s C+N_i D_T\frac{\partial C}{\partial z}\right)\right]dz+\int_{z_l}^{z_u}\frac{\partial N_i}{\partial z}\left(w_s C+D_T\frac{\partial C}{\partial z}\right)dz\\
&=\int_{z_l}^{z_u}N_i\frac{C-C_{t-1}}{\Delta t}dz+\int_{z_l}^{z_u}\frac{\partial N_i}{\partial z}\left(w_s C+D_T\frac{\partial C}{\partial z}\right)dz\\
&-N_i\left(w_s C+D_T\frac{\partial C}{\partial z}\right)\Bigg|_{z_l}^{z_u}=0
\end{aligned} \tag{4.31}$$

For the 1DV steady state, equation (4.31) can be simplified as:

$$\int_{z_l}^{z_u}\frac{\partial N_i}{\partial z}\left(w_s C+D_T\frac{\partial C}{\partial z}\right)dz-N_i\left(w_s C+D_T\frac{\partial C}{\partial z}\right)\Bigg|_{z_l}^{z_u}=0 \tag{4.32}$$

$$\int_{z_l}^{z_u} \frac{\partial N_i}{\partial z}\left(w_s \sum_{j=1}^{n} N_j C_j + D_T \sum_{j=1}^{n} \frac{\partial N_j}{\partial z} C_j \right) dz = N_i \left(w_s C + D_T \frac{\partial C}{\partial z} \right)\Bigg|_{z_l}^{z_u} \tag{4.33}$$

Using Gauss integration (3 Gauss points), we are able to obtain the following matrix form:

$$a_{ij} = \sum_{n=1}^{3} \frac{\partial N_i^{(n)}}{\partial z} w_s^{(n)} N_j^{(n)} \left|\mathrm{J}\right| w_n + \sum_{n=1}^{3} \frac{\partial N_i^{(n)}}{\partial z} D_T^{(n)} \frac{\partial N_j^{(n)}}{\partial z} \left|\mathrm{J}\right| w_n \tag{4.34}$$

$$b_i = N_i \left(w_s C + D_T \frac{\partial C}{\partial z} \right)\Bigg|_{z_l}^{z_u} \tag{4.35}$$

The following boundary conditions must be satisfied both at the free surface (Z_s) and at the interface (Z_{ref}) between the bed-load and the suspended load:

$$\begin{cases} z = Z_s, & \mathrm{D}_T \dfrac{\partial C}{\partial z} + w_s C = 0 \\ z = Z_{ref}, & -\mathrm{D}_T \dfrac{\partial C}{\partial z} - w_s C = \left(E - D\right)_{Z_{ref}} \end{cases} \tag{4.36}$$

4.3.3. Turbulence modelling in 1DV

In the 1DV steady case without buoyancy effect, the *k*-*ε* equations reduce to:

$$-\frac{\partial}{\partial z}\left[\left(\nu + \frac{\nu_t}{\sigma_k} \right) \frac{\partial k}{\partial z} \right] + \varepsilon = \nu_t \left(\frac{\partial u_x}{\partial z} \right)^2 \tag{4.37}$$

$$-\frac{\partial}{\partial z}\left[\left(\nu + \frac{\nu_t}{\sigma_\varepsilon} \right) \frac{\partial \varepsilon}{\partial z} \right] + C_{\varepsilon 2} \frac{\varepsilon^2}{k} = C_{\varepsilon 1} \frac{\varepsilon}{k} \nu_t \left(\frac{\partial u_x}{\partial z} \right)^2 \tag{4.38}$$

Introducing an auxiliary parameter (inverse of the turbulent time scale):

$$\gamma = \frac{\varepsilon}{k} \tag{4.39}$$

This gives the decoupled equations of the *k*-*ε* model (Lew *et al.*, 2001):

$$-\frac{\partial}{\partial z}\left[\left(\nu+\frac{\nu_t}{\sigma_k}\right)\frac{\partial k}{\partial z}\right]+\gamma k=\nu_t\left(\frac{\partial u_x}{\partial z}\right)^2 \tag{4.40}$$

$$-\frac{\partial}{\partial z}\left[\left(\nu+\frac{\nu_t}{\sigma_\varepsilon}\right)\frac{\partial \varepsilon}{\partial z}\right]+C_{\varepsilon 2}\gamma\varepsilon=\gamma C_{\varepsilon 1}\nu_t\left(\frac{\partial u_x}{\partial z}\right)^2 \tag{4.41}$$

Discretization of the *k* equation:

$$\begin{aligned}
&\int_{z_l}^{z_u}\left[-N_i\frac{\partial}{\partial z}\left(\left(\nu+\frac{\nu_t}{\sigma_k}\right)\frac{\partial k}{\partial z}\right)+N_i\gamma k\right]dz\\
&=\int_{z_l}^{z_u}\left[-\frac{\partial}{\partial z}\left(N_i\left(\nu+\frac{\nu_t}{\sigma_k}\right)\frac{\partial k}{\partial z}\right)+\frac{\partial N_i}{\partial z}\left(\nu+\frac{\nu_t}{\sigma_k}\right)\frac{\partial k}{\partial z}+N_i\gamma k\right]dz\\
&=\int_{z_l}^{z_u}\left[\left(\nu+\frac{\nu_t}{\sigma_k}\right)\frac{\partial N_i}{\partial z}\frac{\partial k}{\partial z}+N_i\gamma k\right]dz-N_i\left(\nu+\frac{\nu_t}{\sigma_k}\right)\frac{\partial k}{\partial z}\Bigg|_{z_l}^{z_u}\\
&=\int_{z_l}^{z_u}N_i\nu_t\left(\frac{\partial u_x}{\partial z}\right)^2dz
\end{aligned} \tag{4.42}$$

$$\begin{aligned}
&\int_{z_l}^{z_u}\left[\left(\nu+\frac{\nu_t}{\sigma_k}\right)\frac{\partial N_i}{\partial z}\sum_{j=1}^{n}\frac{\partial N_j}{\partial z}k_j+N_i\gamma\sum_{j=1}^{n}N_jk_j\right]dz\\
&=\int_{z_l}^{z_u}N_i\nu_t\left(\frac{\partial u_x}{\partial z}\right)^2dz+N_i\left(\nu+\frac{\nu_t}{\sigma_k}\right)\frac{\partial k}{\partial z}\Bigg|_{z_l}^{z_u}
\end{aligned} \tag{4.43}$$

Using Gauss integration (3 Gauss points) and the matrix form is obtained:

$$a_{ij}=\sum_{n=1}^{3}\left(\nu+\frac{\nu_t^{(n)}}{\sigma_k}\right)\frac{\partial N_i^{(n)}}{\partial z}\frac{\partial N_j^{(n)}}{\partial z}\left|\mathrm{J}\right|w_n+\sum_{n=1}^{3}\gamma^{(n)}N_i^{(n)}N_j^{(n)}\left|\mathrm{J}\right|w_n \tag{4.44}$$

$$b_i=\sum_{n=1}^{3}N_i^{(n)}\nu_t^{(n)}\left(\frac{\partial u_x}{\partial z}^{(n)}\right)^2\left|\mathrm{J}\right|w_n+N_i\left(\nu+\frac{\nu_t}{\sigma_k}\right)\frac{\partial k}{\partial z}\Bigg|_{z_l}^{z_u} \tag{4.45}$$

Discretization of the ε equation:

$$\int_{z_l}^{z_u}\left[-N_i\frac{\partial}{\partial z}\left(\left(\nu+\frac{\nu_t}{\sigma_\varepsilon}\right)\frac{\partial\varepsilon}{\partial z}\right)+N_iC_{\varepsilon 2}\gamma\varepsilon\right]dz$$
$$=\int_{z_l}^{z_u}\left[-\frac{\partial}{\partial z}\left(N_i\left(\nu+\frac{\nu_t}{\sigma_\varepsilon}\right)\frac{\partial\varepsilon}{\partial z}\right)+\frac{\partial N_i}{\partial z}\left(\nu+\frac{\nu_t}{\sigma_\varepsilon}\right)\frac{\partial\varepsilon}{\partial z}+N_iC_{\varepsilon 2}\gamma\varepsilon\right]dz$$
$$=\int_{z_l}^{z_u}\left[\left(\nu+\frac{\nu_t}{\sigma_\varepsilon}\right)\frac{\partial N_i}{\partial z}\frac{\partial\varepsilon}{\partial z}+N_iC_{\varepsilon 2}\gamma\varepsilon\right]dz-N_i\left(\nu+\frac{\nu_t}{\sigma_\varepsilon}\right)\frac{\partial\varepsilon}{\partial z}\Bigg|_{z_l}^{z_u} \tag{4.46}$$
$$=\int_{z_l}^{z_u}N_iC_{\varepsilon 1}\gamma\nu_t\left(\frac{\partial u_x}{\partial z}\right)^2dz$$

$$\int_{z_l}^{z_u}\left[\left(\nu+\frac{\nu_t}{\sigma_\varepsilon}\right)\frac{\partial N_i}{\partial z}\sum_{j=1}^{n}\frac{\partial N_j}{\partial z}\varepsilon_j+N_iC_{\varepsilon 2}\gamma\sum_{j=1}^{n}N_j\varepsilon_j\right]dz$$
$$=\int_{z_l}^{z_u}N_iC_{\varepsilon 1}\gamma\nu_t\left(\frac{\partial u_x}{\partial z}\right)^2dz+N_i\left(\nu+\frac{\nu_t}{\sigma_\varepsilon}\right)\frac{\partial\varepsilon}{\partial z}\Bigg|_{z_l}^{z_u} \tag{4.47}$$

Using Gauss integration (3 Gauss points) and the matrix form is obtained:

$$a_{ij}=\sum_{n=1}^{3}\left(\nu+\frac{\nu_t^{(n)}}{\sigma_k}\right)\frac{\partial N_i^{(n)}}{\partial z}\frac{\partial N_j^{(n)}}{\partial z}\left|\mathrm{J}\right|w_n+\sum_{n=1}^{3}C_{\varepsilon 2}\gamma^{(n)}N_i^{(n)}N_j^{(n)}\left|\mathrm{J}\right|w_n \tag{4.48}$$

$$b_i=\sum_{n=1}^{3}N_i^{(n)}C_{\varepsilon 1}\gamma^{(n)}\nu_t^{(n)}\left(\frac{\partial u_x}{\partial z}^{(n)}\right)^2\left|\mathrm{J}\right|w_n+N_i\left(\nu+\frac{\nu_t}{\sigma_\varepsilon}\right)\frac{\partial\varepsilon}{\partial z}\Bigg|_{z_l}^{z_u} \tag{4.49}$$

In case of including buoyancy term, equation (4.37) becomes:

$$-\frac{\partial}{\partial z}\left[\left(\nu+\frac{\nu_t}{\sigma_k}\right)\frac{\partial k}{\partial z}\right]+\varepsilon=\nu_t\left(\frac{\partial U_x}{\partial z}\right)^2+\frac{g}{\rho}\frac{\nu_t}{\sigma_t}\frac{\partial\rho}{\partial z} \tag{4.50}$$

The influence of the suspended sediment concentration on the bulk fluid density is given by the equation of state according to Winterwerp and Van Kesteren (2004):

$$\rho(C)=\rho_f+\left(1-\frac{\rho_f}{\rho_s}\right)C \tag{4.51}$$

Then the discretization of the *k* equation can be written as:

$$\int_{z_l}^{z_u}\left[\left(\nu+\frac{\nu_t}{\sigma_k}\right)\frac{\partial N_i}{\partial z}\sum_{j=1}^{n}\frac{\partial N_j}{\partial z}k_j+N_i\gamma\sum_{j=1}^{n}N_j k_j\right]dz$$
$$=\int_{z_l}^{z_u}\left[N_i\nu_t\left(\frac{\partial u_x}{\partial z}\right)^2+N_i\frac{g}{\rho}\frac{\nu_t}{\sigma_t}\frac{\partial\rho}{\partial z}\right]dz+N_i\left(\nu+\frac{\nu_t}{\sigma_k}\right)\frac{\partial k}{\partial z}\Bigg|_{z_l}^{z_u} \tag{4.52}$$

$$b_i=\sum_{n=1}^{3}N_i^{(n)}\nu_t^{(n)}\left(\frac{\partial u_x}{\partial z}^{(n)}\right)^2\left|\mathrm{J}\right|w_n$$
$$+\sum_{n=1}^{3}N_i^{(n)}\frac{g}{\rho^{(n)}}\frac{\nu_t^{(n)}}{\sigma_t}\frac{\partial\rho}{\partial z}^{(n)}\left|\mathrm{J}\right|w_n+N_i\left(\nu+\frac{\nu_t}{\sigma_k}\right)\frac{\partial k}{\partial z}\Bigg|_{z_l}^{z_u} \tag{4.53}$$

The boundary conditions for the TKE are both Dirichlet type at the free surface and the bottom. For the TDR, a Dirichlet condition is imposed at the bottom and a zero flux (Neumann boundary condition) imposed at the free surface. The details about these boundary conditions will be discussed in section 4.4.1.

Numerical schemes for solving the *k-ε* model

The standard *k-ε* model is one of the two-equation turbulence models. This model is only valid for the fully-developed turbulent layer; therefore a wall function has to be used to bridge the gap between viscous layer and turbulent layer.

Besides, the standard *k-ε* model usually requires sophisticated numerical treatment in order to stabilize and accelerate the speed of convergence. Although we only consider the steady state, pseudo time derivatives of *k* and epsilon are still added into equation (4.37) and (4.38). Combined with the introduction of (self-eliminating) artificial diffusion in both left- and right-hand sides of the equations, the converging speed can be reduced from about 15000 iterations to only about 90 iterations.

Hence, the *k-ε* equations become:

$$\frac{\partial k}{\partial t}-\frac{\partial}{\partial z}\left[\left(\nu-\nu_a+\frac{\nu_t}{\sigma_k}\right)\frac{\partial k}{\partial z}\right]+\gamma k=\nu_t\left(\frac{\partial u_x}{\partial z}\right)^2+\frac{\partial}{\partial z}\left(\nu_a\frac{\partial k}{\partial z}\right) \tag{4.54}$$

$$\frac{\partial \varepsilon}{\partial t}-\frac{\partial}{\partial z}\left[\left(\nu-\nu_a+\frac{\nu_t}{\sigma_\varepsilon}\right)\frac{\partial \varepsilon}{\partial z}\right]+C_2\gamma\varepsilon=\gamma C_1\nu_t\left(\frac{\partial u_x}{\partial z}\right)^2+\frac{\partial}{\partial z}\left(\nu_a\frac{\partial \varepsilon}{\partial z}\right) \quad (4.55)$$

Where t = the pseudo time and the artificial viscosity coefficient ν_a=1.0×10^{-5}.

Using the Galerkin method and noticing that

$$\frac{\partial k}{\partial t}=\frac{k_t-k_{t-1}}{\Delta t} \quad (4.56)$$

where k_t = k at current step and k_{t-1} = k at previous step, the discretized form of equation (4.54) becomes:

$$\int_{z_l}^{z_u}\left[\frac{1}{\Delta t}N_i\sum_{j=1}^{n}\frac{\partial N_j}{\partial z}k_j+\left(\nu-\nu_a+\frac{\nu_t}{\sigma_k}\right)\frac{\partial N_i}{\partial z}\sum_{j=1}^{n}\frac{\partial N_j}{\partial z}k_j+N_i\gamma\sum_{j=1}^{n}N_jk_j\right]dz$$
$$=\int_{z_l}^{z_u}\left[\frac{1}{\Delta t}N_ik_{t-1}+N_i\nu_t\left(\frac{\partial u_x}{\partial z}\right)^2+N_i\nu_a\frac{\partial^2 k}{\partial z^2}\right]dz+N_i\left(\nu+\frac{\nu_t}{\sigma_k}\right)\frac{\partial k}{\partial z}\Bigg|_{z_l}^{z_u} \quad (4.57)$$

Using Gauss integration (3 Gauss points) and the matrix form is obtained:

$$a_{ij}=\frac{1}{\Delta t}\sum_{n=1}^{3}N_i^{(n)}N_j^{(n)}\left|\mathrm{J}\right|w_n+\sum_{n=1}^{3}\left(\nu-\nu_a+\frac{\nu_t^{(n)}}{\sigma_k}\right)\frac{\partial N_i^{(n)}}{\partial z}\frac{\partial N_j^{(n)}}{\partial z}\left|\mathrm{J}\right|w_n$$
$$+\sum_{n=1}^{3}\gamma^{(n)}N_i^{(n)}N_j^{(n)}\left|\mathrm{J}\right|w_n \quad (4.58)$$

$$b_i=\frac{1}{\Delta t}\sum_{n=1}^{3}N_i^{(n)}k_{t-1}^{(n)}\left|\mathrm{J}\right|w_n+\sum_{n=1}^{3}N_i^{(n)}\nu_t^{(n)}\left(\frac{\partial u_x}{\partial z}^{(n)}\right)^2\left|\mathrm{J}\right|w_n$$
$$+\sum_{n=1}^{3}N_i^{(n)}\left(\nu_a\frac{\partial^2 k_{t-1}}{\partial z^2}^{(n)}\right)\left|\mathrm{J}\right|w_n+N_i\left(\nu+\frac{\nu_t}{\sigma_k}\right)\frac{\partial k}{\partial z}\Bigg|_{z_l}^{z_u} \quad (4.59)$$

Similarly, the discretized form of equation (4.55) become:

$$\int_{z_l}^{z_u}\left[\frac{1}{\Delta t}N_i\sum_{j=1}^{n}\frac{\partial N_j}{\partial z}\varepsilon_j+\left(\nu-\nu_a+\frac{\nu_t}{\sigma_\varepsilon}\right)\frac{\partial N_i}{\partial z}\sum_{j=1}^{n}\frac{\partial N_j}{\partial z}\varepsilon_j+N_iC_{\varepsilon 2}\gamma\sum_{j=1}^{n}N_j\varepsilon_j\right]dz$$
$$=\int_{z_l}^{z_u}\left[\frac{1}{\Delta t}N_i\varepsilon_{t-1}+N_iC_{\varepsilon 1}\gamma\nu_t\left(\frac{\partial u_x}{\partial z}\right)^2+N_i\nu_a\frac{\partial^2\varepsilon}{\partial z^2}\right]dz+N_i\left(\nu+\frac{\nu_t}{\sigma_\varepsilon}\right)\frac{\partial\varepsilon}{\partial z}\Bigg|_{z_l}^{z_u} \tag{4.60}$$

Use Gauss integration (3 Gauss points) and we obtain the matrix form:

$$a_{ij}=\frac{1}{\Delta t}\sum_{n=1}^{3}N_i^{(n)}N_j^{(n)}\left|\mathrm{J}\right|w_n+\sum_{n=1}^{3}\left(\nu-\nu_a+\frac{\nu_t^{(n)}}{\sigma_k}\right)\frac{\partial N_i^{(n)}}{\partial z}\frac{\partial N_j^{(n)}}{\partial z}\left|\mathrm{J}\right|w_n$$
$$+\sum_{n=1}^{3}C_{\varepsilon 2}\gamma^{(n)}N_i^{(n)}N_j^{(n)}\left|\mathrm{J}\right|w_n \tag{4.61}$$

$$b_i=\frac{1}{\Delta t}\sum_{n=1}^{3}N_i^{(n)}\varepsilon_{t-1}^{(n)}\left|\mathrm{J}\right|w_n+\sum_{n=1}^{3}N_i^{(n)}C_{\varepsilon 1}\gamma^{(n)}\nu_t^{(n)}\left(\frac{\partial u_x}{\partial z}^{(n)}\right)^2\left|\mathrm{J}\right|w_n$$
$$+\sum_{n=1}^{3}N_i^{(n)}\left(\nu_a\frac{\partial^2\varepsilon_{t-1}}{\partial z^2}^{(n)}\right)\left|\mathrm{J}\right|w_n+N_i\left(\nu+\frac{\nu_t}{\sigma_\varepsilon}\right)\frac{\partial\varepsilon}{\partial z}\Bigg|_{z_l}^{z_u} \tag{4.62}$$

Considering the buoyancy term the equation (4.59) becomes:

$$b_i=\frac{1}{\Delta t}\sum_{n=1}^{3}N_i^{(n)}k_{t-1}^{(n)}\left|\mathrm{J}\right|w_n+\sum_{n=1}^{3}N_i^{(n)}\nu_t^{(n)}\left(\frac{\partial u_x}{\partial z}^{(n)}\right)^2\left|\mathrm{J}\right|w_n$$
$$+\sum_{n=1}^{3}N_i^{(n)}\left(\nu_a\frac{\partial^2 k_{t-1}}{\partial z^2}^{(n)}\right)\left|\mathrm{J}\right|w_n+N_i\left(\nu+\frac{\nu_t}{\sigma_k}\right)\frac{\partial k}{\partial z}\Bigg|_{z_l}^{z_u} \tag{4.63}$$
$$+\sum_{n=1}^{3}N_i^{(n)}\frac{g}{\rho^{(n)}}\frac{\nu_t^{(n)}}{\sigma_t}\frac{\partial\rho}{\partial z}^{(n)}\left|\mathrm{J}\right|w_n$$

4.4. Model validation

The 1DV model is validated against the experimental data from Muste *et al.* (2005). In their experiments, the suspended particles were transported in fully developed turbulence open channel flow. The volume fraction of particles was small and inter-particle collisions were limited except for the particle layer at the solid bottom plate. Hence, the primary influence exerted on suspended-particle motion was water motion. The velocity of fluid and particle phase was measured separately and simultaneously using particle image velocimetry (PIV) and particle-tracking velocimetry (PTV) systems, and then the images were processed in order to get mean and turbulence characteristics of particle and water motions in a vertical plane.

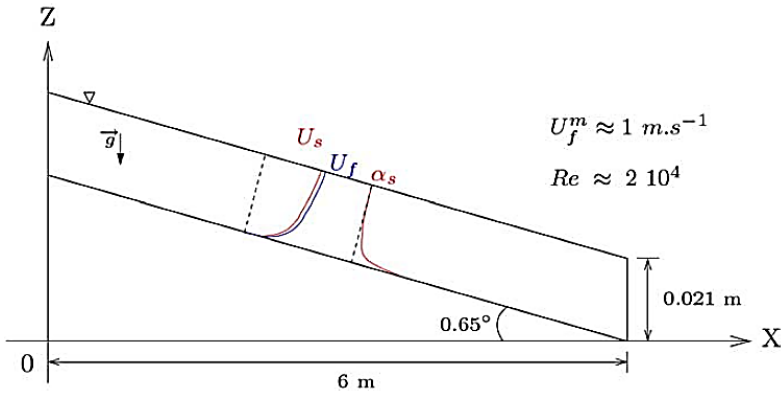

Figure 4.5. Experimental configuration of Muste *et al.* [2005].

Smooth stainless steel is used as the flume's bed and glass as sidewalls. The experiments were conducted using a tilting recirculating flume that is 6.0 m long and 0.15 m wide and the channel slope was kept at 0.0113m/m for all the experiments (Figure 4.5). The resolution of measured flow depth was 0.01 mm.

Two sets of experiments were conducted with natural sand (NS) and a neutrally buoyant sediment (NBS) consisting of crushed Nylon particles. Here, only the NS set of tests was used for validation of the numerical model. The maximum streamwise velocity was approximately 1.0 m/s. The other physical parameters were listed in table 4.1 and 4.2.

Table 4.1. Experimental conditions for the tests (Muste *et al.*, 2005).

	Experiment			
	CW1: Water	**NS1: Natural Sand**	**NS2: Natural Sand**	**NS3: Natural Sand**
Depth, m	0.021	0.021	0.021	0.021
Bed slope	0.0113	0.0113	0.0113	0.0113
Temperature, °C	22–23	23	22	23–24
Sediment density, kg/m^3	-	2650	2650	2650
Size range, mm	-	0.21–0.25	0.21–0.25	0.21–0.25
Fall velocity, m/s	-	0.024	0.024	0.024
Volumetric concentration, ×10^3	0.00	0.46	0.92	1.62

Table 4.2. Parameters of the water-sediment mixture (Muste *et al.*, 2005).

	Experiment CW1	**Experiment NS1**	**Experiment NS2**	**Experiment NS3**
Re	17,670	17,650	17,420	17,340
Fr	1.89	1.81	1.76	1.75
u_*, **m/s**	0.042	0.042	0.043	0.043
κ_m	0.402	0.396	0.389	0.367
Mean bulk velocity, m/s	0.839	0.813	0.796	0.792

In table 4.2, *Re* is the Reynolds number, *Fr* is the Froude number, u_* is the shear velocity, k_m is the von Karman constant of water-sediment mixture.

4.4.1. Numerical settings

The simulations are carried out with a vertical grid that has 101 horizontal planes. The finite element method is able to deal with unstructured grids. However, for this particular case, all the vertical nodes are evenly distributed. The bottom of the flume is considered as hydraulically smooth and a non-slip condition is adopted at the bottom. The initial condition for the velocity is given by the following equations according to the classical mixing-length theory:

$$u(z) = \frac{u_*}{\kappa} \ln\left(\frac{z}{z_0}\right) \tag{4.64}$$

For the hydraulically smooth flow, Nikuradse (1933) gives that:

$$z_0 = 0.11\frac{\nu}{u_*} \tag{4.65}$$

The initial condition for the *k*-ε model is given by:

$$k = \frac{u_*^2}{\sqrt{C_\mu}}\left(1-\frac{z}{h}\right) \tag{4.66}$$

$$\varepsilon = \frac{u_*^3}{\kappa z}\left(1-\frac{z}{h}\right) \tag{4.67}$$

The initial condition for the advection-diffusion of suspended sediment consists of two parts: the initial concentration is set to zero in the whole water column; the initial values of diffusivity coefficients of sediment particles is determined from the initial conditions of the *k*-ε model, which is $D_T = \nu_t/\sigma_t$ with $\nu_t = C_\mu k^2/\epsilon$.

The standard *k*-ε model is only applicable to the high-Reynolds number fully developed turbulence flow. In this particular case, the last two nodes close to the bottom are located in the low-Reynolds region and viscous stress is no longer negligible in this very thin layer. Theoretically, the standard *k*-ε model cannot be used in the last two nodes. In addition, from a numerical perspective instability will occur if including the last two

nodes in the computational domain. Thus, in the current 1DV model, the last cell at the bottom is excluded from the computation and boundary values computed based on the mixing-length theory (law of the wall) are imposed. The boundary conditions are summarized in table 4.3.

Table 4.3. Boundary conditions for solving 1DV model.

Variable	**The bottom cell**			**Free surface**
	Node 1	**Node 2**	**Node 3**	**Node 101**
Velocity u**, m/s**	0	$\frac{u_*}{\kappa}\ln(\frac{z_2}{z_0})$	$\frac{u_*}{\kappa}\ln(\frac{z_3}{z_0})$	$\frac{\partial u}{\partial n}=0$
TKE k**, m²/s²**	$\frac{u_*^2}{\sqrt{C_\mu}}$	$\frac{u_*^2}{\sqrt{C_\mu}}(1-\frac{z_2}{h})$	$\frac{u_*^2}{\sqrt{C_\mu}}(1-\frac{z_3}{h})$	0
TDR ε**, m²/s³**	$\frac{u_*^3}{\kappa z_1}$	$\frac{u_*^3}{\kappa z_2}(1-\frac{z_2}{h})$	$\frac{u_*^3}{\kappa z_3}(1-\frac{z_3}{h})$	$\frac{\partial \epsilon}{\partial n}=0$
Sediment C	$D_T\frac{\partial C}{\partial n}=-E$	-	-	0

Notice that the bottom cell is only excluded in solving momentum conservation equation and k-ε equations. In the advection-diffusion of suspended sediment, the whole water column is included in the computational domain since the diffusivity coefficient can be determined from the already-known TKE and TDR values.

4.4.2. Clear water case

For simulating the clear water case (CW) in Muste *et al.* (2005), the momentum conservation equation of fluid is coupled with the standard k-ε model. The steady state results in terms of streamwise velocity and turbulent eddy viscosity for the clear water conditions are presented in Figures 4.6 and 4.7.

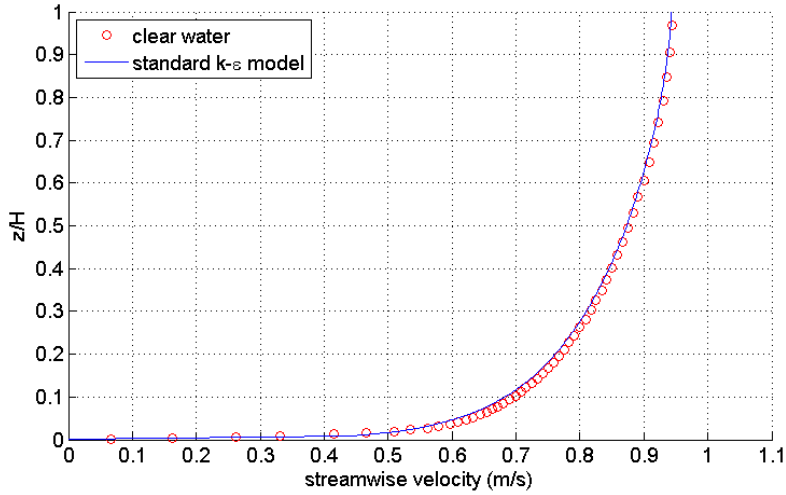

Figure 4.6. Comparison of simulated streamwise velocity with measurements of Muste *et al.* (2005) in clear water conditions.

In general, Figure 4.6 shows a good agreement for the streamwise velocity with the standard k-ε model although there is a slight underestimation especially in the lower part of the water column. The simulated eddy viscosity (Figure 4.7) also gives a good agreement with the measurements except that it slightly overestimates the eddy viscosity in the near-bottom layer.

The underestimation of streamwise velocity can be explained by the slight overestimation of the eddy viscosity in the near-bottom region. The numerical tests showed that the accuracy of the predicted turbulent eddy viscosity in the near-bottom region affects the velocity profile not only in the same near-bottom region but also in the upper part of the water column.

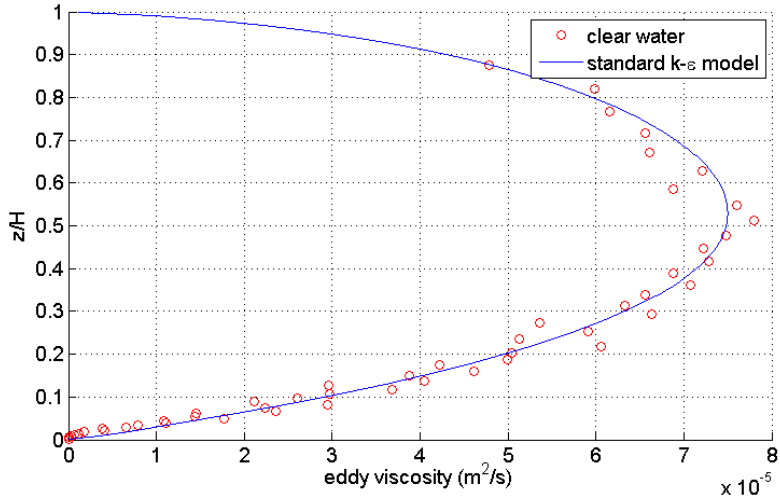

Figure 4.7. Comparison of simulated turbulent viscosity with measurements of Muste *et al.* (2005) in clear water conditions.

4.4.3. Sediment-laden flow

The momentum conservation equation coupled with standard *k-ε* model (with sediment-induced buoyancy effects) and advection-diffusion equation of suspended-sediment is used to simulate the sediment-laden flow in the experiments conducted by Muste *et al.* (2005).

In cohesive sediment dynamics, the sediment-induced buoyancy effects refer to the turbulent vertical mixing damping due to the suspension concentration exceeding the saturation concentration. The damping of turbulence starts at the interface between the newly formed fluid mud layer on the rigid bed and the fluid layer above the fluid mud layer. The turbulence is usually damped strongly, leading to the decrease of the sediment carrying capacity in the upper layer of the flow, and finally resulting in collapse of the turbulence and vertical sediment concentration profile by the snowball effects as shown in Figure 4.8 (Winterwerp & Van Kesteren, 2004). The suspension capacity (maximum amount of sediment that can be carried by the flow without violating energy balance) sometimes can be reduced by an order of magnitude due to the sediment-induced buoyancy effects.

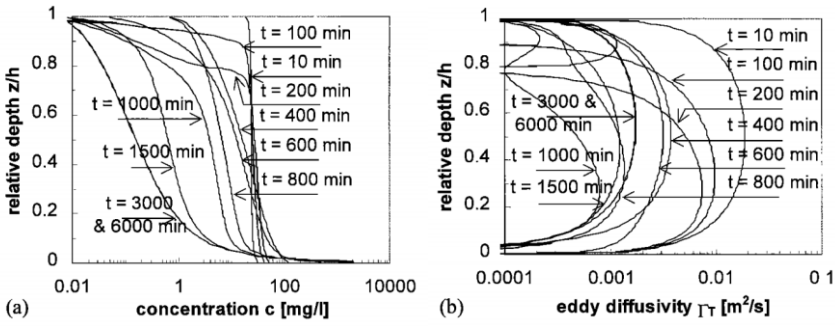

Figure 4.8. Computed time evolution of (a) concentration and (b) eddy diffusivity profiles for C_0 = 0.024 g/L considering the sediment-induced buoyancy effects (Winterwerp, 2001).

However, the above results follow from a numerical experiment where the turbulent Schmidt number has been described as an empirical function of the gradient Richardson number, following a traditional approach taken from atmospheric sciences. No experimental evidence exists for this strong turbulence damping. Moreover, Toorman (2008) demonstrated that the turbulent Schmidt number in the case of particle concentration induced stratification does not depend on the Richardson number.

For non-cohesive sediment too, no full consensus exists on the effects of suspended-sediment on the vertical velocity profile and the turbulence properties (Winterwerp, 2001). However, the sediment-induced buoyancy effects were still observed in the non-cohesive sediment-laden flow by Geifenbaum and Smith (1986), Lau and Chu (1987), and Cellino and Graf (1999), in which the vertical eddy diffusivity appeared to decrease by up to 75% for capacity flow with respect to clear water conditions when sediment concentration was beyond a certain point. Therefore, it is necessary to include the buoyancy term in the k-ε model for simulating the experiments in the study of Muste *et al.* (2005).

For solving the advection-diffusion of suspension, proper boundary conditions are required. Equation (4.36) indicates that sediment flux should be specified as a Neumann type boundary condition at the bottom. Considering the steady state, the equilibrium condition is assumed at the bottom, which means that, the erosion flux should be equal to the deposition flux. Then the equation (4.36) can be reduced to:

$$D_T \frac{\partial C}{\partial n} = -E \tag{4.68}$$

The erosion rate E is calculated using the formulas from Van Rijn (1984), in which a reference level is assumed:

$$c_a = 0.015 \frac{D_{50}}{z_{ref}} \frac{T^{1.5}}{D_*^{0.3}} \tag{4.69}$$

where c_a is the concentration at reference level, D_{50} is the characteristic diameter of sediment particle, z_{erf} is the reference level. T is the transport stage parameter and D_* is the particle parameter.

$$T = \frac{u_*^2 - u_{*,cr}^2}{u_{*,cr}^2} \tag{4.70}$$

$$D_* = D_{50} \left[(\frac{\rho_p}{\rho_f} - 1) \frac{g}{\nu^2} \right]^{1/3} \tag{4.71}$$

in which u_* is the shear velocity, $u_{*,cr}$ is the critical shear velocity for erosion, ρ_p is the sediment density, ρ_f is the water density, g is the gravity acceleration, ν is the kinematic viscosity.

The erosion rate (under equilibrium condition) is given by:

$$E = w_s c_a \tag{4.72}$$

Muste *et al.* (2005) suggested that the reference level can be taken at which a distinct peak in sediment concentration occurred.

The suspension concentration profiles measured by Muste *et al.* (2005) are presented in Figure 4.9. The strange thing in Figure 4.9 is that all the concentration profiles have the highest values just above the bed and then decrease instead of reaching the peaks at the bottom. This phenomenon may be caused by the PTV measuring technique, which does not measure particle concentration directly, but rather particle numbers (fluxes) and excludes immobile particles. Figure 4.9 shows the three different cases (NS1, NS2 and NS3) with different sediment loads (NS1<NS2<NS3). It is obvious that, the higher sediment loads given at the beginning, the higher the peaks occurring above the bed, and the lower the concentration reached at the bottom. This indicates that a bed layer

may have formed and the higher the sediment loads, the thicker the bed layer is.

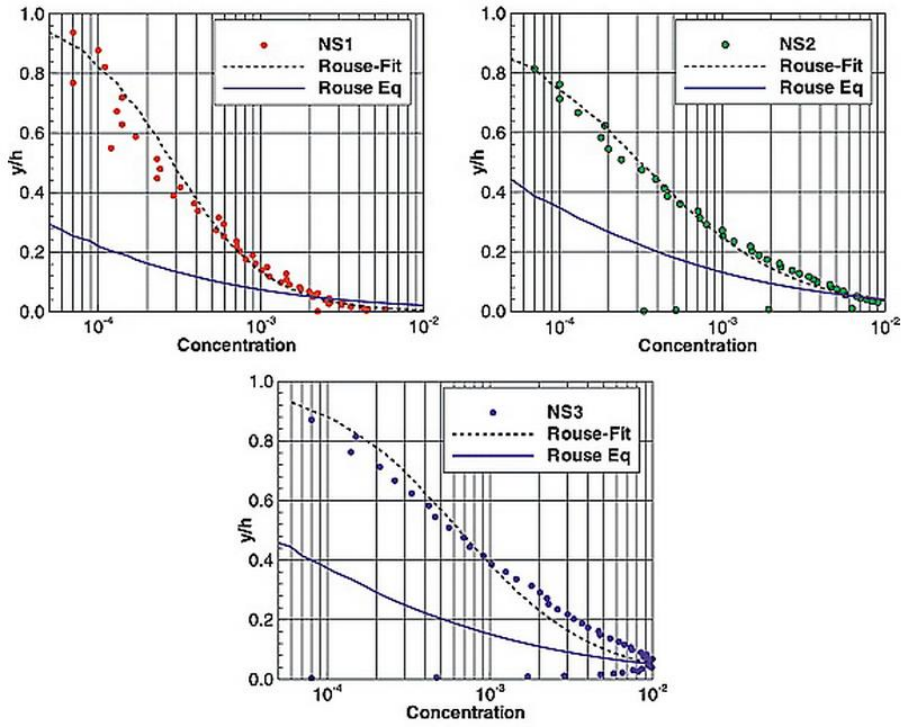

Figure 4.9. Sediment concentrations of NS tests (Muste *et al.*, 2005)

The simulated results for the NS2 test with standard k-ε model are presented in Figures 4.10, 4.11 and 4.12. In this particular case, the reference level is chosen as $1.4D_{50}$, which is where the peak concentration occurs.

In general, the model gives good predictions of the streamwise velocity profile, with slight overestimations in the upper water column. Again, this is caused by the underestimation of eddy viscosity in the lower part of water column. The predicted volumetric suspension concentration has better agreement with the measured data near the bottom, suggesting that the reference level assumed as $1.4D_{50}$ is appropriate. However, for the rest of the water column, the model underestimates the suspension concentration. This confirms that the eddy viscosity is underestimated.

This can be explained by the lack of including sub-grid scale turbulence generated in the wakes of suspended particles.

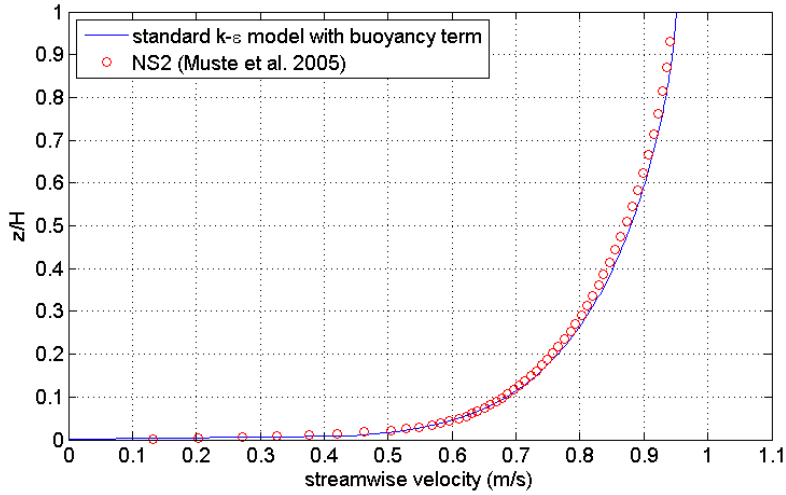

Figure 4.10. Comparison of simulated streamwise velocity with measurements of Muste *et al.* (2005) in the NS2 experiment.

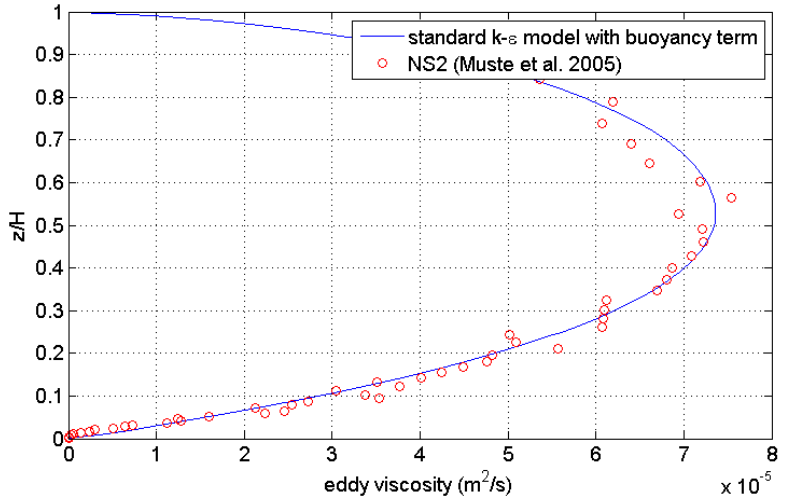

Figure 4.11. Comparison of simulated turbulent eddy viscosity with measurements of Muste *et al.* (2005) in the NS2 experiment.

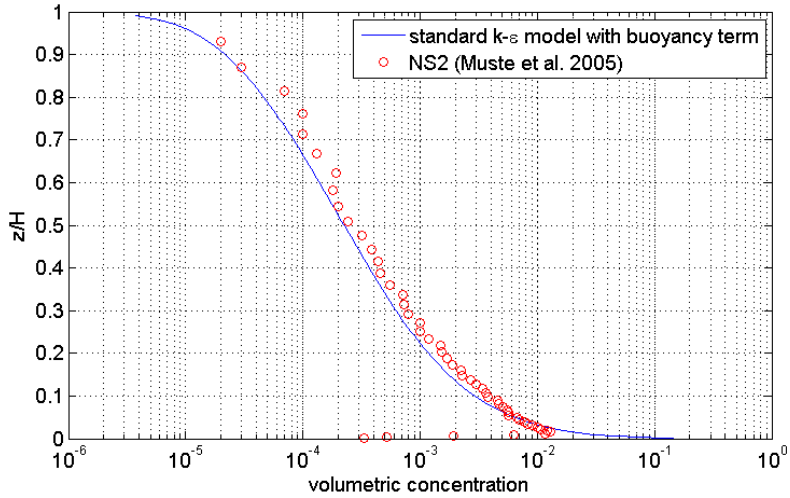

Figure 4.12. Comparison of simulated volumetric suspension concentration with measurements of Muste *et al.* (2005) in the NS2 experiment.

4.5. Investigating turbulence modulation

4.5.1. The terms due to the presence of the second phase

In this section, the extra terms derived from two-phase flow theory are added into the *k-ε* equations and tested in the 1DV model. The numerical tests are carried out systematically. In the beginning, the first two terms in equation (3.15) are tested. Therefore, to be more specific, in current 1DV model, equations (4.37) and (4.38) can be rewritten as:

$$-\frac{\partial}{\partial z}\left[\left(\nu+\frac{\nu_t}{\sigma_k}\right)\frac{\partial k}{\partial z}\right]+\varepsilon = \nu_t\left(\frac{\partial u_x}{\partial z}\right)^2+\frac{g}{\rho}\frac{\nu_t}{\sigma_t}\frac{\partial \rho}{\partial z}-\frac{\partial}{\partial z}\left(\frac{\nu_t}{\sigma_k}\right)\frac{\partial k}{\partial z} \tag{4.73}$$

$$-\frac{\partial}{\partial z}\left[\left(\nu+\frac{\nu_t}{\sigma_\varepsilon}\right)\frac{\partial \varepsilon}{\partial z}\right]+C_{\varepsilon 2}\frac{\varepsilon^2}{k} = C_{\varepsilon 1}\frac{\varepsilon}{k}\nu_t\left(\frac{\partial u_x}{\partial z}\right)^2+C_{\varepsilon 4}\frac{\varepsilon}{k}\left(-\frac{\partial}{\partial z}\left(\frac{\nu_t}{\sigma_k}\right)\frac{\partial k}{\partial z}\right) \tag{4.74}$$

Here, the semi-empirical constants are taken as $\sigma_k = 1$, $\sigma_\varepsilon = 1.3$, $\sigma_t = 0.7$, $C_{\varepsilon 1} = 1.44$, $C_{\varepsilon 2} = 1.92$ (as above), and $C_{\varepsilon 4} = 0.6$. It is worth mentioning here the value of the empirical constant $C_{\varepsilon 4}$ is determined from numerical tests based on the experiments of Muste *et al.* (2005).

Using the auxiliary parameter $\gamma = \epsilon/k$, the above equations can be decoupled and their discretized forms are as follows.

For the modified TKE equation:

$$\int_{z_l}^{z_u}\left[\left(\nu+\frac{\nu_t}{\sigma_k}\right)\frac{\partial N_i}{\partial z}\sum_{j=1}^{n}\frac{\partial N_j}{\partial z}k_j+N_i\gamma\sum_{j=1}^{n}N_j k_j+N_i\frac{\partial}{\partial z}\left(\frac{\nu_t}{\sigma_k}\right)\sum_{j=1}^{n}\frac{\partial N_j}{\partial z}k_j\right]dz = \int_{z_l}^{z_u}\left[N_i\nu_t\left(\frac{\partial u_x}{\partial z}\right)^2+N_i\frac{g}{\rho}\frac{\nu_t}{\sigma_t}\frac{\partial \rho}{\partial z}\right]dz+N_i\left(\nu+\frac{\nu_t}{\sigma_k}\right)\frac{\partial k}{\partial z}\Bigg|_{z_l}^{z_u} \tag{4.75}$$

Using Gauss integration (3 Gauss points) and the matrix form is obtained:

$$a_{ij} = \sum_{n=1}^{3}\left(\nu+\frac{\nu_t^{(n)}}{\sigma_k}\right)\frac{\partial N_i^{(n)}}{\partial z}\frac{\partial N_j^{(n)}}{\partial z}\left|\mathrm{J}\right|w_n+\sum_{n=1}^{3}\gamma^{(n)}N_i^{(n)}N_j^{(n)}\left|\mathrm{J}\right|w_n + \sum_{n=1}^{3}N_i^{(n)}\frac{\partial}{\partial z}\left(\frac{\nu_t}{\sigma_k}\right)^{(n)}\frac{\partial N_j^{(n)}}{\partial z}\left|\mathrm{J}\right|w_n \tag{4.76}$$

$$b_i = \sum_{n=1}^{3}N_i^{(n)}\nu_t^{(n)}\left(\frac{\partial u_x}{\partial z}^{(n)}\right)^2\left|\mathrm{J}\right|w_n+N_i\left(\nu+\frac{\nu_t}{\sigma_k}\right)\frac{\partial k}{\partial z}\Bigg|_{z_l}^{z_u} + \sum_{n=1}^{3}N_i^{(n)}\frac{g}{\rho^{(n)}}\frac{\nu_t^{(n)}}{\sigma_t}\frac{\partial \rho}{\partial z}^{(n)}\left|\mathrm{J}\right|w_n \tag{4.77}$$

For the TDR equation:

$$\int_{z_l}^{z_u}\left[\left(\nu+\frac{\nu_t}{\sigma_\varepsilon}\right)\frac{\partial N_i}{\partial z}\sum_{j=1}^{n}\frac{\partial N_j}{\partial z}\varepsilon_j+N_iC_{\varepsilon 2}\gamma\sum_{j=1}^{n}N_j\varepsilon_j\right]dz$$

$$=\int_{z_l}^{z_u}N_iC_{\varepsilon 1}\gamma\nu_t\left(\frac{\partial u_x}{\partial z}\right)^2dz+N_i\left(\nu+\frac{\nu_t}{\sigma_\varepsilon}\right)\frac{\partial\varepsilon}{\partial z}\Bigg|_{z_l}^{z_u} \tag{4.78}$$

$$-\int_{z_l}^{z_u}N_iC_{\varepsilon 4}\gamma\frac{\partial}{\partial z}\left(\frac{\nu_t}{\sigma_\varepsilon}\right)\frac{\partial k}{\partial z}dz$$

Using Gauss integration (3 Gauss points) and the matrix form is obtained:

$$a_{ij}=\sum_{n=1}^{3}\left(\nu+\frac{\nu_t^{(n)}}{\sigma_k}\right)\frac{\partial N_i^{(n)}}{\partial z}\frac{\partial N_j^{(n)}}{\partial z}\left|\mathrm{J}\right|w_n+\sum_{n=1}^{3}C_{\varepsilon 2}\gamma^{(n)}N_i^{(n)}N_j^{(n)}\left|\mathrm{J}\right|w_n \tag{4.79}$$

$$\begin{aligned}b_i=&\sum_{n=1}^{3}N_i^{(n)}C_{\varepsilon 1}\gamma^{(n)}\nu_t^{(n)}\left(\frac{\partial u_x}{\partial z}^{(n)}\right)^2\left|\mathrm{J}\right|w_n+N_i\left(\nu+\frac{\nu_t}{\sigma_\varepsilon}\right)\frac{\partial\varepsilon}{\partial z}\Bigg|_{z_l}^{z_u}\\&-\sum_{n=1}^{3}C_{\varepsilon 4}\gamma^{(n)}N_i^{(n)}\frac{\partial}{\partial z}\left(\frac{\nu_t}{\sigma_k}\right)^{(n)}\frac{\partial k}{\partial z}^{(n)}\left|\mathrm{J}\right|w_n\end{aligned} \tag{4.80}$$

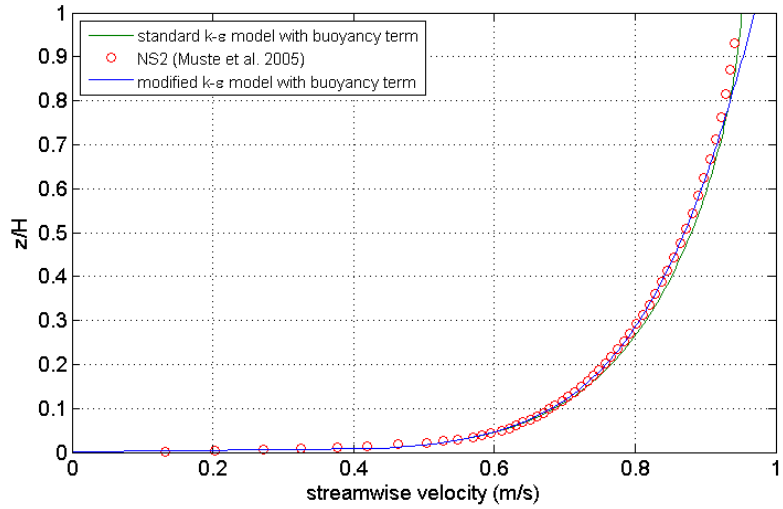

Figure 4.13. Comparison of simulated streamwise velocity by standard and modified *k-ε* models with measurements of Muste *et al.* (2005) in the NS2 experiment.

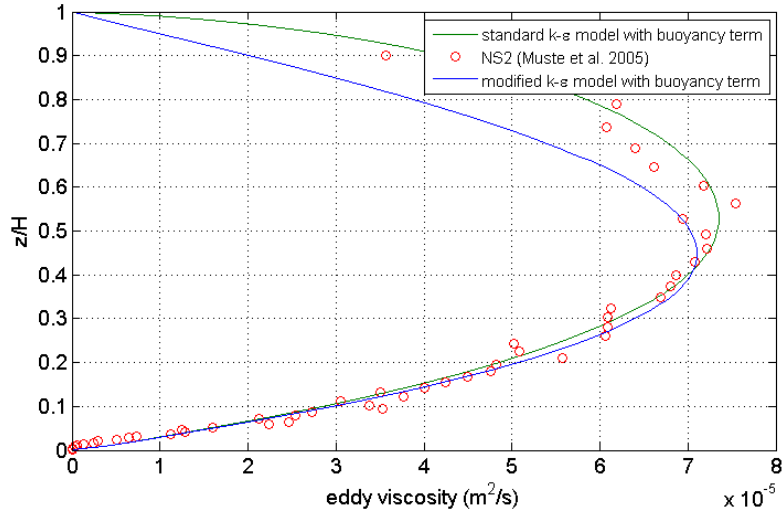

Figure 4.14. Comparison of simulated turbulent eddy viscosity by standard and modified *k-ε* models with measurements of Muste *et al.* (2005) in the NS2 experiment.

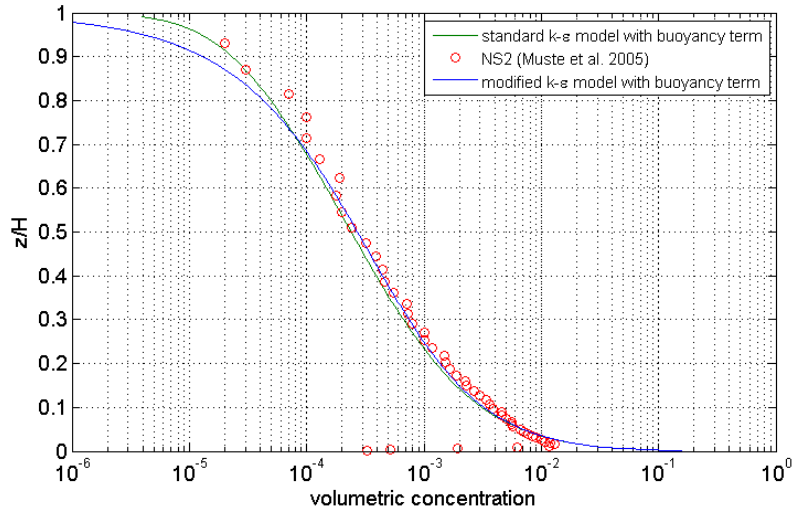

Figure 4.15. Comparison of simulated volumetric suspension concentration by standard and modified k-ε models with measurements of Muste *et al.* (2005) in the NS2 experiment.

The simulated results are shown in Figures 4.13 to 4.15 with the comparison with the standard k-ε model. The influence of the extra term in the equation (4.73) is also revealed. In general, the extra term has better performance in the lower part of the water column but gives worse predictions in the upper water column compared to the standard k-ε model. However, it is worth pointing out that the accuracy of the very low concentrations measured near the surface is also very low.

In the lower water column, the extra term gives better predictions in terms of the stream-wise velocity especially in the range of $0 < z/H < 0.3$. It also increases the turbulence eddy viscosity in the near bottom region which matches better with the measured data, and reasonably, improves the predicted suspension concentration profile, too.

However, the extra term seems unnecessary in the upper water column because it decreases the turbulence eddy viscosity and makes the results deviate from the measurements. Hence, the accuracy of the predicted streamwise velocity and suspension concentration become worse.

Examining the extra term in the right hand side of equation (4.73) we find that, the vertical gradient of k is always negative but the vertical gradient of ν_t is positive in the lower water column and negative in the upper part

due to their profiles. Therefore, it is expected to enhance the turbulence in the near bottom region and show the opposite effects in the upper water column, which is confirmed by the numerical tests illustrated in Figures 4.13 to 4.15.

The reason that the extra terms cannot automatically reduce the damping when the concentration decreases near the surface is due to using the equation (3.29) in the derivation of the modified *k*-*ε* model (the details are given in Appendix II). In such case, the momentum equations become simpler, which makes the derivation process easier and less additional terms appearing after Reynolds-averaging. However, the disadvantage is obvious, which is that the concentration dependency is implicitly contained in one particular term as shown in equation (3.36). Unfortunately, equation (3.36) cannot be used directly in the modified *k*-*ε* model. Therefore, it seems that it is possible to introduce a function that can restrict the turbulence damping in the upper water column whereas maintain the influence of the turbulence enhancement in the near bottom region. From a physical perspective, in the upper water column, the suspension concentration is normally two or three orders of magnitude lower that the near bottom concentration, which means the presence of the particle phase is less important and even negligible. It matters when the concentration is beyond a certain level. Thus, an auxiliary function f_c is incorporated into the extra term to limit its influence in the upper water column:

$$-\frac{\partial}{\partial z}\left[\left(\nu+\frac{\nu_t}{\sigma_k}\right)\frac{\partial k}{\partial z}\right]+\varepsilon = \nu_t\left(\frac{\partial u_x}{\partial z}\right)^2+\frac{g}{\rho}\frac{\nu_t}{\sigma_t}\frac{\partial \rho}{\partial z}-f_c\frac{\partial}{\partial z}\left(\frac{\nu_t}{\sigma_k}\right)\frac{\partial k}{\partial z} \tag{4.81}$$

$$-\frac{\partial}{\partial z}\left[\left(\nu+\frac{\nu_t}{\sigma_\varepsilon}\right)\frac{\partial \varepsilon}{\partial z}\right]+C_{\varepsilon 2}\frac{\varepsilon^2}{k} = C_{\varepsilon 1}\frac{\varepsilon}{k}\nu_t\left(\frac{\partial u_x}{\partial z}\right)^2-f_c C_{\varepsilon 4}\frac{\varepsilon}{k}\left(\frac{\partial}{\partial z}\left(\frac{\nu_t}{\sigma_k}\right)\frac{\partial k}{\partial z}\right) \tag{4.82}$$

$$\text{and } f_c = \begin{cases} \dfrac{C_s}{C_{cr}}, & C_s < C_{cr} \\ 1 \ , & C_s > C_{cr} \end{cases} \tag{4.83}$$

where, C_s is volumetric suspension concentration and C_{cr} is the critical volumetric suspension concentration above which the influence of the presence of the particle phase cannot be neglected. As indicated in the Figure 3.1, when the volumetric concentration exceeds 1.0×10^{-6}, the momentum transfer from the particles is large enough to alter the turbulence. Hence, the two-way coupling becomes important. When the volumetric concentration exceeds 1.0×10^{-3}, the four-way coupling effects becomes important. In this study, $C_{cr} = 1.0\times10^{-4}$. This value is based on the Figure 3.1 and is obtained from the numerical tests. From another perspective, the auxiliary function f_c can also be interpreted as the affected fraction of the fluid, i.e. the effect of the particle-fluid interaction can only be felt by the fluid in the neighbourhood of particles, while the k-ε model yields the average effect over all the fluid. By multiplication proportional to the concentration, the particle-effect is only applied to the affected fraction of the fluid and not to all the fluid.

With the function f_c added in the modified k-ε equations, the 1DV model gives overall better predictions as seen in Figures 4.16, 4.17 and 4.18. The simulated streamwise velocity profile has better agreement with the measured data compared to the other two k-ε models, even in the upper water column. The model increases the turbulence eddy viscosity especially in the lower and middle part of the water column. Therefore, the volumetric suspension concentration profile is also increased, which is closer to the measurements.

As shown in the comparison between the standard k-ε, which is designed for the sediment-free flow, and the modified one with turbulence modulation based on the two-phase flow theory, the eddy viscosity has smaller values in the upper layer with the modified k-ε model. However, in the lower water column, the turbulence is enhanced. The modified model gives better approximation to the measured data from Muste's experiment. The same tendency is also observed in the turbulence kinetic energy profiles. This can be explained by the extra turbulence energy transfer caused by particles. Unlike the fluid, momentum transfer is mainly done by the upwards or downwards turbulent motions, solid particles always try to settle down to the bottom. This downwards movement, brings the energy acquired in the upper water column to the

lower layer. Therefore, we can observe the downwards shift of the eddy viscosity profile.

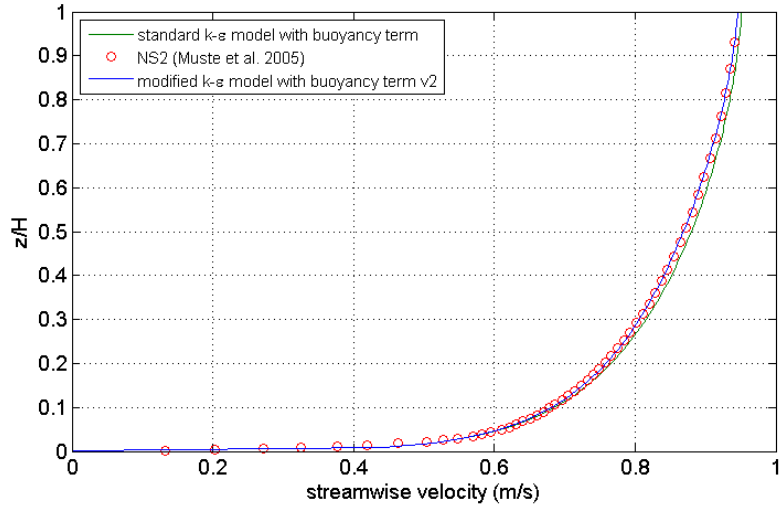

Figure 4.16. Comparison of simulated streamwise velocity by standard and modified k-ε models (v2) with measurements of Muste *et al.* (2005) in the NS2 experiment.

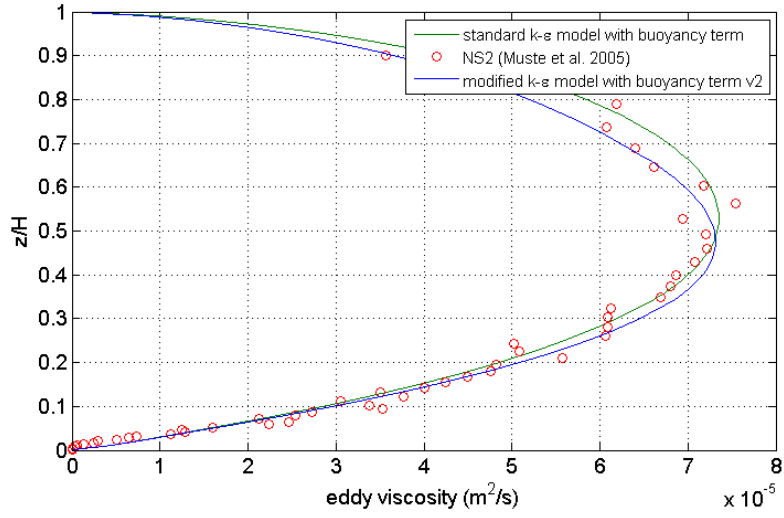

Figure 4.17. Comparison of simulated turbulent eddy viscosity by standard and modified *k-ε* models (v2) with measurements of Muste *et al.* (2005) in the NS2 experiment.

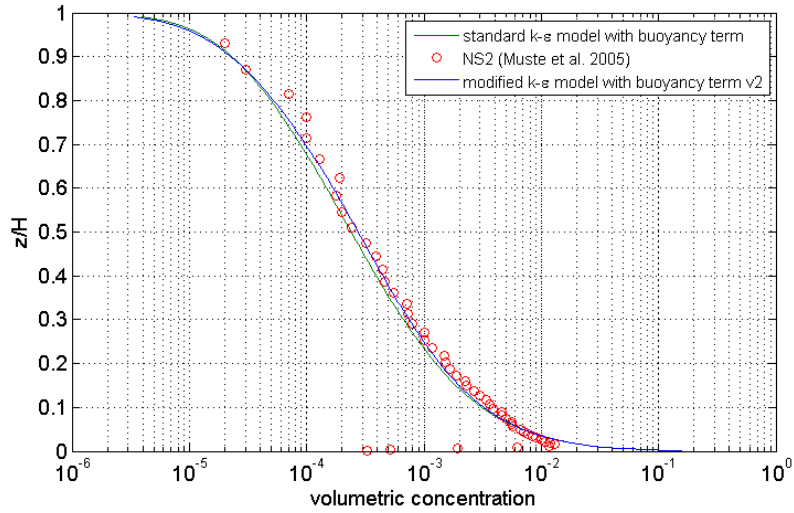

Figure 4.18. Comparison of simulated volumetric suspension concentration by standard and modified *k-ε* models (v2) with measurements of Muste *et al.* (2005) in the NS2 experiment.

However, the TDR becomes larger and larger, the influence of the additional turbulence kinetic energy, therefore, becomes insignificant compared to it. So near the bottom, the differences become smaller too.

4.5.2. The term due to the fluid-particle interactions

The fluid-particle interaction term refers to the last term in the following equation:

$$\Pi_k = \overline{p' \frac{\partial u_i'}{\partial x_i}} + \frac{1}{2} \overline{\rho_f u_i' u_i' \frac{\partial u_j'}{\partial x_j}} - \overline{u_i' \omega_i'}$$

It is called the interaction term because $\omega_i = f_i/(1-\phi)$, in which f_i is defined as the interaction forces exerted on the particle by the fluid and ϕ is volume fraction of particles. To be explicit, the interaction forces consists of drag force, virtual mass force, lift force and Basset history force.

Jha and Bombardelli (2010) performed numerical simulations using two-phase flow model and analysed the effects of the interaction forces. Their research indicates that, in dilute sediment-laden flow, the ratio between

other forces and the drag force are always below 2%, so all forces except the drag force can be disregarded. However, for non-dilute sediment-laden flow, their results show that the lift force is of the order of 3% to 4% of the drag force close to the wall, while the virtual mass force is of the order of 25% of the drag force in the same location. The magnitude of the forces gradually decreases in the direction away from the bed and the relative magnitude of the virtual mass is much larger than the relative magnitude of the lift force at any depth in the flow. However, the Basset force is not considered in their investigation.

The interaction force is usually associated with the lag velocity between two phases. In the experiments of Muste *et al.* (2005), the averaged lag velocity was also measured for NS1, NS2 and NS3 cases. It is important to distinguish the instantaneous lag velocity from the averaged lag velocity because there could not be an actual slip between water and sediment particles in their instantaneous interaction, because that would violate the no-slip condition acting on local fluid boundaries (the particles) (Muste *et al.*, 2005). Therefore, the leading explanation for the average velocity lag in the streamwise direction is the tendency of the sediment particles to reside in the flow structures moving with lower velocities (Sumer & Deigaard, 1981; Kaftori *et al.*, 1995; and Kiger & Pan, 2002). The inverse lag near the bed is because sediment particles are not bounded by viscous shear as fluid particles. The non-slip condition for water movement at the bottom does not apply for the sediment.

Inspired by Greimann *et al.* (1999), the following formula is proposed for approximating the measured lag velocity:

$$\frac{u_{lag}}{w_s} = -\frac{\rho_s}{\rho_f}\left[\left(b_1 \ln\left(\frac{z}{h}\right) + b_2\right)^2 + b_3\right] \tag{4.84}$$

where: u_{lag} is the velocity lag, w_s is the particle settling velocity, ρ_s is the sediment density, ρ_f is the fluid density, z is the vertical coordinate, h is the water depth, b_1, b_2 and b_3 are the empirical parameters to be determined. Using the non-linear least-squares curve fitting, the empirical parameters b_1, b_2 and b_3 for NS1, NS2 and NS3 cases are determined (Table 4.4). The fitted lag velocities are plotted in Figure 4.19.

Increasing particle concentration increases the velocity lag (Muste *et al.*, 2005) except for the near-bottom region. This can be seen in the measurements indicated in Figure 4.19.

Table 4.4. The empirical parameters b_1, b_2 and b_3 for NS cases.

Tests	b_1	b_2	b_3
NS1	0.3704	0.8956	-0.8505
NS2	0.3290	0.8331	-0.9397
NS3	0.2926	0.6550	-0.8578

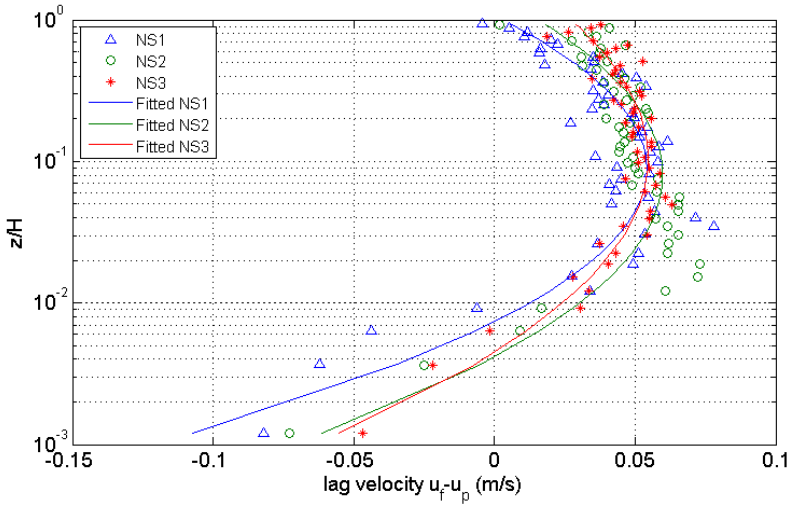

Figure 4.19. The measured and fitted lag velocities for NS cases.

The reason behind this phenomenon is that, above the bed, the particles tend to collide with each other more often when the concentration is higher and the collisions will consume more energy, resulting in larger lag velocity. However, in the near-bottom region, more particles that are non-moving will stay on the bed when the concentration becomes higher. These particles will hinder other moving particles and slow them down. In this sense, close to the bottom, a lower lag velocity is expected when the concentration is higher. Besides, the velocity is also associated with the particle inertia, which means the heavier sediment particle, the larger velocity lag will occur. It is worth mentioning that, the particle size used

in the experiment is 0.21-0.25 mm and the water depth is 2.1 cm. It implies that the measured data in Fig.4.19 is more difficult to be interpreted when z/H is smaller then 0.01, which is about the same as the particle diameter.

In the experiments of Muste *et al.* (2005), the total volumetric sediment concentrations for NS1, NS2 and NS3 are 0.46×10^{-3}, 0.92×10^{-3} and 1.62×10^{-3} respectively. Table 4.4 reveals that the empirical parameters b_1 and b_2 seem proportional to the suspension concentration. Thus, through the numerical analysis, b_1, b_2 and b_3 can be approximated using the following formulas:

$$b_1 = 0.386\left(\frac{1}{C_{total}}\right)^{1/5.35} \tag{4.85}$$

$$b_2 = 0.925\left(\frac{1}{C_{total}}\right)^{1/5.35} \tag{4.86}$$

$$b_3 = -\left(0.75 + 0.037C_{total}\right) \tag{4.87}$$

in which, C_{total} is mass concentration of total suspended sediment. Therefore, the equation (4.84) can be rewritten as:

$$\frac{u_{lag}}{w_s} = -\frac{\rho_s}{\rho_f}\left[\left(\frac{1}{C_{total}}\right)^{2/5.35}\left(0.386\ln\left(\frac{z}{h}\right)+0.925\right)^2 - \left(0.75+0.037C_{total}\right)\right] \tag{4.88}$$

The fitted results given by equation (4.88) together with the measured data are shown in Figure 4.20. The curves calculated from equation (4.88) are labelled with "v2". It can be seen that, for the same particle inertia, the lag velocity becomes larger when the suspension concentration increases, which is in agreement with the experimental observations (Muste *et al.*, 2005).

As mentioned before, the drag force is the dominant force among other interaction forces between particle and fluid phases. Then we deduce the interaction term in equation (3.15). Because of the relation $\omega_i = f_i/(1-\phi)$, using the slip velocity $w_i = v_i - u_i$ (the slip velocity = - lag velocity according to the definition) and considering the force balance on a particle gives:

$$\omega_i = \frac{f_i}{1-\phi} = -\frac{1}{1-\phi}\left((1+r_d)\frac{1}{2}\rho_f C_D \frac{A_P}{V_P} w_i^2\right) \tag{4.89}$$

where v_i is the particle velocity, u_i is the fluid velocity, f_i represents the forces exerted on a particle, ϕ is the volume fraction of the particle phase, ρ_f is the fluid density, C_D is the particle drag coefficient, A_P is the surface area of a spherical particle and V_P is its volume, r_d is the correction constant which represents the ratio of other forces, *e.g.* virtual mass force, lift force and Basset history force, to the drag force.

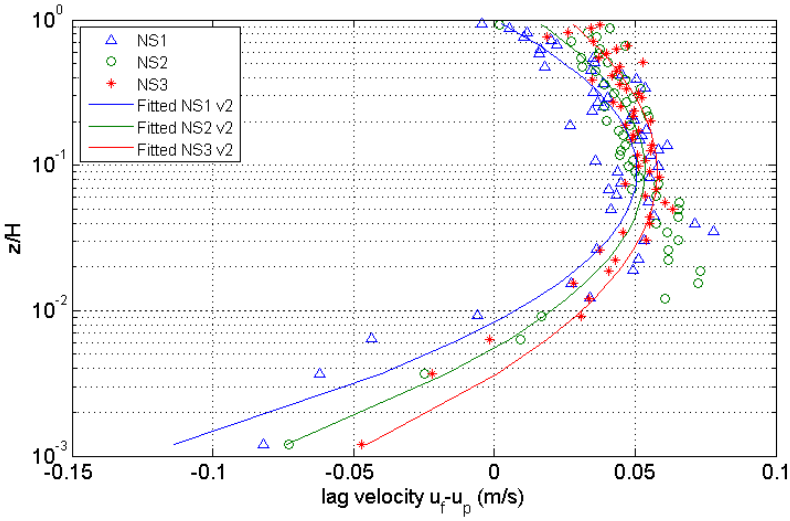

Figure 4.20. The measured and fitted (v2) lag velocities for NS cases.

For the purpose of evaluating the interaction term, it is assumed that ω_i can be seen as a function of w_i^2. Hence,

$$\omega_i \propto w_i^2 = (\overline{w_i} + w_i')^2 = \overline{w_i}^2 + 2\overline{w_i}w_i' + w_i'^2 \tag{4.90}$$

$$\overline{\omega_i} \propto \overline{w_i^2} = \overline{(\overline{w_i} + w_i')^2} = \overline{w_i}^2 + \overline{w_i'^2} \tag{4.91}$$

$$\omega_i' \propto 2\overline{w_i}w_i' + w_i'^2 - \overline{w_i'^2} \tag{4.92}$$

Therefore, the following relation can be established:

$$\overline{u_i'\omega_i'} \propto 2\overline{w_i}\,\overline{u_i'w_i'} + \overline{u_i'w_i'^2} \tag{4.93}$$

Because the slip velocity fluctuations w_i' are considerably small and negligible for suspended sediment transport according to the study of Breugem (2012), the interaction term can be neglected. It is also logical from numerical perspective since the 1DV model has already given good agreement with the measured data even without the interaction term. This is no surprise because of the low suspended loads in this particular set of experiments.

4.5.3. Testing the modified *k-ε* model

Here, the extra terms deduced from previous sections are tested and compared with the experimental data from Cellino (1998). In his experiments, the measurements have been made in a recirculating tilting channel, 16.8m long and 0.60m wide. Sediments were added slowly to the uniform flow until the suspension capacity was achieved. The capacity condition of the flow was verified when a layer of sediment, composed of the same sediment as in the suspension, is always present on the bed (Cellino, 1998).

Table 4.5. Summary of experimental data (Q55S015_Sand_I).

Q	h	h_δ	u_c	B/h	U	S_b
[m³/s]	[m]	[m]	[m/s]	[--]	[m/s]	[%]
0.062	0.120	0.099	1.008	5.0	0.858	0.150
Fr	$u_{*\tau}$	u_{*s}	f	k_s	d_{50}	ρ_s
[--]	[m/s]	[m/s]	[--]	[mm]	[mm]	[kg/m³]
0.79	0.043	0.042	0.020	0.222	0.135	2650
C_s^m	c_{sa}^m	ρ_m	R_i	R_e	v_{ss}	R_{ep}
[kg/m³]	[kg/m³]	[kg/m³]	[--]	[--]	[mm/s]	[--]
4.41	46.05	1002.75	18.120	293800	12.0	9.5

In Table 4.5, Q is the flow discharge, h is the flow depth, h_δ is the height where the maximum velocity u_c has been measured, B is the channel width, U is the depth-averaged longitudinal velocity, R_e is the Reynolds number, ρ_w and ρ_s are water and sediment densities, ρ_m is the depth-averaged mixture density, S_b is the bed slope, Fr is the Froude number, C_s^m is the depth-averaged concentration, c_{sa}^m is the reference concentration, $u_{*\tau}$ is the shear velocity obtained by extrapolating the measured Reynolds-stress profile towards the bed, u_{*S} is the shear velocity obtained by the energy method, f is the friction factor, k_s is the equivalent roughness, R_{ep} is the particle Reynolds number, and R_i is the bulk Richardson number according to Coleman (1981).

The measurements started after 4 hours of flow recirculation in capacity condition and all measurements were taken at the centreline of the cross section located 13m from the entrance of the channel (Cellino, 1998).

The 1DV model is again used to compare with the test case Q55S015_Sand_I whose hydraulic characteristics are summarized in Table 4.5. The flow was steady and uniform, carrying natural sand particles at capacity over a plane bed where a layer of the same sediment was available. In addition, the experiment Q55S015_Sand_I was repeated several times by Cellino, and a series of measured velocity profiles have been used to study the spatial evolution of the flow and its turbulence characteristics.

The modified k-ε equations (4.81) to (4.83) is applied in the 1DV model for simulating Cellino's test case Q55S015_Sand_I. Notice that the concentrated layer (5mm) on the bottom has been excluded in the simulation because the actual bed level is not given in the experimental data. The measured velocity and concentration at about 5mm above the bed are used as boundary conditions.

The numerical settings and boundary conditions are similar as described in section 4.43, except the reference concentration is already given in Table 4.5. The results are shown in Figures 4.21, 4.22 and 4.23.

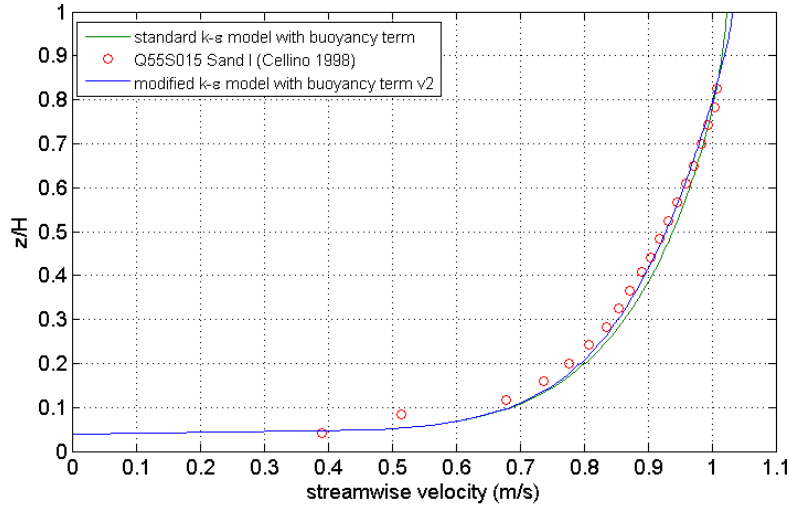

Figure 4.21. Comparison of simulated stream-wise velocity by standard and modified k-ε models (v2) with measurements of Cellino (1998) in the Q55S015_Sand_I experiment.

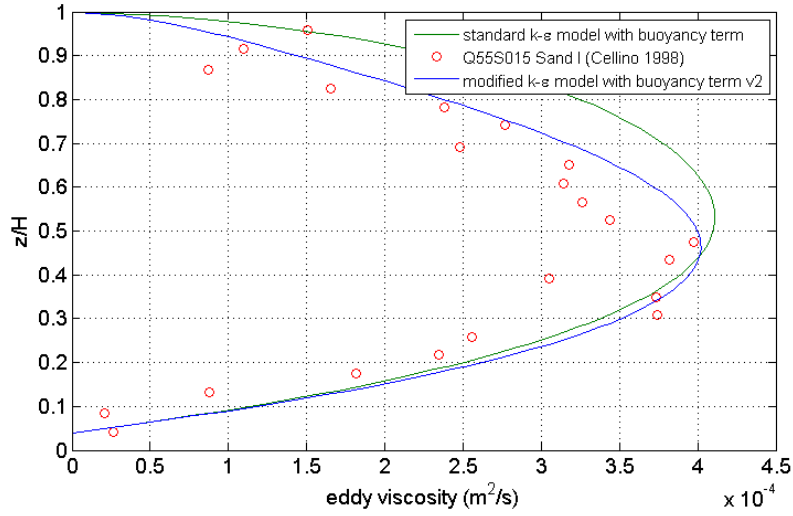

Figure 4.22. Comparison of simulated eddy viscosity by standard and modified k-ε models (v2) with measurements of Cellino (1998) in the Q55S015_Sand_I experiment.

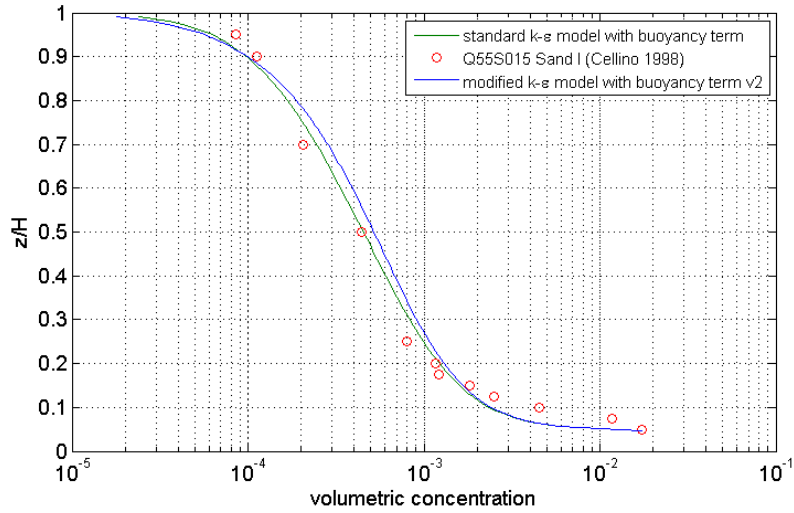

Figure 4.23. Comparison of simulated volumetric suspension concentration by standard and modified *k-ε* models (v2) with measurements of Cellino (1998) in the Q55S015_Sand_I experiment.

As expected, the modified *k-ε* model (v2) with the extra terms derived from two-phase flow theory shows the similar behaviour as seen in section 4.5.1 while simulating the NS test from Muste's experiments. The extra terms correct the eddy viscosity in the upper water column and give better predictions on the streamwise velocity profile, which are closer to the experimental data. However, the volumetric suspension predicted by the modified *k-ε* model (v2) deviates further than the standard model. This is because the turbulence is enhanced by the extra terms near the bottom and it demonstrates that the accuracy of the predicated eddy viscosity near the bottom has influence on the suspension capacity in the whole water column.

Unlike the Muste's experiments that can be considered as fully developed turbulent flow over the water column, Cellino's Q55S015_Sand_I case has a high-concentrated low-Reynolds layer near the bottom and the actual bed level is unknown from the data. This explains the errors being seen in the Figures 4.21 to 4.23. It indicates that the low-Reynolds effects should be included in the model to get right turbulence budget near the bottom and the extra terms in the modified *k-ε* model (v2) will correct the profile in the upper water column. Moreover, the underestimation of suspension concentration in the near bottom region may be caused by

missing the four-way coupling effects (particle-particle collisions) in the 1DV model. This has been pointed out by Hsu (2003), in which he suggested at the bottom region within, perhaps, 10-grain diameters from the bed, the fluid turbulence is small and the dominant mechanism of sediment suspension is particle collisions.

Toorman (in prep.) developed a new two-layer turbulence model which combines a new low-Reynolds two-equation turbulence model (with DNS based damping functions) for the outer layer with the boundary treatment method similar as for high Reynolds k-ε modelling, using a modified mixing-length model for modelling the possible turbulence in the layer on the bed. This will be implemented in the modified k-ε model in future research.

Chapter 5

NEW PROCESS MODELS

5.1. Bottom roughness

Part of the energy from currents and waves is dissipated by friction with the bottom and becomes more and more important with decreasing water depth. In theoretical and numerical models to quantify water and/or sediment movement, this energy loss is described by an empirical or semi-empirical roughness closure (van Rijn, 1993). In practice, it introduces a single roughness parameter (sometimes related to the grain size of the bottom sediment or to bed form dimensions) which is calibrated by comparison of predicted and measured water levels.

Research, supported by laboratory and numerical experiments, has demonstrated that, in the presence of suspended sediments, the traditional approach is not able to predict the correct velocity fields, especially near the bottom (Toorman & Bi, 2013). This has serious implications for flows over shallow areas (*i.e.* near-shore and intertidal areas) and for the estimation of sediment budgets in particular. Therefore, hydrodynamic models for coastal and estuarine areas, in particular when applied to the nearshore and intertidal areas, should be improved by implementation of a more physically based bottom-friction model.

For this purpose, a new modelling strategy developed by Toorman & Bi (2012, 2013) has been implemented in the model for analysing the Western Scheldt estuary. It consists of a new generic friction model which accounts not only for the energy dissipation caused by the flow over the bottom roughness structures, but also for the dissipation induced by the inertia of the suspended particles (Toorman, 2011). The latter is no longer negligible above the bed where high concentrations of suspended matter are encountered. This process explains the drag modulation by suspended matter reported in the literature (Toorman & Bi, 2013, and references therein).

5.1.1. Generalized mixing length theory

The new generic friction model is based on a generalized mixing-length (GML) theory, proposed by Toorman (in prep.) and inspired by the idea of van Driest (1956). By extending the validity of a turbulence model into the low-Reynolds layer, where viscous dissipation (and possibly other dissipation mechanisms, for example, particle collisions) can no longer be neglected, down to the wall with a carefully calibrated damping function f_A, and accounting for the viscous stress in the laminar wall layer, the GML theory allows transient conditions being included in the model. In the case of a rough bottom, the introduction of a subgrid scale viscosity can account for the additional sub-grid scale energy dissipation in the eddies generated between roughness elements. Similarly, turbulence generation in the wake of sediment particles, as already suggested by Elgobashi (1994), can also be taken into account.

The steady state vertical stress balance at a distance z above the bed in open-channel flow of sediment-laden water can be written as:

$$\rho\left(\nu+\nu_{SGS}+\nu_t\right)\frac{\partial U}{\partial z}=\tau_b\left(1-\eta\right) \tag{5.1}$$

where: U = the local flow velocity [m/s], $\tau_b = \rho u_*^2$ = the bed shear stress [kg·m^{-1}·s^{-2}] with u_* the shear velocity [m/s], $\eta = z/h$, with h = the water depth [m], ρ = the density of the sediment-laden water [kg/m^3], ν = the kinematic viscosity of the sediment-laden water [m^2/s] (including concentration effects, such as intergranular friction), ν_t = turbulent eddy viscosity [m^2/s], ν_{SGS} = the subgrid-scale turbulence [m^2/s] generated by vortex shedding in the wake of bed roughness elements and/or of suspended particles. The eddy viscosity in the fully developed outer layer is computed with the well-known parabolic profile, following Prandtl's mixing length theory (Prandtl, 1925) applied to steady open-channel flow (equation 5.1) with neglect of ν and ν_{SGS}). In the inner layer, comprising the intermediate transient layer and the viscous sublayer at the bottom, this eddy viscosity has to be corrected with an empirically determined damping function (f_A).

Rearrangement and non-dimensionalization of equation (5.1) yields:

$$\frac{\partial U_+}{\partial z_+}=\frac{\left(1-\eta\right)}{1+B_+ + f_A\kappa z_+\left(1-\eta\right)} \tag{5.2}$$

in which, $U+ = U/u_*$ = the velocity U non-dimensionalized by the shear velocity u_*, $z+ = zu_*/\nu$ = the distance from the bottom z non-

dimensionalized by the length-scale ν/u_*, $B+ = \nu_{SGS}/\nu$ = a roughness parameter representing the subgrid-scale (SGS) dissipation mechanisms (expressed by the viscosity ν_{SGS}), empirically found to be proportional to the sediment concentration (cf. Figure 5.1), κ = the von Karman coefficient (which may have a lower value than the original constant 0.41 due to sediments in suspension). This new GML model has been calibrated against large eddy simulation (LES) data for open-channel flow over a wavy bottom from Widera *et al.* (2009) and the experimental flume data for sand suspensions from Cellino (1998) (Figure 5.1).

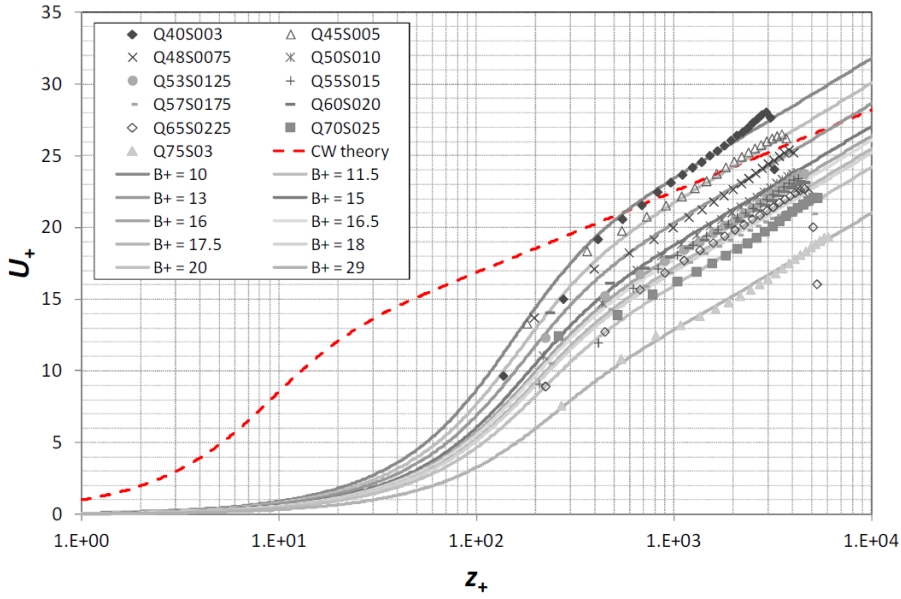

Figure 5.1. Velocity profile for sand-laden turbulent open-channel flow. Flume data for a sand suspension from Cellino (1998) with increasing sediment load, matched with the Generalized Mixing-Length model. Symbols = measurements, full lines = calculations, dashed line = velocity profile for clear water (CW). For this set of experiments κ = 0.27 (Toorman, 2003).

5.1.2. Physics based roughness model

For engineering applications, the above theory has been converted into a 2DH friction model. In principle, this is obtained by computing the depth-

averaged velocity by integration over depth of the theoretical velocity profile and solving the equation for the shear velocity u_*. In order to allow both transient conditions (*i.e.* $5 < h_+ < 100$ – see equation 5.7) and the transition during drying/wetting of tidal flats, it is necessary to combine the laminar and turbulent contributions. However, since equation (5.2) does not allow an analytical solution to be derived, the procedure is first applied separately to the theoretical parabolic profile for laminar flow and the logarithmic profile for fully developed turbulent flow (integrated from the roughness height to the surface). The final bed shear stress is then obtained by superposition of the laminar and the turbulent stress, applying a damping function to the turbulent stress towards the bottom (confirming observations, and simultaneously avoiding numerical problems). Therefore, the bed shear stress can be directly computed as follows (Toorman & Bi, 2012):

$$\begin{aligned}\tau_b / \rho = u_*^{\,2} &= f_A u_{*turb}^{\,2} + u_{*lam}^{\,2} \\ &= f_A \left(\frac{\kappa U}{\ln\left(h / z_0\right) - 1 + z_0 / h} \right)^2 \\ &+ \left(\sqrt{\left(\frac{3}{2}(z_0 + \beta\phi h)\frac{U}{h} \right)^2 + 3\frac{U}{h}\nu(\phi)} + \frac{3}{2}(z_0 + \beta\phi h)\frac{U}{h} \right)^2 \end{aligned} \tag{5.3}$$

where: τ_b = the bed shear stress [kg·m^{-1}·s^{-2}], ρ = the density of water [kg/m^3], u_* = the shear velocity [m/s], u_{*turb} = the shear velocity for fully-developed turbulent open-channel flow [m/s], u_{*lam} = the shear velocity for laminar open-channel flow [m/s], κ = the von Karman coefficient (which decreases from the clear water value 0.41 to lower values depending on the sediment load), U = the local depth-averaged flow velocity [m/s], h = the local water depth [m], β = the suspension friction (or apparent roughness) coefficient which is 0.045 (found using data fitting for Figure 5.1), ν_w = the water viscosity [m^2/s], ϕ = the volumetric suspended particle concentration, and z_0 = the effective roughness length scale [m].

Unlike other models, which assume hydraulic rough conditions, z_0 is computed from the relation in the equation (5.4), which covers the entire range from hydraulic smooth (first term on the right) to hydraulic rough (second term) by the following empirical fit (Toorman, in prep.):

$$z_{0+} = \frac{z_0 u_*}{\nu} = \exp(-\kappa B_0) + f_\beta(k_{s+}) k_{s+} \exp(-\kappa B_\infty) \tag{5.4}$$

where: z_0 and k_s (the equivalent Nikuradse roughness length scale) are non-dimensionalized with ν/u_* to z_{0+} and k_{s+}, B_0 = 5.5 and B_∞ = 8.5, respectively the smooth and rough values of the constant in the non-dimensional logarithmic velocity profiles ($u/u_* = \kappa^{-1} \ln(z/k_s) + B$) (Nikuradse, 1933), and with an empirical damping function:

$$f_\beta\left(k_{s+}\right) = 1 - \exp\left(-k_{s+} \exp\left(-\kappa B_\infty\right)\right) \tag{5.5}$$

which matches the entire Nikuradse (1933) data set. In the present simulation, k_s = 0.03 m, considering small bedforms. Extension to hydraulic smooth conditions is necessary to include the physics of transition to laminar thin film flow on intertidal areas when the water depth goes to zero.

The turbulence damping factor f_A has the following form (similar to the damping function in equation 5.2):

$$f_A = \left(1 - \exp\left(-h_+ / A_+\right)\right)^2 \tag{5.6}$$

with A_+ = 17, an empirical value, and with the water depth non-dimensionalized as:

$$h_+ = \sqrt{3Uh/\nu} \tag{5.7}$$

Finally, the suspension viscosity $\nu(\phi)$ is a function of the suspension concentration and can be expressed empirically as:

$$\nu\left(\phi\right) = \nu\left(1 + \frac{C}{C_{ref}} \frac{h}{h_{ref}}\right) \tag{5.8}$$

The empirical parameters (C_{ref} = 0.222 g/l and h_{ref} = 0.12 m) in equation (5.8) have also been obtained from calibration with the experimental data from Cellino (1998), shown in Figure 5.1.

In summary: the dissipative effect of suspended sediment is incorporated into the closures for the effective roughness (which actually is a length scale related to the turbulent eddies generated by vortex shedding over roughness elements and in the wake of particles) and the suspension viscosity (*e.g.* including steric hindrance and granular friction of dense sand suspension or non-Newtonian behaviour of fluid mud).

Unlike in traditional hydrodynamic models (*e.g.* Hervouet, 2007; Amoudry, 2008), this new bottom-friction model accounts for the water depth and remains valid in turbulent, transient and laminar flows until an intertidal area falls dry. Due to the fact that the classical friction law in traditional models is only valid for fully-developed turbulent flow conditions, an inundation threshold has to be imposed, which keeps the water level at a minimum height, to avoid numerical problems. When two neighbouring nodes with a different bottom level are in that state, a gravity driven flow will be induced from the node at higher elevation to the one at lower elevation. This artificial flow may become too strong and cause erosion, which does not occur in reality. The problem can be reduced by taking a high enough threshold value and/or by temporarily removing grid cells from the computational domain ("masking"). In practice, it turns out that there often remain nodes where the problem persists. The new friction law avoids this problem by increasing the roughness with decreasing water depth and the friction tends to infinity as soon as the inundation threshold, taken equal to the equivalent roughness height z_0, is reached, preventing flow. Masking is no longer necessary and mass conservation is much better guaranteed. Subsequently, the model allows a more accurate (and numerically stable) prediction of hydrodynamics over intertidal flats, since no inundation threshold needs to be specified any longer. Furthermore, for studying morphodynamics of the channel system in the estuary (*e.g.* the Scheldt estuary), a correct representation of residual flow circulations related to ebb and flood channels requires spatial and tidal phase dependent roughness values (Fokkink 1998) , which makes this new bottom-friction model important for the coastal and estuarine studies.

5.2. Erosion & deposition of mixed sediments

The cohesive sediments contain usually a varying amount of sand and the sandy sediments a varying amount of mud. The mud and sand content of a seabed influences the transition between cohesive and non-cohesive sediments (Van den Eynde *et al.*, 2009). This has a major influence on the erosion and deposition behaviour.

For sandy, non-cohesive sediments, it is possible to calculate reasonably well the critical erosion stress and the erosion rate when only grain-size and sorting is known. For cohesive sediments, the erodibility depends mainly upon the degree of cohesion, consolidation, aggregation and compaction, the biological community structure, the sand content of the

sediment and the layering. Mixed sediments may behave as cohesive or non-cohesive sediments, depending on the mud content, *e.g.* the addition of mud increases the sediment shear strength and thus the erosion threshold of a sandy bed (Mitchener & Torfs, 1996).

Furthermore, these mixed sediments do not necessarily occur as well mixed. Frequent alternation of sand and mud layers are observed. These alternations are interpreted as tidal or storm/calm weather influences. Fan *et al.* (2004) describe storm waves as random destructive factors of the sediment bed and highlight them as effective agents of sediment transport and deposition of the sand-dominated layers. This type of segregation can only occur if the cohesive suspended sediment concentration is low.

Recently, some studies have been published that take into account mutual interactions between cohesive and non-cohesive sediments (Van Ledden, 2002; van Ledden *et al.*, 2004; Waeles, 2005; Waeles *et al.*, 2007; Sanford, 2008). It is clear that better predictions of sediment transport are possible if the mutual influence of sand-mud mixtures is incorporated in the model.

5.2.1. Sediment regimes

According to the study of Panagiotopoulos *et al.* (1997), a sand-mud mixture can be categorized as non-cohesive, mixed or cohesive, depending on its sand-mud composition. Each category has its unique characteristics and behaviour. For the application in the general coastal and estuarine systems, the lower bound of the critical mud mass fraction is proposed to be set to 30% (mass fraction relative to total saturated soil, i.e. including pore water mass) and the upper bound is 50%.

The mixture that contains mud less than 30% is in the non-cohesive regime and is considered as sand; those having mud more than 50% is in the cohesive regime and is treated as mud; the rest is in the mixed-sediment regime. The lower and upper bounds of critical mud fractions is suggested by the study of Panagiotopoulos *et al.* (1997) and Mitchener & Torfs (1996), although the values of the limits may differ. As the mud fraction increases, the available space between the sand grains decreases. When the mass fraction of mud is lower than about 30%, the sand grains remain in contact with each other. When the mud fraction exceeds 30%, the mud particles in the spaces between sand particles can form a continuous matrix, and, in this case, pivoting is no longer the main

mechanism responsible for resuspension of sand grains. Consequently, the whole mixture does not behave like a non-cohesive sediment any more. In Mitchener and Torfs' study (1997), the critical shear stress increases significantly, when mud is added to different sand samples with 0% to 30% mud contents (Figure 6.9).

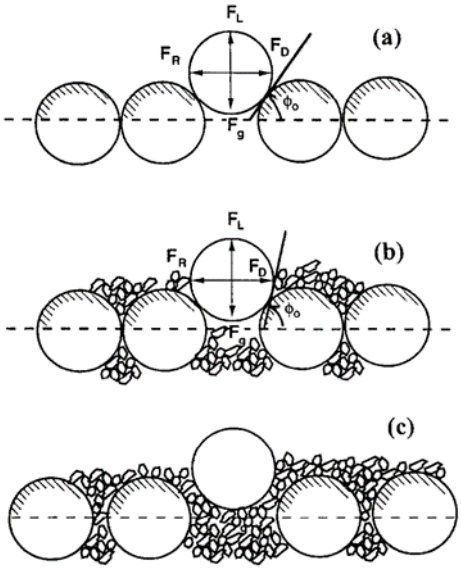

Figure 5.2. Conceptual model showing the mechanism for the initiation of sediment motion for: (a) pure sand particles; (b) sand and mud mixtures with mud content M < 30%; and (c) sand and mud mixtures with mud content M > 30%. (Key: ϕ_0 = angle of internal friction; F_g = weight of the particle; F_L = lift force; F_D = drag force; and F_R = resistance force; *after* Wiberg and Smith, 1987).

There is an optimal ratio of sand content in a mixed bed at which the critical erosion shear stress is a maximum. The optimal sand fraction appears to be between 50% and 70% by weight of sand (Mitchener & Torfs, 1996). Therefore, the lower and upper bounds of critical mud fractions were set at 30% and 50%. These values are also used in the study of Waeles (2005) and Waeles *et al.* (2007).

5.2.2. Erosion of mixed sediment

Coastal beds are usually composed of heterogeneous particles often consisting of sand and mud mixtures. The erosion of mixed sediment is

mainly controlled by the bottom shear stress in coastal and estuarine areas, and often affected by the composition of bed material.

The transport of sand adjusts very quickly to hydrodynamic variations due to the relatively high settling velocities of sand particles. Coarse sand is transported as bed load, whereas for fine sand transport sometimes also occurs in suspension.

Cohesive sediments usually are considered to be transported as suspended load and are calculated by solving an advection-diffusion equation for which erosion and deposition fluxes constitute the boundary conditions at the bed. Erosion of cohesive sediments occurs in different ways, depending on the degree of consolidation (Mehta *et al.*, 1989a, 1989b):

- For freshly deposited mud or fluid mud, the erosion is formulated as an entrainment of mud by the overlying water.
- The erosion of consolidating mud (soft mud) is described by Parchure and Mehta (1985) by an expression to account for a rapid limitation of erosion when the critical shear stress for erosion τ_{ce} increases with depth; τ_{ce} is in the range of 0.1-1 Pa.
- The erosion of consolidated bed is described by the Ariathurai-Partheniades law (Ariathurai, 1974). The critical shear stress for erosion, τ_{ce}, usually is in the range of 1-10 Pa.

It is noteworthy that soft mud has a similar magnitude of critical shear stress for erosion as medium sand, while consolidated mud is as difficult to mobilise as pebbles are.

Following the study of Waeles (2005), the critical shear stress for erosion can be computed as function of the mud fraction (f_m) in each sediment regime:

Non-cohesive regime (f_m < 30%):

$$\tau_{ce} = \tau_{ce,s} + x_1 \cdot f_m \tag{5.9}$$

Mixture regime (30% < f_m <50%):

$$\tau_{ce} = \frac{\tau_{ce,s} + x_1 \cdot f_{m,crit}}{f_{m,crit*} - f_{m,crit}} \left(f_{m,crit*} - f_m \right) + \frac{f_m - f_{m,crit}}{f_{m,crit*} - f_{m,crit}} \tau_{ce,m} \tag{5.10}$$

Cohesive regime (f_m >50%):

$$\tau_{ce} = \tau_{ce,m} \tag{5.11}$$

where: τ_{ce}, $\tau_{ce,s}$ and $\tau_{ce,m}$ = the critical shear stresses [kg·m^{-1}·s^{-2}] for erosion of mixture, sand and mud respectively, x_1 = a calibration constant, $f_{m,crit}$ and $f_{m,crit*}$ = the lower and upper bounds of critical mud fraction, respectively. The detailed discussion on these parameters is presented in section 6.24 in Chapter 6.

Hence, when the bottom shear stress exceeds the critical shear stress for erosion, the bed material starts to be eroded. The erosion rate can be determined depending on the regime of the mixed sediment following the same procedure of Waeles (2005):

$$E_s = \left(1 - f_m\right) \cdot E_{0s} \cdot T^a \tag{5.12}$$

$$E_m = f_m \cdot E_{0s} \cdot T^a \tag{5.13}$$

Mixture regime (30% < f_m <50%):

$$E_s = \left(1 - f_m\right) \cdot \left(E_{0s} + \frac{E_{0m} - E_{0s}}{f_{m,crit*} - f_{m,crit}} \cdot \left(f_m - f_{m,crit} \right) \right) \cdot T^{\left(a + \frac{1-a}{f_{m,crit*} - f_{m,crit}} \cdot \left(f_m - f_{m,crit} \right) \right)} \tag{5.14}$$

$$E_m = f_m \cdot \left(E_{0s} + \frac{E_{0m} - E_{0s}}{f_{m,crit*} - f_{m,crit}} \cdot \left(f_m - f_{m,crit} \right) \right) \cdot T^{\left(a + \frac{1-a}{f_{m,crit*} - f_{m,crit}} \cdot \left(f_m - f_{m,crit} \right) \right)} \tag{5.15}$$

Cohesive regime (f_m >50%):

$$E_s = \left(1 - f_m\right) \cdot E_{0m} \cdot T \tag{5.16}$$

$$E_m = f_m \cdot E_{0m} \cdot T \tag{5.17}$$

in which, E_s and E_m = the erosion rate [kg·m^{-2}·s^{-1}] for sand and mud respectively, E_{0s} and E_{0m} = the erosion constant [kg·m^{-2}·s^{-1}] for non-cohesive regime and cohesive regime respectively, $T = (\tau_b - \tau_{ce})/\tau_{ce}$, τ_b = the bed shear stress [kg·m^{-1}·s^{-2}], τ_{ce} = the critical shear stress [kg·m^{-1}·s^{-2}] for erosion, a = 0.5, a constant suggested in the study of Waeles *et al.* (2007) which is suitable for most cases.

5.2.3. Deposition criterion based on suspension capacity

A new deposition criterion, which has been derived from a suspension capacity condition proposed by Toorman (2000 & 2002), has been introduced in this study, which allows estimating the critical stress for deposition in each node and no longer needs calibration. Since shear flow produces turbulence, the critical "shear stress" for deposition can be related to the total amount of turbulent energy that is required to keep a number of sediment particles in suspension. When the bed shear cannot provide the fluid with enough turbulent energy that is needed to maintain all the suspended particles in the water column, deposition begins. The excessive sediment settles down to the bottom until the energy balance is restored.

The critical shear stress for deposition, obtained by inversion of Toorman's suspension capacity criterion, has been split into two parts in order to deal with sand-mud mixtures. In this case, the total required turbulent energy is also divided over both sediment fractions: part of it is used to keep non-cohesive particles in suspension and the rest is used to keep cohesive particles in suspension. The corresponding "critical stresses" are given in the following equations:

$$\tau_{cd,s} = \frac{\left(1-\rho_w/\rho_s\right) gh}{Rf_s} \frac{w_s C_s}{U} \tag{5.18}$$

$$\tau_{cd,m} = \frac{\left(1-\rho_w/\rho_m\right) gh}{Rf_m} \frac{w_m C_m}{U} \tag{5.19}$$

$$Rf_s = 0.25\left(\frac{u_*}{w_s}\right)^2 \cdot \frac{0.01}{1+0.01\left(\frac{u_*}{w_s}\right)^2} \tag{5.20}$$

$$Rf_m = 0.25\left(\frac{u_*}{w_m}\right)^2 \cdot \frac{0.01}{1+0.01\left(\frac{u_*}{w_m}\right)^2} \tag{5.21}$$

where: $\tau_{cd,s}$ and $\tau_{cd,m}$ = the critical shear stress [kg·m^{-1}·s^{-2}] for sand and mud deposition respectively, ρ_w is the fluid density [kg/m^3], ρ_s = the sand density [kg/m^3], ρ_m = the mud density [kg/m^3], Rf_s and Rf_m = the flux Richardson number for sand and mud at suspension capacity which

expresses the ratio of suspension potential to turbulent kinetic energy (its value is usually < 0.1, based on the analysis of various experimental data sets from field and laboratory measurements; Toorman, 2003), u_* = the shear velocity [m/s], g = the gravity acceleration [m/s^2], w_s and w_m = the settling velocities [m/s] of sand and mud respectively, w_a = the averaged settling velocity [m/s] of mixture, C_s and C_m = the depth-averaged suspension mass concentration [kg/m^3] of sand and mud respectively, U = the magnitude of velocity [m/s].

Krone's deposition law (1962) subsequently is adapted to be used for calculating the deposition flux of each fraction, without violating the energy balance:

$$p_s = \max\left[1 - \frac{C_s}{C_s + C_m}\frac{\tau}{\tau_{cd,s}}, 0\right] \tag{5.22}$$

$$p_m = \max\left[1 - \frac{C_m}{C_s + C_m}\frac{\tau}{\tau_{cd,m}}, 0\right] \tag{5.23}$$

$$D_s = \left(w_s C_s\right) \cdot p_s \tag{5.24}$$

$$D_m = \left(w_m C_m\right) \cdot p_m \tag{5.25}$$

where: p_s and p_m are deposition probabilities of sand and mud respectively, D_s is the deposition flux [kg·m^{-2}·s^{-1}] of sand and D_m is the deposition flux of mud [kg·m^{-2}·s^{-1}].

Chapter 6

APPLICATION TO SCHELDT & BELGIAN COAST

6.1. Overview of the study area

The Scheldt emerges in northern France, on a plateau at Saint-Quentin. In its first kilometres it is just a stream that reaches the Belgian border through French villages and grows to a narrow river there. Fed by tributaries, the Scheldt evolves into a broader river along its way to the North Sea. It is about 350 kilometres long from the source to the mouth, where it becomes a mighty stream flowing into the North Sea. The water level difference between source and mouth is only 100 m, making it a typical lowland river system with low current velocities and thus meanders (Vlaams-Nederlandse Scheldecommissie, 2015).

The Scheldt basin comprises an area of approximately 21,863 km^2 and is situated in the northeast of France, the west of Belgium and the southwest of the Netherlands, where it is inhabited by about 10 million people (477 inhabitants per km^2). Over the years, the Scheldt basin has been divided into three sections. The Upper Scheldt is the part from the source to Ghent, where the Scheldt joins the Lys (Leie). The river has already a length of 185 kilometres. In Ghent, the Scheldt begins to undergo the tidal influences. The part of Ghent which runs through Antwerp to the Dutch border, called the Sea Scheldt (Zeeschelde). Beyond the Belgian-Dutch border begins the broad estuary of the Western Scheldt (Westerschelde). In this part, the Scheldt flows into the North Sea via Terneuzen, Breskens and Vlissingen. Zeeschelde and Westerschelde together form the Scheldt estuary, which is under the influence of the tide.

The Scheldt estuary is defined as the part of the river basin with a tidal influence. It is open to the southern North Sea and extends 160 km in length from the mouth at Vlissingen to Ghent, where sluices stop the tidal wave in the Upper Scheldt. The tidal wave also penetrates most of the upstream areas, entering the major tributaries Rupel and Durme, resulting in approximately 235 km of tidal river in the estuary. In the Scheldt estuary at Vlissingen, the difference between high and low water about four meters. Further inland, the tidal range increases. The farther upstream, the narrower the riverbed and the more the incoming floodwater is pushed up. Near Hamme, where the Durme flows into the

Scheldt, the river reaches its highest water level. Then the impoundment of the water decreases again. The locks around Ghent blocks the tide completely and ensure that the river further upstream is no longer influenced by the sea (Vlaams-Nederlandse Scheldecommissie, 2015).

The Scheldt estuary is one of the youngest and most natural estuaries in Western Europe. It is categorized as the main transition zone or ecotone between the riverine and marine habitats. It consists of an approximately 60 km long fresh water tidal zone stretching from near the mouth of Rupelmonde to Ghent, representing one of the largest freshwater tidal areas in Western Europe. It also has a mixing zone between Rupelmonde and Vlissingen/Breskens. The subtidal delta, seaward of Vlissingen and Breskens, forms the transition between the Western Scheldt and the North Sea. (Fettweis *et al.*, 1998; Kuijper *et al.*, 2004; Meire *et al.*, 2005; van Kessel *et al.*, 2011).

The Scheldt estuary can also be divided into two major parts, the Zeeschelde (105 km), which is the Belgian part from Ghent to the Dutch/Belgian boarder, and the Westerschelde (58 km), known as the Dutch part, covering the middle and lower estuary. The Zeeschelde is mainly a single ebb/flood channel and has a total surface of 44 km^2. Mudflats and marshes in this area are relatively small and approximately account for 28% of total surface. The Zeeschelde hosts one of the largest harbours in Europe – the Port of Antwerp. Therefore, human activities are very active in this region and industrial developments are concentrated along the riverbanks. The intertidal zone is often missing or very narrow. The estuary is almost completely canalized upstream of Dendermonde (Hoffmann & Meire, 1997). The Westerschelde is a well-mixed region. Due to the influences of tidal waves and land changes, the Westerschelde has a complex and dynamic morphology. The flood and ebb channels are interconnected, bordered by several large intertidal flats and salt marshes. The surface of the Westerschelde amounts to 310 km^2, in which 35% of the area is covered by intertidal flats. The average channel depth is approximately 15–20 m (Meire *et al.*, 2005).

In a meso-tidal estuary, where the tidal range is about 2–4 m, tidal action and wave activity both tend to be important in such areas (Allaby, 1999), like the Western Scheldt, where both in- and outflow discharges are large, the net sediment budget is the sum of a large positive and a large negative number.

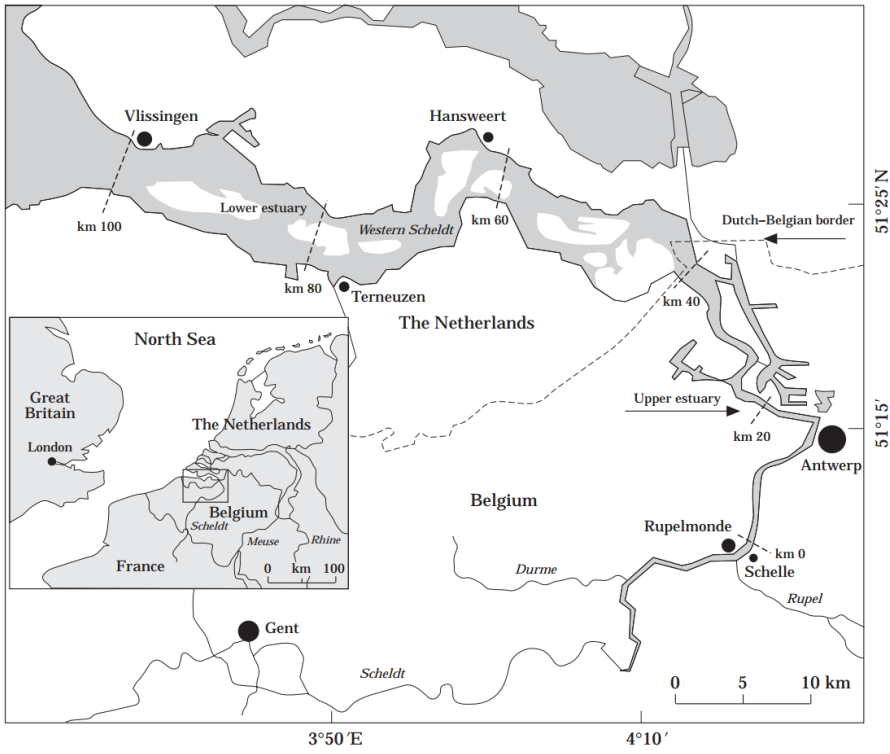

Figure 6.1. The Scheldt Estuary. The mixing zone consists of the upper estuary and the lower estuary or Western Scheldt. Upstream of Rupelmonde the water is entirely fresh while the water movement is still dominated by the tide. The area between Rupelmonde and Gent is therefore called the freshwater estuary (from Verlaan *et al.*, 1997).

A good knowledge of the sediment budget and transport path is not only essential for longer term planning of maintenance dredging activities, it is also of crucial importance for the impact assessment on and the long term prediction of the ecosystem services. However, sediment fluxes are very difficult to measure. It requires simultaneous flow and sediment concentration measurements across different cross-sections of the river, in both horizontal and vertical directions. Sediment concentration and flow measurements close to the bottom, where the largest sediment concentrations occur, are particularly difficult and therefore very rare or non-existent. The estimates of the net sediment balance are therefore largely uncertain. Numerical models can help to look at the sediment processes, such as areas of erosion and deposition, but are in need of

quantitative measurements for calibration and verification. The bottom friction parameter in these models often, if not always, is the main parameter to calibrate or 'tune' the hydrodynamic model, but this also has consequences on the behaviour of the sediment transport model. An additional complication is the fact that sediments are not homogeneous, neither in space nor in time. Transport models that incorporate the possibility to deal with more than one sediment type or class are necessary and available, but the composition of the actual bed is not, or, at most only partially known. Another important aspect is that the geometry of an estuary is usually complex due to its geomorphological features or water circulation patterns. It may also include tidal flats, harbours or navigation channels, which are much smaller, compared to the rest of the domain, thus it requires a more flexible numerical approach to be capable of dealing with all the geometrical complexities.

It is worth mentioning that biogeochemical processes in the Scheldt estuary is also an important topic. Four additional aspects make the Scheldt estuary very particular and different from other estuaries: (1) the Scheldt is a tide-governed estuary, which means greater residence times; (2) the upper estuary received large inputs of biodegradable organic matter which leads to oxygen depletion in winter and anoxic conditions in summer; (3) inputs of toxic pollutants from the industrial zone of Antwerp occur in the upper estuary; (4) the anoxic zone, the zone of pollutant input and the zone of the turbidity maximum coincide geographically (Baeyens, 1998). It is found that pollution by toxic metals is one of the major threats to the estuarine ecosystem. Concentrations of dissolved Pb, Hg, Zn, Cu and Cd in the coastal estuarine water mass are about 2 times higher than in the marine water mass of the Belgian coastal zone (Baeyens *et al.*, 1987). In the estuary itself, the heavy metal concentrations are still significantly higher than in the coastal estuarine water mass (Baeyens *et al.*, 1998). Therefore, a better understanding of the respective biogeochemical cycles of heavy metals in the Scheldt estuary with emphasis on the basic governing processes is essential.

Many numerical studies have been conducted for understanding hydrodynamics, morphological and biogeochemical processes in Scheldt estuary. One of the earliest numerical models for the Scheldt estuary was devised by Baeyens *et al.* (1981) in order to simulate the physical behaviour, including instantaneous water levels and mean velocities over depth, salinity and turbidity in the water column and the sedimentary budget at the bottom. It was a two-dimensional (2D) depth-averaged model with a structured grid based on a multi-operational finite

difference scheme. Later, more efforts were put into the numerical modelling by other researchers and many 2D applications in the Scheldt estuary for simulating sediment transport can be found in studies of Portela & Neves (1994), Verbeek & Jansen (1998), Dam *et al.* (2007), Vanderborght *et al.* (2007), Bolle *et al.* (2010), de Brye *et al.* (2010), Mulder *et al.* (2011), Gourgue *et al.* (2013). Most of them only focus on cohesive sediment or mud transport under different hydrodynamic and salinity conditions. However, one of the trends is that the finite element method has been used more and more in the numerical modelling since it is capable of dealing with complex geometry of the estuaries like the Scheldt with a more flexible unstructured mesh. The first 3D numerical sediment transport model of the Scheldt estuary seems introduced by Cancino & Neves (1994, 1999a, 1999b). It was a fully 3D finite difference baroclinic model system for hydrodynamics and fine suspended sediment transport with the effects of flocculation, deposition and erosion taken into account. Their approach provided a useful basis for a good understanding of the physical processes involved in sediment transport. Another 3D mud transport model was established by Van Kessel *et al.* (2011). Their model showed realistic values for water levels, salinities and residual currents in the major part of the model domain. However, the propagation of the tidal wave was modelled less accurately upstream of Antwerp. One of the advantages of a 3D model is that it can reproduce many complex hydrodynamic processes in the estuary under tidal waves. Therefore, it is also a useful tool for studying the effects of secondary currents in the estuary (Verbeek *et al.*, 1999). Also due to its complexities, the computational cost for a 3D large-scale model is much higher than a 2D model.

The purpose of this study was to test and demonstrate a new modelling methodology that was developed to deal with the complexities of large-scale domains like the Scheldt estuary by taking sub-grid scale physical processes or effects into account, while still trying to maintain the computational efficiency. By including new empirical parameters into physics based laws or criteria, the model can adapt to different situations or scenarios by its own and achieve higher prediction accuracy. Another objective of this study was to make a more realistic model that not only focuses on the cohesive particles, but also has non-cohesive sediment in the system. The reason for considering more than one sediment class in the system is that in real world, the bed material consists of both cohesive and non-cohesive sediments and its composition differs from one location to another. For example, according to the measurement carried out in Western Scheldt, one can find the mud fraction in the upstream is

generally larger than the values found in the downstream. For each type of sediment, the transport mechanism is different and both transport progresses consume energy. From this perspective, the availability of energy to transport sediments in the system is likely to be overestimated when only considering one type of sediment, or, stated differently, the same energy is used twice. The corresponding error is compensated by tuning the model.

6.2. Model set-up

6.2.1. General

The Scheldt model consists of a coupled two-dimensional depth-averaged hydrodynamic and sediment transport model developed using the OpenTELEMAC-MASCARET modelling system with customizations in the source code. The year 2009 has been selected as the simulation period. According to the study of De Ruijter *et al.* (1987), the water column in the Belgian coastal zone is well mixed throughout the entire year. Therefore, a 2D depth-averaged model is appropriate.

6.2.2. Mesh and bathymetry

The model implementation focuses on the Scheldt estuary, which has been extended with a limited part of the Belgian coastal area, including necessary mesh refinements to model in detail the tide-affected docks of the Ports of Antwerp and Zeebrugge.

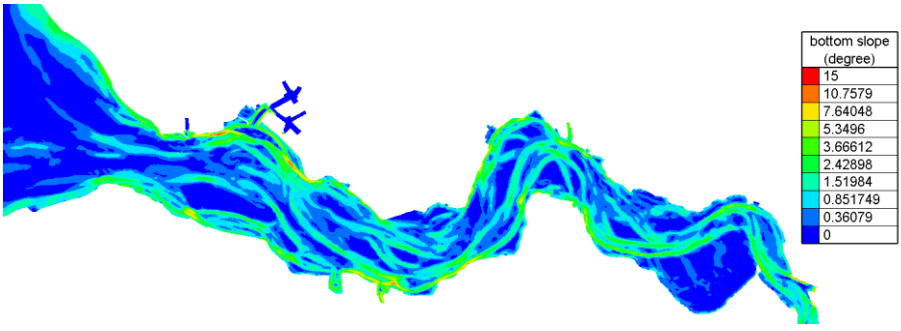

Figure 6.2. Bottom slope of the middle section of the Scheldt estuary

The bathymetry data is taken from the NEVLA model (Hartsuiker, 2004, van Kessel *et al.*, 2011, Maximova *et al.*, 2009b). It covers the whole Western Scheldt, starting from the upstream river and its tributaries in Belgium, extending all the way to the Belgian coast and the southwest coast of the Netherlands, including part of the North Sea. In 2009, a new survey was conducted and subsequently the bathymetric data of the Western Scheldt was updated (Maximova *et al.*, 2009a). The mesh used in the simulations is unstructured and non-uniform. It has 67689 elements and 37527 nodes. In order to reduce the computational cost but maintain the accuracy as much as possible, a space varying resolution is adopted in the mesh.

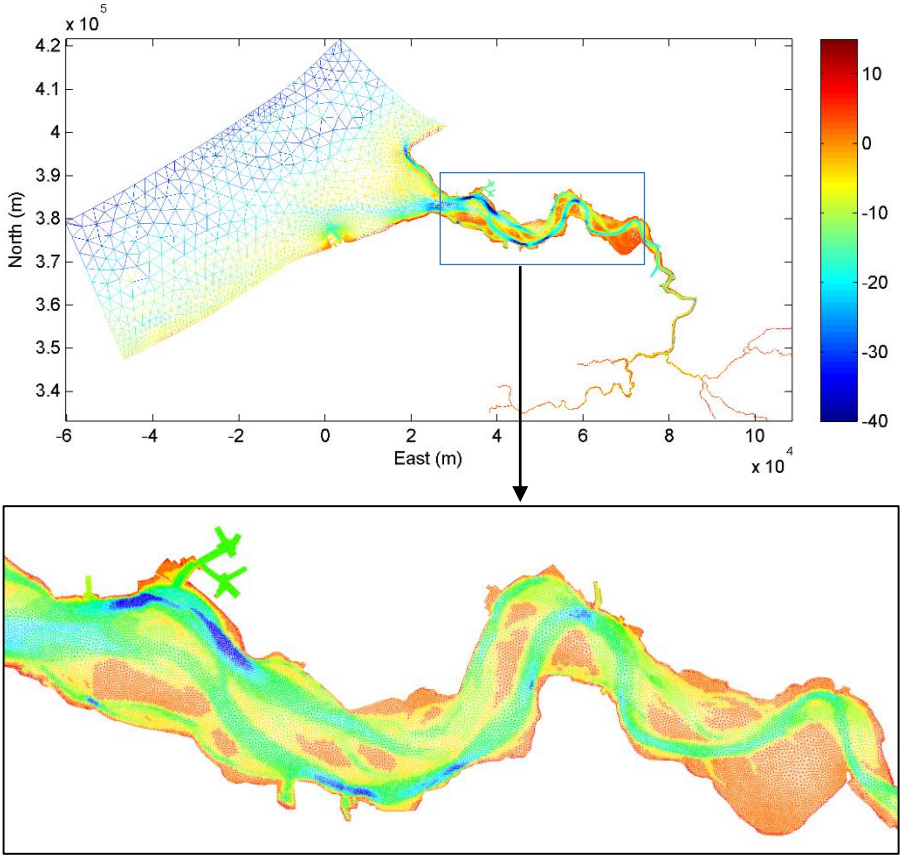

Figure 6.3. Bathymetry (m) and mesh of the Scheldt Estuary (top) with a close-up view (bottom).

For the North Sea, the grid size is from 1,000 to 2,000 meters because the bottom elevation does not change rapidly in this part of the domain and it is not necessary to have every detail in the North Sea. Approaching the coast, the mesh resolution becomes finer and finer. After entering the river mouth, the grid size is optimized in order to be better aligned along iso-depth lines. Figure 6.2 shows the bottom slope of the Scheldt estuary. In the areas with mild slope, the grid size is about 100-200 meters. In the steep areas, the grid size decreases to 50-100 meters. This is due to the complex topography in those relatively shallow areas. There are many tidal flats in this region and the slopes often reach very high values, especially at those nodes close to the tidal flats and banks. Therefore, in such cases a higher resolution could make the computation more stable. It is also necessary to provide sufficient detail when investigating the flow field and sedimentology in the estuary.

6.2.3. Hydrodynamic model

The development of the hydrodynamic model is based on TELEMAC-2D (http://www.opentelemac.org/), which is a finite element solver for use in the field of 2D free-surface flows. It has been used in many studies and research cases (Hervouet *et al.* 2000). The Navier-Stokes equations for incompressible flow are averaged vertically by integration from the bottom to the surface and solved simultaneously in TELEMAC-2D code using the finite-element method, as well as the equation for tracer conservation (equations 2.1 – 2.4) (Hervouet, 2007).

6.2.3.1. Boundary conditions

There are eight open (*i.e.* liquid) boundaries in the model, one downstream (the "sea boundary") and seven upstream (one for each tributary). The rest are closed boundaries. All of the water boundaries have prescribed boundary conditions. The upstream boundaries are modelled as freshwater inflows. The annual-averaged river discharge of the Scheldt River near Schelle, at the confluence of the Rupel and the Scheldt, amounts to 110 m^3/s with approximately equal contributions from both tributaries (Kuijper *et al.*, 2004). Therefore, in this study, a constant discharge is given to the upstream boundaries. The total amount of discharge is divided into two parts. The contribution from the three tributaries in the southwest is split evenly and accounts for half the amount of discharge to the mainstream. Similarly, the rest of the

tributaries in the southeast contribute another half. Numerical tests confirm that the upstream inflow has little influence on the simulated results in most of the domain since the upstream discharge is negligible compared with the inflow from the downstream boundary (the percentage of water flux passing through the upstream boundaries only ranges from 0.01% to 0.03% compared to the amount from the sea boundary). The freshwater inflow normally has a salinity level of 0.5 ppt (Flanders Hydraulics Research, personal communication) and this has been assigned as the value for the salinity tracer as the upstream boundary condition. The downstream boundary is the same as in the NEVLA model, which includes part of the North Sea. The tidal elevation and salinity data are imposed at the downstream boundary. The nodes along the boundary have been adjusted to the same positions as those in the NEVLA model so that tidal elevation along the boundary nodes can be taken identical to the ones that drive the NEVLA model. The original data of tidal elevation along the boundary has a time interval of 10 minutes. Therefore, a numerical interpolation is performed in order to match the model time step (5 seconds). To obtain smooth transitions in the data, a spline interpolation is used. This also enhances the model stability. At the downstream boundary, the salinity data from the NEVLA model are prescribed. The same spline interpolation is used to process the salinity data.

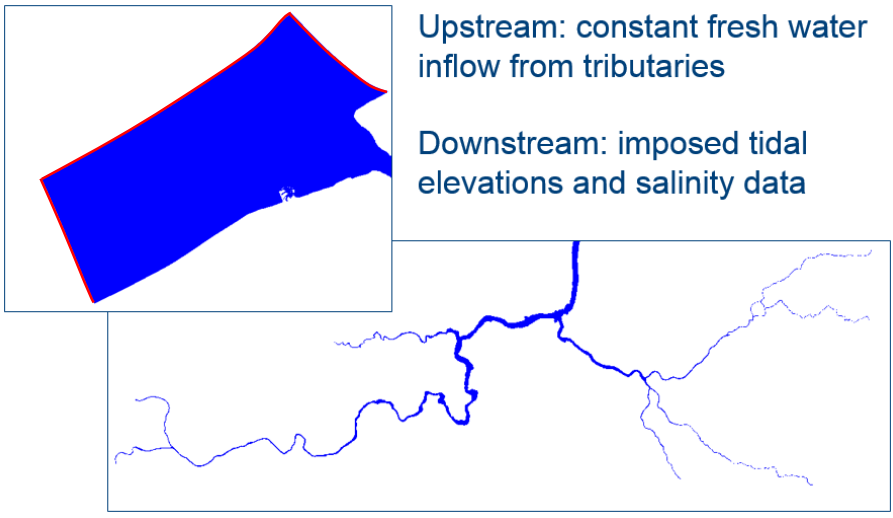

Figure 6.4. Boundary condition locations of the hydrodynamic model.

6.2.3.2. Turbulence modelling

For modelling the turbulent stress, a sub-grid turbulence model developed by Smagorinsky (1963) is adopted in this study. In principle, if the size of finite elements were small enough to allow the reproduction of all mechanisms including the viscous dissipation of very small vortices, turbulence would naturally appear in the solution of the Navier-Stokes equations. This requires the mesh size no larger than the Kolmogorov microscales. The Smagorinsky model adds a turbulent viscosity deduced from a mixing-length model to the molecular viscosity, which compensates for the subgrid-scale turbulent vortices which modelling is inhibited by the size of elements (Hervouet 2007). This method assumes that the energy production and dissipation of the small scales are in equilibrium. The Smagorinsky model can be summarized as:

$$\tau_{ij} - \frac{1}{3}\tau_{kk}\delta_{ij} = -2\rho C_s^2 \Delta^2 \left|\overline{S}\right| S_{ij} \tag{6.1}$$

$$\overline{S} = \sqrt{2S_{ij}S_{ij}} \tag{6.2}$$

The turbulent viscosity is modelled by

$$\nu_t = C_s^2 \Delta^2 \sqrt{2S_{ij}S_{ij}} \tag{6.3}$$

$$S_{ij} = \frac{1}{2}\left(\frac{\partial u_i}{\partial x_j} + \frac{\partial u_j}{\partial x_i}\right) \tag{6.4}$$

where τ_{ij} = the Reynolds stress tensor [kg·m^{-1}·s^{-2}], δ_{ij} = the Kronecker delta, ρ = the water density [kg/m^3], C_s = the dimensionless coefficient which ranges from 0.1 (channel flow) to 0.2 (isotropic turbulence), Δ = the mesh size [m] derived in 2D from the surface of the elements, and S_{ij} = the strain rate tensor of average motion [s^{-1}], the subscripts *i* and *j* are the indices of the Cartesian coordinates.

6.2.3.3. Drying and wetting of tidal flats

Dealing with tidal flats has always been a problematic part of hydrodynamics models. As seen in the bathymetric data, tidal flats are quite extensive all along the Scheldt Estuary, but especially in the lower estuary. Large amounts of saline, brackish or fresh water flow across these tidal flats within each tidal cycle. Therefore, the tidal flats are constantly in transition between wet and dry conditions. Moreover, the

slopes are usually quite steep around the tidal flats and may cause serious numerical problems if an inappropriate drying/flooding scheme is chosen.

Bates and Hervouet (1999) utilized the finite element model TELEMAC-2D and began the wetting/drying process by characterizing all elements as one of four types: fully wet, fully dry, partly wet (dam-break type), and partly wet (flooding type). This categorization allowed them to apply an appropriate mass and momentum correction scheme. Once the element subtype was established, all partially wet elements were included in the computations and steps were taken to correct the mass and momentum discrepancies. In the case of momentum, the authors applied the scheme of Hervouet and Janin (1994), which assumed that the change in velocity with respect to time is equal to the water surface slope times the acceleration because of gravity. In some cases, this resulted in spurious results when the water surface slope was nearly flat, such as in the case of an element flooding from the bottom up. In terms of mass conservation, Bates and Hervouet (1999) applied the scheme of Defina *et al*. (1994). This scheme utilizes the bottom topography and water surface elevation to calculate a scaling factor that is applied to the continuity equation. This scaling factor allows for a true representation of the volume of water present on the element (Medeiros and Hagen 2013).

The above wetting/drying scheme is provided as an option of treatment for tidal flats in TELEMAC-2D. In the present model, this option is adopted, so in this case, all the finite elements are kept within the computational domain. Mass-conservation is guaranteed with this option. Moreover, the new friction law, presented in Section 5.1, also takes into account the wetting and drying on the tidal flats. Contrary to traditional models, the new friction law ensures that the flow resistance becomes infinite when the water depth goes to zero. As demonstrated below, the present model does not require a threshold for the drying/flooding algorithm. This makes the model more robust.

6.2.3.4. Physics based roughness

The Chézy coefficient is used to describe the bottom roughness in the model.

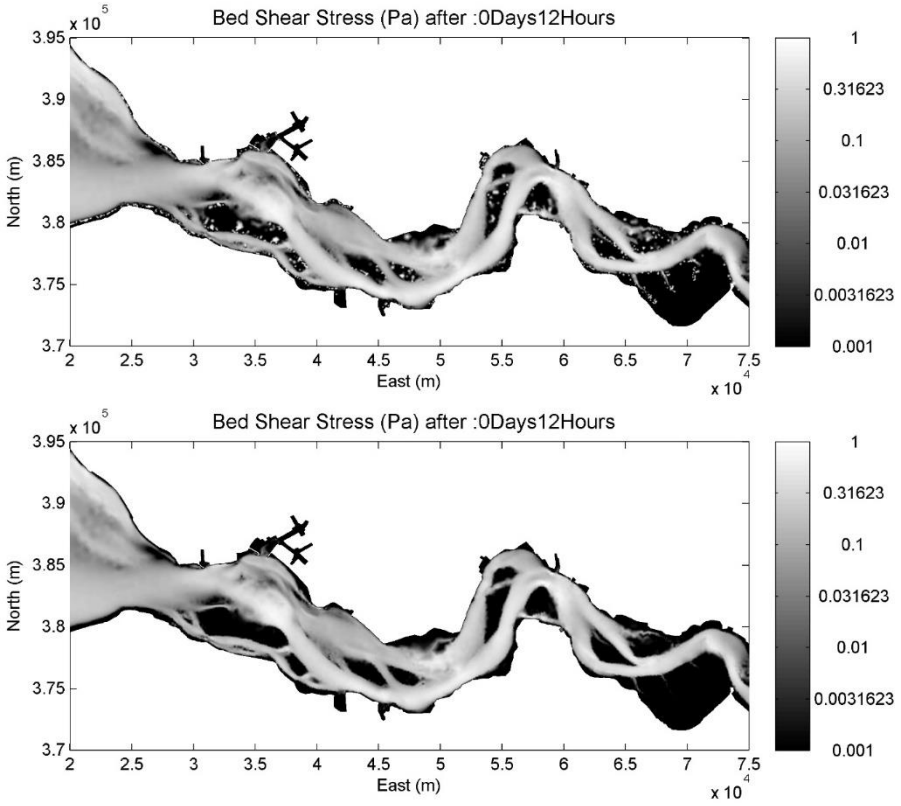

Figure 6.5. Comparison of bed shear stress in the central part of the Western Scheldt estuary for a traditional constant roughness parameter model (top) and the new friction law (bottom), in the case of a very small inundation threshold (1 mm). Without the improved roughness model, excessive erosion is predicted in the intertidal areas, because of the incorrect prediction of the bed shear stress.

The different model behaviour for computation of bed shear stress is clearly demonstrated in Figure 6.5. Figure 6.6 shows the spatial variations in Chézy coefficients obtained from the new bottom friction law described in Section 5.1. The Chézy coefficients at all the nodes are updated at each time step based on the changes of flow field and other influence factors, e.g. suspended sediment concentration.

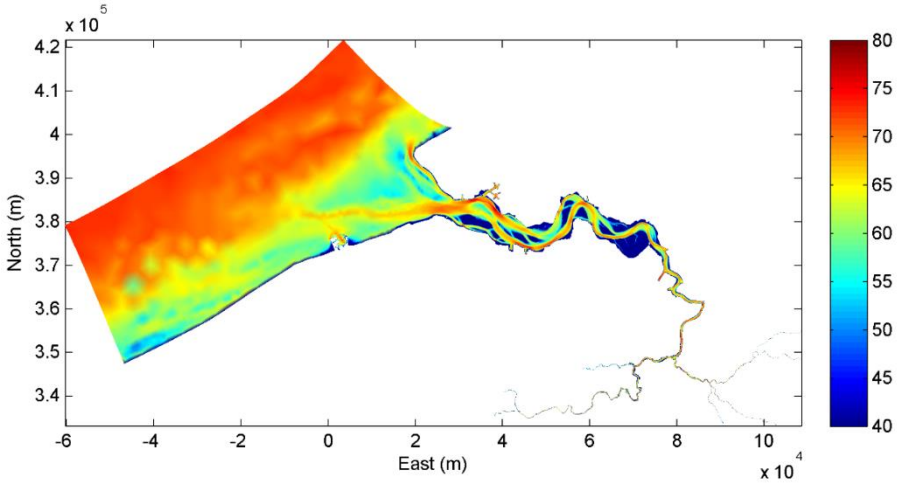

Figure 6.6. Chézy coefficients (at a certain time step) obtained from the new bottom friction law with concentration effects.

6.2.3.5. Salinity

Because of the availability of salinity measurements in the Sea Scheldt, the year 2005 is selected to define the initial conditions of salinity for both winter and summer conditions. Initial conditions of salinity are based on measurements of 16th of February (winter conditions) and on 27th of April (summer conditions). Salinity measurements are available for stations Vlakte van de Raan, Hoofdplaat, Baalhoek, Lillo, Boerenschans, Oosterweel and Hoboken. For the last three measurement points, the dataset of the Oosterweel tunnel project is used (TV SAM) (Van Kessel et. al., 2006).

As mentioned in Section 6.2.3.1, the same salinity data from NEVLA in year 2009 is prescribed at the downstream (sea) boundary.

In order to transform the scattered salinity data into the initial conditions for the hydrodynamic model, the following procedures were applied: the whole domain was divided into eight regions and each one has been assigned a constant salinity level based on the averaged values in Table 6.1; then the hydrodynamic model was started with this initial salinity data. The different regions with different salinity levels began to mix. After three-month simulation period, the salinity was reasonably distributed over the entire domain and the salinity map generated at this

stage by the hydrodynamic model is used as the final initial salinity conditions (Figure 6.7).

Table 6.1. Salinity data in the Scheldt estuary in 2005.

Location	Salinity – winter (ppt)	Salinity – summer (ppt)	Salinity – average (ppt)
Vlakte vd Raan	35	32	33.5
Hoofdplaat	27	27	27
Baalhoek	12	15	13.5
Lillo	1.1	7	4.05
Boerenschans	1	/	2
Oosterweel	0.7	2	1.35
Hoboken	0.3	0.5	0.4

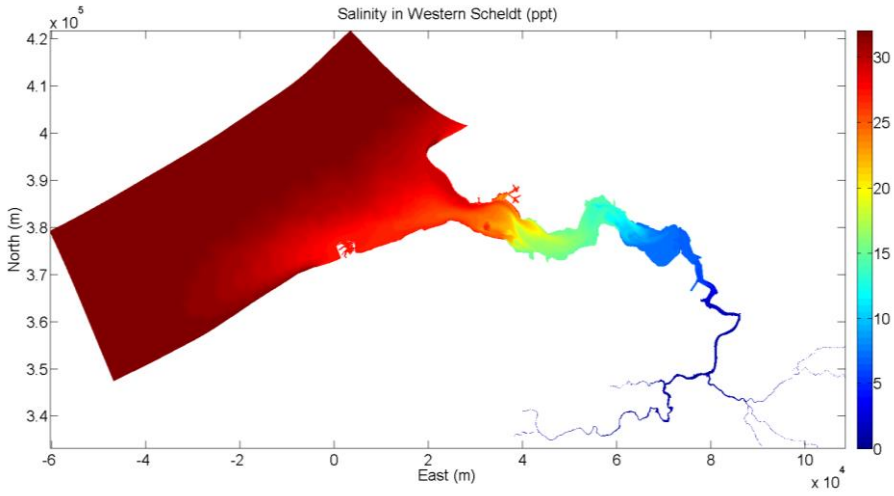

Figure 6.7. Initial salinity distribution map in the Scheldt Estuary.

6.2.4. Sediment model

The sediment transport is modelled using SISYPHE, which is a sediment transport module inside OpenTELEMAC-MASCARET system. SISYPHE can be dynamically coupled with the TELEMAC-2D hydrodynamic model. At each time step, TELEMAC-2D exports the flow conditions to SISYPHE, allowing it to compute the variables related to sediment transport, such as bedload and suspended concentration by mass (g/L). The bed evolution, *i.e.* the changes in bottom elevation, is sent back to TELEMAC-2D. The dynamic two-way coupling keeps the information in the separate modules up to date. When coupled, SISYPHE also shares the same boundary conditions with TELEMAC-2D. In order to fit the purpose of this study, the original code of SISYPHE has been customized.

The main customized subroutines in SISYPHE are as follows:

- *BORD* has been modified for prescribing the time- and space-dependent boundary conditions;
- *CONDIN* has been modified in order to initialise the salinity for the entire domain;
- *CORSTR* contains the new bottom friction law described in Section 5.1.2;
- *INIT_COMPO_COH* has been modified for initialising the bed material composition using the sand fraction data;
- *SUSPENSION_FLUX_MIXTE* has been modified for calculating the erosion flux of mixed-sediment using the equations described in Section 6.2.4.5;
- *SUSPENSION_DEPOT* has been modified for calculating the deposition flux of mixed-sediment using the equations described in Section 6.2.4.5 as well.

6.2.4.1. Boundary conditions

For the boundary conditions, there is no data set suitable for specifying the sediment concentration at both upstream and downstream boundaries in the simulation period. For the non-cohesive sediment, the depth-averaged equilibrium concentration is calculated assuming equilibrium concentration at a reference height above the bed using the formula from Zyserman and Fredsøe (1994) and a Rouse profile correction is then applied. For the cohesive sediment, sediment concentration at boundary nodes is calculated based on the erosion flux at those nodes. No solid discharge is prescribed at open boundaries, but

the sediments are allowed to move freely throughout the computational domain and through all its open boundaries. Compared to the large domain of the estuary, the background concentrations from incoming sediment loads at both upstream and downstream boundaries have limited influence to the coastal area and the main navigation channels in Scheldt. This confirms what has been known for years that most sediments recirculate within the Belgian coastal area (Malherbe, 1991).

6.2.4.2. The composition of bed material

The bed composition in the Western Scheldt is dominated by sand while in certain locations along the Belgian coast as well as far away in the upstream near the Port of Antwerp, high percentages of mud can be observed. Figure 6.8 shows the sand distribution map in the domain, which is used as initial bed composition in the model. Due to the lack of data in the upstream river tributaries (upstream of Schelle), a default sand fraction is assigned to the bottom. The applied value was determined to be 90%, which allows smooth transition from upstream to downstream.

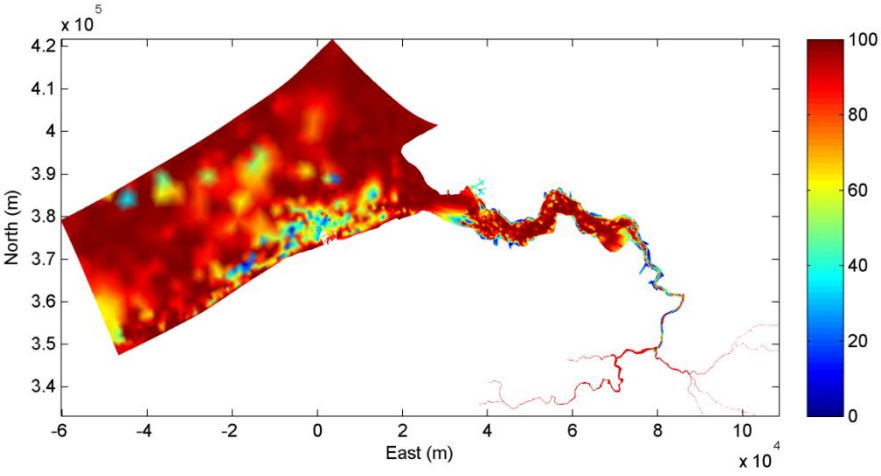

Figure 6.8. Sand fraction by volume (%) distribution map in the Scheldt Estuary (combined data from Rijkswaterstaat, the Netherlands, and RBINS-MUMM, Belgium).

6.2.4.3. Two-layer bed model

The sediment bottom shows varying properties with depth as a result of alternating erosion and deposition events and of self-weight compaction (consolidation). In the top layer, sediment particles are usually freshly deposited to the bed. They are loosely packed and a relatively low shear velocity can bring them back into the water column. The older layers underneath have had time to consolidate. The sediment volume has compacted, the density increased, and the physical properties have changed since deposition due to the effective stress from the gravitational compaction. Therefore, the sediment particles in the lower layer(s) can be much more resistant to the flow and require more energy to be eroded. These insights are translated into a rather simple two-layer bed model: a first layer, which is easily erodible with a thickness of 0.5m and a second layer, which is much more difficult to erode and with a thickness of 1.5m. Although this model is a rather simplistic approximation of the real situation, it contains some essential characteristics such as the limited availability of erodible sediment for resuspension from the bottom.

6.2.4.4. Two types of sediments

The current study considers two types of bed material, non-cohesive (sand) and cohesive (mud) sediment. The properties of bed material used in the model are given in Table 6.2.

In the Scheldt estuary, the effective settling velocity can be affected by many factors, *e.g.* initial suspension concentration, flow unsteadiness, waves and tidal phase effects, which may cause a delayed settling of sediment particles (da Silva *et al.*, 2006). For the cohesive sediment, the commonly used settling velocity in the Scheldt estuary is about 0.001 m/s, which is generally larger than the settling velocity based on the individual particle size, thus, it implicitly accounts for the aggregation of cohesive particles into flocs (Fettweis *et al.*, 2003; van Kessel *et al.*, 2011; Dam and Bliek, 2013). The settling velocity of sand in the Scheldt estuary is set to 0.01 m/s, following the study of Hoogduin *et al.* (2009). Dam *et al.* (2007) used a slightly higher value 0.015 cm/s as the fall velocity of sand in their morphological model of the Western Scheldt Estuary. However, one should realize that the latter value also compensates for the fact that resuspension by waves, which is known to play an important role in the coastal zone, is not accounted for in the present model.

Fettweis and Van den Eynde (2003) suggest that the bulk density of mud found near Zeebrugge is about 1500-1600 kg/m^3 and the critical shear stress for erosion varies between 0.5 Pa (freshly deposited mud) and 0.8 Pa (after 48 h). Due to the existence of two types of sediment particles, the critical shear stress for erosion of a mixture is the combination of the values of sand and mud. The commonly used values for pure sand (0.2 – 0.35 Pa) cannot represent the mixture properties and lead to excessive erosion of the fine fraction in the current mixed-sediment model. Therefore, the numerical tests suggest a higher value (0.6 Pa) for the critical shear stress for erosion. The most significant effect on erosion resistance occurs on the addition of small percentages by weight of mud to sand. This is confirmed by the study of Mitchener and Torfs (1996) (Figure 6.9), in which the critical shear stress for erosion can be easily above 0.5 Pa with just a small fraction (4% - 5%) of cohesive mud added in. In this sense, the commonly used values for pure sand (0.2 – 0.35 Pa) is not suitable as a starting value in the mixed-sediment model for determination of the critical shear stress for mixtures.

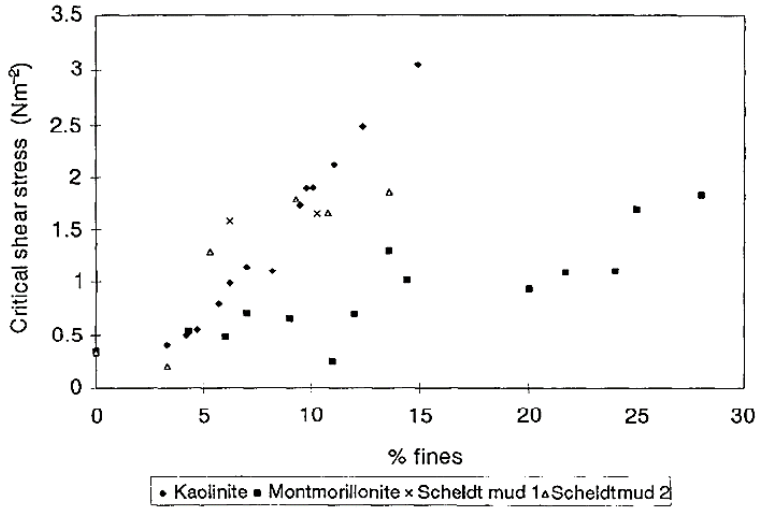

Figure 6.9. Critical shear stress for erosion against % fines (by weight) for different types of cohesive material (*from* Mitchener and Torfs, 1996).

Because the bed composition data shows that a fraction of mud is observed almost everywhere in the domain, the higher value of critical shear stress for erosion of sand is considered as appropriate in this study.

Table 6.2. The properties of the non-cohesive and cohesive sediment.

Type of Sediment	Diameter d_{50}	Density	Settling Velocity	Critical Shear Stress for Erosion (first layer)	Critical Shear Stress for Erosion (second layer)
Non-cohesive (Sand)	300 μm	2650 kg/m^3	0.01 m/s	0.6 Pa	0.6 Pa
Cohesive (Mud)	60 μm	1600 kg/m^3	0.001 m/s	0.5 Pa	0.8 Pa

6.2.4.5. New scheme for erosion & deposition of mixed-sediment

For each type of sediment, the transport mechanism is different. Sand is mainly transported as bedload, cohesive sediment mainly as suspended load, but both modes of transport consume energy. From this perspective, the available energy in the system is likely to be overestimated if only considering cohesive or non-cohesive sediments. Thus, a new scheme accounting for mixed-sediment transport has been developed (Figure. 6.10).

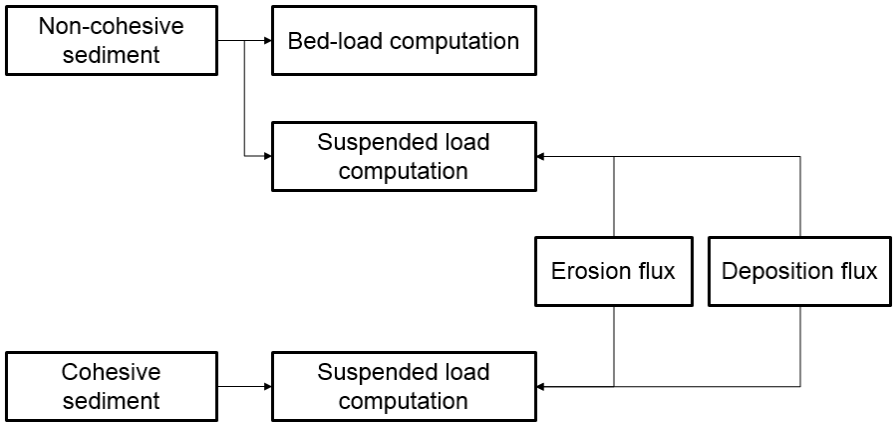

Figure 6.10. Schemes of modelling mixed-sediment transport.

During the erosion phase, the methodology for modelling mixed-sediment from Waeles (2005) is employed. According to his study, the sand-mud mixture can be categorized as non-cohesive, mixed and cohesive, based on its sand-mud composition. Each category has its unique characteristics and behaviour. For the application in the Scheldt Estuary, the lower bound of the critical mud fraction is set to 30% and the upper bound is 50%. The mixture that contains mud less than 30% is in the non-cohesive regime and is considered as sand; those having mud more than 50% is in the cohesive regime and is treated as mud; the rest is in the mixed-sediment regime. The lower and upper bounds of critical mud fractions is suggested by the study of Panagiotopoulos *et al.* (1997) and Mitchener & Torfs (1996). As the mud fraction increases, the available space between the sand grains decreases. When the mass

fraction of mud is lower than about 30% (by weight), the sand grains remain in contact with each other. When the mud fraction exceeds 30%, spaces between sand particles are filled by mud particles, which can form a matrix, and, in this case, pivoting is no longer the main mechanism responsible for resuspension of sand grains. Consequently, the whole mixture does not behave like a non-cohesive sediment any more. In Mitchener and Torfs' study, the critical shear increases significantly, when mud is added to sand (0% to 30% mud). There is an optimal ratio of sand content in a mixed bed at which the critical erosion shear stress is a maximum. The optimal sand fraction appears to be between 50% and 70% by weight of sand (Mitchener & Torfs, 1996). Therefore, the lower and upper bounds of critical mud fractions were set at 30% and 50%. These values are also used in the study of Waeles *et al.* (2007).The critical shear stress for erosion is calculated as a function of the mud fraction (f_m) using the equations (5.9) – (5.11) (Waeles, 2005).

The calibration constant x_1 is 0.5 in the current study, which is considered suitable for the Scheldt estuary according to the studies of Mitchener and Torfs (1996) and Fettweis *et al.* (2003). Figure 6.11 shows the critical shear stress for erosion as a function of the mud fraction in two bed layers. In the non-cohesive regime, sediment particles behave like sand, so the consolidation process is ignored. The critical shear stress for erosion increases when the mud is added to sand. When the mud fraction exceeds 30%, the transitional regime is reached where different behaviour in the upper and lower bed layers is expected. In the upper layer, the excessive mud particles will accumulate and due to the loose form, the critical shear stress for erosion begins to decrease; in the lower layer, the consolidation process will give extra erosion resistance to the bed material. When the mud fraction exceeds 50%, the maximum critical shear stress for erosion is reached in the lower layer, which is 0.8 Pa, the same as for mud consolidated for over 48 hours; while in the upper layer, the sediment behaves like freshly deposited mud, so the same value of 0.5 Pa is assigned. The calibration constant x_1 is set to 0.5 to ensure the critical shear stress for erosion does not exceed the maximum value before the mud fraction exceeding 50%, to preserve the characteristics of the sand-mud mixtures in different regimes.

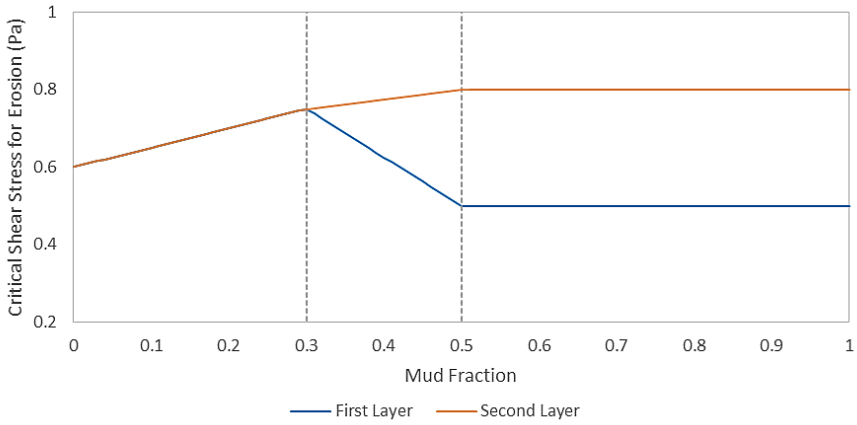

Figure 6.11. Critical shear stress for erosion as function of the mud fraction.

The erosion rate can be determined depending on the regime of the mixed sediment following the same procedure of Waeles (2005) (see equations 5.12 – 5.17). The erosion constants E_{0s} and E_{0m} are determined based on the study of Mitchener and Torfs (1996), in which they used the sand with a median diameter of 230 μm and the mud with a median diameter less than 62.5 μm. They reported that the erosion rate for pure mud beds ($0.05\text{-}0.1\times10^{-3}$ kg·m^{-2}·s^{-1}) was an order of magnitude higher than for the 20% and 40% sand beds ($0.005\text{-}0.03\times10^{-3}$ kg·m^{-2}·s^{-1}). Therefore, in this study the erosion constant E_{0s} for the non-cohesive regime is assumed 0.01×10^{-3} kg·m^{-2}·s^{-1} and the erosion constant E_{0m} for the cohesive regime is 0.1×10^{-3} kg·m^{-2}·s^{-1}.

Since the vertical energy balance is not resolved in a 2DH model, the traditional deposition law, proposed by Krone (1962) is used. A new deposition criterion, which has been derived from a suspension capacity condition proposed by Toorman (2000 & 2002), has been introduced in this study, which allows estimating the critical stress for deposition in each node and no longer needs calibration – see Section 5.2.3. Since shear flow produces turbulence, the critical "shear stress" for deposition can be related to the total amount of turbulent energy that is required to keep a number of sediment particles in suspension. When the bed shear stress cannot provide the fluid with enough energy that is needed to maintain all the suspended particles in the water column, deposition shall begin.

The excessive sediment settles down to the bottom until the energy balance is restored.

The critical shear stress for deposition, obtained by inversion of Toorman's suspension capacity criterion, has been split into two parts in order to deal with sand-mud mixtures. In this case, the total required turbulent energy is also divided over both sediment fractions: part of it is used to keep non-cohesive particles in suspension and the rest is used to keep cohesive particles in suspension. The corresponding "critical stresses" are calculated in the equations (5.18) – (5.21).

Krone's deposition law (1962) subsequently is adapted to be used for calculating the deposition flux of each fraction, without violating the energy balance (see equations 5.22 – 5.25).

The bed evolution is calculated using the Exner equation with an additional source term, allowing the inclusion of external changes caused by the erosion and deposition of sediment particles. The following form of the Exner equation is used in the study:

$$\left(1-n\right)\frac{\partial Z_b}{\partial t}+\nabla\cdot Q_b+\left(E-D\right)=0 \qquad (6.5)$$

where: n is the bed porosity, Z_b is the bottom elevation [m], Q_b is the bedload transport rate per unit width [m²/s], E is the erosion flux and D is the deposition flux [m/s]. It is worth pointing out here that the bed porosity is an estimated value considering cohesive particles filling up part of the spaces between non-cohesive particles, and the erosion and deposition flux (equations 5.12 – 5.17 and equations 5.22 – 5.25) consists of contributions from both cohesive and non-cohesive sediments.

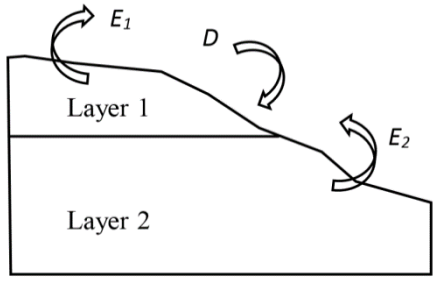

Figure 6.12. Two-layer Bed Model

When computing the bed evolution, an iterative procedure is employed, where at each time step, the top layer is eroded first. Once it is empty, the erosion of the second layer starts. The deposited sediment always has the properties of a fresh deposit, *i.e.* the critical shear stress is as in the first layer. The sand/mud composition, however, is recalculated at each time step based on the mass fraction of sand/mud at each particular location after erosion/deposition processes, and the latest value is assigned to the new deposits (Figure 6.12).

6.3. Calibration and validation

6.3.1. Available data sets

The model has been calibrated against the time series of measurements in 2009 at several locations both in the upstream and in the downstream near the Belgian coast. The available data sets are provided by the Royal Belgian Institute of Natural Sciences, Operational Directorate Nature (former Management Unit of the North Sea Mathematical Models and the Scheldt estuary, MUMM), Flanders Hydraulics Research (Waterbouwkundig Laboratorium) and IMDC, Belgium, and Rijkswaterstaat, Centre for Water Management, the Netherlands.

The measurements close to the Port of Zeebrugge are taken and processed under the framework of "Monitoring and modelling of cohesive sediment transport and evaluation of the effects on the marine ecosystem as a result of dredging and dumping operations" (MOMO) by MUMM and RV Belgica in the period January to December, 2009 (Backers and Hindryckx, 2010). There are four field campaigns carried out and during these campaigns, water level, flow velocity and direction, and turbidity, are continuously measured as well as some basic parameters (temperature, salinity, density, fluorescence, and meteorological data) during one or several measurement cycles. In addition, the necessary water samples are taken for calibration. The measurement locations are indicated in Figure 6.13 and their coordinates are given in Table 6.3. These data are mainly used for calibration of the suspended-sediment concentration and salinity near the Belgian coast.

Table 6.3. Measurement locations from MUMM.

Data Set	WGS coordinates	Corresponding node in model	ADV measured at	OBS measured at
MOMO 2009-02-09 - 2009-03-19	N 51° 21.490', E 003° 07.104'	814	0.36m above bottom (-7.38m TAW)	2.34m above bottom (-5.40m TAW)
MOMO 2009-03-26 - 2009-04-29	N 51° 21.474', E 003° 07.002'	814	0.36m above bottom (-7.38m TAW)	2.34m above bottom (-5.40m TAW)
MOMO 2009-05-04 - 2009-06-15	N 51° 19.572', E 003° 06.545'	779	0.38m above bottom (-4.87m TAW)	2.16m above bottom (-3.09m TAW)

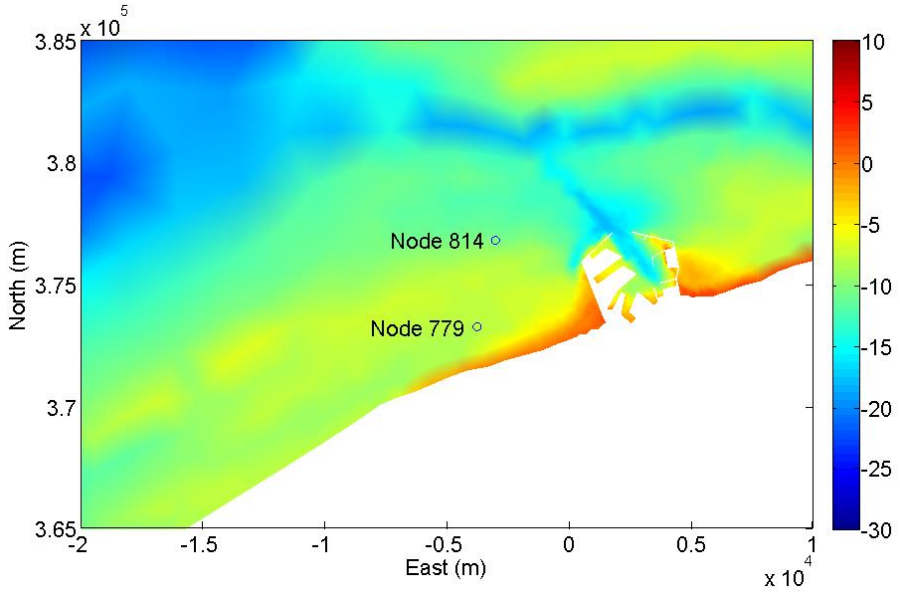

Figure 6.13 Measurement locations from MUMM.

Rijkswaterstaat, Centre for Water Management, the Netherlands, has a monitoring network all over the Scheldt estuary, but those measurements are mainly water level, temperature and wind speed. The time series of measurements can be downloaded from the WTZ database in the Hydro Meteo Centrum. Thus, these data sets are used to calibrate the hydrodynamics in the coastal areas and as a complement to MUMM data. The measurement locations in the interested area are indicated in figure 6.14 and their coordinates are given in Table 6.4.

Table 6.4. Measurement Locations from Rijkswaterstaat, Centre for Water Management, the Netherlands.

Data Set	RD coordinates	Corresponding node
Cadzand	15004.07, 378597.07	4448
Vlissingen	30568.36, 385259.06	8949
Westkapelle	19872.47, 394230.44	5482

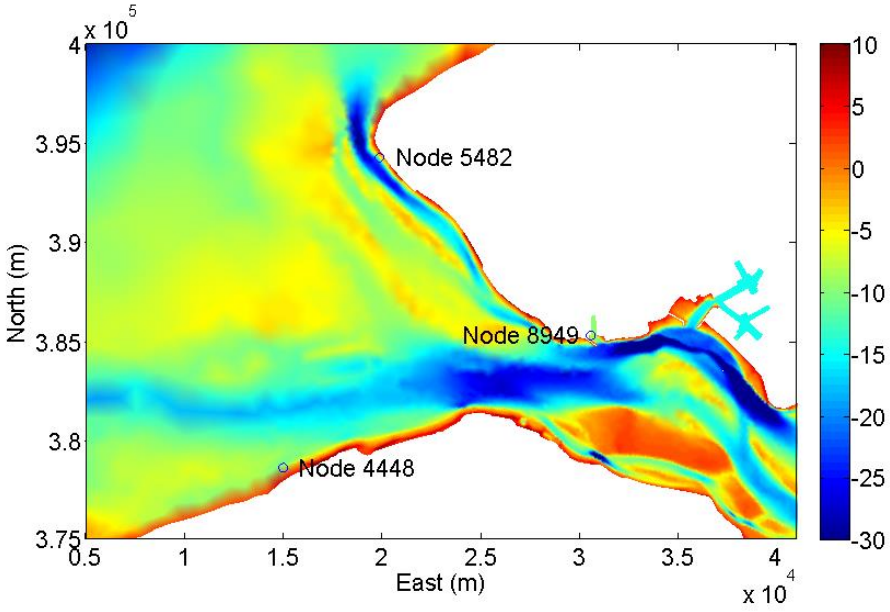

Figure 6.14. Measurement Locations from Rijkswaterstaat, Centre for Water Management (the Netherlands).

The third set of measurements mainly located in the upstream of Scheldt close to the Port of Antwerp, carried out by Flanders Hydraulics Research and IMDC, under the project "Prolonged measurements in Deurganckdok: Follow-up and accretion analysis", which is the long-term measurements conducted in Deurganckdok aiming at the monitoring and analysis of silt accretion (International Marine and Dredging Consultants, 2010). This measurement campaign is an extension of the study "Extension of the study about density currents in the Beneden Zeeschelde" as part of the Long Term Vision for the Scheldt estuary.

Table 6.5. Measurement Locations from Flanders Hydraulics Research and IMDC.

Data Set	RD coordinates	Corresponding node in the model	Measured at
Prosperpolder	75037.24, 374074.43	27326	2.5m above bottom (-1.5m TAW)
Boei84 (Bottom)	77497.29, 370424.16	28492	0.8m above bottom (-8.1m TAW)
Oosterweel (Bottom)	83903.55, 361552.10	30783	1.0m above bottom (-5.8m TAW)

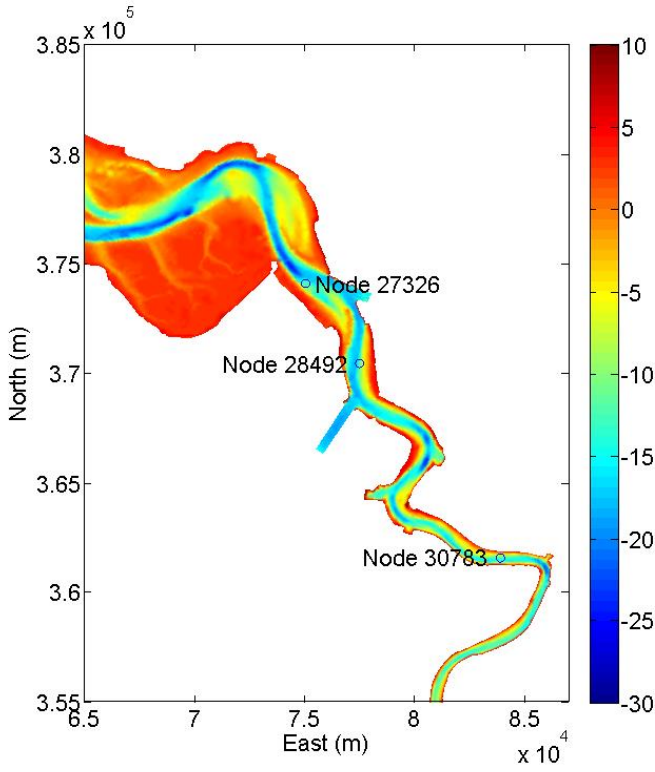

Figure 6.15. Measurement locations from Flanders Hydraulics Research and IMDC.

The available measurements are in the period April 2008 to March 2009, including upstream discharge in the river Scheldt; salt and sediment concentration in the Lower Sea Scheldt taken from permanent data acquisition sites at Oosterweel, Prosperpolder and up- and downstream of the Deurganckdok; near-bed processes in the central trench in the dock, near the entrance as well as near the landward end: near-bed turbidity, near-bed current velocity and bed elevation variations; current, salt and sediment transport at the entrance of Deurganckdok and vertical sediment and salt profiles (e.g. Figure 6.16) recorded with the SiltProfiler equipment (Bollen *et al.*, 2006); and dredging and dumping activities. The measurement locations are indicated in Figure 6.15 and their coordinates are given in Table 6.5. These data sets contain the measurements of water

level, velocity magnitude, salinity level and suspension concentration in the simulation period 2009.

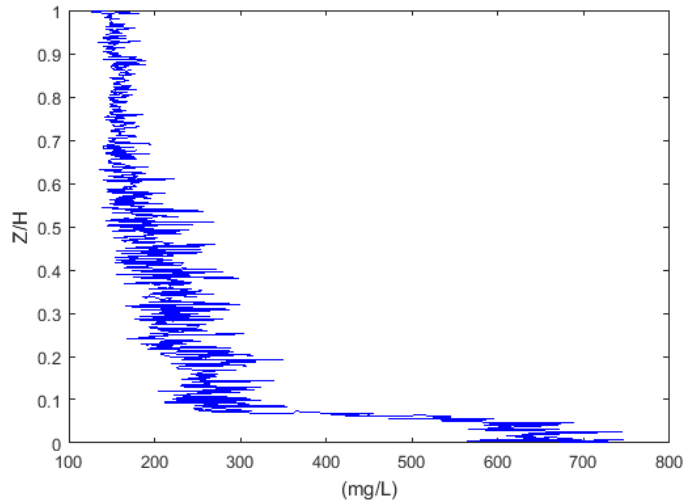

Figure 6.16. Typical suspension concentration profile measured with the Siltprofiler at Deurganckdok at 16th Feb. 2005. The calculated depth-averaged concentration at this particular location is 220.45 mg/L.

6.3.2. Calibration processes

The calibration is carried out for the hydrodynamic model first, since the flow conditions are crucial for the sediment transport. The main parameter calibrated at this step is the bottom friction coefficient (using the Chézy coefficient calculated from the new roughness law in this study). The sediment transport model is considered reliable only when realistic flow conditions can be reproduced. The following features are most valued when evaluating the hydrodynamic model:

- the free surface elevation at the tidal cycle and seasonal time scales;
- the magnitude of the velocity at different locations;
- the salinity level in the mixing zone and in the coastal area.

Once the validity of the hydrodynamic model has been assured, it is then coupled with the sediment transport model for further calibration, since

the implementation of the new friction law (see Section 5.1) and the bed evolution will also alter the flow conditions to a certain extent. This time the calibration not only focuses on the hydrodynamics but also on the suspended-sediment concentration. The critical shear stresses for erosion of sand and mud, as well as their erosion constants are the main parameters for calibration during this step. The model is declared satisfactory if the following features can be represented:

- the order of magnitude of the suspended-sediment concentration throughout the estuary system;
- the tidal and seasonal variations of the suspended-sediment concentration;
- the turbidity maximum areas in the estuary.

6.3.3. Model validation

The model incorporated with the new friction law (see Section 5.1), including the concentration effects, is used during the calibration and validation processes because it is more physics based and it is likely to perform better. For the hydrodynamics in the Scheldt estuary, water level, magnitude of velocity and salinity level are shown in the following figures with comparison to the measured data.

In general, the water levels obtained from the model show good agreement with the measured data throughout the estuary and the upstream river network. It is worth mentioning here that once the new friction law is implemented, the model gives good predictions in terms of water levels without tuning of the bottom friction parameters for specific areas, since the depth dependence is dominant relative to the influence of the roughness height k_s. The comparisons are performed at three locations (nodes 4448, 5482 and 8949) in the downstream near the coast and three locations (nodes 27326, 28492 and 30783) in the upstream, close to the Port of Antwerp. Van Kessel *et al.* (2006) reported the tidal range at Vlissingen during a typical spring-neap tide varies from 2.97m to 4.46m. It first increases towards the upstream as it is affected by convergence and reflection. At Schelle (upstream of Antwerp), the tidal range during a typical spring-neap tide varies from 4.49m to 5.93m, which is larger than at the mouth. Further upstream, the tidal wave decreases due to dissipation. This characteristic is also reproduced by the model. The variations of the free surface at all these locations with the measured data are shown in Figures 6.17–6.22. In the locations close to

Vlissingen (nodes 4448, 5482 and 8949), the tidal range is around 2.8m up to 4.9m. This is smaller than the tidal range in locations in the upstream (nodes 27326, 28492 and 30783) before it reaches Schelle, which is from about 4.2m to 6.0m.

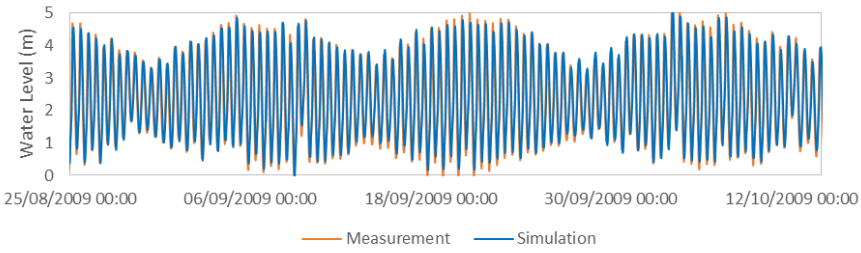

Figure 6.17. Water level at node 4448.

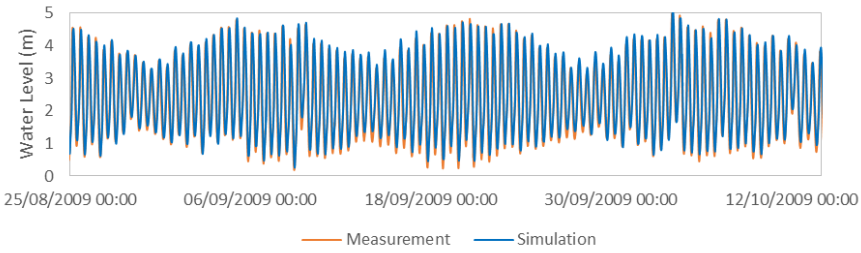

Figure 6.18. Water level at node 5482.

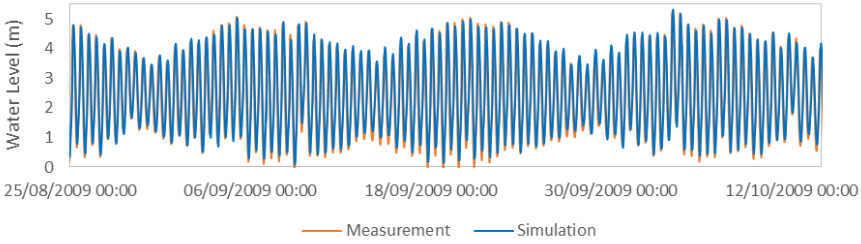

Figure 6.19. Water level at node 8949.

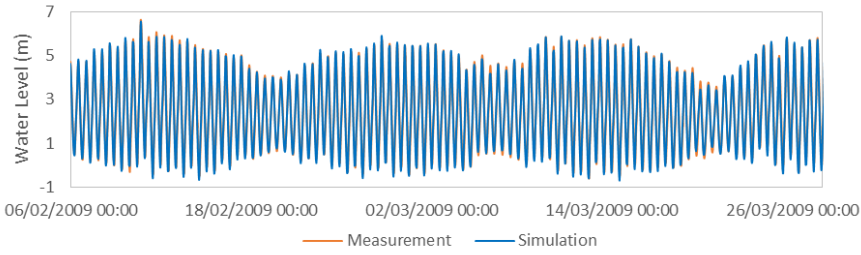

Figure 6.20. Water level at node 27326.

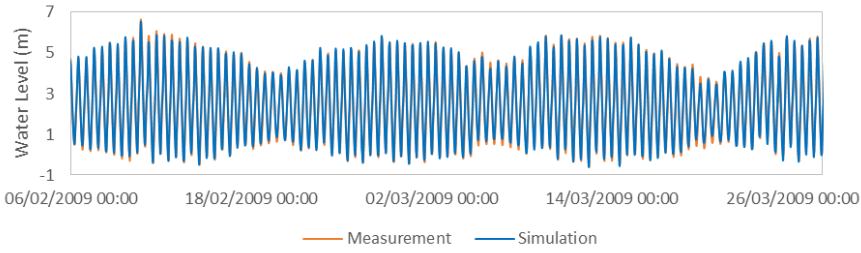

Figure 6.21. Water level at node 28492.

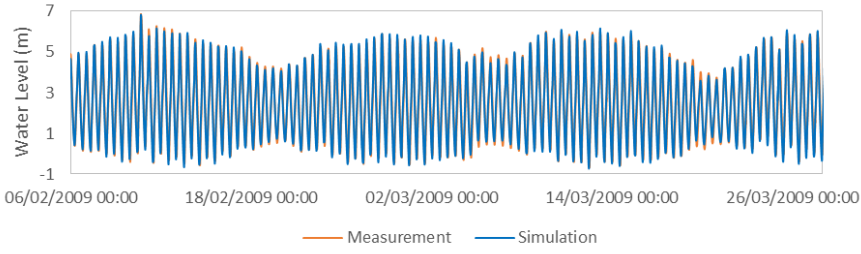

Figure 6.22. Water level at node 30783.

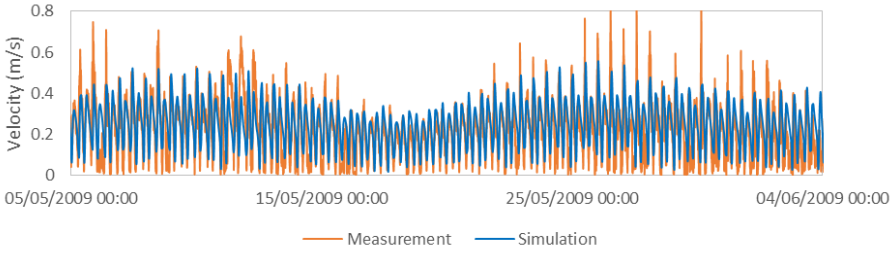

Figure 6.23. Velocity magnitude at node 779.

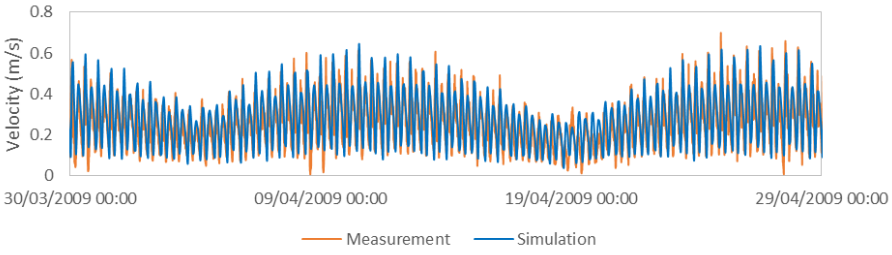

Figure 6.24. Velocity magnitude at node 814.

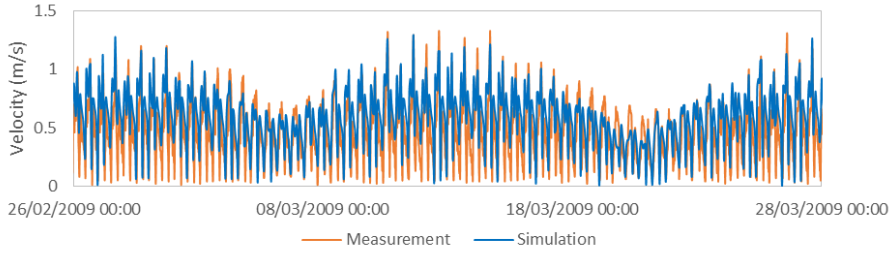

Figure 6.25. Velocity magnitude at node 28492.

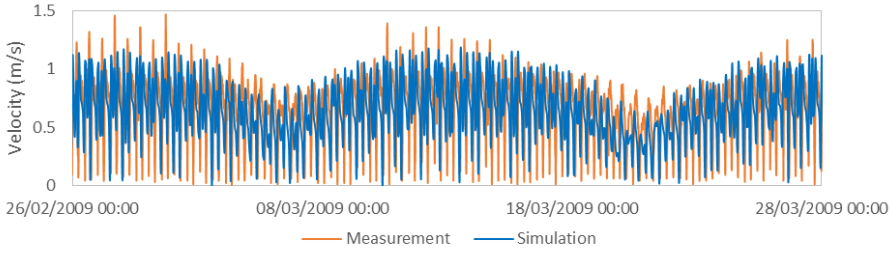

Figure 6.26. Velocity magnitude at node 30783.

The measured velocity magnitude during the simulation period is available at four locations, two near the Port of Zeebrugge (nodes 779 and 814) and the other two (Nodes 28492 and 30783) in the upstream close to the Port of Antwerp. The Figures 6.23–6.26 show the simulation results compared with the measurements. The depths of measurements are given in tables 6.2 and 6.4. The modelled depth-averaged velocities have been converted into the values at the corresponding depths (assuming a logarithmic profile) for proper model-data comparison. In general, the magnitude of the velocity obtained from the model is similar to the measurements except for the Node 779, at which there is

underestimation of the peaks during the high tide. The apparent difference in the minimum velocities are the artefact of the presentation of the velocity in terms of RMS value. The velocities always go through zero from ebb to flood and vice versa. But in general, the velocity in the upstream is larger than in the coastal area, which is consistent with the observations reported by van Kessel *et al.* (2006).

Three locations are selected to compare the salinity level from the results (Figures 6.27–6.29) with the measurements. Node 814 is located in the coastal area near the Port of Zeebrugge. The time series of the measured data is available from February to April 2009. The salinity level near the Belgian coast is about 31g/L. The underestimations of the peaks can be easily seen at 14th and 30th of March. In general, the simulated result predicts the right magnitude of the salinity level but cannot match the measurements in detail at Node 814. Most likely, this can be attributed to the boundary values, which are generated by another numerical model and may not exactly correspond to the reality. The peaks observed in the measurements could be caused by a storm surge, which can bring seawater with higher salinity level to the coastal area. In Figure 6.31, peak values of suspension concentration also occurred at the same period, which indicates that a storm surge was possibly happening around that location and causing higher salinity and suspended sediment concentration in the measurements. The other two locations (Nodes 27326 and 28492) are in the partially mixed zone (Peters, 1975; Nihoul *et al.*, 1978) far away from the downstream. The salinity level in this area fluctuates between 6-10g/L. The results show good agreement with the measured data at both nodes during that period. The more or less constant low value at ebb tide in these upstream nodes can be explained by the constant water discharge imposed as upstream boundary conditions, due to the lack of time series data.

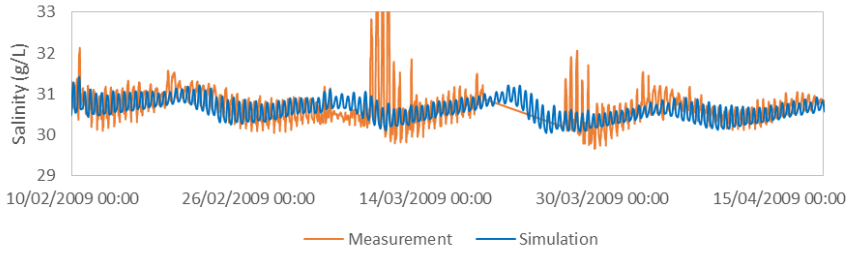

Figure 6.27. Salinity at node 814.

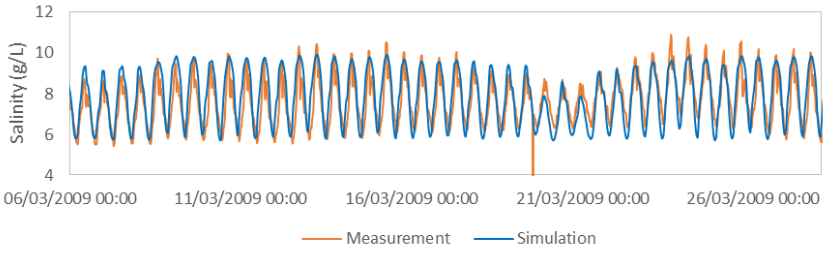

Figure 6.28. Salinity at node 27326.

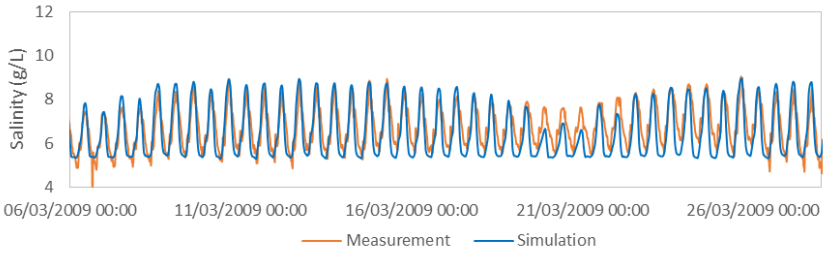

Figure 6.29. Salinity at node 28492.

The suspended-sediment concentration consists of the contributions from both cohesive and non-cohesive sediment. However, the concentration of suspended non-cohesive sediment is about two orders of magnitude lower compared to cohesive sediment because the non-cohesive sediment is mainly transported as bedload, as expected. The results are plotted in Figures 6.30–6.34 with comparison with measurements at five locations (Nodes 779, 814, 27326, 28492 and 30783). Again, for better comparison, the simulated depth-averaged concentrations have been converted into the values at corresponding depths based on the shape of the measured suspension concentration profile of Figure 6.16. In general, the magnitude of the suspension concentration approximately matches the measured data. There are some deviations in the results, *e.g.* underestimations of the peaks at certain time steps. Nevertheless, considering that, the model is depth-averaged and without coupling with the wave model, which becomes important in the coastal areas, this is not surprising. In Figure 6.30, the measured suspension concentration is plotted together with the significant wave height at Node 814. It can be seen that there are correlations between the fluctuations of suspension concentration and the wave actions. The phases of the time series of suspension

concentration generated by the model show agreement with measurements while the underestimation of peaks most likely can be explained by lack of wave action, which is ignored in this study.

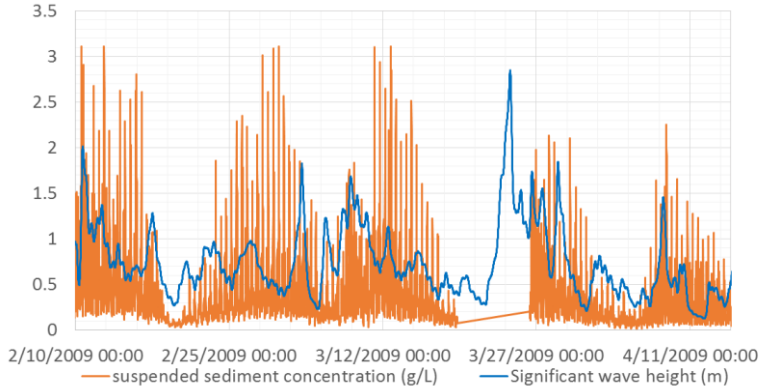

Figure 6.30. Measured suspension concentration at Node 814 (located in front of the Port of Zeebrugge) and the significant wave height around the same location.

It is worth pointing out that, in the upstream locations, especially in nodes 28492 and 30783, the simulated suspension concentration rapidly decreases after reaching the peaks, while the measurements tend to maintain higher concentrations for longer periods. Taking into account the locations, a possible explanation could be disturbance by human activities. Nodes 28492 and 30783 are located in a busy navigation channel in the upstream. The comparison with measured data may indicate that the cruising of a ship, dredging or other activities during the period mid-January to late March were intensive and influenced the suspension concentration. After that, those activities seem to have reduced and the suspended sediment was also less disturbed, which could explain the better agreement with data at the end of March in all three upstream locations.

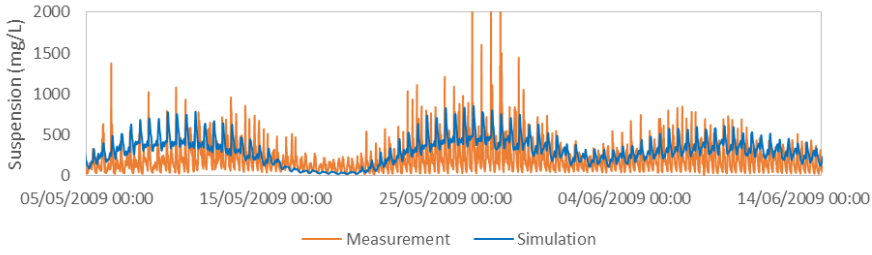

Figure 6.30. Suspended-sediment concentration at node 779.

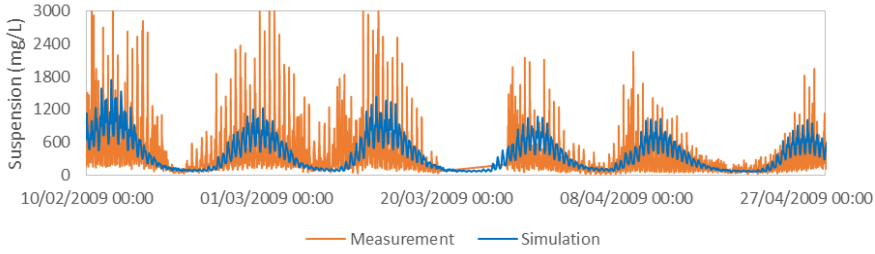

Figure 6.31. Suspended-sediment concentration at node 814.

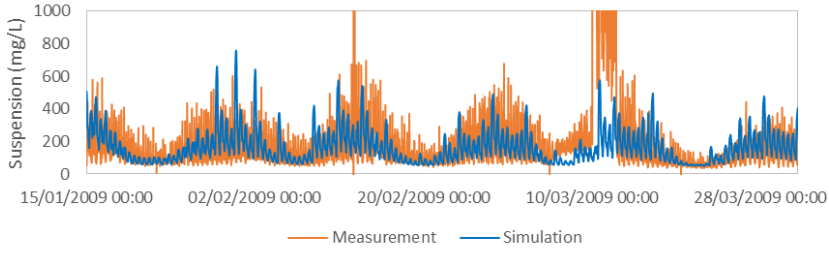

Figure 6.32. Suspended-sediment concentration at node 27326.

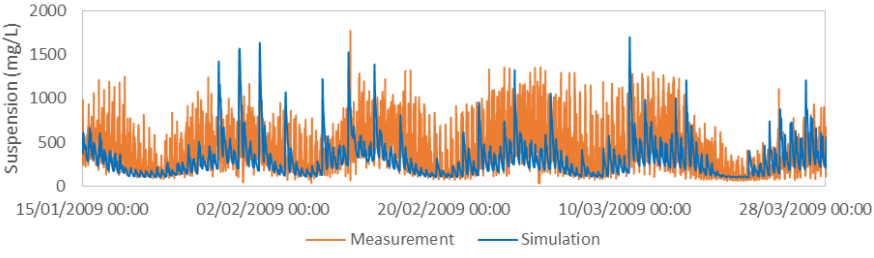

Figure 6.33. Suspended-sediment concentration at node 28492.

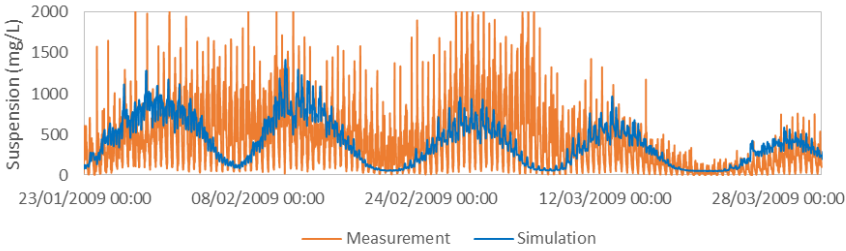

Figure 6.34. Suspended-sediment concentration at node 30783.

Beside of the calibration against the point measurements, the spatial variability of the suspended-sediment concentration has also been examined.

One of the most distinctive features of sediment transport in estuaries, *e.g.* the Scheldt estuary, is the presence of a turbidity maximum. The energetic tidal flow is capable of maintaining quite high concentrations of suspended sediment in the estuary, higher than occur either in the river or in the sea. This feature is called a turbidity maximum and there are two dominant mechanisms that contribute to its maintenance, the residual circulation of water and the tidal asymmetry that produces a net landward movement of sediment (Dyer, 1986). Burchard and Baumert (1998) studied relative importance of these mechanisms numerically and they concluded that in the setting they investigated (an academic idealized 2DV model considering all the mechanisms, e.g. the residual gravitational circulation, tidal velocity asymmetry and tidal mixing asymmetry) the mechanism associated with tidal asymmetry was more important than the one resulting from the residual gravitational circulation.

There are studies in which 2D depth-averaged models were used to investigate the process of the formation and maintenance of estuary turbidity maximum (ETM), e.g. the study of Ellis *et al.* (2008) for the Irish Sea. Although the residual gravitational circulation cannot be accounted for directly, it can be implicitly accounted for by the depth-averaged advection, which reaches a minimum residual transport at the location of the turbidity maximum, and the vertical erosion/deposition processes.

In the Scheldt estuary, turbidity maximum zones are observed in different regions (as indicated in Figure 6.35) where a large amount of sediment particles is accumulated. These sediments are continually

deposited and resuspended by the tidal flow. The distribution of suspended matter is influenced by a range of interrelated processes, *e.g.* temperature and biological activity, fresh water discharge and salinity, hydrodynamic conditions and turbulence, mineralogical composition, chemical conditions, aggregation and flocculation (Meire *et al.*, 2005). The main mechanisms suggested by the Scheldt model in this study is the residual sediment circulation. The occurrence of tidal velocity asymmetry and its interaction with the time-varying concentration field is found in the estuary (see Section 6.4.2 and 6.4.4).

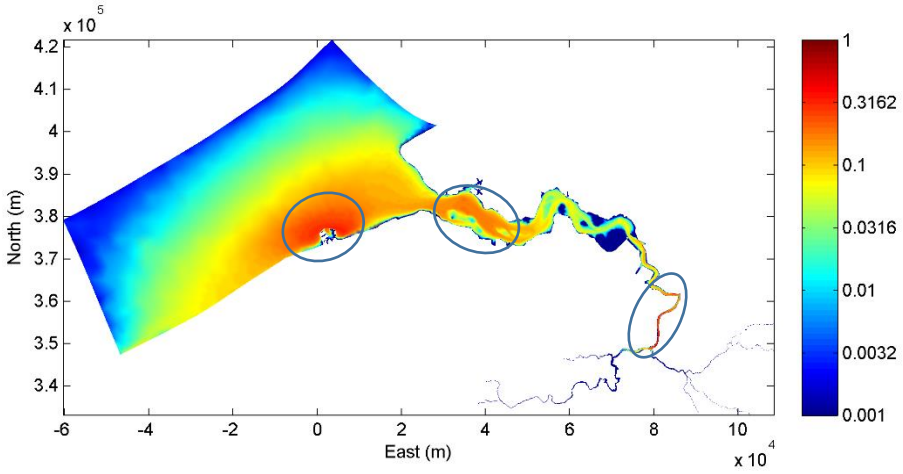

Figure 6.35. Suspension concentration (g/L) averaged over one tidal cycle on 4th December 2009.

Three turbidity maximum zones can be observed in the Scheldt estuary, one in front of the Belgian coast around the Port of Zeebrugge, one at the freshwater/seawater interface in the downstream, and a third one situated at about 50-110 km from the mouth originating from tidal asymmetry (Baeyens *et al.*, 1998; Fettweis *et al.*, 1998; Herman & Heip, 1999). As indicated in Figure 6.35, these turbidity maximum zones are reproduced by the model.

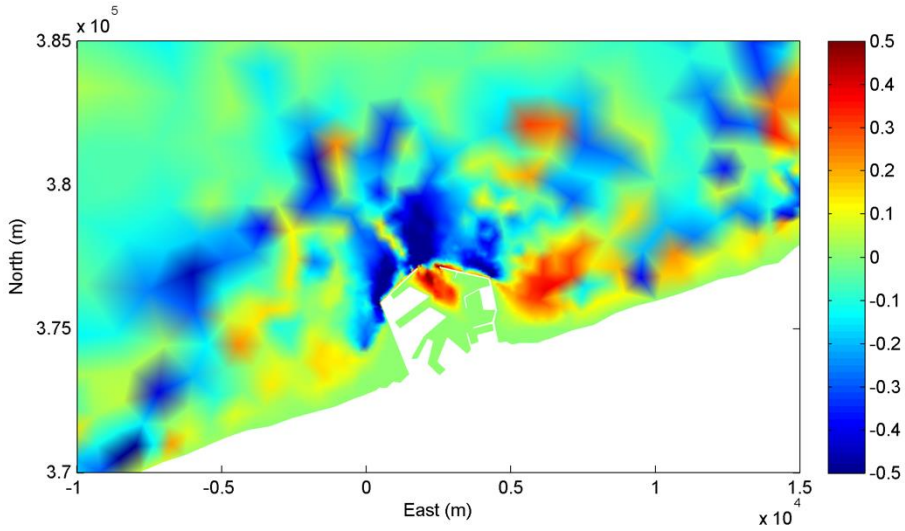

Figure 6.36. Modelled erosion and accumulation (m) of sediment around Port of Zeebrugge after one year.

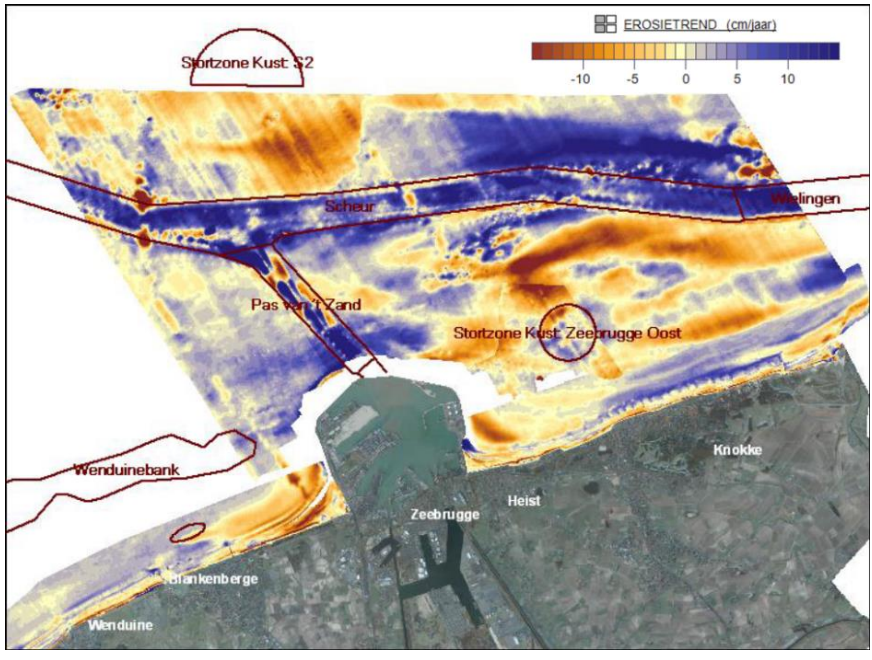

Figure 6.37. Measured erosion and sedimentation near the Port of Zeebrugge between 1999 and 2009 (Janssens *et al.*, 2012).

The Port of Zeebrugge is a major port in Europe and an important multifaceted port in northwestern Belgium. For better port management and toward sustainable development, many research tools were developed for investigating the flow conditions and sedimentation around Zeebrugge, in order to provide scientific advice to policy makers by simulating many different scenarios. In order to evaluate the quality of the model particularly in this area, the erosion and sedimentation around the Port of Zeebrugge after one-year simulation is carefully examined. The reference data are from the Quest4D project in which they measured topography and bathymetry changes over the period 1999-2009 and observed long-term morphological evolution of the Belgian coast and shelf (Janssens *et al.*, 2012). Comparing the modelled erosion and sedimentation patterns with the measurements (Figures 6.36 and 6.37), many similarities can be discovered. Erosion occurs along the two breakwaters and develops towards the sea. The sedimentation zone appears on the right side of the port. These two patterns can be observed in Figure 6.37. The most obvious difference is that the sedimentation also develops inside the port near the entrance to the sea while it is not shown in Figure 6.37 due to lack of data. Since our model has not been optimized for the nearshore (a.o. too coarse mesh resolution and no wave effects), there remains potential for further future improvements.

The agreement between the sedimentation and erosion patterns and magnitude reproduced by the model around the Port of Zeebrugge and the observations from the Quest4D project (Figures 6.35 and 6.36) also supports that the settling velocities chosen for this study are appropriate.

6.4. Results

The calibrated model is then used to investigate the sediment transport in the Scheldt Estuary, and more importantly, to evaluate the concentration effects in the new bottom friction law and its influence on the sediment flux.

6.4.1. Movements of turbidity maximum areas

The Figure 6.39 shows the sediment concentration evolving in one tidal cycle on 4th December 2009. The model shows that the movements of the turbidity maximum near the Port of Zeebrugge is always counter-

clockwise. Sediment is accumulated at the east side of the port, and then transported around the port towards the south-west and finally stays at the west side of the port. This is consistent with the erosion and sedimentation patterns found in the observations (Janssens *et al.*, 2012) and the modelled results (Figures 6.36 and 6.37). For the turbidity maximum in the upstream, its movement seems to react rapidly to the tidal waves. During the ebb tide, the turbidity maximum shifts towards the downstream and then shifts backwards during the flood tide.

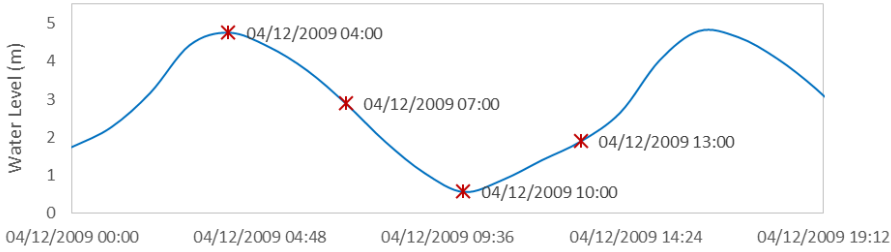

Figure 6.38. A typical tidal cycle in the Scheldt estuary

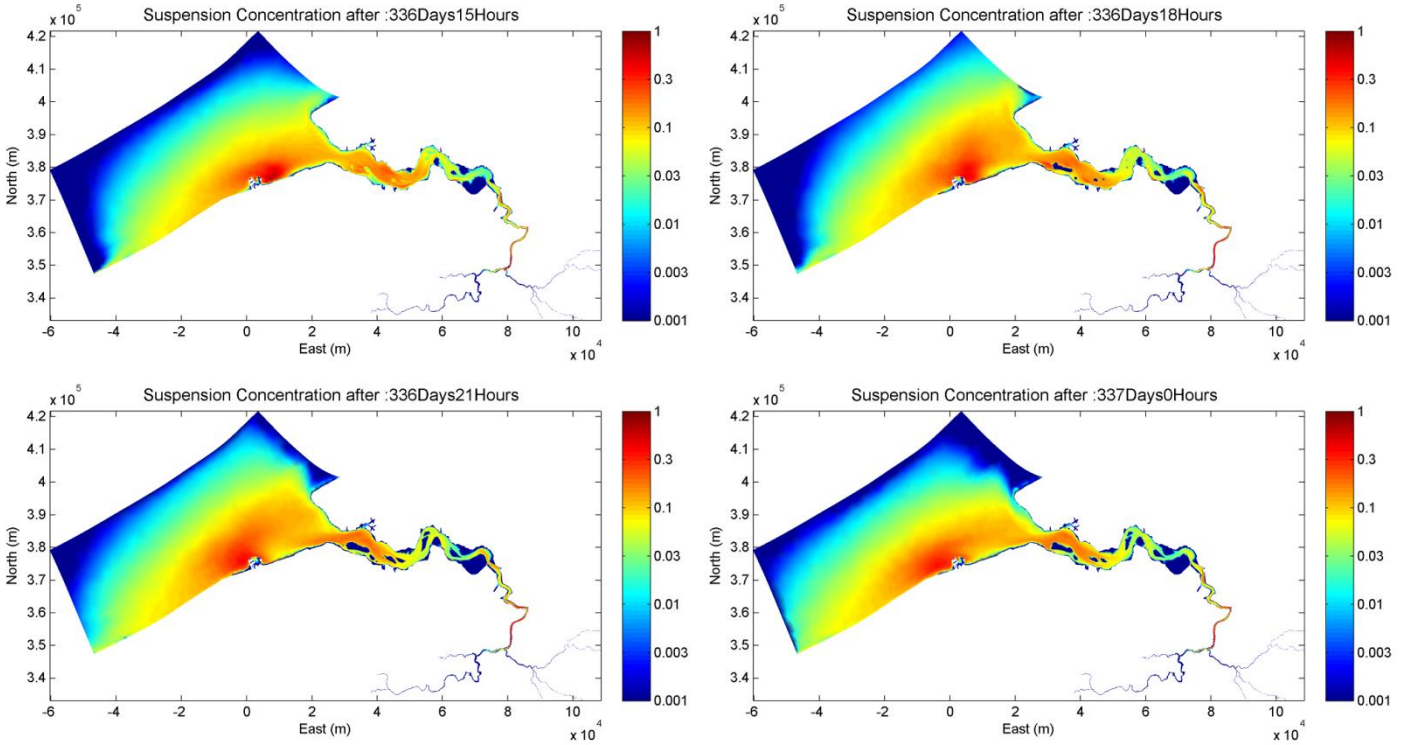

Figure 6.39. Suspension concentration (g/L) evolving within a typical tidal cycle.

6.4.2. Residual sediment circulations

The model also shows the ability to represent the residual flow circulations related to ebb and flood channels.

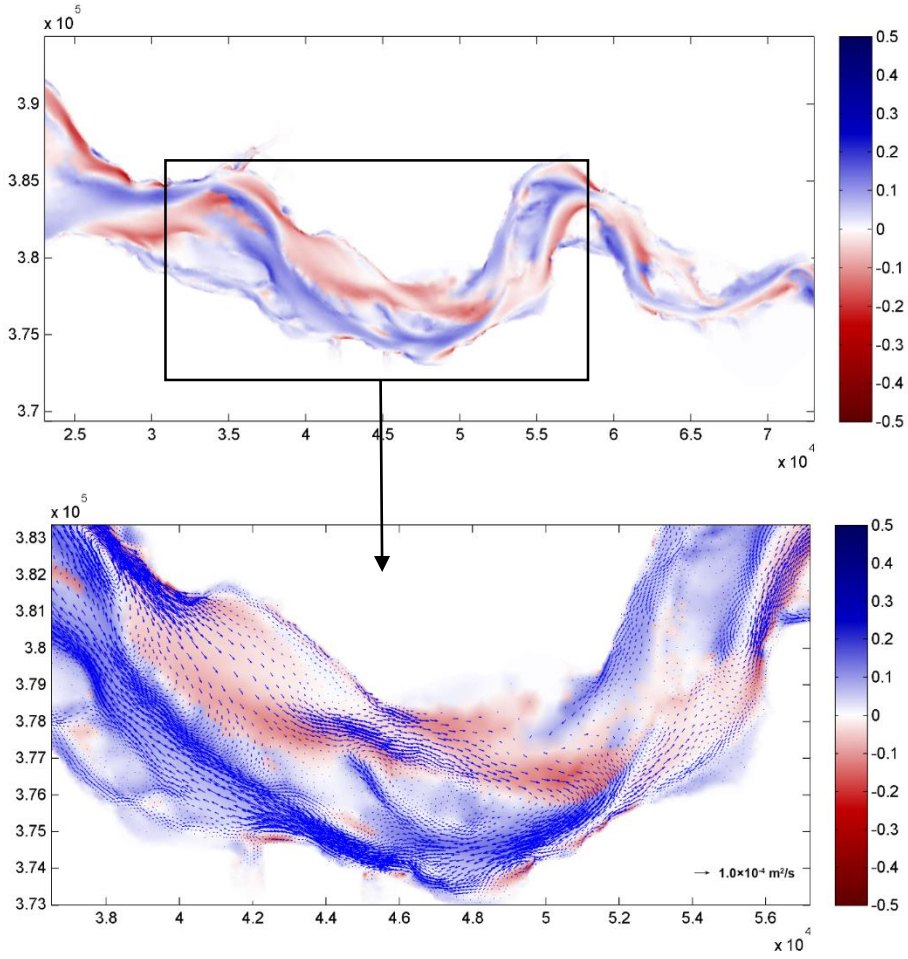

Figure 6.40. Computed residual velocity (m/s, upper figure) and the bedload transport (m^2/s, lower figure) over a period of one year. The red areas indicate the flood-dominated channels and the blue areas are the ebb-dominated channels. It also reveals the sediment circulation patterns and residual transport paths in the Terneuzen section of the Scheldt estuary.

Figure 6.40 reveals the flood/ebb channel system in the Terneuzen section of the Scheldt estuary with bedload transport, which is in good agreement with the study of Jeuken (2000). According to her study, the flood/ebb channel system is responsible for the residual sediment transport patterns found in the Scheldt, *i.e.* the sediment circulation and the transport paths. More sediment is transported landward in the flood channels and seaward in the ebb channels during a tidal cycle. The similar residual circulation patterns can also be found in the movement of suspended sediment in the estuary (see Section 6.4.4). This is also helpful for explaining the erosion/sedimentation occurring in the Scheldt.

6.4.3. Evaluation of the new bottom friction law

For demonstrating the new physics based bottom friction law, two more test cases were created besides the standard model. The standard model incorporates the full version of the new friction law including the concentration effects denoted as the DepCsR. The other two are the test case with constant roughness coefficient (Chézy coefficient = 65, obtained by calibration with water depth data, denoted as ConR) and the test case with the new friction law excluding the concentration effects (denoted as DepR). The rest of the model settings are identical in all the test cases.

The suspended-sediment distribution from all three cases averaged over the same tidal cycle on 4th December 2009 are put together for comparison. As it can be seen from figure 6.41 – 6.43, similar sediment distribution patterns are found in both the ConR and DepR cases. However, the suspension concentration in the North Sea and in the upstream close to the port of Antwerp is reduced with the simplified version of the new friction law (without the concentration effects). In the DepR case, less suspended sediment appears in the river mouth. It also does not reach the southwest of the port of Zeebrugge as far as the ConR case. The DepCsR case shows a different sediment transport pattern compared with the other two cases. In general, higher suspension concentrations are obtained with the new friction law including the concentration effects, especially near the coast and in the upstream. The suspended sediment spreads further near the coastal area and the turbidity maximum close to the port of Antwerp also extends further towards the downstream (Figure 6.44), which is closer to the observations. It is situated at about 50-110 km from the mouth originating from tidal asymmetry (Baeyens et al., 1998; Fettweis et al., 1998; Herman & Heip, 1999).

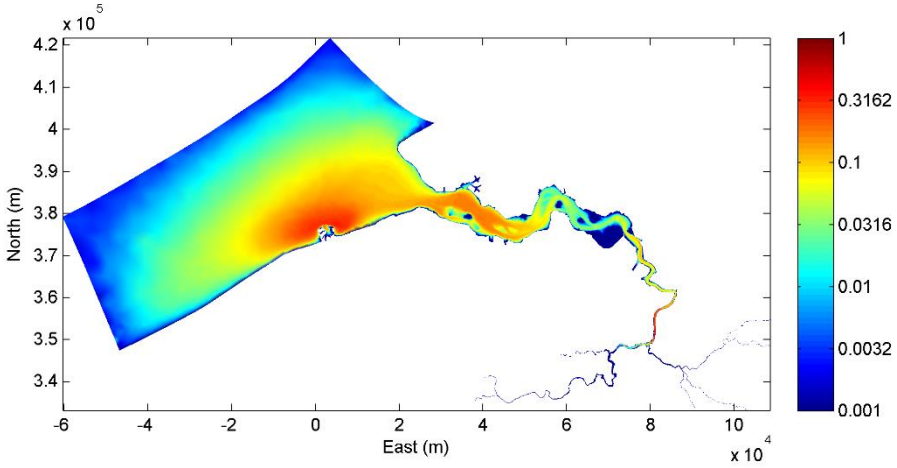

Figure 6.41. Suspended sediments concentration (g/L) from ConR case averaged over one tidal cycle.

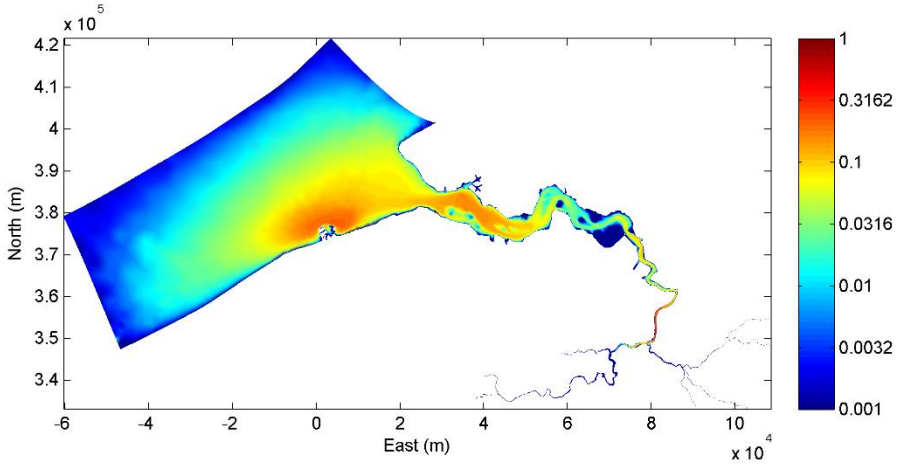

Figure 6.42. Suspended sediments concentration (g/L) from DepR case averaged over one tidal cycle.

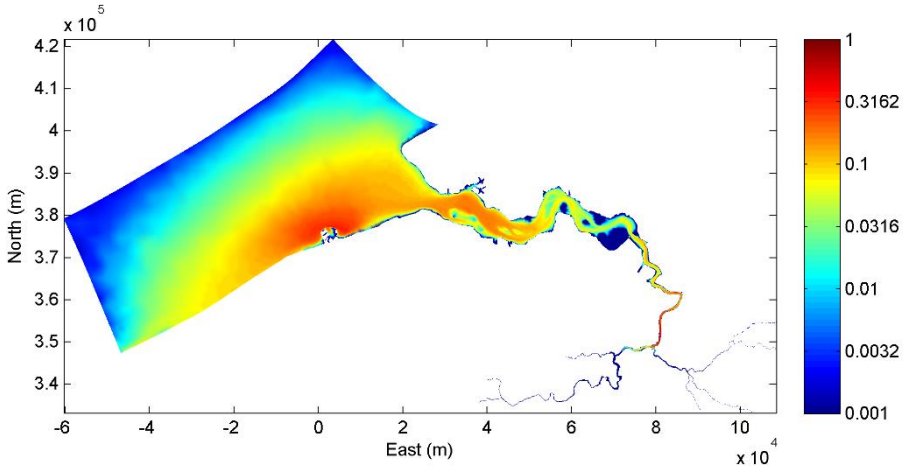

Figure 6.43. Suspended sediments concentration (g/L) from DepCsR case averaged over one tidal cycle.

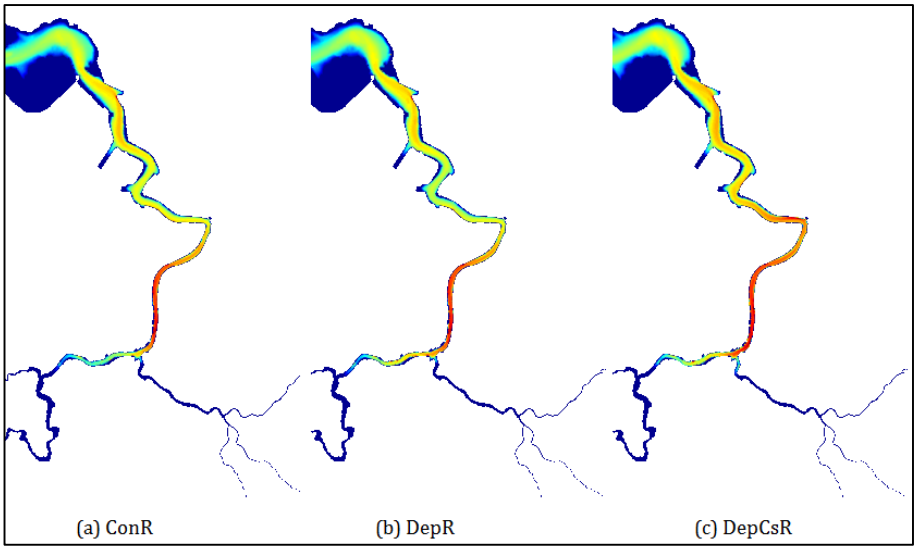

Figure 6.44. Comparison of Suspended sediments concentration (g/L) averaged over one tidal cycle (from Figures 6.41 – 6.43) in the upstream around the Port of Antwerp.

Differences of averaged suspension concentration over the same tidal cycle between DepR and the ConR cases are shown in Figure 6.45, and the differences between DepCsR and the ConR cases in Figure 6.46. Positive

values mean higher concentration compared to the ConR case and vice versa. Figure 6.45 shows that the new roughness law without considering the concentration effects used in the DepR case predicts less suspended sediment around the Port of Zeebrugge than using constant roughness in the ConR case. There are also underestimations in the navigation channels near the river mouth compared with ConR case while the concentration level in the turbidity maximum area close to Antwerp is higher. The better model performance can be clearly seen in the DepCsR case (Figure 6.46) with the new roughness law including the concentration effects, in which both the predictions in the upstream turbidity maximum zone, as mentioned earlier, and the predicted concentration levels of suspended sediment in the coastal area have been improved. As indicated in Figure 6.39, the suspended sediment is brought up from the northeast of the Port of Zeebrugge and then transported along the Belgian coast towards the southwest within a tidal cycle. The excess concentration in the coastal area, shown in figure 6.45, implies that the suspended sediments can be transported further southwest along the coast in the DepCsR case than the ConR case. This trend is confirmed by the processed SeaWiFS remote sensing images by Fettweis *et al.* (2007), which shows the seasonal averages (winter situation, similar as in figures 6.41 – 6.46) of vertically corrected SPM concentration in the southern North Sea.

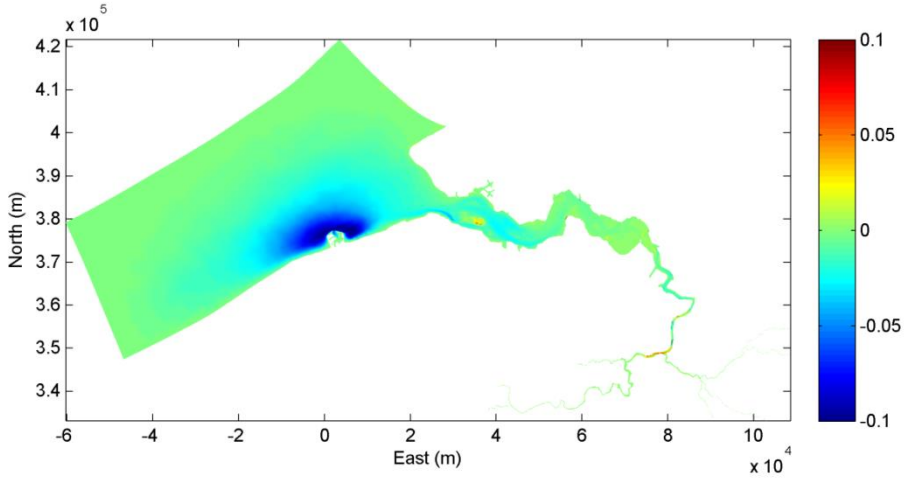

Figure 6.45. Differences of suspension concentration (g/L) predicted in the DepR case compared with the ConR case over the same tidal cycle on 4th December 2009.

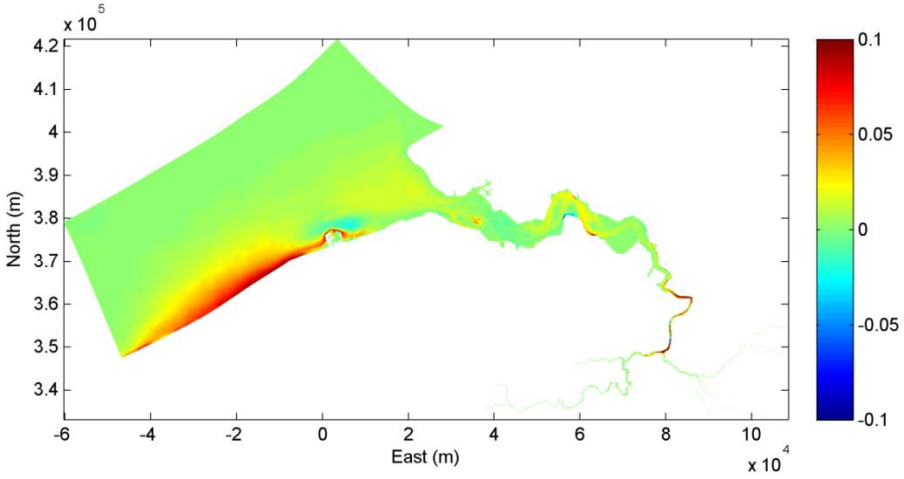

Figure 6.46. Differences of suspension concentration (g/L) predicted in the DepCsR case compared with the ConR case over the same tidal cycle on 4th December 2009.

6.4.4. Analysis of sediment fluxes in the Scheldt

In addition to the suspension concentration, the sediment flux has also been examined. Again, the results from all three cases were analysed and compared.

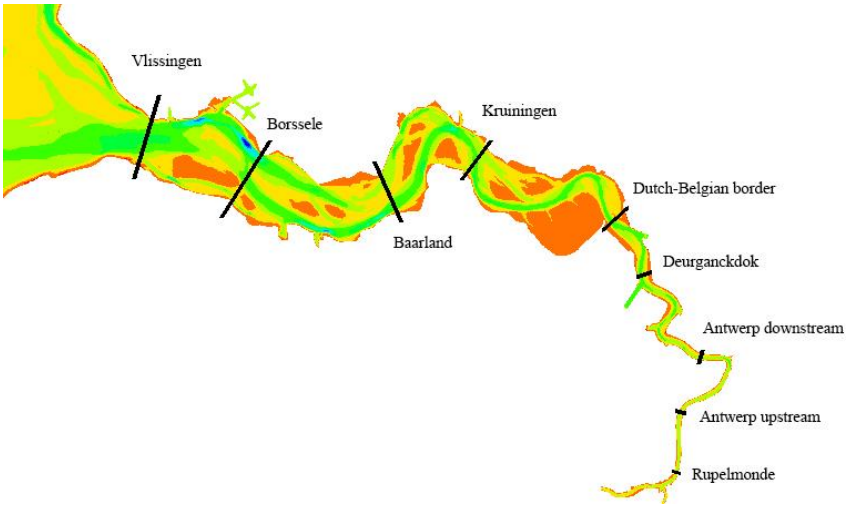

Figure 6.47. Transects defined in the model for calculating sediment fluxes.

For a better understanding of the sediment circulation in the Scheldt, the entire research domain has been divided by nine transects (Figure 6.47). The accumulated sediment fluxes were calculated and plotted in figures 6.48 – 6.56. The positive value means the sediment flux has a direction normal to the transect pointing to the downstream (seaward) while the negative value means the opposite direction (landward).

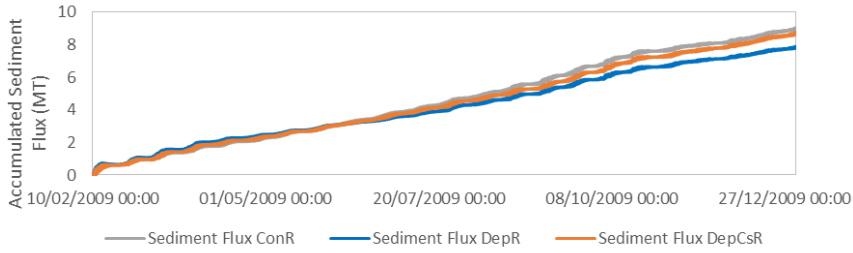

Figure 6.48. Comparison of accumulated sediment flux in one year at Vlissingen.

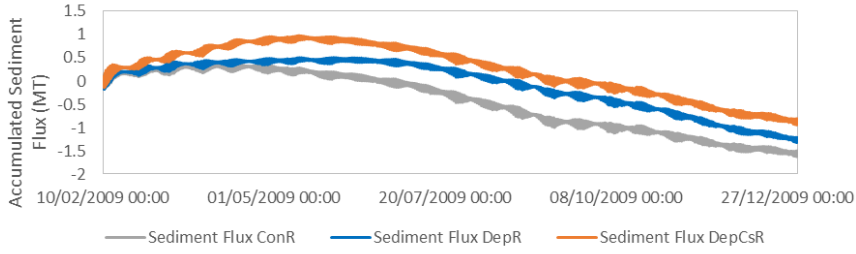

Figure 6.49. Comparison of accumulated sediment flux in one year at Borssele.

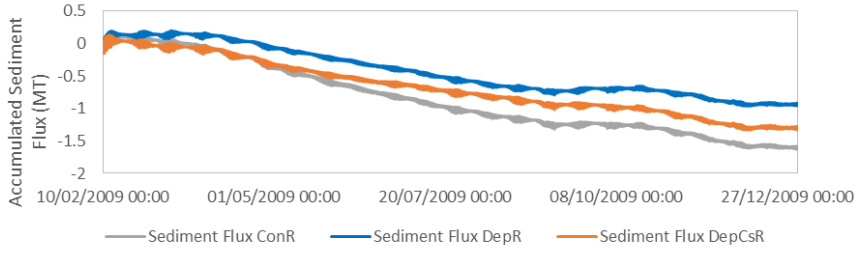

Figure 6.50. Comparison of accumulated sediment flux in one year at Baarland.

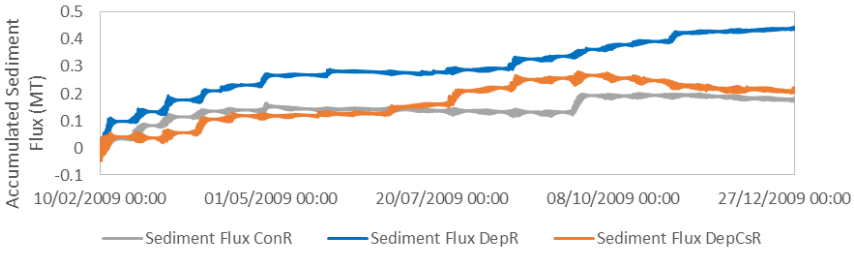

Figure 6.51. Comparison of accumulated sediment flux in one year at Kruiningen.

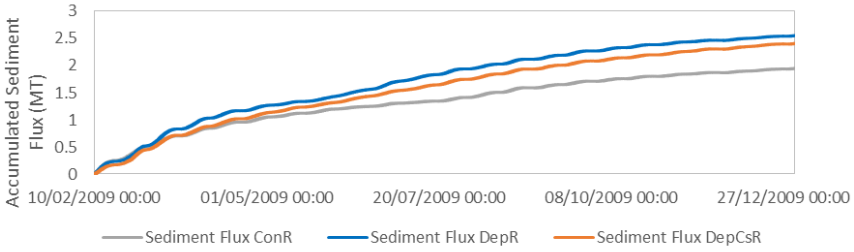

Figure 6.52. Comparison of accumulated sediment flux in one year at Dutch-Belgian boarder.

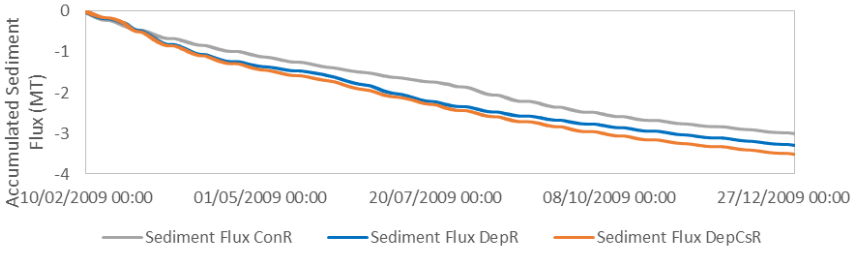

Figure 6.53. Comparison of accumulated sediment flux in one year at Deurganckdok.

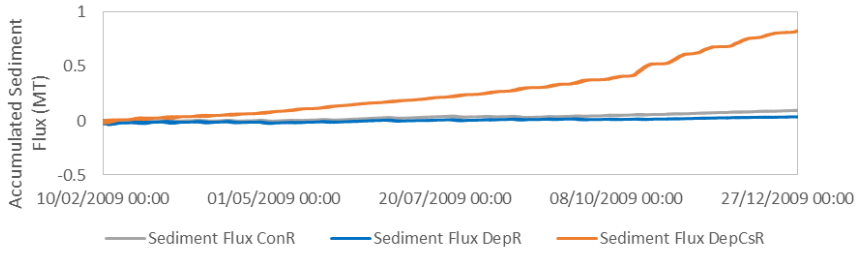

Figure 6.54. Comparison of accumulated sediment flux in one year downstream of Antwerp City

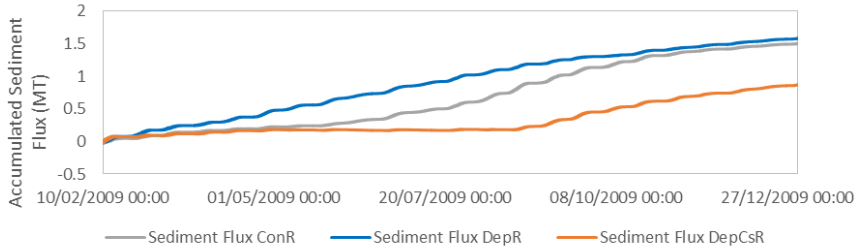

Figure 6.55. Comparison of accumulated sediment flux in one year upstream of Antwerp City

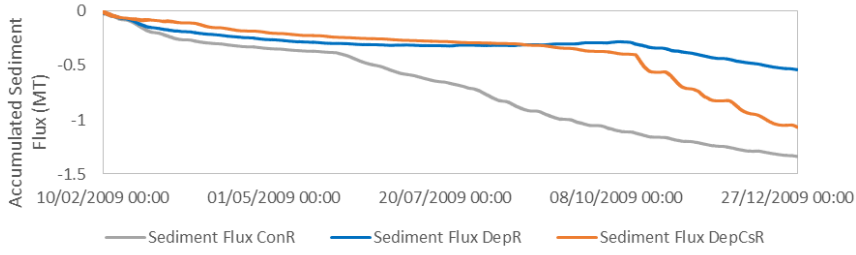

Figure 6.56. Comparison of accumulated sediment flux in one year at Rupelmonde.

The initial (model warming-up) period (the first 40 days of the year) for each case is eliminated in order to avoid its influence. All the sediment fluxes start from zero at 00:00:00, 10th Feb 2009 and accumulate over time. The results explain how the turbidity maximum areas are formed in the River Scheldt. The turbidity maximum near the river mouth is caused

by the sediment fluxes coming from two opposite directions – suspended sediment being transported upstream at Borssele and transported downstream at Kruiningen, finally they converge at the locations in between, shifting back and forth due to the flood or ebb tide. Another turbidity maximum is formed in the same way. The sediment flux is towards the upstream at Deurganckdok, joining the sediment flux in the opposite direction from upstream Antwerp. The reason behind the sediment flux coming from different directions is the tidal asymmetry – the non-linear processes governed by the basin morphology when astronomic tidal waves propagate into the estuary (Bolle *et al.*, 2010). For this particular case, the horizontal tide is considered as asymmetric since the differences can be easily found between the ebb and flood velocities from the results. Figures 6.57 and 6.58 show the velocity components at node 28492 (in the downstream of Deurganckdok) from 6000 to 7000 hours of the simulation. The velocity components are asymmetric in both directions and the magnitude of the velocity towards upstream is almost 30% - 40% larger than the opposite direction. It also reveals that the sediment flux is already in the upstream direction before reaching the transect at Deurganckdok.

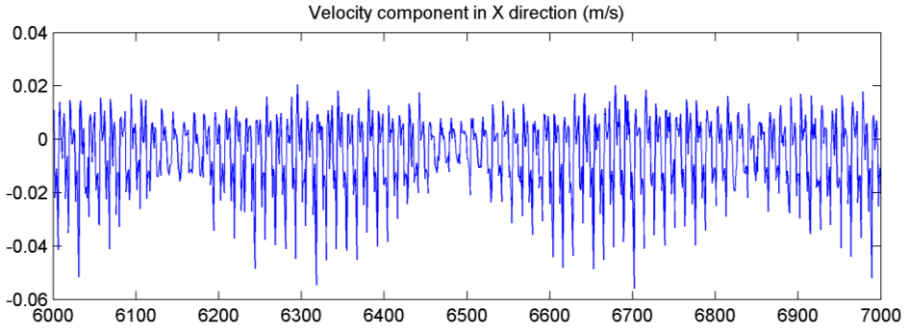

Figure 6.57. Velocity component U in X direction at node 28492 (location is indicated in Figure 6.15) from 6000 to 7000 hours

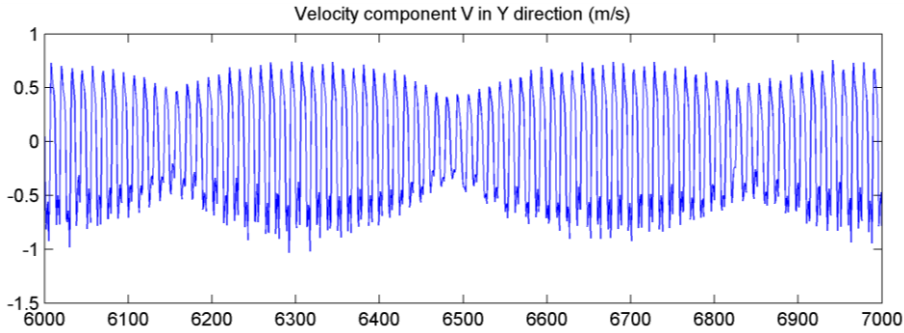

Figure 6.58. Velocity component V in Y direction at node 28492 (location is indicated in Figure 6.15) from 6000 to 7000 hours.

Comparing the calculated sediment fluxes in all three cases at each transect does not give clear insight on how the new bottom friction law affects the sediment flux at a particular place. It is also determined by the bottom topography, flow conditions and many other factors. However, one thing is sure, that the concentration effects cannot only alter the distribution of suspended sediments in the estuary, but also have an influence on the sediment flux in the entire domain and it tends to be more important in the upstream.

6.4.5. Wave effects on the sediment mass balance

The mass balance for the Scheldt estuary is one of the enigmas that still is not resolved. A few attempts have been carried out in the 1990s, which suggest a small yearly import of mud from the sea into the Western Scheldt where it deposits (Wartel & van Eck, 2000). The most recent data and simulations suggest that the net inflow of fine-grained sediment during flood is of the same order of magnitude as the outflow during ebb (order 400,000 Tons/day; van Kessel & Vanlede, 2010). These results are confirmed by the present model. However, the residual transport over a tidal cycle is the difference between nearly equally large numbers and very sensitive to proper model settings. Estimations based on the change in bottom topography over many years and a known inflow from the continental side suggest confirmation of the earlier trend of net import of mud over the transect Vlissingen-Breskens, increasing in recent years, attributed to the subsequent deepenings (Dam & Cleveringa, 2013). However, the mud transport model set up by Deltares, without morphodynamics, predicted a small net export for the year 2006 (van

Kessel & Vanlede, 2010). The present model, the first one accounting simultaneously for both sand and mud transport and including morphodynamics, even predicts a net export roughly five times larger over the year 2009.

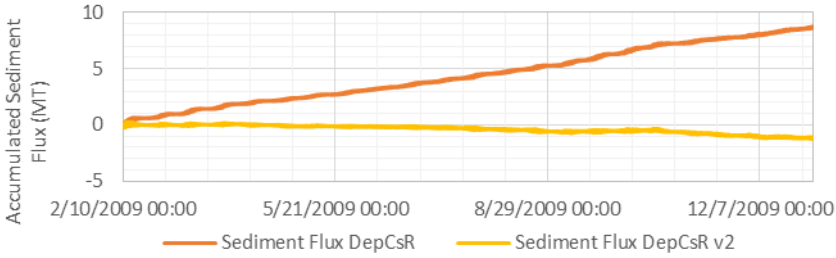

Figure 6.59. Comparison of accumulated sediment flux with and without wave influence in one year at Vlissingen. The "v2" result is obtained by an assumed augmentation of the SPM concentration during floods with an average 12% caused by wave-induced resuspension (see text for details).

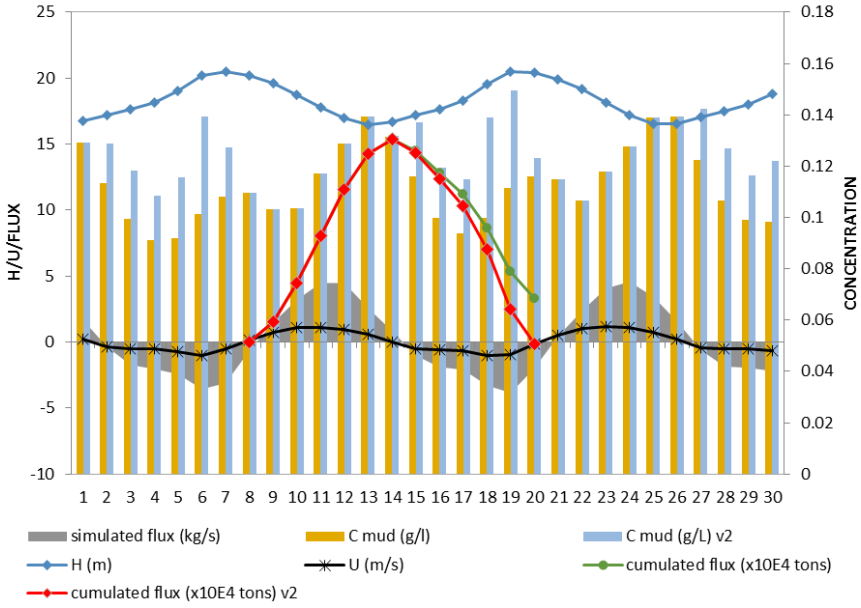

Figure 6.60. Hourly computed values of depth-averaged SPM concentrations and mud fluxes and effect of artificial increase of SPM concentrations during the flood phase (indicated "v2" in Figure 6.58). Computed values of water levels and depth-averaged flow velocity are

also shown. Results for a tidal cycle (from 2009-12-30, 19:00hr to 2010-01-01, 00:00hr) in a point roughly halfway in the cross section between Vlissingen and Breskens at the mouth of the estuary. Cumulated fluxes are for the full cross-section.

In order to trace the likely reason for the discrepancy, despite the overall good predictions of the model, a sensitivity analysis has been carried out for an arbitrary tidal cycle near the end of the simulation. The simulated sediment flux (positive sign means exporting seaward, and vice versa) passing through the Vlissingen-Breskens transect at the end of December 2009 is shown in Figured 6.59 and 6.60. For this particular cycle, the net export of mud is found to reach roughly 30,000 tons/cycle. The export is simply explained by the fact that during flood the flow velocity is lower than at ebb, while the flood SPM concentration varies between 90 and 120 mg/l, whereas the ebb SPM varies between 100 and 140 mg/l. These values lie in the range of the few scattered data available, giving an average of 130 mg/l (van Kessel *et al*, 2011). With only a slight increase of on average 20% in the mud SPM during flood, the residual flux over one tide reverses sign. Unfortunately, there are no systematic SPM measurements over a tidal cycle available for this location at this moment. Nevertheless, it can easily be imagined that the SPM values at the seaside are underestimated in the model since resuspension by waves has not been modelled.

In Figure 6.60, the total SPM with "wave-induced" resuspension is approximated heuristically (using a weak power law function), allowing the SPM to increase gradually during the flood tidal phase when the flow moves landward. This time, the cumulated sediment flux (1.6 Kt/cycle or 1.17 Mt/yr) reverses the residual flux direction to import from the seaside, and its value is also much closer to the one found in the latest study for the Flemish-Dutch Scheldt Commission (VNSC: Vlaams-Nederlandse Scheldecommissie) (Cleveringa, 2013) where the conclusion is a net import of the order 0.75 Mm^3/yr, which corresponds to 0.9-1.2 Mt/yr (depending on the assumed mud density). To obtain the same net flux over the entire year 2009, the suspended concentration at sea needs an average increase of only 12% (Figure 6.59). These computations show the high sensitivity to assumptions and calculation procedures.

The whole Scheldt estuary can be divided into different "cells", in which the residual sediment transport mostly circulates within the cells. In this

sense, the sensitivity of the sediment flux at the transect Vlissingen-Breskens is also related to this particular place, which is located at the boundary of one "cell". Here, the residual flow velocity is usually low and can be easily affected by other factors, e.g. waves.

Notice that in other two transects upstream of Vlissingen-Breskens, the simulated sediment fluxes (Figures 6.49 and 6.50) are much closer to the values found in the VNSC study (Cleveringa, 2013) at the similar cross-sections in terms of both direction and magnitude (0.8-1.1 Mt/yr at both Borssele and Baarland, import from the seaside), which suggests that this kind of impact on the net sediment flux is specifically important in the coastal areas up to the river mouth and becomes very limited in the upstream. This strengthens the assumption about the role of the wave-induced sediment flux.

However, the simulated results on sediment fluxes may not necessarily correspond to reality. The reason for caution is the fact that the transport in the present 2DH model is governed by the depth-averaged velocity. For instance, in the present 2DH model the bedload transport shows the same accumulated flux pattern as the suspended load, which is not as expected. In reality, the transport at the surface may go in the opposite direction relative to the near-bottom and bedload transport as a result of freshwater-seawater interaction and inertia. Therefore, it is strongly recommended to set up a 3D model where surface and bed currents can be computed individually, before drawing conclusions on actual residual fluxes, their direction and magnitude.

Chapter 7

CONCLUSION & RECOMMENDATIONS

7.1. Conclusion and recommendation on the 1DV model

In order to investigate the turbulence modulation due to particles in sediment-laden flow, a 1DV model has been developed in which the Navier-Stokes equations, k-ε model and advection-diffusion equation are coupled and solved numerically. For better describing the fluid-particle interactions, relevant experimental work is studied as well as the basics of two-phase flow theory. The extra terms were derived from two-fluid two-phase flow governing equations and have been tested and validated with studies of Muste *et al.* (2005) and Cellino (1998).

It comes to conclusions that the extra terms in the modified k-ε model (v2) are able to improve the turbulent eddy viscosity profile especially in the upper water column. In both simulations for Muste's NS2 and Cellino's Q55S015_Sand_I experiments, the extra terms are capable to give better agreement with the measured data in terms of eddy viscosity and streamwise velocity. It appears that the extra terms due to the presence of the particle phase have most influence to the turbulence.

After many numerical tests with the 1DV model, it is reasonable to make a conclusion that the advection-diffusion equation used in the traditional sediment transport model is not sufficient for complex situations where the reference concentration at the bottom is usually unknown. It is possible to apply the two-phase approach here for improving the prediction of suspended sediment movements.

It is also worth mentioning that the major limitation of the modified k-ε model (v2) is that it cannot deal with the low-Reynolds effects near the bottom at this moment. However, the preliminary tests show that the extra terms can be added into the low-Reynolds k-ε model (Toorman, in preparation) and show improvements in the prediction of turbulence eddy velocity particularly in the upper water column. Currently the low-Reynolds k-ε model proposed by Toorman is under test and the future step is to combine it with the extra terms to improve the overall performance of the k-ε model turbulence model.

For the future research, the first improvement can be done by using the particle force balance equation to solve the slip velocity. Then the next step is to include the low-Reynolds effects, implement the new two-layer low-Reynolds turbulence model. Later, in order to increase the prediction accuracy, it is necessary to include the particle collision, which turns out to be a major mechanism for keeping particles in suspension in the near-bottom layer. After that, it is planned to extend the model to 2DV unsteady non-uniform flow to study e.g. wave-induced sediment transport, which is believed to be able to account for more mechanisms happening in the near-bottom layer.

7.2. Conclusion and recommendation on the Scheldt model

The KU Leuven-Telemac Western Scheldt model has been established and used as the first high-resolution mixed-sediment transport model to study the transport patterns and sediment flux in the Scheldt estuary. A new physics based friction law, based on a generalized mixing-length theory (GML), has been incorporated in this model. A new deposition criterion based on a suspension capacity condition has been implemented as well. The critical shear stress for deposition is no longer taken constant, but related to the available energy for suspending particles. Its instantaneous value is obtained from the local suspension capacity condition. It is no longer a pure material parameter but a function of sediment concentration, settling velocity, water depth and bed shear stress. The model deals with two types of sediments, sand and mud, and the bed composition of the entire domain is defined non-uniformly based on survey data. A unified way of calculating erosion/deposition was used in this study. The model has been calibrated against measurements at different locations and is able to reproduce a realistic flow field in general. Due to the complexity of the research domain, more data are required for further validation and subsequent improvements.

Numerical simulations have been carried out to compare and analyse the model results obtained for different friction laws. Three bottom friction laws have been implemented and applied to the same test case (identical model set-up and initial conditions), partially calibrated and validated with field data from 2009. The first model applies a constant roughness coefficient, which at present is the most current practice in engineering studies. The second model employed a depth-dependent formulation,

obtained by integration of the standard logarithmic velocity profile (Prandtl-von Karman). The third model is an extension of the second, including viscous stresses, effective bed roughness (dissipation by separation vortex generation) and additional dissipation mechanisms that become important in high-concentrations as found above the bed (*i.e.* inter-particle friction and collisions, and particle wake turbulence) resulting in a bed shear stress predictor. In each case, the computed friction has been converted into an equivalent Chézy friction coefficient. The comparison of all the three cases shows that the third model has better predictions in terms of distributions of suspended sediments in the Scheldt estuary, especially in the turbidity maximum zones in the upstream and the general transport patterns near the Belgian coast. It also demonstrate that the subgrid scale effects, such as additional viscous stresses and dissipation mechanisms induced by sediment particles, etc., in the high concentrated layer are important and indeed have big influence to the large scale domain.

Since the new bed shear stress closure is constructed as the superposition of the turbulent and the laminar part, it allows the simulation of both transient conditions and the transition during drying or wetting of tidal flats. Nikuradse's empirical roughness model is implemented allowing accounting for both hydraulic smooth and hydraulic rough conditions. The latter is important since the tidal induced oscillatory flow may fulfil either condition, depending on the phase of the tidal cycle.

An additional advantage of the new friction law is the fact that its value automatically tends to infinity when the water depth goes to zero. Therefore, the drying and flooding of intertidal flats can now be modelled without specifying an inundation threshold. This proved to work very well for the many intertidal areas in the Western Scheldt. The benefit is that intertidal morphodynamics can now be modelled at great detail for the first time. Erosion and deposition in these areas can now be estimated with much higher accuracy, as well as their contribution to the overall net fluxes. Besides, the new friction law can adapt to different topographies due to its physics based characteristics and provides the hydrodynamic model with better performance in terms of water levels and velocity field without tuning of the bottom friction coefficient.

The sensitivity of the model to the bed friction model has been evaluated by intercomparison of the computed sediment budget at the mouth of the estuary. This has always remained a point of discussion, since previous model results did not match with estimates based on field data, even opposite directions have been claimed. Near-bottom sediment transport,

which is hard to model and which escapes from most measuring techniques, most likely plays an important role in explaining the differences. The comparison of the three friction models indeed results in different evolutions of the net sediment budget calculated at different transects across the entire estuary. These differences are also reflected in significant differences in local erosion-sedimentation patterns.

The asymmetrical tide is also reproduced in the model and could be interpreted as the main reason of the occurrence of the turbidity maximum areas in the Scheldt. The model captures the sediment fluxes from two different directions converging in the upstream and downstream, resulting in the accumulation of suspended sediment in those areas.

Nevertheless, the fact that the flow at the surface may be in opposite direction than the near-bottom current, is expected to have a great impact on the actual residual fluxes of both suspended load and bedload. Therefore, it is necessary to develop a 3D version of the model, before any conclusions can be drawn on direction and magnitude of the fluxes. A 3D version of the present model is currently under development.

To understand how to achieve this, the 1DV model research enters the picture. The currently used new friction law is based on the assumption of a logarithmic velocity profile and a Rousian concentration profile, which are no longer valid when high-suspended sediment concentrations occur and the velocity profile deviates. In the 3D version of the friction law, the bed shear stress needs to be computed from the computed velocity profile above the bed, which requires the model adaptations tested in the 1DV model.

For the future research, the model will be extended to a full 3D model (3D hydrodynamics coupled with 3D sediment transport). The wave effects will be included because it is an important influence factor for predicting the sediment balance in the Scheldt estuary. Besides, a flocculation model is also important for the cohesive sediment transport and will be incorporated into the model. The model is expected to yield even better results when the dynamics of flocculation is incorporated, following the computational efficient methodology proposed by Lee *et al.* (2014). These two major aspects are believed to improve the model and make it more realistic for the complex estuary system.

In the current study, results at certain locations are found difficult to be well interpreted due to the lack of additional information, e.g. the information of dredging activities in the navigation channel and the

meteo data in the area of interest. This data can be found in relevant institutes or government departments. For the future research, this kind of data will be collected for refining the calibration and validation process.

7.3. Conclusions and recommendations on developments in the TELEMAC-2D/SISYPHE model

It has been proved by many other studies that the TELEMAC modelling system is powerful and reliable for many types of free surface flow problems. Besides the various options and flexibilities provided by TELEMAC out of the box, the source code is also highly customizable for specific research purposes. In the TELEMAC system, the modules can always be coupled, e.g. the sediment transport module SISYPHE can be coupled with hydrodynamics, the hydrodynamic model can be coupled with the waves module TOMAWAC, or even to be more complex, the hydrodynamic model coupled with sediment transport and wave models, which provides the possibility for more realistic applications.

During the model development, also some limitations have been encountered in the TELEMAC system, especially in the implementation of the new roughness law. It has been found that, in the coupled sediment-hydrodynamic model, the variables such as the velocity components passed from the hydrodynamic model to the sediment transport model are the values from the previous time step. The roughness coefficient calculated at the current time step does not correspond the real roughness at the same time step. It sometimes can cause errors or instability issues at certain locations during the drying/wetting processes. This could be improved by making a sub-iteration loop, in which the new roughness law is calculated and the velocity is updated. Nevertheless, this has to be investigated further in a future study.

Another limitation is encountered during the implementation of the new scheme for computing erosion/deposition of mixtures in the SISYPHE. The original process flow is not optimised for mixed-sediment transport. It only provides one variable for storing the deposition flux. Therefore, that variable is used either for non-cohesive or cohesive sediment at once and cannot account for the combination of both. This has been improved by defining an additional global variable for deposition flux and is used together with the original variable.

A summary of the original contributions is presented in Appendix IV.

APPENDIX I

DERIVING GOVERNING EQUATIONS FOR TWO-PHASE/MIXTURE MODEL

The governing equations for two-phase/mixture model can be derived by performing Reynolds-averaging to the conservation equations of fluid and particle phase respectively (Toorman 2013).

Conservation of mass

In the case of non-cohesive sediments (like sand), the solids mass conservation is:

$$\frac{\partial \phi}{\partial t} + \frac{\partial (v_j \phi)}{\partial x_j} = 0 \tag{A.1}$$

And fluid mass conservation:

$$\frac{\partial (1-\phi)}{\partial t} + \frac{\partial (u_j (1-\phi))}{\partial x_j} = 0 \tag{A.2}$$

where ϕ = the volume fraction of the particle phase, v the particle velocity, u the fluid velocity.

Conservation of momentum

The volume-averaged momentum conservation equation for the particle phase is written as:

$$\frac{\partial (\rho_p \phi v_i)}{\partial t} + \frac{\partial (\rho_p \phi v_i v_j)}{\partial x_j} = -\phi \frac{\partial p}{\partial x_i} + \rho_p \phi g \delta_{iz} + f_i + \phi \frac{\partial \sigma_{pij}}{\partial x_j} \tag{A.3}$$

or, using mass conservation equation

$$\rho_p \frac{\partial v_i}{\partial t} + \rho_p v_j \frac{\partial v_i}{\partial x_j} = -\frac{\partial p}{\partial x_i} + \rho_p g \delta_{iz} + \frac{f_i}{\phi} + \frac{\partial \sigma_{pij}}{\partial x_j} \tag{A.4}$$

For the fluid phase one can write the equivalent:

$$\frac{\partial(\rho_f(1-\phi)u_i)}{\partial t}+\frac{\partial(\rho_f(1-\phi)u_iu_j)}{\partial x_j} = -(1-\phi)\frac{\partial p}{\partial x_i}+\rho_f(1-\phi)g\delta_{iz}-f_i+(1-\phi)\frac{\partial \sigma_{fij}}{\partial x_j} \tag{A.5}$$

or, using mass conservation equation

$$\rho_f\frac{\partial u_i}{\partial t}+\rho_f u_j\frac{\partial u_i}{\partial x_j}=-\frac{\partial p}{\partial x_i}+\rho_f g\delta_{iz}-\frac{f_i}{1-\phi}+\frac{\partial \sigma_{fij}}{\partial x_j} \tag{A.6}$$

where f represents the interaction force between the two phases.

The most elegant form of equations is obtained in terms of Reynolds-averaged related fluid velocity and solids velocity (equation 3.7), related to Reynolds-averaged properties by Toorman (2008). Perform the Reynolds-averaging to equation (mass conservation of particle) and (mass conservation of fluid) and introduce the ensemble-averaged velocities then we get:

$$\frac{\partial\bar{\phi}}{\partial t}+\frac{\partial(\overline{v_j}\bar{\phi}+\overline{v_j'\phi'})}{\partial x_j}=\frac{\partial\bar{\phi}}{\partial t}+\frac{\partial((\overline{v_j}+V_{Dj})\bar{\phi})}{\partial x_j}=\frac{\partial\bar{\phi}}{\partial t}+\frac{\partial(V_j\bar{\phi})}{\partial x_j}=0 \tag{A.7}$$

$$\frac{\partial(1-\bar{\phi})}{\partial t}+\frac{\partial(\overline{u_j}(1-\bar{\phi})-\overline{u_j'\phi'})}{\partial x_j}=\frac{\partial(1-\bar{\phi})}{\partial t}+\frac{\partial(\overline{u_j}(1-\bar{\phi})+U_{Dj}\bar{\phi})}{\partial x_j} =\frac{\partial(1-\bar{\phi})}{\partial t}+\frac{\partial(U_j(1-\bar{\phi}))}{\partial x_j}=0 \tag{A.8}$$

Combining the above equations yields:

$$\frac{\partial(U_j(1-\bar{\phi})+V_j\bar{\phi})}{\partial x_j}=\frac{\partial(U_j+W_j\bar{\phi})}{\partial x_j}=0 \tag{A.9}$$

Summing up the momentum equation for each gives the suspension momentum balance:

$$\frac{\partial(\rho_p \phi v_i)}{\partial t} + \frac{\partial(\rho_p \phi v_i v_j)}{\partial x_j} + \frac{\partial(\rho_f (1-\phi) u_i)}{\partial t} + \frac{\partial(\rho_f (1-\phi) u_i u_j)}{\partial x_j} = -\frac{\partial p}{\partial x_i} + \rho g \delta_{iz} + \frac{\partial \sigma_{ij}}{\partial x_j} \tag{A.10}$$

where the suspension density is defined as $\rho = \rho_p \overline{\phi} + \rho_f (1 - \overline{\phi})$ and is the sum of the internal particle and fluid stresses and it follows that

$$\frac{\partial \sigma_{ij}}{\partial x_j} = \phi \frac{\partial \sigma_{pij}}{\partial x_j} + (1-\phi) \frac{\partial \sigma_{fij}}{\partial x_j} \tag{A.11}$$

Performing the Reynolds-averaging to the LHS of the above equation leads to:

$$\begin{aligned} LHS &= \frac{\partial(\rho_p \phi v_i)}{\partial t} + \frac{\partial(\rho_p \phi v_i v_j)}{\partial x_j} + \frac{\partial(\rho_f (1-\phi) u_i)}{\partial t} + \frac{\partial(\rho_f (1-\phi) u_i u_j)}{\partial x_j} \\ &= \frac{\partial(\rho_p \overline{\phi}\,\overline{v_i})}{\partial t} + \frac{\partial(\rho_p \overline{\phi}\,\overline{v_i}\,\overline{v_j})}{\partial x_j} + \frac{\partial(\rho_f (1-\overline{\phi})\overline{u_i})}{\partial t} + \frac{\partial(\rho_f (1-\overline{\phi})\overline{u_i}\,\overline{u_j})}{\partial x_j} \\ &+ \frac{\partial(\rho_p \overline{v_i'\phi'} - \rho_f \overline{u_i'\phi'})}{\partial t} + \frac{\partial(\rho_p \overline{\phi}\,\overline{v_i'v_j'} + \rho_f (1-\overline{\phi})\overline{u_i'u_j'})}{\partial x_j} \\ &+ \frac{\partial(\rho_p \overline{v_i'\phi'}\,\overline{v_j} - \rho_f \overline{u_i'\phi'}\,\overline{u_j})}{\partial x_j} + \frac{\partial(\rho_p \overline{v_i}\,\overline{v_j'\phi'} - \rho_f \overline{u_i}\,\overline{u_j'\phi'})}{\partial x_j} \\ &+ \frac{\partial(\rho_p \overline{\phi' v_i' v_j'} - \rho_f \overline{\phi' u_i' u_j'})}{\partial x_j} \end{aligned} \tag{A.12}$$

Notice that the last term in the equation is dropped off because the third-correlation terms are too small. Hence,

$$LHS = \rho_p(\frac{\partial(\bar{\phi}\bar{v_i})}{\partial t} + \frac{\partial(\bar{\phi}(\bar{v_i}\bar{v_j} + \overline{v_i'v_j'}))}{\partial x_j} + \frac{\partial(\overline{v_i'\phi'})}{\partial t} + \frac{\partial(\overline{v_i'\phi'}\bar{v_j} + \bar{v_i}\overline{v_j'\phi'})}{\partial x_j})$$

$$+\rho_f(\frac{\partial((1-\bar{\phi})\bar{u_i})}{\partial t} + \frac{\partial((1-\bar{\phi})(\bar{u_i}\bar{u_j} + \overline{u_i'u_j'}))}{\partial x_j} - \frac{\partial(\overline{u_i'\phi'})}{\partial t} - \frac{\partial(\overline{u_i'\phi'}\bar{u_j} + \bar{u_i}\overline{u_j'\phi'})}{\partial x_j})$$

$$= \rho_p(\frac{\partial(\bar{\phi}\bar{v_i})}{\partial t} + \frac{\partial(\bar{\phi}(\bar{v_i}\bar{v_j}))}{\partial x_j}) + \rho_f(\frac{\partial((1-\bar{\phi})\bar{u_i})}{\partial t} + \frac{\partial((1-\bar{\phi})(\bar{u_i}\bar{u_j}))}{\partial x_j})$$

$$+\frac{\partial}{\partial x_j}(\rho_p\bar{\phi}(\overline{v_i'v_j'}) + \rho_f(1-\bar{\phi})(\overline{u_i'u_j'}))$$

$$+\rho_p(\frac{\partial(\overline{v_i'\phi'})}{\partial t} + \frac{\partial(\overline{v_i'\phi'}\bar{v_j} + \bar{v_i}\overline{v_j'\phi'})}{\partial x_j}) - \rho_f(\frac{\partial(\overline{u_i'\phi'})}{\partial t} + \frac{\partial(\overline{u_i'\phi'}\bar{u_j} + \bar{u_i}\overline{u_j'\phi'})}{\partial x_j})$$

$$= \rho_p(\frac{\partial(\bar{\phi}V_i)}{\partial t} + \frac{\partial(\bar{\phi}(V_i\bar{v_j}))}{\partial x_j}) + \rho_f(\frac{\partial((1-\bar{\phi})U_i)}{\partial t} + \frac{\partial((1-\bar{\phi})(U_i\bar{u_j}))}{\partial x_j})$$

$$+\frac{\partial}{\partial x_j}(\rho_p\bar{\phi}(\overline{v_i'v_j'}) + \rho_f(1-\bar{\phi})(\overline{u_i'u_j'}))$$

$$+\rho_p(\frac{\partial(\bar{v_i}(V_i - \bar{v_j})\bar{\phi})}{\partial x_j}) + \rho_f(\frac{\partial(\bar{u_i}(U_i - \bar{u_j})(1-\bar{\phi}))}{\partial x_j})$$

$$=\rho_p(\frac{\partial(\bar{\phi}V_i)}{\partial t} + \frac{\partial(\bar{\phi}(V_i\bar{v_j} + \bar{v_i}(V_j - \bar{v_j})))}{\partial x_j})$$

$$+\rho_f(\frac{\partial((1-\bar{\phi})U_i)}{\partial t} + \frac{\partial((1-\bar{\phi})(U_i\bar{u_j} + \bar{u_i}(U_j - \bar{u_j})))}{\partial x_j})$$

$$+\frac{\partial}{\partial x_j}(\rho_p\bar{\phi}(\overline{v_i'v_j'}) + \rho_f(1-\bar{\phi})(\overline{u_i'u_j'}))$$

$$=\rho_p(\frac{\partial(\bar{\phi}V_i)}{\partial t} + \frac{\partial(\bar{\phi}(\bar{v_j}V_{Di} + V_j\bar{v_i}))}{\partial x_j})$$

$$+\rho_f(\frac{\partial((1-\bar{\phi})U_i)}{\partial t} + \frac{\partial((1-\bar{\phi})(\bar{u_j}U_{Di} + U_j\bar{u_i}))}{\partial x_j})$$

$$+\frac{\partial}{\partial x_j}(\rho_p\bar{\phi}(\overline{v_i'v_j'})+\rho_f(1-\bar{\phi})(\overline{u_i'u_j'}))$$

$$=\rho_p(\frac{\partial(\bar{\phi}V_i)}{\partial t}+\frac{\partial(\bar{\phi}(V_jV_i))}{\partial x_j})+\rho_f(\frac{\partial((1-\bar{\phi})U_i)}{\partial t}+\frac{\partial((1-\bar{\phi})(U_jU_i))}{\partial x_j})$$

$$-\frac{\partial}{\partial x_j}(\rho_p\bar{\phi}(V_{Dj}V_{Di})+\rho_f(1-\bar{\phi})(U_{Dj}U_{Di}))$$

$$+\frac{\partial}{\partial x_j}(\rho_p\bar{\phi}(\overline{v_i'v_j'})+\rho_f(1-\bar{\phi})(\overline{u_i'u_j'})) \tag{A.13}$$

Again, using mass conservation of particle and fluid respectively, and notice that

$$\rho_p(\frac{\partial(\bar{\phi}V_i)}{\partial t}+\frac{\partial(\bar{\phi}(V_jV_i))}{\partial x_j})$$

$$=\rho_p(\bar{\phi}\frac{\partial V_i}{\partial t}+\bar{\phi}V_j\frac{\partial V_i}{\partial x_j}+V_i(\frac{\partial\bar{\phi}}{\partial t}+\frac{\partial(\bar{\phi}V_j)}{\partial x_j})) \tag{A.14}$$

$$=\rho_p\bar{\phi}(\frac{\partial V_i}{\partial t}+V_j\frac{\partial V_i}{\partial x_j})$$

Similarly,

$$\rho_f(\frac{\partial((1-\bar{\phi})U_i)}{\partial t}+\frac{\partial((1-\bar{\phi})(U_jU_i))}{\partial x_j})$$

$$=\rho_f((1-\bar{\phi})\frac{\partial U_i}{\partial t}+(1-\bar{\phi})U_j\frac{\partial U_i}{\partial x_j}+U_i(\frac{\partial(1-\bar{\phi})}{\partial t}+\frac{\partial((1-\bar{\phi})U_j)}{\partial x_j})) \tag{A.15}$$

$$=\rho_f(1-\bar{\phi})(\frac{\partial U_i}{\partial t}+U_j\frac{\partial U_i}{\partial x_j})$$

the final form of LHS becomes:

$$LHS = \rho_p \bar{\phi}(\frac{\partial V_i}{\partial t} + V_j \frac{\partial V_i}{\partial x_j}) + \rho_f (1-\bar{\phi})(\frac{\partial U_i}{\partial t} + U_j \frac{\partial U_i}{\partial x_j})$$
$$- \frac{\partial}{\partial x_j}(\rho_p \bar{\phi}(V_{Dj} V_{Di}) + \rho_f (1-\bar{\phi})(U_{Dj} U_{Di})) \quad \text{(A.16)}$$
$$+ \frac{\partial}{\partial x_j}(\rho_p \bar{\phi}(\overline{v_i' v_j'}) + \rho_f (1-\bar{\phi})(\overline{u_i' u_j'}))$$

Together with the definition of ensemble-averaged slip velocity and performing Reynolds-averaging to the RHS of equation momentum conservation suspension and we have:

$$\rho(\frac{\partial U_i}{\partial t} + U_j \frac{\partial U_i}{\partial x_j}) = -\frac{\partial \overline{p}}{\partial x_i} + \rho g \delta_{iz} + \frac{\partial \overline{\sigma_{ij}}}{\partial x_j} + \frac{\partial(\sigma_{Tij} + \sigma_{Dij})}{\partial x_j}$$
$$- \rho_p \bar{\phi}(\frac{\partial W_i}{\partial t} + U_j \frac{\partial W_i}{\partial x_j} + W_j \frac{\partial (U_i + W_i)}{\partial x_j}) \quad \text{(A.17)}$$

APPENDIX II

DERIVING *k-ε* TURBULENCE MODEL FOR TWO-PHASE/MIXTURE MODEL

The procedures of Wilcox (1998) are followed to derive the Reynolds-Stress equation. That is, the conservation of momentum equation is multiplied by a fluctuating property and time average the product. Let $\mathcal{N}(u_i)$ be the conservation of momentum operator of fluid, viz.,

$$\mathcal{N}(u_i) = \rho_f \frac{\partial u_i}{\partial t} + \rho_f u_k \frac{\partial u_i}{\partial x_k} + \frac{\partial p}{\partial x_i} - \rho_f g \delta_{iz} + \omega_i - \mu \frac{\partial^2 u_i}{\partial x_k^2} \tag{B.1}$$

with

$$\omega_i = \frac{f_i}{1-\phi} \tag{B.2}$$

and f_i being the actual interaction force between two phases. Thus, the conservation of momentum equation can be written as:

$$\mathcal{N}(u_i) = 0 \tag{B.3}$$

Then the following time average can be formed:

$$\overline{u_i' \mathcal{N}(u_j) + u_j' \mathcal{N}(u_i)} = 0 \tag{B.4}$$

First, we consider the **unsteady term**:

$$
\begin{aligned}
&\overline{u_i'(\rho_f \frac{\partial u_j}{\partial t}) + u_j'(\rho_f \frac{\partial u_i}{\partial t})} \\
&= \overline{\rho_f u_i'(\frac{\partial \overline{u_j}}{\partial t} + \frac{\partial u_j'}{\partial t})} + \overline{\rho_f u_j'(\frac{\partial \overline{u_i}}{\partial t} + \frac{\partial u_i'}{\partial t})} \\
&= \overline{\rho_f u_i' \frac{\partial \overline{u_j}}{\partial t}} + \overline{\rho_f u_i' \frac{\partial u_j'}{\partial t}} + \overline{\rho_f u_j' \frac{\partial \overline{u_i}}{\partial t}} + \overline{\rho_f u_j' \frac{\partial u_i'}{\partial t}} \\
&= \overline{\rho_f u_i' \frac{\partial u_j'}{\partial t}} + \overline{\rho_f u_j' \frac{\partial u_i'}{\partial t}} \\
&= \overline{\frac{\partial(\rho_f u_i' u_j')}{\partial t}} \\
&= -\frac{\partial \tau_{ij}}{\partial t}
\end{aligned}
\tag{B.5}
$$

Turning to the **convective term**, gives:

$$
\begin{aligned}
&\overline{\rho_f u_i' u_k \frac{\partial u_j}{\partial x_k} + \rho_f u_j' u_k \frac{\partial u_i}{\partial x_k}} \\
&= \overline{\rho_f u_i'(\overline{u_k} + u_k')(\frac{\partial \overline{u_j}}{\partial x_k} + \frac{\partial u_j'}{\partial x_k})} + \overline{\rho_f u_j'(\overline{u_k} + u_k')(\frac{\partial \overline{u_i}}{\partial x_k} + \frac{\partial u_i'}{\partial x_k})} \\
&= \overline{\rho_f u_i' \overline{u_k} \frac{\partial u_j'}{\partial x_k}} + \overline{\rho_f u_i' u_k' (\frac{\partial \overline{u_j}}{\partial x_k} + \frac{\partial u_j'}{\partial x_k})} + \overline{\rho_f u_j' \overline{u_k} \frac{\partial u_i'}{\partial x_k}} + \overline{\rho_f u_j' u_k' (\frac{\partial \overline{u_i}}{\partial x_k} + \frac{\partial u_i'}{\partial x_k})} \\
&= \overline{u_k} \overline{\frac{\partial(\rho_f u_i' u_j')}{\partial x_k}} + \frac{\partial \overline{u_j}}{\partial x_k} \overline{\rho_f u_i' u_k'} + \frac{\partial \overline{u_i}}{\partial x_k} \overline{\rho_f u_j' u_k'} + \overline{\rho_f u_k' \frac{\partial(u_i' u_j')}{\partial x_k}} \\
&= -\overline{u_k} \frac{\partial \tau_{ij}}{\partial x_k} - \tau_{ik} \frac{\partial \overline{u_j}}{\partial x_k} - \tau_{jk} \frac{\partial \overline{u_i}}{\partial x_k} + \frac{\partial}{\partial x_k}(\overline{\rho_f u_i' u_j' u_k'}) - \overline{\rho_f u_i' u_j' \frac{\partial u_k'}{\partial x_k}}
\end{aligned}
\tag{B.6}
$$

Notice that in equation (B.6), the last term on the RHS cannot be eliminated due to the existence of two phases in the system. In the mass conservation equation of fluid, the divergence of velocity is not equal to zero. This is different from the standard single-phase model.

Then the **pressure gradient term** is as follows:

$$\begin{aligned}\overline{u_i'\frac{\partial p}{\partial x_j}+u_j'\frac{\partial p}{\partial x_i}} &= \overline{u_i'\frac{\partial(\overline{p}+p')}{\partial x_j}}+\overline{u_j'\frac{\partial(\overline{p}+p')}{\partial x_i}} \\ &= \overline{u_i'\frac{\partial p'}{\partial x_j}+u_j'\frac{\partial p'}{\partial x_i}}\end{aligned} \tag{B.7}$$

And the **viscous term** yields:

$$\begin{aligned}&\overline{\mu(u_i'\frac{\partial^2 u_j}{\partial x_k^2}+u_j'\frac{\partial^2 u_i}{\partial x_k^2})} = \overline{\mu u_i'\frac{\partial^2(\overline{u_j}+u_j')}{\partial x_k^2}}+\overline{\mu u_j'\frac{\partial^2(\overline{u_i}+u_i')}{\partial x_k^2}} \\ &= \overline{\mu u_i'\frac{\partial^2 u_j'}{\partial x_k^2}}+\overline{\mu u_j'\frac{\partial^2 u_i'}{\partial x_k^2}} \\ &= \overline{\mu\frac{\partial}{\partial x_k}(u_i'\frac{\partial u_j'}{\partial x_k})}+\overline{\mu\frac{\partial}{\partial x_k}(u_j'\frac{\partial u_i'}{\partial x_k})}-\overline{2\mu\frac{\partial u_i'}{\partial x_k}\frac{\partial u_j'}{\partial x_k}} \\ &= \overline{\mu\frac{\partial(u_i'u_j')}{\partial x_k^2}}-\overline{2\mu\frac{\partial u_i'}{\partial x_k}\frac{\partial u_j'}{\partial x_k}} \\ &= -\nu\frac{\partial^2\tau_{ij}}{\partial x_k^2}-\overline{2\mu\frac{\partial u_i'}{\partial x_k}\frac{\partial u_j'}{\partial x_k}}\end{aligned} \tag{B.8}$$

Because the gravity term disappears after time averaging, the last one is the **interaction term**:

$$\begin{aligned}\overline{u_i'\omega_j+u_j'\omega_i} &= \overline{u_i'(\overline{\omega_j}+\omega_j')}+\overline{u_j'(\overline{\omega_i}+\omega_i')} \\ &= \overline{u_i'\omega_j'}+\overline{u_j'\omega_i'}\end{aligned} \tag{B.9}$$

where ω is not the original interaction force between two phases but the "force intensity" since it is averaged over the volume fraction of fluid as it is defined before.

Collecting terms and we arrive at the equation for the Reynolds stress tensor.

$$\frac{\partial \tau_{ij}}{\partial t} + \overline{u}_k \frac{\partial \tau_{ij}}{\partial x_k}$$
$$= -\tau_{ik} \frac{\partial \overline{u_j}}{\partial x_k} - \tau_{jk} \frac{\partial \overline{u_i}}{\partial x_k} + \overline{2\mu \frac{\partial u_i'}{\partial x_k} \frac{\partial u_j'}{\partial x_k}} + \overline{u_i' \frac{\partial p'}{\partial x_j} + u_j' \frac{\partial p'}{\partial x_i}} \tag{B.10}$$
$$+ \frac{\partial}{\partial x_k} (\nu \frac{\partial \tau_{ij}}{\partial x_k} + \overline{\rho_f u_i' u_j' u_k'}) - \overline{\rho_f u_i' u_j' \frac{\partial u_k'}{\partial x_k}} + \overline{u_i' \omega_j'} + \overline{u_j' \omega_i'}$$

With a little rearrangement of terms, we can cast the Reynolds-stress equation in the form which is similar to the standard Reynolds-stress equation, viz.,

$$\frac{\partial \tau_{ij}}{\partial t} + \overline{u}_k \frac{\partial \tau_{ij}}{\partial x_k} = -\tau_{ik} \frac{\partial \overline{u_j}}{\partial x_k} - \tau_{jk} \frac{\partial \overline{u_i}}{\partial x_k} + \epsilon_{ij} - \Pi_{ij}$$
$$+ \frac{\partial}{\partial x_k} (\nu \frac{\partial \tau_{ij}}{\partial x_k} + C_{ijk}) - \overline{\rho_f u_i' u_j' \frac{\partial u_k'}{\partial x_k}} + \overline{u_i' \omega_j'} + \overline{u_j' \omega_i'} \tag{B.11}$$

where

$$\Pi_{ij} = \overline{p' (\frac{\partial u_i'}{\partial x_j} + \frac{\partial u_j'}{\partial x_i})} \tag{B.12}$$

$$\epsilon_{ij} = \overline{2\mu \frac{\partial u_i'}{\partial x_k} \frac{\partial u_j'}{\partial x_k}} \tag{B.13}$$

$$C_{ijk} = \overline{\rho_f u_i' u_j' u_k'} + \overline{p' u_i'} \delta_{jk} + \overline{p' u_j'} \delta_{ik} \tag{B.14}$$

Comparing equation (28) with the standard form of Reynolds-stress equation (Wilcox, 1998), we can find extra terms appearing due to the interactions between two phases and the phase exchanging within the control volume.

Taking the trace of the Reynolds stress tensor yields:

$$\tau_{ii} = -\rho_f \overline{u_i' u_i'} = -2\rho k \quad with \quad k = \frac{1}{2} \overline{u_i' u_i'} \tag{B.15}$$

Thus, the trace of the Reynolds stress tensor is proportional to the turbulence kinetic energy. Therefore, we can derive a corresponding equation for k by taking the trace of the Reynolds stress equation. After contracting equation (28) and defining the turbulence dissipation rate as

$$\epsilon = \overline{\nu \frac{\partial u_i'}{\partial x_j} \frac{\partial u_i'}{\partial x_j}} \tag{B.16}$$

The following transport equation for the turbulence kinetic energy is obtained:

$$\rho_f \frac{\partial k}{\partial t} + \rho_f \overline{u}_j \frac{\partial k}{\partial x_j} = \tau_{ij} \frac{\partial \overline{u_i}}{\partial x_j} - \rho_f \epsilon + \frac{\partial}{\partial x_j} (\mu \frac{\partial k}{\partial x_j} - \frac{1}{2} \overline{\rho_f u_i' u_i' u_j'} - \overline{p' u_j'}) + \overline{p' \frac{\partial u_i'}{\partial x_i}} + \frac{1}{2} \overline{\rho_f u_i' u_i' \frac{\partial u_j'}{\partial x_j}} - \overline{u_i' \omega_i'} \tag{B.17}$$

The DNS results (Mansour *et al.*, 1988) indicate that the turbulent transport term and the pressure diffusion term are quite small for simple flows, thus the assumption used by Wilcox (1998) is also adopted here:

$$\frac{1}{2} \overline{\rho_f u_i' u_i' u_j'} + \overline{p' u_j'} = -\frac{\mu_t}{\sigma_k} \frac{\partial k}{\partial x_j} \tag{B.18}$$

where σ_k is a closure coefficient. With the equation (35), we get a new transport equation for the turbulence kinetic energy which is very similar to the *k* equation in the standard *k-ε* turbulence model:

$$\rho_f \frac{\partial k}{\partial t} + \rho_f \overline{u}_j \frac{\partial k}{\partial x_j} = \tau_{ij} \frac{\partial \overline{u_i}}{\partial x_j} - \rho_f \epsilon + \frac{\partial}{\partial x_j} ((\mu + \frac{\mu_t}{\sigma_k}) \frac{\partial k}{\partial x_j}) + \Pi_k \tag{B.19}$$

with the extra term Π_k which is due to the interaction between two phases:

$$\Pi_k = \overline{p' \frac{\partial u_i'}{\partial x_i}} + \frac{1}{2} \overline{\rho_f u_i' u_i' \frac{\partial u_j'}{\partial x_j}} - \overline{u_i' \omega_i'} \tag{B.20}$$

The next is formulating the energy dissipation equation. Define the turbulence dissipation rate in equation (33) and the exact equation for ε is derived by taking the following moment of the Navier-Stokes equation.

$$\overline{2\nu \frac{\partial u_i'}{\partial x_j} \frac{\partial}{\partial x_j}(\mathcal{N}(u_i))} = 0 \tag{B.21}$$

where $\mathcal{N}(u_i)$ is the operator defined in the beginning.

First, the **unsteady term** gives:

$$\begin{aligned}
\overline{2\nu \frac{\partial u_i'}{\partial x_j} \frac{\partial}{\partial x_j}(\rho_f \frac{\partial u_i}{\partial t})} &= \overline{2\nu\rho_f \frac{\partial u_i'}{\partial x_j} \frac{\partial}{\partial x_j}(\frac{\partial \overline{u_i}}{\partial t} + \frac{\partial u_i'}{\partial t})} \\
&= \overline{2\nu\rho_f \frac{\partial u_i'}{\partial x_j} \frac{\partial}{\partial x_j}(\frac{\partial u_i'}{\partial t})} \\
&= \overline{\rho_f \frac{\partial}{\partial t}(\nu \frac{\partial u_i'}{\partial x_j} \frac{\partial u_i'}{\partial x_j})} \\
&= \rho_f \frac{\partial \epsilon}{\partial t}
\end{aligned} \tag{B.22}$$

Then, the **convective term** gives:

$$\begin{aligned}
&\overline{2\nu \frac{\partial u_i'}{\partial x_j} \frac{\partial}{\partial x_j}(\rho_f u_k \frac{\partial u_i}{\partial x_k})} \\
&= \overline{2\nu\rho_f \frac{\partial u_i'}{\partial x_j} \frac{\partial}{\partial x_j}(\overline{u_k} \frac{\partial \overline{u_i}}{\partial x_k} + u_k' \frac{\partial \overline{u_i}}{\partial x_k} + \overline{u_k} \frac{\partial u_i'}{\partial x_k} + u_k' \frac{\partial u_i'}{\partial x_k})} \\
&= \overline{2\mu \frac{\partial u_i'}{\partial x_j} \frac{\partial}{\partial x_j}(u_k' \frac{\partial \overline{u_i}}{\partial x_k})} + \overline{2\mu \frac{\partial u_i'}{\partial x_j} \frac{\partial}{\partial x_j}(\overline{u_k} \frac{\partial u_i'}{\partial x_k})} + \overline{2\mu \frac{\partial u_i'}{\partial x_j} \frac{\partial}{\partial x_j}(u_k' \frac{\partial u_i'}{\partial x_k})} \\
&= 2\mu \frac{\partial \overline{u_i}}{\partial x_k} \overline{\frac{\partial u_i'}{\partial x_j} \frac{\partial u_k'}{\partial x_j}} + 2\mu \overline{u_k' \frac{\partial u_i'}{\partial x_j}} \frac{\partial^2 \overline{u_i}}{\partial x_k \partial x_j} + 2\mu \frac{\partial \overline{u_k}}{\partial x_j} \overline{\frac{\partial u_i'}{\partial x_j} \frac{\partial u_i'}{\partial x_k}} + \rho_f \overline{u_k} \frac{\partial \epsilon}{\partial x_k} \\
&+ 2\mu \overline{\frac{\partial u_i'}{\partial x_j} \frac{\partial u_k'}{\partial x_j} \frac{\partial u_i'}{\partial x_k}} + \mu \overline{\frac{\partial}{\partial x_k}(u_k' \frac{\partial u_i'}{\partial x_j} \frac{\partial u_i'}{\partial x_j})} - \mu \overline{\frac{\partial u_k'}{\partial x_k} \frac{\partial u_i'}{\partial x_j} \frac{\partial u_i'}{\partial x_j}}
\end{aligned} \tag{B.23}$$

Next is the **pressure gradient term**:

$$\begin{aligned}\overline{2\nu\frac{\partial u_i'}{\partial x_j}\frac{\partial}{\partial x_j}\left(\frac{\partial p}{\partial x_i}\right)} &= \overline{2\nu\frac{\partial u_i'}{\partial x_j}\frac{\partial}{\partial x_j}\left(\frac{\partial \overline{p}}{\partial x_i}+\frac{\partial p'}{\partial x_i}\right)} \\ &= \overline{2\nu\frac{\partial u_i'}{\partial x_j}\frac{\partial}{\partial x_j}\left(\frac{\partial p'}{\partial x_i}\right)} \\ &= 2\nu\overline{\frac{\partial}{\partial x_i}\left(\frac{\partial p'}{\partial x_j}\frac{\partial u_i'}{\partial x_j}\right)} - 2\nu\overline{\frac{\partial p'}{\partial x_i}\frac{\partial^2 u_i'}{\partial x_j \partial x_j}}\end{aligned} \tag{B.24}$$

And then **the viscous term** yields:

$$\begin{aligned}&\overline{2\nu\frac{\partial u_i'}{\partial x_j}\frac{\partial}{\partial x_j}\left(\mu\frac{\partial^2 u_i}{\partial x_k^2}\right)} \\ &= \overline{2\nu\mu\frac{\partial u_i'}{\partial x_j}\frac{\partial}{\partial x_j}\left(\frac{\partial^2 \overline{u_i}}{\partial x_k^2}+\frac{\partial^2 u_i'}{\partial x_k^2}\right)} \\ &= \overline{2\nu\mu\frac{\partial u_i'}{\partial x_j}\frac{\partial^2}{\partial x_k^2}\left(\frac{\partial u_i'}{\partial x_j}\right)} \\ &= 2\nu\mu\overline{\frac{\partial}{\partial x_k}\left(\frac{\partial u_i'}{\partial x_j}\frac{\partial}{\partial x_k}\left(\frac{\partial u_i'}{\partial x_j}\right)\right)} - 2\nu\mu\overline{\frac{\partial}{\partial x_k}\left(\frac{\partial u_i'}{\partial x_j}\right)\frac{\partial}{\partial x_k}\left(\frac{\partial u_i'}{\partial x_j}\right)} \\ &= \mu\frac{\partial}{\partial x_k}\left(\frac{\partial \epsilon}{\partial x_k}\right) - 2\nu\mu\overline{\frac{\partial}{\partial x_k}\left(\frac{\partial u_i'}{\partial x_j}\right)\frac{\partial}{\partial x_k}\left(\frac{\partial u_i'}{\partial x_j}\right)}\end{aligned} \tag{B.25}$$

Finally, the **interaction term** gives:

$$\begin{aligned}\overline{2\nu\frac{\partial u_i'}{\partial x_j}\frac{\partial \omega_i}{\partial x_j}} &= \overline{2\nu\frac{\partial u_i'}{\partial x_j}\frac{\partial}{\partial x_j}\left(\overline{\omega_i}+\omega_i'\right)} \\ &= 2\nu\overline{\frac{\partial u_i'}{\partial x_j}\frac{\partial \omega_i'}{\partial x_j}}\end{aligned} \tag{B.26}$$

Put all the terms together we have:

$$
\begin{aligned}
&\rho_f \frac{\partial \epsilon}{\partial t} + \rho_f \overline{u_k} \frac{\partial \epsilon}{\partial x_k} \\
&= -2\mu \left(\frac{\partial \overline{u_i}}{\partial x_k} \overline{\frac{\partial u_i'}{\partial x_j} \frac{\partial u_k'}{\partial x_j}} + \frac{\partial \overline{u_k}}{\partial x_j} \overline{\frac{\partial u_i'}{\partial x_j} \frac{\partial u_i'}{\partial x_k}} \right) \\
&-2\mu \overline{u_k' \frac{\partial u_i'}{\partial x_j}} \frac{\partial^2 \overline{u_i}}{\partial x_k \partial x_j} - 2\mu \overline{\frac{\partial u_i'}{\partial x_j} \frac{\partial u_k'}{\partial x_j} \frac{\partial u_i'}{\partial x_k}} - 2\nu\mu \overline{\frac{\partial}{\partial x_k} \left(\frac{\partial u_i'}{\partial x_j} \right) \frac{\partial}{\partial x_k} \left(\frac{\partial u_i'}{\partial x_j} \right)} \\
&+ \frac{\partial}{\partial x_k} \left(\mu \frac{\partial \epsilon}{\partial x_k} - \mu \overline{u_k' \frac{\partial u_i'}{\partial x_j} \frac{\partial u_i'}{\partial x_j}} \right) - 2\nu \overline{\frac{\partial}{\partial x_i} \left(\frac{\partial p'}{\partial x_j} \frac{\partial u_i'}{\partial x_j} \right)} \\
&+ \mu \overline{\frac{\partial u_k'}{\partial x_k} \frac{\partial u_i'}{\partial x_j} \frac{\partial u_i'}{\partial x_j}} + 2\nu \overline{\frac{\partial p'}{\partial x_i} \frac{\partial^2 u_i'}{\partial x_j \partial x_j}} - 2\nu \overline{\frac{\partial u_i'}{\partial x_j} \frac{\partial \omega_i'}{\partial x_j}}
\end{aligned}
\tag{B.27}
$$

Rearrange the terms and adjust the notations, one obtains:

$$
\begin{aligned}
&\rho_f \frac{\partial \epsilon}{\partial t} + \rho_f \overline{u_j} \frac{\partial \epsilon}{\partial x_j} \\
&= -2\mu \frac{\partial \overline{u_i}}{\partial x_j} \left(\overline{\frac{\partial u_i'}{\partial x_k} \frac{\partial u_j'}{\partial x_k}} + \overline{\frac{\partial u_k'}{\partial x_j} \frac{\partial u_k'}{\partial x_i}} \right) - 2\mu \overline{u_k' \frac{\partial u_i'}{\partial x_j}} \frac{\partial^2 \overline{u_i}}{\partial x_k \partial x_j} \\
&-2\mu \overline{\frac{\partial u_i'}{\partial x_k} \frac{\partial u_i'}{\partial x_j} \frac{\partial u_k'}{\partial x_j}} - 2\mu\nu \overline{\frac{\partial}{\partial x_k} \left(\frac{\partial u_i'}{\partial x_j} \right) \frac{\partial}{\partial x_k} \left(\frac{\partial u_i'}{\partial x_j} \right)} \\
&+ \frac{\partial}{\partial x_j} \left(\mu \frac{\partial \epsilon}{\partial x_j} - \mu \overline{u_j' \frac{\partial u_i'}{\partial x_k} \frac{\partial u_i'}{\partial x_k}} - 2\nu \left(\overline{\frac{\partial p'}{\partial x_i} \frac{\partial u_j'}{\partial x_i}} \right) \right) + \Pi_\varepsilon
\end{aligned}
\tag{B.28}
$$

where Π_ε is the extra term compared with the ε equation in the standard k-ε model:

$$
\Pi_\varepsilon = \mu \overline{\frac{\partial u_k'}{\partial x_k} \frac{\partial u_i'}{\partial x_j} \frac{\partial u_i'}{\partial x_j}} + 2\nu \overline{\frac{\partial p'}{\partial x_i} \frac{\partial^2 u_i'}{\partial x_j \partial x_j}} - 2\nu \overline{\frac{\partial u_i'}{\partial x_j} \frac{\partial \omega_i'}{\partial x_j}}
\tag{B.29}
$$

The above equation can also be written as:

$$\rho_f \frac{\partial \epsilon}{\partial t} + \rho_f \overline{u}_j \frac{\partial \epsilon}{\partial x_j} = C_{\epsilon 1} \frac{\epsilon}{k} \tau_{ij} \frac{\partial \overline{u_i}}{\partial x_j} - C_{\epsilon 2} \rho_f \frac{\epsilon^2}{k} + \frac{\partial}{\partial x_j}((\mu + \frac{\mu_t}{\sigma_\epsilon}) \frac{\partial \epsilon}{\partial x_j}) + \Pi_\varepsilon \quad \text{(B.30)}$$

where $C_{\varepsilon 1}$,$C_{\varepsilon 2}$ and σ_ε are the closure coefficients.

APPENDIX III

SOURCE CODE OF THE 1DV MODEL

The source code is written in Python script as it can be run across the platforms (Windows, Linux, Mac OS, *etc.*) and it is completely free. Two additional packages need to be installed along with Python before running the 1DV model: numpy (the fundamental package for scientific computing with Python - www.numpy.org) and matplotlib (a python plotting library which produces publication quality figures in a variety of hardcopy formats and interactive environments across platforms – matplotlib.org). The Python version 2.7.10, numpy version 1.10.1 and matplotlib version 1.5.0 are used in the development of the code.

The process flow of the 1DV model is shown in Figure C.1 and the structure of the source code is illustrated in Figure C.2.

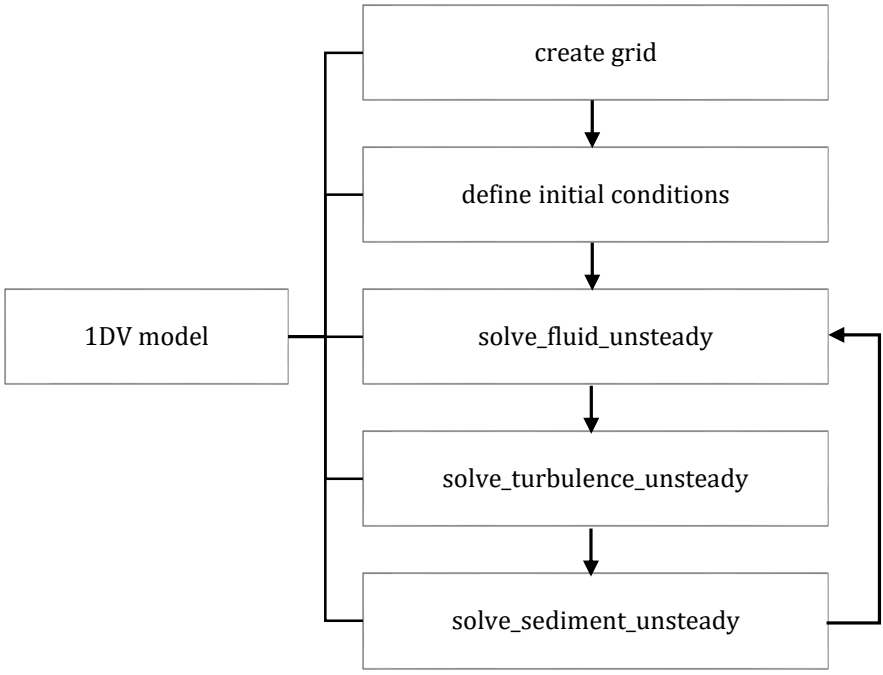

Figure C.1. The process flow of the 1DV model.

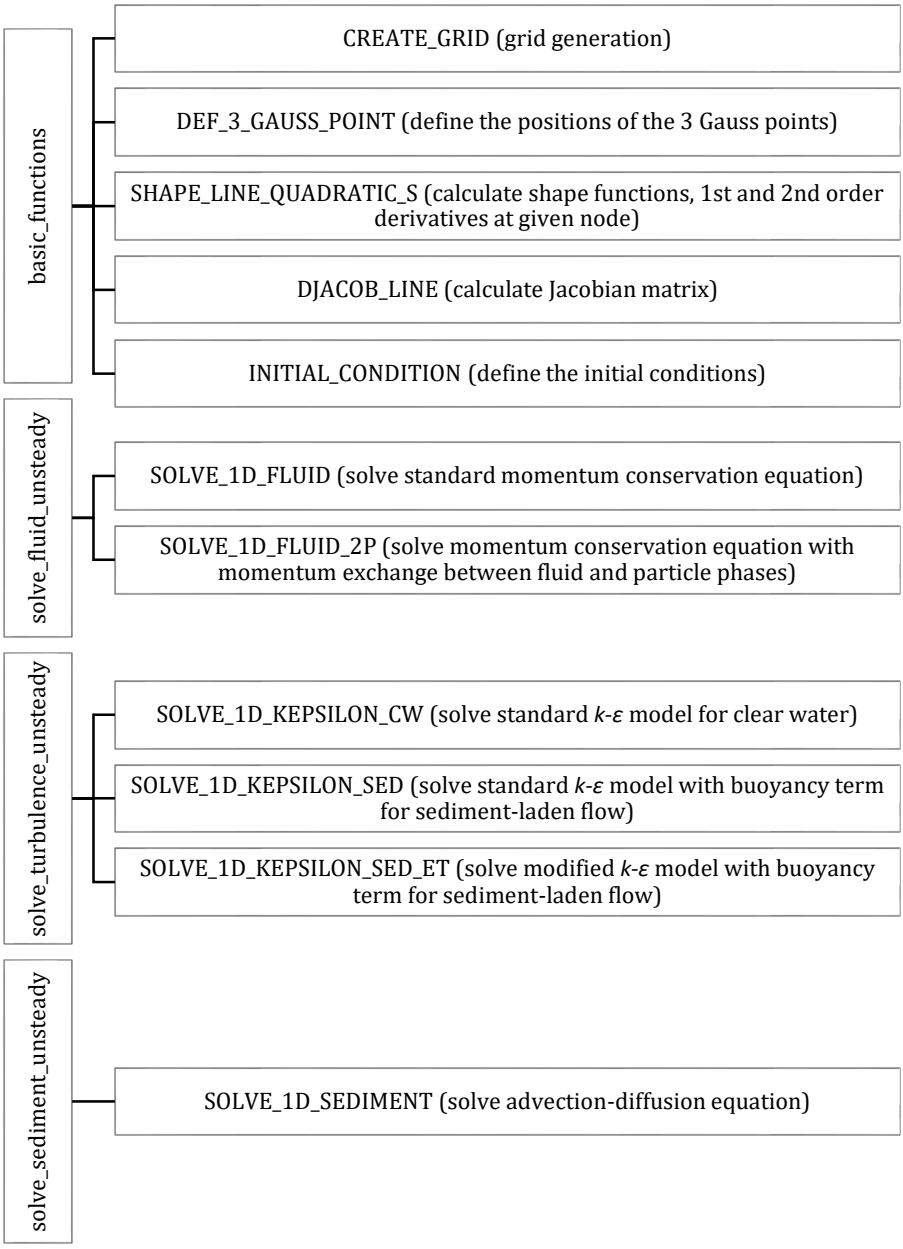

Figure C.2. The structure of the source code.

1. basic_functions.py

```
import numpy as np

#=========================================================

def CREATE_GRID(NELEM,GSIZE):

#  DEFINE ELEMENT PROPERTIES
   NNODL = 3
   NPOIN = NELEM*NNODL-(NELEM-1)

#  INITIALIZE VARIABLES
   COORD = np.zeros(NPOIN)
   LNODS = np.zeros((NELEM,NNODL))

#  FORM THE GRID WITH INPUT PARAMETERS
   for IPOIN in range (0,NPOIN):
         COORD[IPOIN]=0.0+GSIZE*(IPOIN)

#  CREATE THE CONNECTION TABLE
   for IELEM in range (0,NELEM):
      for INODL in range (0,NNODL):
         LNODS[IELEM,INODL]=INODL+(IELEM)*2

   return NPOIN,NNODL,COORD,LNODS

#=========================================================

def DEF_3_GAUSS_POINT():

#  DEFINE GAUSS POINTS
   NGAUS = 3
   POSGP = np.zeros(NGAUS)
   WEIGP = np.zeros(NGAUS)

   POSGP[0] = -np.sqrt(0.6)
   POSGP[1] = 0.0
   POSGP[2] = np.sqrt(0.6)
   WEIGP[0] = 5.0/9.0
   WEIGP[1] = 8.0/9.0
   WEIGP[2] = 5.0/9.0

   return POSGP,WEIGP

#=========================================================

def SHAPE_LINE_QUADRATIC_S(Z):

   SHAPE = np.zeros(3)
   DERIV = np.zeros(3)
   SDERIV = np.zeros(3)

   SHAPE[0] = 0.5*Z*(Z-1.0)
   SHAPE[1] = -(Z+1.0)*(Z-1.0)
   SHAPE[2] = 0.5*Z*(Z+1.0)
```

```
   DERIV[0] = Z-0.5
   DERIV[1] = -2.0*Z
   DERIV[2] = Z+0.5

   SDERIV[0] = 1.0
   SDERIV[1] = -2.0
   SDERIV[2] = 1.0

   return SHAPE,DERIV,SDERIV

#=========================================================

def DJACOB_LINE(COORD,LNODS,NNODL,IELEM,DERIV):

#  CALCULATE JACOBIAN MATRIX

   TEMPY=0.0

   for INODL in range(0,NNODL):
         TEMPY=TEMPY+DERIV[INODL]*COORD[LNODS[IELEM,INODL]]

   DJACK=TEMPY

#  CALCULATE THE INVERSE OF JACOBIAN MATRIX
   DJACI=1.0/DJACK

   return DJACK,DJACI

#=========================================================

def INITIAL_CONDITION(NPOIN,COORD,DP_DX,CMU,KAPPA):

   UX0 = np.zeros(NPOIN)
   K0 = np.zeros(NPOIN)
   EP0 = np.zeros(NPOIN)
   NU_T0 = np.zeros(NPOIN)

#  CALCULATE SHEAR VELOCITY
   USTAR = np.sqrt(-(COORD[NPOIN-1]-COORD[0])/1.0e3*DP_DX)

#  SOLVE THE INITIAL VELOCITY PROFILE
   UX0 = (USTAR*(1/0.41*np.log(USTAR*COORD/1.0e-6)+5.2))
   UX0[0] = 0.0

#  INITIALIZE K AND EPSILON
   K0 = USTAR**2/np.sqrt(CMU)*(1-COORD/(COORD[NPOIN-1]-COORD[0]))
   EP0 = USTAR**3/(KAPPA*COORD)*(1-COORD/(COORD[NPOIN-1]-COORD[0]))
   NU_T0 = KAPPA*USTAR*COORD*(1-COORD/(COORD[NPOIN-1]-COORD[0]))

#  INITIALIZE CONCENTRATION
   C0 = np.zeros(NPOIN)
   C0[:] = 1.0e-3

   return USTAR,UX0,K0,EP0,NU_T0,C0
```

2. solve_fluid_unsteady.py

```
import numpy as np
from basic_functions import *

#=======================================================

def
SOLVE_1D_FLUID(COORD,LNODS,NPOIN,NELEM,NNODL,POSGP,WEIGP,DP_DX,USTAR,DELTA_T,
MU_EN,UXN):

#  INITIALIZE VARIABLES
   GA = np.zeros((NPOIN,NPOIN))
   GF = np.zeros(NPOIN)
   LA = np.zeros((NNODL,NNODL))
   LF = np.zeros(NNODL)
   UX = np.zeros(NPOIN)

#  LOOP FOR ALL THE ELEMENTS
   for IELEM in range(1,NELEM):

#      SHAPE FUNCTIONS AT GAUSS POINT 1
       SHAPE1, DERIV1, SDERIV1 = SHAPE_LINE_QUADRATIC_S(POSGP[0])
       DJACK1, DJACI1 = DJACOB_LINE(COORD,LNODS,NNODL,IELEM,DERIV1)
#      SHAPE FUNCTIONS AT GAUSS POINT 2
       SHAPE2, DERIV2, SDERIV2 = SHAPE_LINE_QUADRATIC_S(POSGP[1])
       DJACK2, DJACI2 = DJACOB_LINE(COORD,LNODS,NNODL,IELEM,DERIV2)
#      SHAPE FUNCTIONS AT GAUSS POINT 3
       SHAPE3, DERIV3, SDERIV3 =SHAPE_LINE_QUADRATIC_S(POSGP[2])
       DJACK3, DJACI3 = DJACOB_LINE(COORD,LNODS,NNODL,IELEM,DERIV3)

#      GLOBAL DERIVATIVE AND GAUSS WEIGHTING AREAS AT GAUSS POINTS
       GDERIV1 = DJACI1*DERIV1
       GDERIV2 = DJACI2*DERIV2
       GDERIV3 = DJACI3*DERIV3

       AREAW1 = DJACK1*WEIGP[0]
       AREAW2 = DJACK2*WEIGP[1]
       AREAW3 = DJACK3*WEIGP[2]

#      UX AT GAUSS POINTS
       UX1 =
SHAPE1[0]*UXN[LNODS[IELEM,0]]+SHAPE1[1]*UXN[LNODS[IELEM,1]]+SHAPE1[2]*UXN[LNO
DS[IELEM,2]]
       UX2 =
SHAPE2[0]*UXN[LNODS[IELEM,0]]+SHAPE2[1]*UXN[LNODS[IELEM,1]]+SHAPE2[2]*UXN[LNO
DS[IELEM,2]]
       UX3 =
SHAPE3[0]*UXN[LNODS[IELEM,0]]+SHAPE3[1]*UXN[LNODS[IELEM,1]]+SHAPE3[2]*UXN[LNO
DS[IELEM,2]]

#      EFFECTIVE VISCOSITY AT GAUSS POINTS
       MU_E1 =
SHAPE1[0]*MU_EN[LNODS[IELEM,0]]+SHAPE1[1]*MU_EN[LNODS[IELEM,1]]+SHAPE1[2]*MU_
EN[LNODS[IELEM,2]]
```

```
       MU_E2 =
SHAPE2[0]*MU_EN[LNODS[IELEM,0]]+SHAPE2[1]*MU_EN[LNODS[IELEM,1]]+SHAPE2[2]*MU_
EN[LNODS[IELEM,2]]
       MU_E3 =
SHAPE3[0]*MU_EN[LNODS[IELEM,0]]+SHAPE3[1]*MU_EN[LNODS[IELEM,1]]+SHAPE3[2]*MU_
EN[LNODS[IELEM,2]]

#      CONSTRUCT THE LOCAL MATRIX OF COEFFICIENT
       LA[0,0] =
((SHAPE1[0]*SHAPE1[0]*AREAW1+SHAPE2[0]*SHAPE2[0]*AREAW2+SHAPE3[0]*SHAPE3[0]*A
REAW3)/DELTA_T)+(MU_E1*GDERIV1[0]*GDERIV1[0]*AREAW1+MU_E2*GDERIV2[0]*GDERIV2[
0]*AREAW2+MU_E3*GDERIV3[0]*GDERIV3[0]*AREAW3)
       LA[0,1] =
((SHAPE1[0]*SHAPE1[1]*AREAW1+SHAPE2[0]*SHAPE2[1]*AREAW2+SHAPE3[0]*SHAPE3[1]*A
REAW3)/DELTA_T)+(MU_E1*GDERIV1[0]*GDERIV1[1]*AREAW1+MU_E2*GDERIV2[0]*GDERIV2[
1]*AREAW2+MU_E3*GDERIV3[0]*GDERIV3[1]*AREAW3)
       LA[0,2] =
((SHAPE1[0]*SHAPE1[2]*AREAW1+SHAPE2[0]*SHAPE2[2]*AREAW2+SHAPE3[0]*SHAPE3[2]*A
REAW3)/DELTA_T)+(MU_E1*GDERIV1[0]*GDERIV1[2]*AREAW1+MU_E2*GDERIV2[0]*GDERIV2[
2]*AREAW2+MU_E3*GDERIV3[0]*GDERIV3[2]*AREAW3)

       LA[1,0] =
((SHAPE1[1]*SHAPE1[0]*AREAW1+SHAPE2[1]*SHAPE2[0]*AREAW2+SHAPE3[1]*SHAPE3[0]*A
REAW3)/DELTA_T)+(MU_E1*GDERIV1[1]*GDERIV1[0]*AREAW1+MU_E2*GDERIV2[1]*GDERIV2[
0]*AREAW2+MU_E3*GDERIV3[1]*GDERIV3[0]*AREAW3)
       LA[1,1] =
((SHAPE1[1]*SHAPE1[1]*AREAW1+SHAPE2[1]*SHAPE2[1]*AREAW2+SHAPE3[1]*SHAPE3[1]*A
REAW3)/DELTA_T)+(MU_E1*GDERIV1[1]*GDERIV1[1]*AREAW1+MU_E2*GDERIV2[1]*GDERIV2[
1]*AREAW2+MU_E3*GDERIV3[1]*GDERIV3[1]*AREAW3)
       LA[1,2] =
((SHAPE1[1]*SHAPE1[2]*AREAW1+SHAPE2[1]*SHAPE2[2]*AREAW2+SHAPE3[1]*SHAPE3[2]*A
REAW3)/DELTA_T)+(MU_E1*GDERIV1[1]*GDERIV1[2]*AREAW1+MU_E2*GDERIV2[1]*GDERIV2[
2]*AREAW2+MU_E3*GDERIV3[1]*GDERIV3[2]*AREAW3)

       LA[2,0] =
((SHAPE1[2]*SHAPE1[0]*AREAW1+SHAPE2[2]*SHAPE2[0]*AREAW2+SHAPE3[2]*SHAPE3[0]*A
REAW3)/DELTA_T)+(MU_E1*GDERIV1[2]*GDERIV1[0]*AREAW1+MU_E2*GDERIV2[2]*GDERIV2[
0]*AREAW2+MU_E3*GDERIV3[2]*GDERIV3[0]*AREAW3)
       LA[2,1] =
((SHAPE1[2]*SHAPE1[1]*AREAW1+SHAPE2[2]*SHAPE2[1]*AREAW2+SHAPE3[2]*SHAPE3[1]*A
REAW3)/DELTA_T)+(MU_E1*GDERIV1[2]*GDERIV1[1]*AREAW1+MU_E2*GDERIV2[2]*GDERIV2[
1]*AREAW2+MU_E3*GDERIV3[2]*GDERIV3[1]*AREAW3)
       LA[2,2] =
((SHAPE1[2]*SHAPE1[2]*AREAW1+SHAPE2[2]*SHAPE2[2]*AREAW2+SHAPE3[2]*SHAPE3[2]*A
REAW3)/DELTA_T)+(MU_E1*GDERIV1[2]*GDERIV1[2]*AREAW1+MU_E2*GDERIV2[2]*GDERIV2[
2]*AREAW2+MU_E3*GDERIV3[2]*GDERIV3[2]*AREAW3)

#      ASSEMBLE THE GLOBAL MATRIX
       for IDIME in range(0,NNODL):
           for JDIME in range(0,NNODL):
               GA[LNODS[IELEM,IDIME],LNODS[IELEM,JDIME]] =
GA[LNODS[IELEM,IDIME],LNODS[IELEM,JDIME]]+LA[IDIME,JDIME]

#      FORM THE LOCAL RHS COEFFICIENTS AND ASSEMBLE INTO GLOBAL RHS VECTOR
```

```
       LF[0] =
((UX1*SHAPE1[0]*AREAW1+UX2*SHAPE2[0]*AREAW2+UX3*SHAPE3[0]*AREAW3)/DELTA_T)-
(SHAPE1[0]*AREAW1+SHAPE2[0]*AREAW2+SHAPE3[0]*AREAW3)*DP_DX
       LF[1] =
((UX1*SHAPE1[1]*AREAW1+UX2*SHAPE2[1]*AREAW2+UX3*SHAPE3[1]*AREAW3)/DELTA_T)-
(SHAPE1[1]*AREAW1+SHAPE2[1]*AREAW2+SHAPE3[1]*AREAW3)*DP_DX
       LF[2] =
((UX1*SHAPE1[2]*AREAW1+UX2*SHAPE2[2]*AREAW2+UX3*SHAPE3[2]*AREAW3)/DELTA_T)-
(SHAPE1[2]*AREAW1+SHAPE2[2]*AREAW2+SHAPE3[2]*AREAW3)*DP_DX

       for IDIME in range(0,NNODL):
           GF[LNODS[IELEM,IDIME]] = GF[LNODS[IELEM,IDIME]]+LF[IDIME]

#  DEAL WITH THE BOUNDARY CONDITIONS
   for IPOIN in range(0,NPOIN):
#      WALL BOUNDARY
       GA[2,IPOIN] = 0.0

#  WALL BOUNDARY
   GA[2,2] = 1.0

#  WALL BOUNDARY
   GF[2] = USTAR*(1/0.41*np.log(USTAR*COORD[2]/1.0e-6)+5.2)

#  SOLVE LINEAR EQUATIONS
   UX[2:] = np.linalg.solve(GA[2:,2:],GF[2:])

   UX[1] = USTAR*(1/0.41*np.log(USTAR*COORD[1]/1.0e-6)+5.2)
   UX[0] = 0.0

   return UX

#=========================================================

def
SOLVE_1D_FLUID_2P(COORD,LNODS,NPOIN,NELEM,NNODL,POSGP,WEIGP,DP_DX,USTAR,DELTA
_T,MU_EN,UXN,CN,RHO_S,WS):

#  INITIALIZE VARIABLES
   GA = np.zeros((NPOIN,NPOIN))
   GF = np.zeros(NPOIN)
   LA = np.zeros((NNODL,NNODL))
   LF = np.zeros(NNODL)
   UX = np.zeros(NPOIN)

   WZ0=WS

#  LOOP FOR ALL THE ELEMENTS
   for IELEM in range(1,NELEM):

#      SHAPE FUNCTIONS AT GAUSS POINT 1
       SHAPE1, DERIV1, SDERIV1 = SHAPE_LINE_QUADRATIC_S(POSGP[0])
       DJACK1, DJACI1 = DJACOB_LINE(COORD,LNODS,NNODL,IELEM,DERIV1)
#      SHAPE FUNCTIONS AT GAUSS POINT 2
       SHAPE2, DERIV2, SDERIV2 = SHAPE_LINE_QUADRATIC_S(POSGP[1])
       DJACK2, DJACI2 = DJACOB_LINE(COORD,LNODS,NNODL,IELEM,DERIV2)
#      SHAPE FUNCTIONS AT GAUSS POINT 3
```

```
        SHAPE3, DERIV3, SDERIV3 =SHAPE_LINE_QUADRATIC_S(POSGP[2])
        DJACK3, DJACI3 = DJACOB_LINE(COORD,LNODS,NNODL,IELEM,DERIV3)

#       GLOBAL DERIVATIVE AND GAUSS WEIGHTING AREAS AT GAUSS POINTS
        GDERIV1 = DJACI1*DERIV1
        GDERIV2 = DJACI2*DERIV2
        GDERIV3 = DJACI3*DERIV3

        AREAW1 = DJACK1*WEIGP[0]
        AREAW2 = DJACK2*WEIGP[1]
        AREAW3 = DJACK3*WEIGP[2]

#       UX AT GAUSS POINTS
        UX1 =
SHAPE1[0]*UXN[LNODS[IELEM,0]]+SHAPE1[1]*UXN[LNODS[IELEM,1]]+SHAPE1[2]*UXN[LNO
DS[IELEM,2]]
        UX2 =
SHAPE2[0]*UXN[LNODS[IELEM,0]]+SHAPE2[1]*UXN[LNODS[IELEM,1]]+SHAPE2[2]*UXN[LNO
DS[IELEM,2]]
        UX3 =
SHAPE3[0]*UXN[LNODS[IELEM,0]]+SHAPE3[1]*UXN[LNODS[IELEM,1]]+SHAPE3[2]*UXN[LNO
DS[IELEM,2]]

#       EFFECTIVE VISCOSITY AT GAUSS POINTS
        MU_E1 =
SHAPE1[0]*MU_EN[LNODS[IELEM,0]]+SHAPE1[1]*MU_EN[LNODS[IELEM,1]]+SHAPE1[2]*MU_
EN[LNODS[IELEM,2]]
        MU_E2 =
SHAPE2[0]*MU_EN[LNODS[IELEM,0]]+SHAPE2[1]*MU_EN[LNODS[IELEM,1]]+SHAPE2[2]*MU_
EN[LNODS[IELEM,2]]
        MU_E3 =
SHAPE3[0]*MU_EN[LNODS[IELEM,0]]+SHAPE3[1]*MU_EN[LNODS[IELEM,1]]+SHAPE3[2]*MU_
EN[LNODS[IELEM,2]]

#       C AT GAUSS POINTS

C1=SHAPE1[0]*CN[LNODS[IELEM,0]]+SHAPE1[1]*CN[LNODS[IELEM,1]]+SHAPE1[2]*CN[LNO
DS[IELEM,2]]

C2=SHAPE2[0]*CN[LNODS[IELEM,0]]+SHAPE2[1]*CN[LNODS[IELEM,1]]+SHAPE2[2]*CN[LNO
DS[IELEM,2]]

C3=SHAPE3[0]*CN[LNODS[IELEM,0]]+SHAPE3[1]*CN[LNODS[IELEM,1]]+SHAPE3[2]*CN[LNO
DS[IELEM,2]]

#       WZ AT GAUSS POINTS
        WZ1=WZ0*(1-C1)**4.65
        WZ2=WZ0*(1-C2)**4.65
        WZ3=WZ0*(1-C3)**4.65

#       CONSTRUCT THE LOCAL MATRIX OF COEFFICIENT
        LA[0,0] =
((SHAPE1[0]*SHAPE1[0]*AREAW1+SHAPE2[0]*SHAPE2[0]*AREAW2+SHAPE3[0]*SHAPE3[0]*A
REAW3)/DELTA_T)+(MU_E1*GDERIV1[0]*GDERIV1[0]*AREAW1+MU_E2*GDERIV2[0]*GDERIV2[
0]*AREAW2+MU_E3*GDERIV3[0]*GDERIV3[0]*AREAW3)+RHO_S*(C1*WZ1*SHAPE1[0]*GDERIV1
[0]*AREAW1+C2*WZ2*SHAPE2[0]*GDERIV2[0]*AREAW2+C3*WZ3*SHAPE3[0]*GDERIV3[0]*ARE
AW3)
```

```
       LA[0,1] =
((SHAPE1[0]*SHAPE1[1]*AREAW1+SHAPE2[0]*SHAPE2[1]*AREAW2+SHAPE3[0]*SHAPE3[1]*A
REAW3)/DELTA_T)+(MU_E1*GDERIV1[0]*GDERIV1[1]*AREAW1+MU_E2*GDERIV2[0]*GDERIV2[
1]*AREAW2+MU_E3*GDERIV3[0]*GDERIV3[1]*AREAW3)+RHO_S*(C1*WZ1*SHAPE1[0]*GDERIV1
[1]*AREAW1+C2*WZ2*SHAPE2[0]*GDERIV2[1]*AREAW2+C3*WZ3*SHAPE3[0]*GDERIV3[1]*ARE
AW3)
       LA[0,2] =
((SHAPE1[0]*SHAPE1[2]*AREAW1+SHAPE2[0]*SHAPE2[2]*AREAW2+SHAPE3[0]*SHAPE3[2]*A
REAW3)/DELTA_T)+(MU_E1*GDERIV1[0]*GDERIV1[2]*AREAW1+MU_E2*GDERIV2[0]*GDERIV2[
2]*AREAW2+MU_E3*GDERIV3[0]*GDERIV3[2]*AREAW3)+RHO_S*(C1*WZ1*SHAPE1[0]*GDERIV1
[2]*AREAW1+C2*WZ2*SHAPE2[0]*GDERIV2[2]*AREAW2+C3*WZ3*SHAPE3[0]*GDERIV3[2]*ARE
AW3)

       LA[1,0] =
((SHAPE1[1]*SHAPE1[0]*AREAW1+SHAPE2[1]*SHAPE2[0]*AREAW2+SHAPE3[1]*SHAPE3[0]*A
REAW3)/DELTA_T)+(MU_E1*GDERIV1[1]*GDERIV1[0]*AREAW1+MU_E2*GDERIV2[1]*GDERIV2[
0]*AREAW2+MU_E3*GDERIV3[1]*GDERIV3[0]*AREAW3)+RHO_S*(C1*WZ1*SHAPE1[1]*GDERIV1
[0]*AREAW1+C2*WZ2*SHAPE2[1]*GDERIV2[0]*AREAW2+C3*WZ3*SHAPE3[1]*GDERIV3[0]*ARE
AW3)
       LA[1,1] =
((SHAPE1[1]*SHAPE1[1]*AREAW1+SHAPE2[1]*SHAPE2[1]*AREAW2+SHAPE3[1]*SHAPE3[1]*A
REAW3)/DELTA_T)+(MU_E1*GDERIV1[1]*GDERIV1[1]*AREAW1+MU_E2*GDERIV2[1]*GDERIV2[
1]*AREAW2+MU_E3*GDERIV3[1]*GDERIV3[1]*AREAW3)+RHO_S*(C1*WZ1*SHAPE1[1]*GDERIV1
[1]*AREAW1+C2*WZ2*SHAPE2[1]*GDERIV2[1]*AREAW2+C3*WZ3*SHAPE3[1]*GDERIV3[1]*ARE
AW3)
       LA[1,2] =
((SHAPE1[1]*SHAPE1[2]*AREAW1+SHAPE2[1]*SHAPE2[2]*AREAW2+SHAPE3[1]*SHAPE3[2]*A
REAW3)/DELTA_T)+(MU_E1*GDERIV1[1]*GDERIV1[2]*AREAW1+MU_E2*GDERIV2[1]*GDERIV2[
2]*AREAW2+MU_E3*GDERIV3[1]*GDERIV3[2]*AREAW3)+RHO_S*(C1*WZ1*SHAPE1[1]*GDERIV1
[2]*AREAW1+C2*WZ2*SHAPE2[1]*GDERIV2[2]*AREAW2+C3*WZ3*SHAPE3[1]*GDERIV3[2]*ARE
AW3)

       LA[2,0] =
((SHAPE1[2]*SHAPE1[0]*AREAW1+SHAPE2[2]*SHAPE2[0]*AREAW2+SHAPE3[2]*SHAPE3[0]*A
REAW3)/DELTA_T)+(MU_E1*GDERIV1[2]*GDERIV1[0]*AREAW1+MU_E2*GDERIV2[2]*GDERIV2[
0]*AREAW2+MU_E3*GDERIV3[2]*GDERIV3[0]*AREAW3)+RHO_S*(C1*WZ1*SHAPE1[2]*GDERIV1
[0]*AREAW1+C2*WZ2*SHAPE2[2]*GDERIV2[0]*AREAW2+C3*WZ3*SHAPE3[2]*GDERIV3[0]*ARE
AW3)
       LA[2,1] =
((SHAPE1[2]*SHAPE1[1]*AREAW1+SHAPE2[2]*SHAPE2[1]*AREAW2+SHAPE3[2]*SHAPE3[1]*A
REAW3)/DELTA_T)+(MU_E1*GDERIV1[2]*GDERIV1[1]*AREAW1+MU_E2*GDERIV2[2]*GDERIV2[
1]*AREAW2+MU_E3*GDERIV3[2]*GDERIV3[1]*AREAW3)+RHO_S*(C1*WZ1*SHAPE1[2]*GDERIV1
[1]*AREAW1+C2*WZ2*SHAPE2[2]*GDERIV2[1]*AREAW2+C3*WZ3*SHAPE3[2]*GDERIV3[1]*ARE
AW3)
       LA[2,2] =
((SHAPE1[2]*SHAPE1[2]*AREAW1+SHAPE2[2]*SHAPE2[2]*AREAW2+SHAPE3[2]*SHAPE3[2]*A
REAW3)/DELTA_T)+(MU_E1*GDERIV1[2]*GDERIV1[2]*AREAW1+MU_E2*GDERIV2[2]*GDERIV2[
2]*AREAW2+MU_E3*GDERIV3[2]*GDERIV3[2]*AREAW3)+RHO_S*(C1*WZ1*SHAPE1[2]*GDERIV1
[2]*AREAW1+C2*WZ2*SHAPE2[2]*GDERIV2[2]*AREAW2+C3*WZ3*SHAPE3[2]*GDERIV3[2]*ARE
AW3)

#      ASSEMBLE THE GLOBAL MATRIX
       for IDIME in range(0,NNODL):
           for JDIME in range(0,NNODL):
               GA[LNODS[IELEM,IDIME],LNODS[IELEM,JDIME]] =
GA[LNODS[IELEM,IDIME],LNODS[IELEM,JDIME]]+LA[IDIME,JDIME]
```

```
#      FORM THE LOCAL RHS COEFFICIENTS AND ASSEMBLE INTO GLOBAL RHS VECTOR

       LF[0] =
((UX1*SHAPE1[0]*AREAW1+UX2*SHAPE2[0]*AREAW2+UX3*SHAPE3[0]*AREAW3)/DELTA_T)-
(SHAPE1[0]*AREAW1+SHAPE2[0]*AREAW2+SHAPE3[0]*AREAW3)*DP_DX
       LF[1] =
((UX1*SHAPE1[1]*AREAW1+UX2*SHAPE2[1]*AREAW2+UX3*SHAPE3[1]*AREAW3)/DELTA_T)-
(SHAPE1[1]*AREAW1+SHAPE2[1]*AREAW2+SHAPE3[1]*AREAW3)*DP_DX
       LF[2] =
((UX1*SHAPE1[2]*AREAW1+UX2*SHAPE2[2]*AREAW2+UX3*SHAPE3[2]*AREAW3)/DELTA_T)-
(SHAPE1[2]*AREAW1+SHAPE2[2]*AREAW2+SHAPE3[2]*AREAW3)*DP_DX

       for IDIME in range(0,NNODL):
           GF[LNODS[IELEM,IDIME]] = GF[LNODS[IELEM,IDIME]]+LF[IDIME]

#  DEAL WITH THE BOUNDARY CONDITIONS
   for IPOIN in range(0,NPOIN):
#      WALL BOUNDARY
       GA[2,IPOIN] = 0.0

#  WALL BOUNDARY
   GA[2,2] = 1.0

#  WALL BOUNDARY
   GF[2] = USTAR*(1/0.41*np.log(USTAR*COORD[2]/1.0e-6)+5.2)

#  SOLVE LINEAR EQUATIONS
   UX[2:] = np.linalg.solve(GA[2:,2:],GF[2:])

   UX[1] = USTAR*(1/0.41*np.log(USTAR*COORD[1]/1.0e-6)+5.2)
   UX[0] = 0.0

   return UX
```

3. solve_turbulence_unsteady.py

```
import numpy as np
from basic_functions import *

#=========================================================

def
SOLVE_1D_KEPSILON_CW(COORD,LNODS,NPOIN,NELEM,NNODL,POSGP,WEIGP,DELTA_T,NU,KN,
EPN,UXN):

#  INITIALIZE VARIABLES
   GK = np.zeros((NPOIN,NPOIN))
   GFK = np.zeros(NPOIN)
   LK = np.zeros((NNODL,NNODL))
   LFK = np.zeros(NNODL)

   GEP = np.zeros((NPOIN,NPOIN))
   GFEP = np.zeros(NPOIN)
   LEP = np.zeros((NNODL,NNODL))
```

```
   LFEP = np.zeros(NNODL)

   K = np.zeros(NPOIN)
   EP = np.zeros(NPOIN)

#  DEFINE CONSTANTS
   SIGMA_K = 1.0
   SIGMA_EP = 1.3
   CMU = 0.09
   C1 = 1.44
   C2 = 1.92

#  LOOP FOR ALL THE ELEMENTS
   for IELEM in range(1,NELEM):

#      SHAPE FUNCTIONS AT GAUSS POINT 1
       SHAPE1, DERIV1, SDERIV1 = SHAPE_LINE_QUADRATIC_S(POSGP[0])
       DJACK1, DJACI1 = DJACOB_LINE(COORD,LNODS,NNODL,IELEM,DERIV1)
#      SHAPE FUNCTIONS AT GAUSS POINT 2
       SHAPE2, DERIV2, SDERIV2 = SHAPE_LINE_QUADRATIC_S(POSGP[1])
       DJACK2, DJACI2 = DJACOB_LINE(COORD,LNODS,NNODL,IELEM,DERIV2)
#      SHAPE FUNCTIONS AT GAUSS POINT 3
       SHAPE3, DERIV3, SDERIV3 = SHAPE_LINE_QUADRATIC_S(POSGP[2])
       DJACK3, DJACI3 = DJACOB_LINE(COORD,LNODS,NNODL,IELEM,DERIV3)

#      GLOBAL DERIVATIVE AND GAUSS WEIGHTING AREAS AT GAUSS POINTS
       GDERIV1 = DJACI1*DERIV1
       GDERIV2 = DJACI2*DERIV2
       GDERIV3 = DJACI3*DERIV3

       AREAW1 = DJACK1*WEIGP[0]
       AREAW2 = DJACK2*WEIGP[1]
       AREAW3 = DJACK3*WEIGP[2]

#      K AT GAUSS POINTS
       K1 =
SHAPE1[0]*KN[LNODS[IELEM,0]]+SHAPE1[1]*KN[LNODS[IELEM,1]]+SHAPE1[2]*KN[LNODS[
IELEM,2]]
       K2 =
SHAPE2[0]*KN[LNODS[IELEM,0]]+SHAPE2[1]*KN[LNODS[IELEM,1]]+SHAPE2[2]*KN[LNODS[
IELEM,2]]
       K3 =
SHAPE3[0]*KN[LNODS[IELEM,0]]+SHAPE3[1]*KN[LNODS[IELEM,1]]+SHAPE3[2]*KN[LNODS[
IELEM,2]]

#      EPSILON AT GAUSS POINTS
       EP1 =
SHAPE1[0]*EPN[LNODS[IELEM,0]]+SHAPE1[1]*EPN[LNODS[IELEM,1]]+SHAPE1[2]*EPN[LNO
DS[IELEM,2]]
       EP2 =
SHAPE2[0]*EPN[LNODS[IELEM,0]]+SHAPE2[1]*EPN[LNODS[IELEM,1]]+SHAPE2[2]*EPN[LNO
DS[IELEM,2]]
       EP3 =
SHAPE3[0]*EPN[LNODS[IELEM,0]]+SHAPE3[1]*EPN[LNODS[IELEM,1]]+SHAPE3[2]*EPN[LNO
DS[IELEM,2]]

#      GAMMA AT GAUSS POINTS
```

```
       GAMMA1 = EP1/K1
       GAMMA2 = EP2/K2
       GAMMA3 = EP3/K3

#      EDDY VISCOSITY AT GAUSS POINTS
       NUT1 = CMU*K1**2/EP1
       NUT2 = CMU*K2**2/EP2
       NUT3 = CMU*K3**2/EP3

#      CONSTRUCT THE LOCAL MATRIX OF COEFFICIENT

#      FOR K
       LK[0,0] =
((SHAPE1[0]*SHAPE1[0]*AREAW1+SHAPE2[0]*SHAPE2[0]*AREAW2+SHAPE3[0]*SHAPE3[0]*A
REAW3)/DELTA_T)+((NU+NUT1/SIGMA_K)*GDERIV1[0]*GDERIV1[0]*AREAW1+(NU+NUT2/SIGM
A_K)*GDERIV2[0]*GDERIV2[0]*AREAW2+(NU+NUT3/SIGMA_K)*GDERIV3[0]*GDERIV3[0]*ARE
AW3)+(GAMMA1*SHAPE1[0]*SHAPE1[0]*AREAW1+GAMMA2*SHAPE2[0]*SHAPE2[0]*AREAW2+GAM
MA3*SHAPE3[0]*SHAPE3[0]*AREAW3)
       LK[0,1] =
((SHAPE1[0]*SHAPE1[1]*AREAW1+SHAPE2[0]*SHAPE2[1]*AREAW2+SHAPE3[0]*SHAPE3[1]*A
REAW3)/DELTA_T)+((NU+NUT1/SIGMA_K)*GDERIV1[0]*GDERIV1[1]*AREAW1+(NU+NUT2/SIGM
A_K)*GDERIV2[0]*GDERIV2[1]*AREAW2+(NU+NUT3/SIGMA_K)*GDERIV3[0]*GDERIV3[1]*ARE
AW3)+(GAMMA1*SHAPE1[0]*SHAPE1[1]*AREAW1+GAMMA2*SHAPE2[0]*SHAPE2[1]*AREAW2+GAM
MA3*SHAPE3[0]*SHAPE3[1]*AREAW3)
       LK[0,2] =
((SHAPE1[0]*SHAPE1[2]*AREAW1+SHAPE2[0]*SHAPE2[2]*AREAW2+SHAPE3[0]*SHAPE3[2]*A
REAW3)/DELTA_T)+((NU+NUT1/SIGMA_K)*GDERIV1[0]*GDERIV1[2]*AREAW1+(NU+NUT2/SIGM
A_K)*GDERIV2[0]*GDERIV2[2]*AREAW2+(NU+NUT3/SIGMA_K)*GDERIV3[0]*GDERIV3[2]*ARE
AW3)+(GAMMA1*SHAPE1[0]*SHAPE1[2]*AREAW1+GAMMA2*SHAPE2[0]*SHAPE2[2]*AREAW2+GAM
MA3*SHAPE3[0]*SHAPE3[2]*AREAW3)

       LK[1,0] =
((SHAPE1[1]*SHAPE1[0]*AREAW1+SHAPE2[1]*SHAPE2[0]*AREAW2+SHAPE3[1]*SHAPE3[0]*A
REAW3)/DELTA_T)+((NU+NUT1/SIGMA_K)*GDERIV1[1]*GDERIV1[0]*AREAW1+(NU+NUT2/SIGM
A_K)*GDERIV2[1]*GDERIV2[0]*AREAW2+(NU+NUT3/SIGMA_K)*GDERIV3[1]*GDERIV3[0]*ARE
AW3)+(GAMMA1*SHAPE1[1]*SHAPE1[0]*AREAW1+GAMMA2*SHAPE2[1]*SHAPE2[0]*AREAW2+GAM
MA3*SHAPE3[1]*SHAPE3[0]*AREAW3)
       LK[1,1] =
((SHAPE1[1]*SHAPE1[1]*AREAW1+SHAPE2[1]*SHAPE2[1]*AREAW2+SHAPE3[1]*SHAPE3[1]*A
REAW3)/DELTA_T)+((NU+NUT1/SIGMA_K)*GDERIV1[1]*GDERIV1[1]*AREAW1+(NU+NUT2/SIGM
A_K)*GDERIV2[1]*GDERIV2[1]*AREAW2+(NU+NUT3/SIGMA_K)*GDERIV3[1]*GDERIV3[1]*ARE
AW3)+(GAMMA1*SHAPE1[1]*SHAPE1[1]*AREAW1+GAMMA2*SHAPE2[1]*SHAPE2[1]*AREAW2+GAM
MA3*SHAPE3[1]*SHAPE3[1]*AREAW3)
       LK[1,2] =
((SHAPE1[1]*SHAPE1[2]*AREAW1+SHAPE2[1]*SHAPE2[2]*AREAW2+SHAPE3[1]*SHAPE3[2]*A
REAW3)/DELTA_T)+((NU+NUT1/SIGMA_K)*GDERIV1[1]*GDERIV1[2]*AREAW1+(NU+NUT2/SIGM
A_K)*GDERIV2[1]*GDERIV2[2]*AREAW2+(NU+NUT3/SIGMA_K)*GDERIV3[1]*GDERIV3[2]*ARE
AW3)+(GAMMA1*SHAPE1[1]*SHAPE1[2]*AREAW1+GAMMA2*SHAPE2[1]*SHAPE2[2]*AREAW2+GAM
MA3*SHAPE3[1]*SHAPE3[2]*AREAW3)

       LK[2,0] =
((SHAPE1[2]*SHAPE1[0]*AREAW1+SHAPE2[2]*SHAPE2[0]*AREAW2+SHAPE3[2]*SHAPE3[0]*A
REAW3)/DELTA_T)+((NU+NUT1/SIGMA_K)*GDERIV1[2]*GDERIV1[0]*AREAW1+(NU+NUT2/SIGM
A_K)*GDERIV2[2]*GDERIV2[0]*AREAW2+(NU+NUT3/SIGMA_K)*GDERIV3[2]*GDERIV3[0]*ARE
AW3)+(GAMMA1*SHAPE1[2]*SHAPE1[0]*AREAW1+GAMMA2*SHAPE2[2]*SHAPE2[0]*AREAW2+GAM
MA3*SHAPE3[2]*SHAPE3[0]*AREAW3)
```

```
       LK[2,1] =
((SHAPE1[2]*SHAPE1[1]*AREAW1+SHAPE2[2]*SHAPE2[1]*AREAW2+SHAPE3[2]*SHAPE3[1]*A
REAW3)/DELTA_T)+((NU+NUT1/SIGMA_K)*GDERIV1[2]*GDERIV1[1]*AREAW1+(NU+NUT2/SIGM
A_K)*GDERIV2[2]*GDERIV2[1]*AREAW2+(NU+NUT3/SIGMA_K)*GDERIV3[2]*GDERIV3[1]*ARE
AW3)+(GAMMA1*SHAPE1[2]*SHAPE1[1]*AREAW1+GAMMA2*SHAPE2[2]*SHAPE2[1]*AREAW2+GAM
MA3*SHAPE3[2]*SHAPE3[1]*AREAW3)
       LK[2,2] =
((SHAPE1[2]*SHAPE1[2]*AREAW1+SHAPE2[2]*SHAPE2[2]*AREAW2+SHAPE3[2]*SHAPE3[2]*A
REAW3)/DELTA_T)+((NU+NUT1/SIGMA_K)*GDERIV1[2]*GDERIV1[2]*AREAW1+(NU+NUT2/SIGM
A_K)*GDERIV2[2]*GDERIV2[2]*AREAW2+(NU+NUT3/SIGMA_K)*GDERIV3[2]*GDERIV3[2]*ARE
AW3)+(GAMMA1*SHAPE1[2]*SHAPE1[2]*AREAW1+GAMMA2*SHAPE2[2]*SHAPE2[2]*AREAW2+GAM
MA3*SHAPE3[2]*SHAPE3[2]*AREAW3)

#      FOR EPSILON
       LEP[0,0] =
((SHAPE1[0]*SHAPE1[0]*AREAW1+SHAPE2[0]*SHAPE2[0]*AREAW2+SHAPE3[0]*SHAPE3[0]*A
REAW3)/DELTA_T)+((NU+NUT1/SIGMA_EP)*GDERIV1[0]*GDERIV1[0]*AREAW1+(NU+NUT2/SIG
MA_EP)*GDERIV2[0]*GDERIV2[0]*AREAW2+(NU+NUT3/SIGMA_EP)*GDERIV3[0]*GDERIV3[0]*
AREAW3)+(C2*GAMMA1*SHAPE1[0]*SHAPE1[0]*AREAW1+C2*GAMMA2*SHAPE2[0]*SHAPE2[0]*A
REAW2+C2*GAMMA3*SHAPE3[0]*SHAPE3[0]*AREAW3)
       LEP[0,1] =
((SHAPE1[0]*SHAPE1[1]*AREAW1+SHAPE2[0]*SHAPE2[1]*AREAW2+SHAPE3[0]*SHAPE3[1]*A
REAW3)/DELTA_T)+((NU+NUT1/SIGMA_EP)*GDERIV1[0]*GDERIV1[1]*AREAW1+(NU+NUT2/SIG
MA_EP)*GDERIV2[0]*GDERIV2[1]*AREAW2+(NU+NUT3/SIGMA_EP)*GDERIV3[0]*GDERIV3[1]*
AREAW3)+(C2*GAMMA1*SHAPE1[0]*SHAPE1[1]*AREAW1+C2*GAMMA2*SHAPE2[0]*SHAPE2[1]*A
REAW2+C2*GAMMA3*SHAPE3[0]*SHAPE3[1]*AREAW3)
       LEP[0,2] =
((SHAPE1[0]*SHAPE1[2]*AREAW1+SHAPE2[0]*SHAPE2[2]*AREAW2+SHAPE3[0]*SHAPE3[2]*A
REAW3)/DELTA_T)+((NU+NUT1/SIGMA_EP)*GDERIV1[0]*GDERIV1[2]*AREAW1+(NU+NUT2/SIG
MA_EP)*GDERIV2[0]*GDERIV2[2]*AREAW2+(NU+NUT3/SIGMA_EP)*GDERIV3[0]*GDERIV3[2]*
AREAW3)+(C2*GAMMA1*SHAPE1[0]*SHAPE1[2]*AREAW1+C2*GAMMA2*SHAPE2[0]*SHAPE2[2]*A
REAW2+C2*GAMMA3*SHAPE3[0]*SHAPE3[2]*AREAW3)

       LEP[1,0] =
((SHAPE1[1]*SHAPE1[0]*AREAW1+SHAPE2[1]*SHAPE2[0]*AREAW2+SHAPE3[1]*SHAPE3[0]*A
REAW3)/DELTA_T)+((NU+NUT1/SIGMA_EP)*GDERIV1[1]*GDERIV1[0]*AREAW1+(NU+NUT2/SIG
MA_EP)*GDERIV2[1]*GDERIV2[0]*AREAW2+(NU+NUT3/SIGMA_EP)*GDERIV3[1]*GDERIV3[0]*
AREAW3)+(C2*GAMMA1*SHAPE1[1]*SHAPE1[0]*AREAW1+C2*GAMMA2*SHAPE2[1]*SHAPE2[0]*A
REAW2+C2*GAMMA3*SHAPE3[1]*SHAPE3[0]*AREAW3)
       LEP[1,1] =
((SHAPE1[1]*SHAPE1[1]*AREAW1+SHAPE2[1]*SHAPE2[1]*AREAW2+SHAPE3[1]*SHAPE3[1]*A
REAW3)/DELTA_T)+((NU+NUT1/SIGMA_EP)*GDERIV1[1]*GDERIV1[1]*AREAW1+(NU+NUT2/SIG
MA_EP)*GDERIV2[1]*GDERIV2[1]*AREAW2+(NU+NUT3/SIGMA_EP)*GDERIV3[1]*GDERIV3[1]*
AREAW3)+(C2*GAMMA1*SHAPE1[1]*SHAPE1[1]*AREAW1+C2*GAMMA2*SHAPE2[1]*SHAPE2[1]*A
REAW2+C2*GAMMA3*SHAPE3[1]*SHAPE3[1]*AREAW3)
       LEP[1,2] =
((SHAPE1[1]*SHAPE1[2]*AREAW1+SHAPE2[1]*SHAPE2[2]*AREAW2+SHAPE3[1]*SHAPE3[2]*A
REAW3)/DELTA_T)+((NU+NUT1/SIGMA_EP)*GDERIV1[1]*GDERIV1[2]*AREAW1+(NU+NUT2/SIG
MA_EP)*GDERIV2[1]*GDERIV2[2]*AREAW2+(NU+NUT3/SIGMA_EP)*GDERIV3[1]*GDERIV3[2]*
AREAW3)+(C2*GAMMA1*SHAPE1[1]*SHAPE1[2]*AREAW1+C2*GAMMA2*SHAPE2[1]*SHAPE2[2]*A
REAW2+C2*GAMMA3*SHAPE3[1]*SHAPE3[2]*AREAW3)

       LEP[2,0] =
((SHAPE1[2]*SHAPE1[0]*AREAW1+SHAPE2[2]*SHAPE2[0]*AREAW2+SHAPE3[2]*SHAPE3[0]*A
REAW3)/DELTA_T)+((NU+NUT1/SIGMA_EP)*GDERIV1[2]*GDERIV1[0]*AREAW1+(NU+NUT2/SIG
MA_EP)*GDERIV2[2]*GDERIV2[0]*AREAW2+(NU+NUT3/SIGMA_EP)*GDERIV3[2]*GDERIV3[0]*
```

```
AREAW3)+(C2*GAMMA1*SHAPE1[2]*SHAPE1[0]*AREAW1+C2*GAMMA2*SHAPE2[2]*SHAPE2[0]*A
REAW2+C2*GAMMA3*SHAPE3[2]*SHAPE3[0]*AREAW3)
       LEP[2,1] =
((SHAPE1[2]*SHAPE1[1]*AREAW1+SHAPE2[2]*SHAPE2[1]*AREAW2+SHAPE3[2]*SHAPE3[1]*A
REAW3)/DELTA_T)+((NU+NUT1/SIGMA_EP)*GDERIV1[2]*GDERIV1[1]*AREAW1+(NU+NUT2/SIG
MA_EP)*GDERIV2[2]*GDERIV2[1]*AREAW2+(NU+NUT3/SIGMA_EP)*GDERIV3[2]*GDERIV3[1]*
AREAW3)+(C2*GAMMA1*SHAPE1[2]*SHAPE1[1]*AREAW1+C2*GAMMA2*SHAPE2[2]*SHAPE2[1]*A
REAW2+C2*GAMMA3*SHAPE3[2]*SHAPE3[1]*AREAW3)
       LEP[2,2] =
((SHAPE1[2]*SHAPE1[2]*AREAW1+SHAPE2[2]*SHAPE2[2]*AREAW2+SHAPE3[2]*SHAPE3[2]*A
REAW3)/DELTA_T)+((NU+NUT1/SIGMA_EP)*GDERIV1[2]*GDERIV1[2]*AREAW1+(NU+NUT2/SIG
MA_EP)*GDERIV2[2]*GDERIV2[2]*AREAW2+(NU+NUT3/SIGMA_EP)*GDERIV3[2]*GDERIV3[2]*
AREAW3)+(C2*GAMMA1*SHAPE1[2]*SHAPE1[2]*AREAW1+C2*GAMMA2*SHAPE2[2]*SHAPE2[2]*A
REAW2+C2*GAMMA3*SHAPE3[2]*SHAPE3[2]*AREAW3)

#      ASSEMBLE THE GLOBAL MATRIX
       for IDIME in range(0,NNODL):
           for JDIME in range(0,NNODL):
               GK[LNODS[IELEM,IDIME],LNODS[IELEM,JDIME]] =
GK[LNODS[IELEM,IDIME],LNODS[IELEM,JDIME]]+LK[IDIME,JDIME]
               GEP[LNODS[IELEM,IDIME],LNODS[IELEM,JDIME]] =
GEP[LNODS[IELEM,IDIME],LNODS[IELEM,JDIME]]+LEP[IDIME,JDIME]

#      FORM THE LOCAL RHS COEFFICIENTS AND ASSEMBLE INTO GLOBAL RHS VECTOR

#      (DUX_DZ)**2 AT GAUSS POINTS
       DUX_DZ_S1 =
(GDERIV1[0]*UXN[LNODS[IELEM,0]]+GDERIV1[1]*UXN[LNODS[IELEM,1]]+GDERIV1[2]*UXN
[LNODS[IELEM,2]])**2
       DUX_DZ_S2 =
(GDERIV2[0]*UXN[LNODS[IELEM,0]]+GDERIV2[1]*UXN[LNODS[IELEM,1]]+GDERIV2[2]*UXN
[LNODS[IELEM,2]])**2
       DUX_DZ_S3 =
(GDERIV3[0]*UXN[LNODS[IELEM,0]]+GDERIV3[1]*UXN[LNODS[IELEM,1]]+GDERIV3[2]*UXN
[LNODS[IELEM,2]])**2

#      CONSTRUCT THE LOCAL VECTOR OF RHS
       LFK[0] =
((K1*SHAPE1[0]*AREAW1+K2*SHAPE2[0]*AREAW2+K3*SHAPE3[0]*AREAW3)/DELTA_T)+(NUT1
*DUX_DZ_S1*SHAPE1[0]*AREAW1+NUT2*DUX_DZ_S2*SHAPE2[0]*AREAW2+NUT3*DUX_DZ_S3*SH
APE3[0]*AREAW3)
       LFK[1] =
((K1*SHAPE1[1]*AREAW1+K2*SHAPE2[1]*AREAW2+K3*SHAPE3[1]*AREAW3)/DELTA_T)+(NUT1
*DUX_DZ_S1*SHAPE1[1]*AREAW1+NUT2*DUX_DZ_S2*SHAPE2[1]*AREAW2+NUT3*DUX_DZ_S3*SH
APE3[1]*AREAW3)
       LFK[2] =
((K1*SHAPE1[2]*AREAW1+K2*SHAPE2[2]*AREAW2+K3*SHAPE3[2]*AREAW3)/DELTA_T)+(NUT1
*DUX_DZ_S1*SHAPE1[2]*AREAW1+NUT2*DUX_DZ_S2*SHAPE2[2]*AREAW2+NUT3*DUX_DZ_S3*SH
APE3[2]*AREAW3)

       LFEP[0] =
((EP1*SHAPE1[0]*AREAW1+EP2*SHAPE2[0]*AREAW2+EP3*SHAPE3[0]*AREAW3)/DELTA_T)+(C
1*GAMMA1*NUT1*DUX_DZ_S1*SHAPE1[0]*AREAW1+C1*GAMMA2*NUT2*DUX_DZ_S2*SHAPE2[0]*A
REAW2+C1*GAMMA3*NUT3*DUX_DZ_S3*SHAPE3[0]*AREAW3)
       LFEP[1] =
((EP1*SHAPE1[1]*AREAW1+EP2*SHAPE2[1]*AREAW2+EP3*SHAPE3[1]*AREAW3)/DELTA_T)+(C
```

```
1*GAMMA1*NUT1*DUX_DZ_S1*SHAPE1[1]*AREAW1+C1*GAMMA2*NUT2*DUX_DZ_S2*SHAPE2[1]*A
REAW2+C1*GAMMA3*NUT3*DUX_DZ_S3*SHAPE3[1]*AREAW3)
       LFEP[2] =
((EP1*SHAPE1[2]*AREAW1+EP2*SHAPE2[2]*AREAW2+EP3*SHAPE3[2]*AREAW3)/DELTA_T)+(C
1*GAMMA1*NUT1*DUX_DZ_S1*SHAPE1[2]*AREAW1+C1*GAMMA2*NUT2*DUX_DZ_S2*SHAPE2[2]*A
REAW2+C1*GAMMA3*NUT3*DUX_DZ_S3*SHAPE3[2]*AREAW3)

       for IDIME in range(0,NNODL):
           GFK[LNODS[IELEM,IDIME]] = GFK[LNODS[IELEM,IDIME]]+LFK[IDIME]
           GFEP[LNODS[IELEM,IDIME]] = GFEP[LNODS[IELEM,IDIME]]+LFEP[IDIME]

#  DEAL WITH THE BOUNDARY CONDITIONS
   for IPOIN in range(0,NPOIN):
#      WALL BOUNDARY
       GK[2,IPOIN] = 0.0
       GEP[2,IPOIN] = 0.0
#      FREE SURFACE
       GK[NPOIN-1,IPOIN] = 0.0

#  WALL BOUNDARY
   GK[2,2] = 1.0
   GEP[2,2] = 1.0
#  FREE SURFACE
   GK[NPOIN-1,NPOIN-1] = 1.0

#  IMPOSE BOUNDARY VALUES
#  WALL BOUNDARY
   GFK[2] = KN[2]
   GFEP[2] = EPN[2]
#  FREE SURFACE
   GFK[NPOIN-1] = 0.0

#  SOLVE LINEAR EQUATIONS
   K[2:] = np.linalg.solve(GK[2:,2:],GFK[2:])
   EP[2:] = np.linalg.solve(GEP[2:,2:],GFEP[2:])

#  UPDATE NU_T
   K[0]=KN[0]
   K[1]=KN[1]
   EP[0]=EPN[0]
   EP[1]=EPN[1]
   NU_T=CMU*K**2/EP

   return K, EP, NU_T

#============================================================

def
SOLVE_1D_KEPSILON_SED(COORD,LNODS,NPOIN,NELEM,NNODL,POSGP,WEIGP,DELTA_T,NU,RH
O_W,RHO_S,KN,EPN,UXN,CN):

#  INITIALIZE VARIABLES
   GK = np.zeros((NPOIN,NPOIN))
   GFK = np.zeros(NPOIN)
   LK = np.zeros((NNODL,NNODL))
   LFK = np.zeros(NNODL)
```

```
   GEP = np.zeros((NPOIN,NPOIN))
   GFEP = np.zeros(NPOIN)
   LEP = np.zeros((NNODL,NNODL))
   LFEP = np.zeros(NNODL)

   K = np.zeros(NPOIN)
   EP = np.zeros(NPOIN)

#  DEFINE CONSTANTS
   SIGMA_K = 1.0
   SIGMA_EP = 1.3
   CMU = 0.09
   C1 = 1.44
   C2 = 1.92
   G = 9.81
   SIGMA_0 = 0.7

#  MIXTURE BULK DENSITY
   RHO = RHO_W+(1-RHO_W/RHO_S)*(CN*RHO_S)

#  LOOP FOR ALL THE ELEMENTS
   for IELEM in range(1,NELEM):

#      SHAPE FUNCTIONS AT GAUSS POINT 1
       SHAPE1, DERIV1, SDERIV1 = SHAPE_LINE_QUADRATIC_S(POSGP[0])
       DJACK1, DJACI1 = DJACOB_LINE(COORD,LNODS,NNODL,IELEM,DERIV1)
#      SHAPE FUNCTIONS AT GAUSS POINT 2
       SHAPE2, DERIV2, SDERIV2 = SHAPE_LINE_QUADRATIC_S(POSGP[1])
       DJACK2, DJACI2 = DJACOB_LINE(COORD,LNODS,NNODL,IELEM,DERIV2)
#      SHAPE FUNCTIONS AT GAUSS POINT 3
       SHAPE3, DERIV3, SDERIV3 = SHAPE_LINE_QUADRATIC_S(POSGP[2])
       DJACK3, DJACI3 = DJACOB_LINE(COORD,LNODS,NNODL,IELEM,DERIV3)

#      GLOBAL DERIVATIVE AND GAUSS WEIGHTING AREAS AT GAUSS POINTS
       GDERIV1 = DJACI1*DERIV1
       GDERIV2 = DJACI2*DERIV2
       GDERIV3 = DJACI3*DERIV3

       AREAW1 = DJACK1*WEIGP[0]
       AREAW2 = DJACK2*WEIGP[1]
       AREAW3 = DJACK3*WEIGP[2]

#      K AT GAUSS POINTS
       K1 =
SHAPE1[0]*KN[LNODS[IELEM,0]]+SHAPE1[1]*KN[LNODS[IELEM,1]]+SHAPE1[2]*KN[LNODS[
IELEM,2]]
       K2 =
SHAPE2[0]*KN[LNODS[IELEM,0]]+SHAPE2[1]*KN[LNODS[IELEM,1]]+SHAPE2[2]*KN[LNODS[
IELEM,2]]
       K3 =
SHAPE3[0]*KN[LNODS[IELEM,0]]+SHAPE3[1]*KN[LNODS[IELEM,1]]+SHAPE3[2]*KN[LNODS[
IELEM,2]]

#      EPSILON AT GAUSS POINTS
       EP1 =
SHAPE1[0]*EPN[LNODS[IELEM,0]]+SHAPE1[1]*EPN[LNODS[IELEM,1]]+SHAPE1[2]*EPN[LNO
DS[IELEM,2]]
```

```
      EP2 =
SHAPE2[0]*EPN[LNODS[IELEM,0]]+SHAPE2[1]*EPN[LNODS[IELEM,1]]+SHAPE2[2]*EPN[LNO
DS[IELEM,2]]
      EP3 =
SHAPE3[0]*EPN[LNODS[IELEM,0]]+SHAPE3[1]*EPN[LNODS[IELEM,1]]+SHAPE3[2]*EPN[LNO
DS[IELEM,2]]

#     GAMMA AT GAUSS POINTS
      GAMMA1 = EP1/K1
      GAMMA2 = EP2/K2
      GAMMA3 = EP3/K3

#     EDDY VISCOSITY AT GAUSS POINTS
      NUT1 = CMU*K1**2/EP1
      NUT2 = CMU*K2**2/EP2
      NUT3 = CMU*K3**2/EP3

#     CONSTRUCT THE LOCAL MATRIX OF COEFFICIENT

#     FOR K
      LK[0,0] =
((SHAPE1[0]*SHAPE1[0]*AREAW1+SHAPE2[0]*SHAPE2[0]*AREAW2+SHAPE3[0]*SHAPE3[0]*A
REAW3)/DELTA_T)+((NU+NUT1/SIGMA_K)*GDERIV1[0]*GDERIV1[0]*AREAW1+(NU+NUT2/SIGM
A_K)*GDERIV2[0]*GDERIV2[0]*AREAW2+(NU+NUT3/SIGMA_K)*GDERIV3[0]*GDERIV3[0]*ARE
AW3)+(GAMMA1*SHAPE1[0]*SHAPE1[0]*AREAW1+GAMMA2*SHAPE2[0]*SHAPE2[0]*AREAW2+GAM
MA3*SHAPE3[0]*SHAPE3[0]*AREAW3)
      LK[0,1] =
((SHAPE1[0]*SHAPE1[1]*AREAW1+SHAPE2[0]*SHAPE2[1]*AREAW2+SHAPE3[0]*SHAPE3[1]*A
REAW3)/DELTA_T)+((NU+NUT1/SIGMA_K)*GDERIV1[0]*GDERIV1[1]*AREAW1+(NU+NUT2/SIGM
A_K)*GDERIV2[0]*GDERIV2[1]*AREAW2+(NU+NUT3/SIGMA_K)*GDERIV3[0]*GDERIV3[1]*ARE
AW3)+(GAMMA1*SHAPE1[0]*SHAPE1[1]*AREAW1+GAMMA2*SHAPE2[0]*SHAPE2[1]*AREAW2+GAM
MA3*SHAPE3[0]*SHAPE3[1]*AREAW3)
      LK[0,2] =
((SHAPE1[0]*SHAPE1[2]*AREAW1+SHAPE2[0]*SHAPE2[2]*AREAW2+SHAPE3[0]*SHAPE3[2]*A
REAW3)/DELTA_T)+((NU+NUT1/SIGMA_K)*GDERIV1[0]*GDERIV1[2]*AREAW1+(NU+NUT2/SIGM
A_K)*GDERIV2[0]*GDERIV2[2]*AREAW2+(NU+NUT3/SIGMA_K)*GDERIV3[0]*GDERIV3[2]*ARE
AW3)+(GAMMA1*SHAPE1[0]*SHAPE1[2]*AREAW1+GAMMA2*SHAPE2[0]*SHAPE2[2]*AREAW2+GAM
MA3*SHAPE3[0]*SHAPE3[2]*AREAW3)

      LK[1,0] =
((SHAPE1[1]*SHAPE1[0]*AREAW1+SHAPE2[1]*SHAPE2[0]*AREAW2+SHAPE3[1]*SHAPE3[0]*A
REAW3)/DELTA_T)+((NU+NUT1/SIGMA_K)*GDERIV1[1]*GDERIV1[0]*AREAW1+(NU+NUT2/SIGM
A_K)*GDERIV2[1]*GDERIV2[0]*AREAW2+(NU+NUT3/SIGMA_K)*GDERIV3[1]*GDERIV3[0]*ARE
AW3)+(GAMMA1*SHAPE1[1]*SHAPE1[0]*AREAW1+GAMMA2*SHAPE2[1]*SHAPE2[0]*AREAW2+GAM
MA3*SHAPE3[1]*SHAPE3[0]*AREAW3)
      LK[1,1] =
((SHAPE1[1]*SHAPE1[1]*AREAW1+SHAPE2[1]*SHAPE2[1]*AREAW2+SHAPE3[1]*SHAPE3[1]*A
REAW3)/DELTA_T)+((NU+NUT1/SIGMA_K)*GDERIV1[1]*GDERIV1[1]*AREAW1+(NU+NUT2/SIGM
A_K)*GDERIV2[1]*GDERIV2[1]*AREAW2+(NU+NUT3/SIGMA_K)*GDERIV3[1]*GDERIV3[1]*ARE
AW3)+(GAMMA1*SHAPE1[1]*SHAPE1[1]*AREAW1+GAMMA2*SHAPE2[1]*SHAPE2[1]*AREAW2+GAM
MA3*SHAPE3[1]*SHAPE3[1]*AREAW3)
      LK[1,2] =
((SHAPE1[1]*SHAPE1[2]*AREAW1+SHAPE2[1]*SHAPE2[2]*AREAW2+SHAPE3[1]*SHAPE3[2]*A
REAW3)/DELTA_T)+((NU+NUT1/SIGMA_K)*GDERIV1[1]*GDERIV1[2]*AREAW1+(NU+NUT2/SIGM
A_K)*GDERIV2[1]*GDERIV2[2]*AREAW2+(NU+NUT3/SIGMA_K)*GDERIV3[1]*GDERIV3[2]*ARE
AW3)+(GAMMA1*SHAPE1[1]*SHAPE1[2]*AREAW1+GAMMA2*SHAPE2[1]*SHAPE2[2]*AREAW2+GAM
MA3*SHAPE3[1]*SHAPE3[2]*AREAW3)
```

```
       LK[2,0] =
((SHAPE1[2]*SHAPE1[0]*AREAW1+SHAPE2[2]*SHAPE2[0]*AREAW2+SHAPE3[2]*SHAPE3[0]*A
REAW3)/DELTA_T)+((NU+NUT1/SIGMA_K)*GDERIV1[2]*GDERIV1[0]*AREAW1+(NU+NUT2/SIGM
A_K)*GDERIV2[2]*GDERIV2[0]*AREAW2+(NU+NUT3/SIGMA_K)*GDERIV3[2]*GDERIV3[0]*ARE
AW3)+(GAMMA1*SHAPE1[2]*SHAPE1[0]*AREAW1+GAMMA2*SHAPE2[2]*SHAPE2[0]*AREAW2+GAM
MA3*SHAPE3[2]*SHAPE3[0]*AREAW3)
       LK[2,1] =
((SHAPE1[2]*SHAPE1[1]*AREAW1+SHAPE2[2]*SHAPE2[1]*AREAW2+SHAPE3[2]*SHAPE3[1]*A
REAW3)/DELTA_T)+((NU+NUT1/SIGMA_K)*GDERIV1[2]*GDERIV1[1]*AREAW1+(NU+NUT2/SIGM
A_K)*GDERIV2[2]*GDERIV2[1]*AREAW2+(NU+NUT3/SIGMA_K)*GDERIV3[2]*GDERIV3[1]*ARE
AW3)+(GAMMA1*SHAPE1[2]*SHAPE1[1]*AREAW1+GAMMA2*SHAPE2[2]*SHAPE2[1]*AREAW2+GAM
MA3*SHAPE3[2]*SHAPE3[1]*AREAW3)
       LK[2,2] =
((SHAPE1[2]*SHAPE1[2]*AREAW1+SHAPE2[2]*SHAPE2[2]*AREAW2+SHAPE3[2]*SHAPE3[2]*A
REAW3)/DELTA_T)+((NU+NUT1/SIGMA_K)*GDERIV1[2]*GDERIV1[2]*AREAW1+(NU+NUT2/SIGM
A_K)*GDERIV2[2]*GDERIV2[2]*AREAW2+(NU+NUT3/SIGMA_K)*GDERIV3[2]*GDERIV3[2]*ARE
AW3)+(GAMMA1*SHAPE1[2]*SHAPE1[2]*AREAW1+GAMMA2*SHAPE2[2]*SHAPE2[2]*AREAW2+GAM
MA3*SHAPE3[2]*SHAPE3[2]*AREAW3)

#      FOR EPSILON
       LEP[0,0] =
((SHAPE1[0]*SHAPE1[0]*AREAW1+SHAPE2[0]*SHAPE2[0]*AREAW2+SHAPE3[0]*SHAPE3[0]*A
REAW3)/DELTA_T)+((NU+NUT1/SIGMA_EP)*GDERIV1[0]*GDERIV1[0]*AREAW1+(NU+NUT2/SIG
MA_EP)*GDERIV2[0]*GDERIV2[0]*AREAW2+(NU+NUT3/SIGMA_EP)*GDERIV3[0]*GDERIV3[0]*
AREAW3)+(C2*GAMMA1*SHAPE1[0]*SHAPE1[0]*AREAW1+C2*GAMMA2*SHAPE2[0]*SHAPE2[0]*A
REAW2+C2*GAMMA3*SHAPE3[0]*SHAPE3[0]*AREAW3)
       LEP[0,1] =
((SHAPE1[0]*SHAPE1[1]*AREAW1+SHAPE2[0]*SHAPE2[1]*AREAW2+SHAPE3[0]*SHAPE3[1]*A
REAW3)/DELTA_T)+((NU+NUT1/SIGMA_EP)*GDERIV1[0]*GDERIV1[1]*AREAW1+(NU+NUT2/SIG
MA_EP)*GDERIV2[0]*GDERIV2[1]*AREAW2+(NU+NUT3/SIGMA_EP)*GDERIV3[0]*GDERIV3[1]*
AREAW3)+(C2*GAMMA1*SHAPE1[0]*SHAPE1[1]*AREAW1+C2*GAMMA2*SHAPE2[0]*SHAPE2[1]*A
REAW2+C2*GAMMA3*SHAPE3[0]*SHAPE3[1]*AREAW3)
       LEP[0,2] =
((SHAPE1[0]*SHAPE1[2]*AREAW1+SHAPE2[0]*SHAPE2[2]*AREAW2+SHAPE3[0]*SHAPE3[2]*A
REAW3)/DELTA_T)+((NU+NUT1/SIGMA_EP)*GDERIV1[0]*GDERIV1[2]*AREAW1+(NU+NUT2/SIG
MA_EP)*GDERIV2[0]*GDERIV2[2]*AREAW2+(NU+NUT3/SIGMA_EP)*GDERIV3[0]*GDERIV3[2]*
AREAW3)+(C2*GAMMA1*SHAPE1[0]*SHAPE1[2]*AREAW1+C2*GAMMA2*SHAPE2[0]*SHAPE2[2]*A
REAW2+C2*GAMMA3*SHAPE3[0]*SHAPE3[2]*AREAW3)

       LEP[1,0] =
((SHAPE1[1]*SHAPE1[0]*AREAW1+SHAPE2[1]*SHAPE2[0]*AREAW2+SHAPE3[1]*SHAPE3[0]*A
REAW3)/DELTA_T)+((NU+NUT1/SIGMA_EP)*GDERIV1[1]*GDERIV1[0]*AREAW1+(NU+NUT2/SIG
MA_EP)*GDERIV2[1]*GDERIV2[0]*AREAW2+(NU+NUT3/SIGMA_EP)*GDERIV3[1]*GDERIV3[0]*
AREAW3)+(C2*GAMMA1*SHAPE1[1]*SHAPE1[0]*AREAW1+C2*GAMMA2*SHAPE2[1]*SHAPE2[0]*A
REAW2+C2*GAMMA3*SHAPE3[1]*SHAPE3[0]*AREAW3)
       LEP[1,1] =
((SHAPE1[1]*SHAPE1[1]*AREAW1+SHAPE2[1]*SHAPE2[1]*AREAW2+SHAPE3[1]*SHAPE3[1]*A
REAW3)/DELTA_T)+((NU+NUT1/SIGMA_EP)*GDERIV1[1]*GDERIV1[1]*AREAW1+(NU+NUT2/SIG
MA_EP)*GDERIV2[1]*GDERIV2[1]*AREAW2+(NU+NUT3/SIGMA_EP)*GDERIV3[1]*GDERIV3[1]*
AREAW3)+(C2*GAMMA1*SHAPE1[1]*SHAPE1[1]*AREAW1+C2*GAMMA2*SHAPE2[1]*SHAPE2[1]*A
REAW2+C2*GAMMA3*SHAPE3[1]*SHAPE3[1]*AREAW3)
       LEP[1,2] =
((SHAPE1[1]*SHAPE1[2]*AREAW1+SHAPE2[1]*SHAPE2[2]*AREAW2+SHAPE3[1]*SHAPE3[2]*A
REAW3)/DELTA_T)+((NU+NUT1/SIGMA_EP)*GDERIV1[1]*GDERIV1[2]*AREAW1+(NU+NUT2/SIG
MA_EP)*GDERIV2[1]*GDERIV2[2]*AREAW2+(NU+NUT3/SIGMA_EP)*GDERIV3[1]*GDERIV3[2]*
```

```
AREAW3)+(C2*GAMMA1*SHAPE1[1]*SHAPE1[2]*AREAW1+C2*GAMMA2*SHAPE2[1]*SHAPE2[2]*A
REAW2+C2*GAMMA3*SHAPE3[1]*SHAPE3[2]*AREAW3)

       LEP[2,0] =
((SHAPE1[2]*SHAPE1[0]*AREAW1+SHAPE2[2]*SHAPE2[0]*AREAW2+SHAPE3[2]*SHAPE3[0]*A
REAW3)/DELTA_T)+((NU+NUT1/SIGMA_EP)*GDERIV1[2]*GDERIV1[0]*AREAW1+(NU+NUT2/SIG
MA_EP)*GDERIV2[2]*GDERIV2[0]*AREAW2+(NU+NUT3/SIGMA_EP)*GDERIV3[2]*GDERIV3[0]*
AREAW3)+(C2*GAMMA1*SHAPE1[2]*SHAPE1[0]*AREAW1+C2*GAMMA2*SHAPE2[2]*SHAPE2[0]*A
REAW2+C2*GAMMA3*SHAPE3[2]*SHAPE3[0]*AREAW3)
       LEP[2,1] =
((SHAPE1[2]*SHAPE1[1]*AREAW1+SHAPE2[2]*SHAPE2[1]*AREAW2+SHAPE3[2]*SHAPE3[1]*A
REAW3)/DELTA_T)+((NU+NUT1/SIGMA_EP)*GDERIV1[2]*GDERIV1[1]*AREAW1+(NU+NUT2/SIG
MA_EP)*GDERIV2[2]*GDERIV2[1]*AREAW2+(NU+NUT3/SIGMA_EP)*GDERIV3[2]*GDERIV3[1]*
AREAW3)+(C2*GAMMA1*SHAPE1[2]*SHAPE1[1]*AREAW1+C2*GAMMA2*SHAPE2[2]*SHAPE2[1]*A
REAW2+C2*GAMMA3*SHAPE3[2]*SHAPE3[1]*AREAW3)
       LEP[2,2] =
((SHAPE1[2]*SHAPE1[2]*AREAW1+SHAPE2[2]*SHAPE2[2]*AREAW2+SHAPE3[2]*SHAPE3[2]*A
REAW3)/DELTA_T)+((NU+NUT1/SIGMA_EP)*GDERIV1[2]*GDERIV1[2]*AREAW1+(NU+NUT2/SIG
MA_EP)*GDERIV2[2]*GDERIV2[2]*AREAW2+(NU+NUT3/SIGMA_EP)*GDERIV3[2]*GDERIV3[2]*
AREAW3)+(C2*GAMMA1*SHAPE1[2]*SHAPE1[2]*AREAW1+C2*GAMMA2*SHAPE2[2]*SHAPE2[2]*A
REAW2+C2*GAMMA3*SHAPE3[2]*SHAPE3[2]*AREAW3)

#      ASSEMBLE THE GLOBAL MATRIX
       for IDIME in range(0,NNODL):
           for JDIME in range(0,NNODL):
               GK[LNODS[IELEM,IDIME],LNODS[IELEM,JDIME]] =
GK[LNODS[IELEM,IDIME],LNODS[IELEM,JDIME]]+LK[IDIME,JDIME]
               GEP[LNODS[IELEM,IDIME],LNODS[IELEM,JDIME]] =
GEP[LNODS[IELEM,IDIME],LNODS[IELEM,JDIME]]+LEP[IDIME,JDIME]

#      FORM THE LOCAL RHS COEFFICIENTS AND ASSEMBLE INTO GLOBAL RHS VECTOR

#      (DUX_DZ)**2 AT GAUSS POINTS
       DUX_DZ_S1 =
(GDERIV1[0]*UXN[LNODS[IELEM,0]]+GDERIV1[1]*UXN[LNODS[IELEM,1]]+GDERIV1[2]*UXN
[LNODS[IELEM,2]])**2
       DUX_DZ_S2 =
(GDERIV2[0]*UXN[LNODS[IELEM,0]]+GDERIV2[1]*UXN[LNODS[IELEM,1]]+GDERIV2[2]*UXN
[LNODS[IELEM,2]])**2
       DUX_DZ_S3 =
(GDERIV3[0]*UXN[LNODS[IELEM,0]]+GDERIV3[1]*UXN[LNODS[IELEM,1]]+GDERIV3[2]*UXN
[LNODS[IELEM,2]])**2

#      RHO AND DRHO_DZ AT GAUSS POINTS
       RHO1 =
SHAPE1[0]*RHO[LNODS[IELEM,0]]+SHAPE1[1]*RHO[LNODS[IELEM,1]]+SHAPE1[2]*RHO[LNO
DS[IELEM,2]]
       RHO2 =
SHAPE2[0]*RHO[LNODS[IELEM,0]]+SHAPE2[1]*RHO[LNODS[IELEM,1]]+SHAPE2[2]*RHO[LNO
DS[IELEM,2]]
       RHO3 =
SHAPE3[0]*RHO[LNODS[IELEM,0]]+SHAPE3[1]*RHO[LNODS[IELEM,1]]+SHAPE3[2]*RHO[LNO
DS[IELEM,2]]

       DRHO_DZ1 =
GDERIV1[0]*RHO[LNODS[IELEM,0]]+GDERIV1[1]*RHO[LNODS[IELEM,1]]+GDERIV1[2]*RHO[
LNODS[IELEM,2]]
```

```
       DRHO_DZ2 =
GDERIV2[0]*RHO[LNODS[IELEM,0]]+GDERIV2[1]*RHO[LNODS[IELEM,1]]+GDERIV2[2]*RHO[
LNODS[IELEM,2]]
       DRHO_DZ3 =
GDERIV3[0]*RHO[LNODS[IELEM,0]]+GDERIV3[1]*RHO[LNODS[IELEM,1]]+GDERIV3[2]*RHO[
LNODS[IELEM,2]]

#      SIGMA_S AND RI AT GAUSS POINTS
       SIGMA_S1 = SIGMA_0
       SIGMA_S2 = SIGMA_0
       SIGMA_S3 = SIGMA_0

#      CONSTRUCT THE LOCAL VECTOR OF RHS
       LFK[0] =
((K1*SHAPE1[0]*AREAW1+K2*SHAPE2[0]*AREAW2+K3*SHAPE3[0]*AREAW3)/DELTA_T)+(NUT1
*DUX_DZ_S1*SHAPE1[0]*AREAW1+NUT2*DUX_DZ_S2*SHAPE2[0]*AREAW2+NUT3*DUX_DZ_S3*SH
APE3[0]*AREAW3)+(G/RHO1*NUT1/SIGMA_S1*DRHO_DZ1*SHAPE1[0]*AREAW1+G/RHO2*NUT2/S
IGMA_S2*DRHO_DZ2*SHAPE2[0]*AREAW2+G/RHO3*NUT3/SIGMA_S3*DRHO_DZ3*SHAPE3[0]*ARE
AW3)
       LFK[1] =
((K1*SHAPE1[1]*AREAW1+K2*SHAPE2[1]*AREAW2+K3*SHAPE3[1]*AREAW3)/DELTA_T)+(NUT1
*DUX_DZ_S1*SHAPE1[1]*AREAW1+NUT2*DUX_DZ_S2*SHAPE2[1]*AREAW2+NUT3*DUX_DZ_S3*SH
APE3[1]*AREAW3)+(G/RHO1*NUT1/SIGMA_S1*DRHO_DZ1*SHAPE1[1]*AREAW1+G/RHO2*NUT2/S
IGMA_S2*DRHO_DZ2*SHAPE2[1]*AREAW2+G/RHO3*NUT3/SIGMA_S3*DRHO_DZ3*SHAPE3[1]*ARE
AW3)
       LFK[2] =
((K1*SHAPE1[2]*AREAW1+K2*SHAPE2[2]*AREAW2+K3*SHAPE3[2]*AREAW3)/DELTA_T)+(NUT1
*DUX_DZ_S1*SHAPE1[2]*AREAW1+NUT2*DUX_DZ_S2*SHAPE2[2]*AREAW2+NUT3*DUX_DZ_S3*SH
APE3[2]*AREAW3)+(G/RHO1*NUT1/SIGMA_S1*DRHO_DZ1*SHAPE1[2]*AREAW1+G/RHO2*NUT2/S
IGMA_S2*DRHO_DZ2*SHAPE2[2]*AREAW2+G/RHO3*NUT3/SIGMA_S3*DRHO_DZ3*SHAPE3[2]*ARE
AW3)

       LFEP[0] =
((EP1*SHAPE1[0]*AREAW1+EP2*SHAPE2[0]*AREAW2+EP3*SHAPE3[0]*AREAW3)/DELTA_T)+(C
1*GAMMA1*NUT1*DUX_DZ_S1*SHAPE1[0]*AREAW1+C1*GAMMA2*NUT2*DUX_DZ_S2*SHAPE2[0]*A
REAW2+C1*GAMMA3*NUT3*DUX_DZ_S3*SHAPE3[0]*AREAW3)
       LFEP[1] =
((EP1*SHAPE1[1]*AREAW1+EP2*SHAPE2[1]*AREAW2+EP3*SHAPE3[1]*AREAW3)/DELTA_T)+(C
1*GAMMA1*NUT1*DUX_DZ_S1*SHAPE1[1]*AREAW1+C1*GAMMA2*NUT2*DUX_DZ_S2*SHAPE2[1]*A
REAW2+C1*GAMMA3*NUT3*DUX_DZ_S3*SHAPE3[1]*AREAW3)
       LFEP[2] =
((EP1*SHAPE1[2]*AREAW1+EP2*SHAPE2[2]*AREAW2+EP3*SHAPE3[2]*AREAW3)/DELTA_T)+(C
1*GAMMA1*NUT1*DUX_DZ_S1*SHAPE1[2]*AREAW1+C1*GAMMA2*NUT2*DUX_DZ_S2*SHAPE2[2]*A
REAW2+C1*GAMMA3*NUT3*DUX_DZ_S3*SHAPE3[2]*AREAW3)

       for IDIME in range(0,NNODL):
           GFK[LNODS[IELEM,IDIME]] = GFK[LNODS[IELEM,IDIME]]+LFK[IDIME]
           GFEP[LNODS[IELEM,IDIME]] = GFEP[LNODS[IELEM,IDIME]]+LFEP[IDIME]

#  DEAL WITH THE BOUNDARY CONDITIONS
   for IPOIN in range(0,NPOIN):
#      WALL BOUNDARY
       GK[2,IPOIN] = 0.0
       GEP[2,IPOIN] = 0.0
#      FREE SURFACE
       GK[NPOIN-1,IPOIN] = 0.0
```

```
#  WALL BOUNDARY
   GK[2,2] = 1.0
   GEP[2,2] = 1.0
#  FREE SURFACE
   GK[NPOIN-1,NPOIN-1] = 1.0

#  IMPOSE BOUNDARY VALUES
#  WALL BOUNDARY
   GFK[2] = KN[2]
   GFEP[2] = EPN[2]
#  FREE SURFACE
   GFK[NPOIN-1] = 0.0

#  SOLVE LINEAR EQUATIONS
   K[2:] = np.linalg.solve(GK[2:,2:],GFK[2:])
   EP[2:] = np.linalg.solve(GEP[2:,2:],GFEP[2:])

#  UPDATE NU_T
   K[0]=KN[0]
   K[1]=KN[1]
   EP[0]=EPN[0]
   EP[1]=EPN[1]
   NU_T=CMU*K**2/EP

   return K, EP, NU_T

#=============================================================

def
SOLVE_1D_KEPSILON_SED_ET(COORD,LNODS,NPOIN,NELEM,NNODL,POSGP,WEIGP,DELTA_T,NU
,RHO_W,RHO_S,KN,EPN,NU_TN,UXN,CN):

#  INITIALIZE VARIABLES
   GK = np.zeros((NPOIN,NPOIN))
   GFK = np.zeros(NPOIN)
   LK = np.zeros((NNODL,NNODL))
   LFK = np.zeros(NNODL)

   GEP = np.zeros((NPOIN,NPOIN))
   GFEP = np.zeros(NPOIN)
   LEP = np.zeros((NNODL,NNODL))
   LFEP = np.zeros(NNODL)

   K = np.zeros(NPOIN)
   EP = np.zeros(NPOIN)

#  DEFINE CONSTANTS
   SIGMA_K = 1.0
   SIGMA_EP = 1.3
   CMU = 0.09
   C1 = 1.44
   C2 = 1.92
   C3 = 0.6
   G = 9.81
   SIGMA_0 = 0.7

#  MIXTURE BULK DENSITY
```

```
   RHO = RHO_W+(1-RHO_W/RHO_S)*(CN*RHO_S)

#  LOOP FOR ALL THE ELEMENTS
   for IELEM in range(1,NELEM):

#      SHAPE FUNCTIONS AT GAUSS POINT 1
       SHAPE1, DERIV1, SDERIV1 = SHAPE_LINE_QUADRATIC_S(POSGP[0])
       DJACK1, DJACI1 = DJACOB_LINE(COORD,LNODS,NNODL,IELEM,DERIV1)
#      SHAPE FUNCTIONS AT GAUSS POINT 2
       SHAPE2, DERIV2, SDERIV2 = SHAPE_LINE_QUADRATIC_S(POSGP[1])
       DJACK2, DJACI2 = DJACOB_LINE(COORD,LNODS,NNODL,IELEM,DERIV2)
#      SHAPE FUNCTIONS AT GAUSS POINT 3
       SHAPE3, DERIV3, SDERIV3 = SHAPE_LINE_QUADRATIC_S(POSGP[2])
       DJACK3, DJACI3 = DJACOB_LINE(COORD,LNODS,NNODL,IELEM,DERIV3)

#      GLOBAL DERIVATIVE AND GAUSS WEIGHTING AREAS AT GAUSS POINTS
       GDERIV1 = DJACI1*DERIV1
       GDERIV2 = DJACI2*DERIV2
       GDERIV3 = DJACI3*DERIV3

       AREAW1 = DJACK1*WEIGP[0]
       AREAW2 = DJACK2*WEIGP[1]
       AREAW3 = DJACK3*WEIGP[2]

#      K AT GAUSS POINTS
       K1 =
SHAPE1[0]*KN[LNODS[IELEM,0]]+SHAPE1[1]*KN[LNODS[IELEM,1]]+SHAPE1[2]*KN[LNODS[
IELEM,2]]
       K2 =
SHAPE2[0]*KN[LNODS[IELEM,0]]+SHAPE2[1]*KN[LNODS[IELEM,1]]+SHAPE2[2]*KN[LNODS[
IELEM,2]]
       K3 =
SHAPE3[0]*KN[LNODS[IELEM,0]]+SHAPE3[1]*KN[LNODS[IELEM,1]]+SHAPE3[2]*KN[LNODS[
IELEM,2]]

#      EPSILON AT GAUSS POINTS
       EP1 =
SHAPE1[0]*EPN[LNODS[IELEM,0]]+SHAPE1[1]*EPN[LNODS[IELEM,1]]+SHAPE1[2]*EPN[LNO
DS[IELEM,2]]
       EP2 =
SHAPE2[0]*EPN[LNODS[IELEM,0]]+SHAPE2[1]*EPN[LNODS[IELEM,1]]+SHAPE2[2]*EPN[LNO
DS[IELEM,2]]
       EP3 =
SHAPE3[0]*EPN[LNODS[IELEM,0]]+SHAPE3[1]*EPN[LNODS[IELEM,1]]+SHAPE3[2]*EPN[LNO
DS[IELEM,2]]

#      GAMMA AT GAUSS POINTS
       GAMMA1 = EP1/K1
       GAMMA2 = EP2/K2
       GAMMA3 = EP3/K3

#      EDDY VISCOSITY AT GAUSS POINTS
       NUT1 = CMU*K1**2/EP1
       NUT2 = CMU*K2**2/EP2
       NUT3 = CMU*K3**2/EP3

#      DERIVATIVE OF EDDY VISCOSITY AT GAUSS POINTS
```

```
       DNUT_DZ_1 =
GDERIV1[0]*NU_TN[LNODS[IELEM,0]]+GDERIV1[1]*NU_TN[LNODS[IELEM,1]]+GDERIV1[2]*
NU_TN[LNODS[IELEM,2]]
       DNUT_DZ_2 =
GDERIV2[0]*NU_TN[LNODS[IELEM,0]]+GDERIV2[1]*NU_TN[LNODS[IELEM,1]]+GDERIV2[2]*
NU_TN[LNODS[IELEM,2]]
       DNUT_DZ_3 =
GDERIV3[0]*NU_TN[LNODS[IELEM,0]]+GDERIV3[1]*NU_TN[LNODS[IELEM,1]]+GDERIV3[2]*
NU_TN[LNODS[IELEM,2]]

#      C AT GAUSS POINTS
       C01 =
SHAPE1[0]*CN[LNODS[IELEM,0]]+SHAPE1[1]*CN[LNODS[IELEM,1]]+SHAPE1[2]*CN[LNODS[
IELEM,2]]
       C02 =
SHAPE2[0]*CN[LNODS[IELEM,0]]+SHAPE2[1]*CN[LNODS[IELEM,1]]+SHAPE2[2]*CN[LNODS[
IELEM,2]]
       C03 =
SHAPE3[0]*CN[LNODS[IELEM,0]]+SHAPE3[1]*CN[LNODS[IELEM,1]]+SHAPE3[2]*CN[LNODS[
IELEM,2]]

#      DERIVATIVE OF K AND EPSILON AT GAUSS POINTS

DK_DZ_1=GDERIV1[0]*KN[LNODS[IELEM,0]]+GDERIV1[1]*KN[LNODS[IELEM,1]]+GDERIV1[2
]*KN[LNODS[IELEM,2]]

DK_DZ_2=GDERIV2[0]*KN[LNODS[IELEM,0]]+GDERIV2[1]*KN[LNODS[IELEM,1]]+GDERIV2[2
]*KN[LNODS[IELEM,2]]

DK_DZ_3=GDERIV3[0]*KN[LNODS[IELEM,0]]+GDERIV3[1]*KN[LNODS[IELEM,1]]+GDERIV3[2
]*KN[LNODS[IELEM,2]]

#      AUXILARY FUNCTION FOR EXTRA TERMS
       if C01 < 1.0e-4:
           FTD_1 = 1.0*C01/1.0e-04
       else:
           FTD_1 = 1

       if C02 < 1.0e-4:
           FTD_2 = 1.0*C02/1.0e-04
       else:
           FTD_2 = 1

       if C03 < 1.0e-4:
           FTD_3 = 1.0*C03/1.0e-04
       else:
           FTD_3 = 1

#      CONSTRUCT THE LOCAL MATRIX OF COEFFICIENT

#      FOR K
       LK[0,0] =
((SHAPE1[0]*SHAPE1[0]*AREAW1+SHAPE2[0]*SHAPE2[0]*AREAW2+SHAPE3[0]*SHAPE3[0]*A
REAW3)/DELTA_T)+((NU+NUT1/SIGMA_K)*GDERIV1[0]*GDERIV1[0]*AREAW1+(NU+NUT2/SIGM
A_K)*GDERIV2[0]*GDERIV2[0]*AREAW2+(NU+NUT3/SIGMA_K)*GDERIV3[0]*GDERIV3[0]*ARE
AW3)+(GAMMA1*SHAPE1[0]*SHAPE1[0]*AREAW1+GAMMA2*SHAPE2[0]*SHAPE2[0]*AREAW2+GAM
MA3*SHAPE3[0]*SHAPE3[0]*AREAW3)+(FTD_1*SHAPE1[0]*DNUT_DZ_1*GDERIV1[0]*AREAW1+
```

```
FTD_2*SHAPE2[0]*DNUT_DZ_2*GDERIV2[0]*AREAW2+FTD_3*SHAPE3[0]*DNUT_DZ_3*GDERIV3
[0]*AREAW3)/SIGMA_K
      LK[0,1] =
((SHAPE1[0]*SHAPE1[1]*AREAW1+SHAPE2[0]*SHAPE2[1]*AREAW2+SHAPE3[0]*SHAPE3[1]*A
REAW3)/DELTA_T)+((NU+NUT1/SIGMA_K)*GDERIV1[0]*GDERIV1[1]*AREAW1+(NU+NUT2/SIGM
A_K)*GDERIV2[0]*GDERIV2[1]*AREAW2+(NU+NUT3/SIGMA_K)*GDERIV3[0]*GDERIV3[1]*ARE
AW3)+(GAMMA1*SHAPE1[0]*SHAPE1[1]*AREAW1+GAMMA2*SHAPE2[0]*SHAPE2[1]*AREAW2+GAM
MA3*SHAPE3[0]*SHAPE3[1]*AREAW3)+(FTD_1*SHAPE1[0]*DNUT_DZ_1*GDERIV1[1]*AREAW1+
FTD_2*SHAPE2[0]*DNUT_DZ_2*GDERIV2[1]*AREAW2+FTD_3*SHAPE3[0]*DNUT_DZ_3*GDERIV3
[1]*AREAW3)/SIGMA_K
      LK[0,2] =
((SHAPE1[0]*SHAPE1[2]*AREAW1+SHAPE2[0]*SHAPE2[2]*AREAW2+SHAPE3[0]*SHAPE3[2]*A
REAW3)/DELTA_T)+((NU+NUT1/SIGMA_K)*GDERIV1[0]*GDERIV1[2]*AREAW1+(NU+NUT2/SIGM
A_K)*GDERIV2[0]*GDERIV2[2]*AREAW2+(NU+NUT3/SIGMA_K)*GDERIV3[0]*GDERIV3[2]*ARE
AW3)+(GAMMA1*SHAPE1[0]*SHAPE1[2]*AREAW1+GAMMA2*SHAPE2[0]*SHAPE2[2]*AREAW2+GAM
MA3*SHAPE3[0]*SHAPE3[2]*AREAW3)+(FTD_1*SHAPE1[0]*DNUT_DZ_1*GDERIV1[2]*AREAW1+
FTD_2*SHAPE2[0]*DNUT_DZ_2*GDERIV2[2]*AREAW2+FTD_3*SHAPE3[0]*DNUT_DZ_3*GDERIV3
[2]*AREAW3)/SIGMA_K

      LK[1,0] =
((SHAPE1[1]*SHAPE1[0]*AREAW1+SHAPE2[1]*SHAPE2[0]*AREAW2+SHAPE3[1]*SHAPE3[0]*A
REAW3)/DELTA_T)+((NU+NUT1/SIGMA_K)*GDERIV1[1]*GDERIV1[0]*AREAW1+(NU+NUT2/SIGM
A_K)*GDERIV2[1]*GDERIV2[0]*AREAW2+(NU+NUT3/SIGMA_K)*GDERIV3[1]*GDERIV3[0]*ARE
AW3)+(GAMMA1*SHAPE1[1]*SHAPE1[0]*AREAW1+GAMMA2*SHAPE2[1]*SHAPE2[0]*AREAW2+GAM
MA3*SHAPE3[1]*SHAPE3[0]*AREAW3)+(FTD_1*SHAPE1[1]*DNUT_DZ_1*GDERIV1[0]*AREAW1+
FTD_2*SHAPE2[1]*DNUT_DZ_2*GDERIV2[0]*AREAW2+FTD_3*SHAPE3[1]*DNUT_DZ_3*GDERIV3
[0]*AREAW3)/SIGMA_K
      LK[1,1] =
((SHAPE1[1]*SHAPE1[1]*AREAW1+SHAPE2[1]*SHAPE2[1]*AREAW2+SHAPE3[1]*SHAPE3[1]*A
REAW3)/DELTA_T)+((NU+NUT1/SIGMA_K)*GDERIV1[1]*GDERIV1[1]*AREAW1+(NU+NUT2/SIGM
A_K)*GDERIV2[1]*GDERIV2[1]*AREAW2+(NU+NUT3/SIGMA_K)*GDERIV3[1]*GDERIV3[1]*ARE
AW3)+(GAMMA1*SHAPE1[1]*SHAPE1[1]*AREAW1+GAMMA2*SHAPE2[1]*SHAPE2[1]*AREAW2+GAM
MA3*SHAPE3[1]*SHAPE3[1]*AREAW3)+(FTD_1*SHAPE1[1]*DNUT_DZ_1*GDERIV1[1]*AREAW1+
FTD_2*SHAPE2[1]*DNUT_DZ_2*GDERIV2[1]*AREAW2+FTD_3*SHAPE3[1]*DNUT_DZ_3*GDERIV3
[1]*AREAW3)/SIGMA_K
      LK[1,2] =
((SHAPE1[1]*SHAPE1[2]*AREAW1+SHAPE2[1]*SHAPE2[2]*AREAW2+SHAPE3[1]*SHAPE3[2]*A
REAW3)/DELTA_T)+((NU+NUT1/SIGMA_K)*GDERIV1[1]*GDERIV1[2]*AREAW1+(NU+NUT2/SIGM
A_K)*GDERIV2[1]*GDERIV2[2]*AREAW2+(NU+NUT3/SIGMA_K)*GDERIV3[1]*GDERIV3[2]*ARE
AW3)+(GAMMA1*SHAPE1[1]*SHAPE1[2]*AREAW1+GAMMA2*SHAPE2[1]*SHAPE2[2]*AREAW2+GAM
MA3*SHAPE3[1]*SHAPE3[2]*AREAW3)+(FTD_1*SHAPE1[1]*DNUT_DZ_1*GDERIV1[2]*AREAW1+
FTD_2*SHAPE2[1]*DNUT_DZ_2*GDERIV2[2]*AREAW2+FTD_3*SHAPE3[1]*DNUT_DZ_3*GDERIV3
[2]*AREAW3)/SIGMA_K

      LK[2,0] =
((SHAPE1[2]*SHAPE1[0]*AREAW1+SHAPE2[2]*SHAPE2[0]*AREAW2+SHAPE3[2]*SHAPE3[0]*A
REAW3)/DELTA_T)+((NU+NUT1/SIGMA_K)*GDERIV1[2]*GDERIV1[0]*AREAW1+(NU+NUT2/SIGM
A_K)*GDERIV2[2]*GDERIV2[0]*AREAW2+(NU+NUT3/SIGMA_K)*GDERIV3[2]*GDERIV3[0]*ARE
AW3)+(GAMMA1*SHAPE1[2]*SHAPE1[0]*AREAW1+GAMMA2*SHAPE2[2]*SHAPE2[0]*AREAW2+GAM
MA3*SHAPE3[2]*SHAPE3[0]*AREAW3)+(FTD_1*SHAPE1[2]*DNUT_DZ_1*GDERIV1[0]*AREAW1+
FTD_2*SHAPE2[2]*DNUT_DZ_2*GDERIV2[0]*AREAW2+FTD_3*SHAPE3[2]*DNUT_DZ_3*GDERIV3
[0]*AREAW3)/SIGMA_K
      LK[2,1] =
((SHAPE1[2]*SHAPE1[1]*AREAW1+SHAPE2[2]*SHAPE2[1]*AREAW2+SHAPE3[2]*SHAPE3[1]*A
REAW3)/DELTA_T)+((NU+NUT1/SIGMA_K)*GDERIV1[2]*GDERIV1[1]*AREAW1+(NU+NUT2/SIGM
A_K)*GDERIV2[2]*GDERIV2[1]*AREAW2+(NU+NUT3/SIGMA_K)*GDERIV3[2]*GDERIV3[1]*ARE
AW3)+(GAMMA1*SHAPE1[2]*SHAPE1[1]*AREAW1+GAMMA2*SHAPE2[2]*SHAPE2[1]*AREAW2+GAM
```

```
MA3*SHAPE3[2]*SHAPE3[1]*AREAW3)+(FTD_1*SHAPE1[2]*DNUT_DZ_1*GDERIV1[1]*AREAW1+
FTD_2*SHAPE2[2]*DNUT_DZ_2*GDERIV2[1]*AREAW2+FTD_3*SHAPE3[2]*DNUT_DZ_3*GDERIV3
[1]*AREAW3)/SIGMA_K
       LK[2,2] =
((SHAPE1[2]*SHAPE1[2]*AREAW1+SHAPE2[2]*SHAPE2[2]*AREAW2+SHAPE3[2]*SHAPE3[2]*A
REAW3)/DELTA_T)+((NU+NUT1/SIGMA_K)*GDERIV1[2]*GDERIV1[2]*AREAW1+(NU+NUT2/SIGM
A_K)*GDERIV2[2]*GDERIV2[2]*AREAW2+(NU+NUT3/SIGMA_K)*GDERIV3[2]*GDERIV3[2]*ARE
AW3)+(GAMMA1*SHAPE1[2]*SHAPE1[2]*AREAW1+GAMMA2*SHAPE2[2]*SHAPE2[2]*AREAW2+GAM
MA3*SHAPE3[2]*SHAPE3[2]*AREAW3)+(FTD_1*SHAPE1[2]*DNUT_DZ_1*GDERIV1[2]*AREAW1+
FTD_2*SHAPE2[2]*DNUT_DZ_2*GDERIV2[2]*AREAW2+FTD_3*SHAPE3[2]*DNUT_DZ_3*GDERIV3
[2]*AREAW3)/SIGMA_K

#      FOR EPSILON
       LEP[0,0] =
((SHAPE1[0]*SHAPE1[0]*AREAW1+SHAPE2[0]*SHAPE2[0]*AREAW2+SHAPE3[0]*SHAPE3[0]*A
REAW3)/DELTA_T)+((NU+NUT1/SIGMA_EP)*GDERIV1[0]*GDERIV1[0]*AREAW1+(NU+NUT2/SIG
MA_EP)*GDERIV2[0]*GDERIV2[0]*AREAW2+(NU+NUT3/SIGMA_EP)*GDERIV3[0]*GDERIV3[0]*
AREAW3)+(C2*GAMMA1*SHAPE1[0]*SHAPE1[0]*AREAW1+C2*GAMMA2*SHAPE2[0]*SHAPE2[0]*A
REAW2+C2*GAMMA3*SHAPE3[0]*SHAPE3[0]*AREAW3)
       LEP[0,1] =
((SHAPE1[0]*SHAPE1[1]*AREAW1+SHAPE2[0]*SHAPE2[1]*AREAW2+SHAPE3[0]*SHAPE3[1]*A
REAW3)/DELTA_T)+((NU+NUT1/SIGMA_EP)*GDERIV1[0]*GDERIV1[1]*AREAW1+(NU+NUT2/SIG
MA_EP)*GDERIV2[0]*GDERIV2[1]*AREAW2+(NU+NUT3/SIGMA_EP)*GDERIV3[0]*GDERIV3[1]*
AREAW3)+(C2*GAMMA1*SHAPE1[0]*SHAPE1[1]*AREAW1+C2*GAMMA2*SHAPE2[0]*SHAPE2[1]*A
REAW2+C2*GAMMA3*SHAPE3[0]*SHAPE3[1]*AREAW3)
       LEP[0,2] =
((SHAPE1[0]*SHAPE1[2]*AREAW1+SHAPE2[0]*SHAPE2[2]*AREAW2+SHAPE3[0]*SHAPE3[2]*A
REAW3)/DELTA_T)+((NU+NUT1/SIGMA_EP)*GDERIV1[0]*GDERIV1[2]*AREAW1+(NU+NUT2/SIG
MA_EP)*GDERIV2[0]*GDERIV2[2]*AREAW2+(NU+NUT3/SIGMA_EP)*GDERIV3[0]*GDERIV3[2]*
AREAW3)+(C2*GAMMA1*SHAPE1[0]*SHAPE1[2]*AREAW1+C2*GAMMA2*SHAPE2[0]*SHAPE2[2]*A
REAW2+C2*GAMMA3*SHAPE3[0]*SHAPE3[2]*AREAW3)

       LEP[1,0] =
((SHAPE1[1]*SHAPE1[0]*AREAW1+SHAPE2[1]*SHAPE2[0]*AREAW2+SHAPE3[1]*SHAPE3[0]*A
REAW3)/DELTA_T)+((NU+NUT1/SIGMA_EP)*GDERIV1[1]*GDERIV1[0]*AREAW1+(NU+NUT2/SIG
MA_EP)*GDERIV2[1]*GDERIV2[0]*AREAW2+(NU+NUT3/SIGMA_EP)*GDERIV3[1]*GDERIV3[0]*
AREAW3)+(C2*GAMMA1*SHAPE1[1]*SHAPE1[0]*AREAW1+C2*GAMMA2*SHAPE2[1]*SHAPE2[0]*A
REAW2+C2*GAMMA3*SHAPE3[1]*SHAPE3[0]*AREAW3)
       LEP[1,1] =
((SHAPE1[1]*SHAPE1[1]*AREAW1+SHAPE2[1]*SHAPE2[1]*AREAW2+SHAPE3[1]*SHAPE3[1]*A
REAW3)/DELTA_T)+((NU+NUT1/SIGMA_EP)*GDERIV1[1]*GDERIV1[1]*AREAW1+(NU+NUT2/SIG
MA_EP)*GDERIV2[1]*GDERIV2[1]*AREAW2+(NU+NUT3/SIGMA_EP)*GDERIV3[1]*GDERIV3[1]*
AREAW3)+(C2*GAMMA1*SHAPE1[1]*SHAPE1[1]*AREAW1+C2*GAMMA2*SHAPE2[1]*SHAPE2[1]*A
REAW2+C2*GAMMA3*SHAPE3[1]*SHAPE3[1]*AREAW3)
       LEP[1,2] =
((SHAPE1[1]*SHAPE1[2]*AREAW1+SHAPE2[1]*SHAPE2[2]*AREAW2+SHAPE3[1]*SHAPE3[2]*A
REAW3)/DELTA_T)+((NU+NUT1/SIGMA_EP)*GDERIV1[1]*GDERIV1[2]*AREAW1+(NU+NUT2/SIG
MA_EP)*GDERIV2[1]*GDERIV2[2]*AREAW2+(NU+NUT3/SIGMA_EP)*GDERIV3[1]*GDERIV3[2]*
AREAW3)+(C2*GAMMA1*SHAPE1[1]*SHAPE1[2]*AREAW1+C2*GAMMA2*SHAPE2[1]*SHAPE2[2]*A
REAW2+C2*GAMMA3*SHAPE3[1]*SHAPE3[2]*AREAW3)

       LEP[2,0] =
((SHAPE1[2]*SHAPE1[0]*AREAW1+SHAPE2[2]*SHAPE2[0]*AREAW2+SHAPE3[2]*SHAPE3[0]*A
REAW3)/DELTA_T)+((NU+NUT1/SIGMA_EP)*GDERIV1[2]*GDERIV1[0]*AREAW1+(NU+NUT2/SIG
MA_EP)*GDERIV2[2]*GDERIV2[0]*AREAW2+(NU+NUT3/SIGMA_EP)*GDERIV3[2]*GDERIV3[0]*
AREAW3)+(C2*GAMMA1*SHAPE1[2]*SHAPE1[0]*AREAW1+C2*GAMMA2*SHAPE2[2]*SHAPE2[0]*A
REAW2+C2*GAMMA3*SHAPE3[2]*SHAPE3[0]*AREAW3)
```

```
        LEP[2,1] =
((SHAPE1[2]*SHAPE1[1]*AREAW1+SHAPE2[2]*SHAPE2[1]*AREAW2+SHAPE3[2]*SHAPE3[1]*A
REAW3)/DELTA_T)+((NU+NUT1/SIGMA_EP)*GDERIV1[2]*GDERIV1[1]*AREAW1+(NU+NUT2/SIG
MA_EP)*GDERIV2[2]*GDERIV2[1]*AREAW2+(NU+NUT3/SIGMA_EP)*GDERIV3[2]*GDERIV3[1]*
AREAW3)+(C2*GAMMA1*SHAPE1[2]*SHAPE1[1]*AREAW1+C2*GAMMA2*SHAPE2[2]*SHAPE2[1]*A
REAW2+C2*GAMMA3*SHAPE3[2]*SHAPE3[1]*AREAW3)
        LEP[2,2] =
((SHAPE1[2]*SHAPE1[2]*AREAW1+SHAPE2[2]*SHAPE2[2]*AREAW2+SHAPE3[2]*SHAPE3[2]*A
REAW3)/DELTA_T)+((NU+NUT1/SIGMA_EP)*GDERIV1[2]*GDERIV1[2]*AREAW1+(NU+NUT2/SIG
MA_EP)*GDERIV2[2]*GDERIV2[2]*AREAW2+(NU+NUT3/SIGMA_EP)*GDERIV3[2]*GDERIV3[2]*
AREAW3)+(C2*GAMMA1*SHAPE1[2]*SHAPE1[2]*AREAW1+C2*GAMMA2*SHAPE2[2]*SHAPE2[2]*A
REAW2+C2*GAMMA3*SHAPE3[2]*SHAPE3[2]*AREAW3)

#       ASSEMBLE THE GLOBAL MATRIX
        for IDIME in range(0,NNODL):
            for JDIME in range(0,NNODL):
                GK[LNODS[IELEM,IDIME],LNODS[IELEM,JDIME]] =
GK[LNODS[IELEM,IDIME],LNODS[IELEM,JDIME]]+LK[IDIME,JDIME]
                GEP[LNODS[IELEM,IDIME],LNODS[IELEM,JDIME]] =
GEP[LNODS[IELEM,IDIME],LNODS[IELEM,JDIME]]+LEP[IDIME,JDIME]

#       FORM THE LOCAL RHS COEFFICIENTS AND ASSEMBLE INTO GLOBAL RHS VECTOR

#       (DUX_DZ)**2 AT GAUSS POINTS
        DUX_DZ_S1 =
(GDERIV1[0]*UXN[LNODS[IELEM,0]]+GDERIV1[1]*UXN[LNODS[IELEM,1]]+GDERIV1[2]*UXN
[LNODS[IELEM,2]])**2
        DUX_DZ_S2 =
(GDERIV2[0]*UXN[LNODS[IELEM,0]]+GDERIV2[1]*UXN[LNODS[IELEM,1]]+GDERIV2[2]*UXN
[LNODS[IELEM,2]])**2
        DUX_DZ_S3 =
(GDERIV3[0]*UXN[LNODS[IELEM,0]]+GDERIV3[1]*UXN[LNODS[IELEM,1]]+GDERIV3[2]*UXN
[LNODS[IELEM,2]])**2

#       RHO AND DRHO_DZ AT GAUSS POINTS
        RHO1 =
SHAPE1[0]*RHO[LNODS[IELEM,0]]+SHAPE1[1]*RHO[LNODS[IELEM,1]]+SHAPE1[2]*RHO[LNO
DS[IELEM,2]]
        RHO2 =
SHAPE2[0]*RHO[LNODS[IELEM,0]]+SHAPE2[1]*RHO[LNODS[IELEM,1]]+SHAPE2[2]*RHO[LNO
DS[IELEM,2]]
        RHO3 =
SHAPE3[0]*RHO[LNODS[IELEM,0]]+SHAPE3[1]*RHO[LNODS[IELEM,1]]+SHAPE3[2]*RHO[LNO
DS[IELEM,2]]

        DRHO_DZ1 =
GDERIV1[0]*RHO[LNODS[IELEM,0]]+GDERIV1[1]*RHO[LNODS[IELEM,1]]+GDERIV1[2]*RHO[
LNODS[IELEM,2]]
        DRHO_DZ2 =
GDERIV2[0]*RHO[LNODS[IELEM,0]]+GDERIV2[1]*RHO[LNODS[IELEM,1]]+GDERIV2[2]*RHO[
LNODS[IELEM,2]]
        DRHO_DZ3 =
GDERIV3[0]*RHO[LNODS[IELEM,0]]+GDERIV3[1]*RHO[LNODS[IELEM,1]]+GDERIV3[2]*RHO[
LNODS[IELEM,2]]

#       SIGMA_S AND RI AT GAUSS POINTS
        SIGMA_S1 = SIGMA_0
```

```
       SIGMA_S2 = SIGMA_0
       SIGMA_S3 = SIGMA_0

#      CONSTRUCT THE LOCAL VECTOR OF RHS
       LFK[0] =
((K1*SHAPE1[0]*AREAW1+K2*SHAPE2[0]*AREAW2+K3*SHAPE3[0]*AREAW3)/DELTA_T)+(NUT1
*DUX_DZ_S1*SHAPE1[0]*AREAW1+NUT2*DUX_DZ_S2*SHAPE2[0]*AREAW2+NUT3*DUX_DZ_S3*SH
APE3[0]*AREAW3)+(G/RHO1*NUT1/SIGMA_S1*DRHO_DZ1*SHAPE1[0]*AREAW1+G/RHO2*NUT2/S
IGMA_S2*DRHO_DZ2*SHAPE2[0]*AREAW2+G/RHO3*NUT3/SIGMA_S3*DRHO_DZ3*SHAPE3[0]*ARE
AW3)
       LFK[1] =
((K1*SHAPE1[1]*AREAW1+K2*SHAPE2[1]*AREAW2+K3*SHAPE3[1]*AREAW3)/DELTA_T)+(NUT1
*DUX_DZ_S1*SHAPE1[1]*AREAW1+NUT2*DUX_DZ_S2*SHAPE2[1]*AREAW2+NUT3*DUX_DZ_S3*SH
APE3[1]*AREAW3)+(G/RHO1*NUT1/SIGMA_S1*DRHO_DZ1*SHAPE1[1]*AREAW1+G/RHO2*NUT2/S
IGMA_S2*DRHO_DZ2*SHAPE2[1]*AREAW2+G/RHO3*NUT3/SIGMA_S3*DRHO_DZ3*SHAPE3[1]*ARE
AW3)
       LFK[2] =
((K1*SHAPE1[2]*AREAW1+K2*SHAPE2[2]*AREAW2+K3*SHAPE3[2]*AREAW3)/DELTA_T)+(NUT1
*DUX_DZ_S1*SHAPE1[2]*AREAW1+NUT2*DUX_DZ_S2*SHAPE2[2]*AREAW2+NUT3*DUX_DZ_S3*SH
APE3[2]*AREAW3)+(G/RHO1*NUT1/SIGMA_S1*DRHO_DZ1*SHAPE1[2]*AREAW1+G/RHO2*NUT2/S
IGMA_S2*DRHO_DZ2*SHAPE2[2]*AREAW2+G/RHO3*NUT3/SIGMA_S3*DRHO_DZ3*SHAPE3[2]*ARE
AW3)

       LFEP[0] =
((EP1*SHAPE1[0]*AREAW1+EP2*SHAPE2[0]*AREAW2+EP3*SHAPE3[0]*AREAW3)/DELTA_T)+(C
1*GAMMA1*NUT1*DUX_DZ_S1*SHAPE1[0]*AREAW1+C1*GAMMA2*NUT2*DUX_DZ_S2*SHAPE2[0]*A
REAW2+C1*GAMMA3*NUT3*DUX_DZ_S3*SHAPE3[0]*AREAW3)-
(FTD_1*C3*GAMMA1*DK_DZ_1*DNUT_DZ_1*SHAPE1[0]*AREAW1+FTD_2*C3*GAMMA2*DK_DZ_2*D
NUT_DZ_2*SHAPE2[0]*AREAW2+FTD_3*C3*GAMMA3*DK_DZ_3*DNUT_DZ_3*SHAPE3[0]*AREAW3)
/SIGMA_K
       LFEP[1] =
((EP1*SHAPE1[1]*AREAW1+EP2*SHAPE2[1]*AREAW2+EP3*SHAPE3[1]*AREAW3)/DELTA_T)+(C
1*GAMMA1*NUT1*DUX_DZ_S1*SHAPE1[1]*AREAW1+C1*GAMMA2*NUT2*DUX_DZ_S2*SHAPE2[1]*A
REAW2+C1*GAMMA3*NUT3*DUX_DZ_S3*SHAPE3[1]*AREAW3)-
(FTD_1*C3*GAMMA1*DK_DZ_1*DNUT_DZ_1*SHAPE1[1]*AREAW1+FTD_2*C3*GAMMA2*DK_DZ_2*D
NUT_DZ_2*SHAPE2[1]*AREAW2+FTD_3*C3*GAMMA3*DK_DZ_3*DNUT_DZ_3*SHAPE3[1]*AREAW3)
/SIGMA_K
       LFEP[2] =
((EP1*SHAPE1[2]*AREAW1+EP2*SHAPE2[2]*AREAW2+EP3*SHAPE3[2]*AREAW3)/DELTA_T)+(C
1*GAMMA1*NUT1*DUX_DZ_S1*SHAPE1[2]*AREAW1+C1*GAMMA2*NUT2*DUX_DZ_S2*SHAPE2[2]*A
REAW2+C1*GAMMA3*NUT3*DUX_DZ_S3*SHAPE3[2]*AREAW3)-
(FTD_1*C3*GAMMA1*DK_DZ_1*DNUT_DZ_1*SHAPE1[2]*AREAW1+FTD_2*C3*GAMMA2*DK_DZ_2*D
NUT_DZ_2*SHAPE2[2]*AREAW2+FTD_3*C3*GAMMA3*DK_DZ_3*DNUT_DZ_3*SHAPE3[2]*AREAW3)
/SIGMA_K

       for IDIME in range(0,NNODL):
           GFK[LNODS[IELEM,IDIME]] = GFK[LNODS[IELEM,IDIME]]+LFK[IDIME]
           GFEP[LNODS[IELEM,IDIME]] = GFEP[LNODS[IELEM,IDIME]]+LFEP[IDIME]

#  DEAL WITH THE BOUNDARY CONDITIONS
   for IPOIN in range(0,NPOIN):
#      WALL BOUNDARY
       GK[2,IPOIN] = 0.0
       GEP[2,IPOIN] = 0.0
#      FREE SURFACE
       GK[NPOIN-1,IPOIN] = 0.0
```

```
#  WALL BOUNDARY
   GK[2,2] = 1.0
   GEP[2,2] = 1.0
#  FREE SURFACE
   GK[NPOIN-1,NPOIN-1] = 1.0

#  IMPOSE BOUNDARY VALUES
#  WALL BOUNDARY
   GFK[2] = KN[2]
   GFEP[2] = EPN[2]
#  FREE SURFACE
   GFK[NPOIN-1] = 0.0

#  SOLVE LINEAR EQUATIONS
   K[2:] = np.linalg.solve(GK[2:,2:],GFK[2:])
   EP[2:] = np.linalg.solve(GEP[2:,2:],GFEP[2:])

#  UPDATE NU_T
   K[0]=KN[0]
   K[1]=KN[1]
   EP[0]=EPN[0]
   EP[1]=EPN[1]
   NU_T=CMU*K**2/EP

   return K, EP, NU_T
```

4. solve_sediment_unsteady.py

```
import numpy as np
from basic_functions import *

def
SOLVE_1D_SEDIMENT_US(COORD,LNODS,NPOIN,NELEM,NNODL,POSGP,WEIGP,DELTA_T,NU,CN,
NU_TN,WS):

#  INITIALIZE VARIABLES
   GC = np.zeros((NPOIN,NPOIN))
   GFC = np.zeros(NPOIN)
   LC = np.zeros((NNODL,NNODL))
   LFC = np.zeros(NNODL)

#  DEFINE CONSTANTS
   SIGMA_T = 0.7
   DT = (NU_TN/SIGMA_T+NU)

#  LOOP FOR ALL THE ELEMENTS
   for IELEM in range(0,NELEM):

#      SHAPE FUNCTIONS AT GAUSS POINT 1
       SHAPE1, DERIV1, SDERIV1 = SHAPE_LINE_QUADRATIC_S(POSGP[0])
       DJACK1, DJACI1 = DJACOB_LINE(COORD,LNODS,NNODL,IELEM,DERIV1)
#      SHAPE FUNCTIONS AT GAUSS POINT 2
       SHAPE2, DERIV2, SDERIV2 = SHAPE_LINE_QUADRATIC_S(POSGP[1])
       DJACK2, DJACI2 = DJACOB_LINE(COORD,LNODS,NNODL,IELEM,DERIV2)
```

```
#       SHAPE FUNCTIONS AT GAUSS POINT 3
        SHAPE3, DERIV3, SDERIV3 = SHAPE_LINE_QUADRATIC_S(POSGP[2])
        DJACK3, DJACI3 = DJACOB_LINE(COORD,LNODS,NNODL,IELEM,DERIV3)

#       GLOBAL DERIVATIVE AND GAUSS WEIGHTING AREAS AT GAUSS POINTS
        GDERIV1 = DJACI1*DERIV1
        GDERIV2 = DJACI2*DERIV2
        GDERIV3 = DJACI3*DERIV3

        AREAW1 = DJACK1*WEIGP[0]
        AREAW2 = DJACK2*WEIGP[1]
        AREAW3 = DJACK3*WEIGP[2]

#       C AT GAUSS POINTS
        C1 =
SHAPE1[0]*CN[LNODS[IELEM,0]]+SHAPE1[1]*CN[LNODS[IELEM,1]]+SHAPE1[2]*CN[LNODS[
IELEM,2]]
        C2 =
SHAPE2[0]*CN[LNODS[IELEM,0]]+SHAPE2[1]*CN[LNODS[IELEM,1]]+SHAPE2[2]*CN[LNODS[
IELEM,2]]
        C3 =
SHAPE3[0]*CN[LNODS[IELEM,0]]+SHAPE3[1]*CN[LNODS[IELEM,1]]+SHAPE3[2]*CN[LNODS[
IELEM,2]]

#       DT AT GAUSS POINTS
        DT1 =
SHAPE1[0]*DT[LNODS[IELEM,0]]+SHAPE1[1]*DT[LNODS[IELEM,1]]+SHAPE1[2]*DT[LNODS[
IELEM,2]]
        DT2 =
SHAPE2[0]*DT[LNODS[IELEM,0]]+SHAPE2[1]*DT[LNODS[IELEM,1]]+SHAPE2[2]*DT[LNODS[
IELEM,2]]
        DT3 =
SHAPE3[0]*DT[LNODS[IELEM,0]]+SHAPE3[1]*DT[LNODS[IELEM,1]]+SHAPE3[2]*DT[LNODS[
IELEM,2]]

#       CONSTRUCT THE LOCAL MATRIX OF COEFFICIENT
        LC[0,0] =
((SHAPE1[0]*SHAPE1[0]*AREAW1+SHAPE2[0]*SHAPE2[0]*AREAW2+SHAPE3[0]*SHAPE3[0]*A
REAW3)/DELTA_T)+(GDERIV1[0]*(WS*SHAPE1[0]+DT1*GDERIV1[0])*AREAW1+GDERIV2[0]*(
WS*SHAPE2[0]+DT2*GDERIV2[0])*AREAW2+GDERIV3[0]*(WS*SHAPE3[0]+DT3*GDERIV3[0])*
AREAW3)
        LC[0,1] =
((SHAPE1[0]*SHAPE1[1]*AREAW1+SHAPE2[0]*SHAPE2[1]*AREAW2+SHAPE3[0]*SHAPE3[1]*A
REAW3)/DELTA_T)+(GDERIV1[0]*(WS*SHAPE1[1]+DT1*GDERIV1[1])*AREAW1+GDERIV2[0]*(
WS*SHAPE2[1]+DT2*GDERIV2[1])*AREAW2+GDERIV3[0]*(WS*SHAPE3[1]+DT3*GDERIV3[1])*
AREAW3)
        LC[0,2] =
((SHAPE1[0]*SHAPE1[2]*AREAW1+SHAPE2[0]*SHAPE2[2]*AREAW2+SHAPE3[0]*SHAPE3[2]*A
REAW3)/DELTA_T)+(GDERIV1[0]*(WS*SHAPE1[2]+DT1*GDERIV1[2])*AREAW1+GDERIV2[0]*(
WS*SHAPE2[2]+DT2*GDERIV2[2])*AREAW2+GDERIV3[0]*(WS*SHAPE3[2]+DT3*GDERIV3[2])*
AREAW3)

        LC[1,0] =
((SHAPE1[1]*SHAPE1[0]*AREAW1+SHAPE2[1]*SHAPE2[0]*AREAW2+SHAPE3[1]*SHAPE3[0]*A
REAW3)/DELTA_T)+(GDERIV1[1]*(WS*SHAPE1[0]+DT1*GDERIV1[0])*AREAW1+GDERIV2[1]*(
WS*SHAPE2[0]+DT2*GDERIV2[0])*AREAW2+GDERIV3[1]*(WS*SHAPE3[0]+DT3*GDERIV3[0])*
AREAW3)
```

```
       LC[1,1] =
((SHAPE1[1]*SHAPE1[1]*AREAW1+SHAPE2[1]*SHAPE2[1]*AREAW2+SHAPE3[1]*SHAPE3[1]*A
REAW3)/DELTA_T)+(GDERIV1[1]*(WS*SHAPE1[1]+DT1*GDERIV1[1])*AREAW1+GDERIV2[1]*(
WS*SHAPE2[1]+DT2*GDERIV2[1])*AREAW2+GDERIV3[1]*(WS*SHAPE3[1]+DT3*GDERIV3[1])*
AREAW3)
       LC[1,2] =
((SHAPE1[1]*SHAPE1[2]*AREAW1+SHAPE2[1]*SHAPE2[2]*AREAW2+SHAPE3[1]*SHAPE3[2]*A
REAW3)/DELTA_T)+(GDERIV1[1]*(WS*SHAPE1[2]+DT1*GDERIV1[2])*AREAW1+GDERIV2[1]*(
WS*SHAPE2[2]+DT2*GDERIV2[2])*AREAW2+GDERIV3[1]*(WS*SHAPE3[2]+DT3*GDERIV3[2])*
AREAW3)

       LC[2,0] =
((SHAPE1[2]*SHAPE1[0]*AREAW1+SHAPE2[2]*SHAPE2[0]*AREAW2+SHAPE3[2]*SHAPE3[0]*A
REAW3)/DELTA_T)+(GDERIV1[2]*(WS*SHAPE1[0]+DT1*GDERIV1[0])*AREAW1+GDERIV2[2]*(
WS*SHAPE2[0]+DT2*GDERIV2[0])*AREAW2+GDERIV3[2]*(WS*SHAPE3[0]+DT3*GDERIV3[0])*
AREAW3)
       LC[2,1] =
((SHAPE1[2]*SHAPE1[1]*AREAW1+SHAPE2[2]*SHAPE2[1]*AREAW2+SHAPE3[2]*SHAPE3[1]*A
REAW3)/DELTA_T)+(GDERIV1[2]*(WS*SHAPE1[1]+DT1*GDERIV1[1])*AREAW1+GDERIV2[2]*(
WS*SHAPE2[1]+DT2*GDERIV2[1])*AREAW2+GDERIV3[2]*(WS*SHAPE3[1]+DT3*GDERIV3[1])*
AREAW3)
       LC[2,2] =
((SHAPE1[2]*SHAPE1[2]*AREAW1+SHAPE2[2]*SHAPE2[2]*AREAW2+SHAPE3[2]*SHAPE3[2]*A
REAW3)/DELTA_T)+(GDERIV1[2]*(WS*SHAPE1[2]+DT1*GDERIV1[2])*AREAW1+GDERIV2[2]*(
WS*SHAPE2[2]+DT2*GDERIV2[2])*AREAW2+GDERIV3[2]*(WS*SHAPE3[2]+DT3*GDERIV3[2])*
AREAW3)

#      ASSEMBLE THE GLOBAL MATRIX
       for IDIME in range(0,NNODL):
           for JDIME in range(0,NNODL):
               GC[LNODS[IELEM,IDIME],LNODS[IELEM,JDIME]] =
GC[LNODS[IELEM,IDIME],LNODS[IELEM,JDIME]]+LC[IDIME,JDIME]

#      FORM THE LOCAL RHS COEFFICIENTS AND ASSEMBLE INTO GLOBAL RHS VECTOR
       LFC[0] =
((C1*SHAPE1[0]*AREAW1+C2*SHAPE2[0]*AREAW2+C3*SHAPE3[0]*AREAW3)/DELTA_T)+0.0
       LFC[1] =
((C1*SHAPE1[1]*AREAW1+C2*SHAPE2[1]*AREAW2+C3*SHAPE3[1]*AREAW3)/DELTA_T)+0.0
       LFC[2] =
((C1*SHAPE1[2]*AREAW1+C2*SHAPE2[2]*AREAW2+C3*SHAPE3[2]*AREAW3)/DELTA_T)+0.0

#      DEAL WITH THE BOUNDARY FLUX
#        if (IELEM==1)
#
LFC(1)=((C1*SHAPE1[0]*AREAW1+C2*SHAPE2[0]*AREAW2+C3*SHAPE3[0]*AREAW3)/DELTA_T
)+(WS*CN(1))
#        elseif (IELEM==NELEM)
#
LFC(3)=((C1*SHAPE1[2]*AREAW1+C2*SHAPE2[2]*AREAW2+C3*SHAPE3[2]*AREAW3)/DELTA_T
)+(WS*CN(NPOIN))
#        end

       for IDIME in range(0,NNODL):
           GFC[LNODS[IELEM,IDIME]] = GFC[LNODS[IELEM,IDIME]]+LFC[IDIME]

#  DEAL WITH THE BOUNDARY CONDITIONS
#    for IPOIN=1:NPOIN
```

```
#      WALL BOUNDARY
#        GC(1,IPOIN)=0.0
#      FREE SURFACE
#        GC(NPOIN,IPOIN)=0.0
#    end

#  WALL BOUNDARY
#    GC(1,1)=1.0
#  FREE SURFACE
#    GC(NPOIN,NPOIN)=1.0

#  IMPOSE BOUNDARY VALUES
#  WALL BOUNDARY
#    GFC(1)=1.0e-3
#  FREE SURFACE
#    GFC(NPOIN)=0.0

#  SOLVE LINEAR EQUATIONS
   C = np.linalg.solve(GC,GFC)

   return C
```

5. Master.py

```
import warnings
warnings.filterwarnings('ignore')

print("==========================")
print("Yes, Master! Let's start!!")
print("==========================")

import numpy as np
import matplotlib.pyplot as plt
from basic_functions import *
from solve_fluid_unsteady import *
from solve_turbulence_unsteady import *
from solve_sediment_unsteady import *

#=========================================================

#  DEFINE PHYSICAL PARAMETERS
KAPPA = 0.402
CMU = 0.09
NU = 1.0e-6
RHO_W = 1.0e3
DELTA_T = 20
WS = 0.01
RHO_S = 2.65e3
DP_DX = -5.0

print("1. Let me create a grid for you.")
NELEM = 50
GSIZE = 0.005
NPOIN,NNODL,COORD,LNODS = CREATE_GRID(NELEM,GSIZE)
```

```
print("2. Now I'm going to define three Gauss points.")
POSGP,WEIGP = DEF_3_GAUSS_POINT()

print("3. I guess you're going to need some shape functions.")
SHAPE1,DERIV1,SDERIV1 = SHAPE_LINE_QUADRATIC_S(POSGP[0])
SHAPE2,DERIV2,SDERIV2 = SHAPE_LINE_QUADRATIC_S(POSGP[1])
SHAPE3,DERIV3,SDERIV3 = SHAPE_LINE_QUADRATIC_S(POSGP[2])

print("4. The initial conditions have been set up.")
USTAR,UX0,K0,EP0,NU_T0,C0 = INITIAL_CONDITION(NPOIN,COORD,DP_DX,CMU,KAPPA)
UXN = UX0
KN = K0
EPN = EP0
NU_TN = NU_T0
MU_EN = (NU+NU_TN)*RHO_W
CN = C0

print("5. Entering the loop for solving the equations!!")
ERROR = np.zeros(NPOIN)
ERROR[:] = 1.0
STEP = 1
while max(ERROR)>1.0e-8:
   UX =
SOLVE_1D_FLUID(COORD,LNODS,NPOIN,NELEM,NNODL,POSGP,WEIGP,DP_DX,USTAR,DELTA_T,
MU_EN,UXN)
   UXN = 0.5*(UX+UXN)
   K, EP, NU_T =
SOLVE_1D_KEPSILON_SED(COORD,LNODS,NPOIN,NELEM,NNODL,POSGP,WEIGP,DELTA_T,NU,RH
O_W,RHO_S,KN,EPN,UXN,CN)
   KN = 0.5*(K+KN)
   EPN = 0.5*(EP+EPN)
   NU_TN = 0.5*(NU_T+NU_TN)
   MU_EN = (NU+NU_TN)*RHO_W
   C =
SOLVE_1D_SEDIMENT(COORD,LNODS,NPOIN,NELEM,NNODL,POSGP,WEIGP,DELTA_T,NU,CN,NU_
TN,WS)
   ERROR = abs((C-CN)/CN)
   print("   ERROR is {} at iteration step {}".format(np.max(ERROR),STEP))
   CN=0.5*(C+CN)
   STEP=STEP+1

print("6. It's time to show you the results!!")
plt.figure(1)
plt.plot(UX, COORD)
plt.xlabel('streamwise velocity (m/s)')
plt.ylabel('water depth (m)')
plt.legend(['UX'],loc=2,fontsize=11)
plt.figure(2)
plt.plot(K0, COORD, EP0, COORD, NU_T0, COORD)
plt.ylabel('water depth (m)')
plt.legend(['K','EP','NU_T'],loc=1,fontsize=11)
plt.figure(3)
plt.plot(C, COORD)
plt.xlabel('suspended sediment concentration (m/s)')
plt.ylabel('water depth (m)')
plt.xscale('log')
```

```
plt.legend(['C'],loc=1,fontsize=11)
plt.show()

print ("Streamwise velocity UX:")
print UX
print ("Turbulence kinetic energy K:")
print K
print ("Turbulence dissipation rate EP:")
print EP
print ("Turbulent eddy viscosity NU_T:")
print NU_T
print ("Suspended sediment concentration C:")
print C

print ("7. Well done. Enjoy!!")
```

APPENDIX IV

ORIGINAL CONTRIBUTIONS AND PUBLICATIONS

CONTRIBUTION LIST

In this dissertation, the author contributed in the following aspects:

- The derivation of modified k-ε equations based on two-phase flow theory;
- The derivation of closures for the additional turbulence modulation terms due to fluid-sediment interaction;
- The development and validation of 1DV finite element model;
- The development of mixed-sediment transport model for the Scheldt estuary and the Belgian coast using TELEMAC modelling system;
- The implementation of the new roughness law developed by Toorman (in prep.);
- The implementation of equations of erosion of mixtures proposed by Waeles (2005);
- The implementation of the new deposition criterion proposed by Toorman (in prep.) and extension to the mixed-sediment transport model;
- The development of variety of tools for pre- and post-processing of the data and the simulated results;
- The calibration and validation of the Scheldt mode and the analysis of the results.

PUBLICATION LIST

(Peer-reviewed journals)

Bi, Q., Toorman, E. (2015). Mixed-sediment transport modelling in the Scheldt estuary with a physics based bottom friction law. Ocean Dynamics, 65 (4), 555-587.

(Contributions in academic book)

Monbaliu, J., Bi, Q., Bouma, T., Toorman, E., van Belzen, J., Willems, P. (2014). Extreme estuarine water levels and channel morphology, effect on flood extents and habitat resilience; the Scheldt Estuary, Belgium and the Netherlands. In: Zanuttigh B., Nicholis R. (Eds.), Coastal Risk Management in a Changing Climate, Chapt. 7.1 Elsevier.

(Contributions in scientific report)

Toorman, E., Bi, Q. (2012). Section 2.4, EU FP7 FIELD_AC Report D3.3. In Liste, M., Monbaliu, J., (Eds.). Improvements to sea-bed boundary conditions. (pp. 19-31).

(Proceedings of international conference)

Monbaliu, J., Bi, Q., Ortega Yamamoto, H., Toorman, E., Willems, P. (2014). Correlating surge and inland flow and a physics bed roughness model for sediment laden flows are tools for improved estimation of hydrodynamics and morphodynamics in view of climate change. EU Symposium on Ocean Observation and Its Applications. Taiwan, 4-6 November 2014 (pp. 1-8).

(Presentations and abstracts)

Bi, Q., Toorman, E. (2015). On two-phase/mixture modelling of sediment transport and turbulence modulation due to fluid-particle interactions. Book of Abstracts, 13th International Conference on Cohesive Sediment Transport Processes. INTERCOH. Leuven, 7-11 September 2015, 10-11.

Bi, Q., Toorman, E. (2014). A new sediment transport model for the Western Scheldt. JONSMOD 2014 Abstracts. JONSMOD. Brussels, 12-14 May 2014, 44-45.

Toorman, E., Bi, Q. (2013). A practical model for drag modulation by suspended sediment, with application to the Scheldt estuary. INTERCOH2013 Book of Abstracts. Int. Conf. on Cohesive Sediment Transport. Gainesville, Florida, 20-24 October 2013, 7-8.

Bi, Q., Toorman, E. (2013). Two-dimensional modelling of mixed sediment transport in the Western Scheldt. TELEMAC-MASCARET User Conference. Karlsruhe (DE), 16-18 October 2013.

Toorman, E., Bi, Q. (2013). Hybrid two-phase/mixture modelling of sediment transport. Abstracts THESIS-2013 (CDRom). Symposium on Two-phase Modelling for Sediment Dynamics. Chatou (France), 10-12 June 2013, 4 pp..

Bi, Q., Toorman, E. (2013). Modelling of hydrodynamic and morphological processes in the Scheldt Estuary with a new bed roughness model. Book of abstracts – VLIZ Young Scientists' Day. Brugge, Belgium, 15 February 2013. VLIZ Special Publication: vol. 63. VLIZ Young Scientists' Day. Brugge, Belgium, 14-15 February 2013, 15-15.

Toorman, E., Bi, Q. (2011). Dealing with benthic high-concentrated layers and fluid mud in cohesive sediment transport modelling. INTERCOH'11. Book of Abstracts. Int. Conf. on Cohesive Sediment Transport Processes. Shanghai, China, 18-21 October 2011, 85-86.

REFERENCES

Amoudry, L. (2008). A review on coastal sediment transport modelling. POL Internal Document No.189, Proudman Oceanographic Laboratory, Liverpool, 44 pp.

Allaby, A. and Allaby, M. (1999). "mesotidal." A Dictionary of Earth Sciences. Retrieved November 23, 2015 from Encyclopedia.com: http://www.encyclopedia.com/doc/1O13-mesotidal.html

Ariathurai, C. R. (1974). A finite element model for sediment transport in estuaries (Doctoral dissertation, University of California, Davis).

Backers, J. & Hindryckx, K. (2010). RV Belgica: rapport van de RV Belgica meetcampagnes en verankering van meetsystemen MOMO - 2009. Beheerseenheid Mathematisch Model Noordzee. Meetdienst Oostende: Oostende, different pagination + data CD-ROM (in Dutch).

Baeyens, W. (1998). Trace metals in the Westerschelde Estuary: a case study of a polluted, partially anoxic estuary (Vol. 128). Springer Science & Business Media.

Baeyens, W., Adam, Y., Mommaerts, J. P., & Pichot, G. (1981). Numerical simulations of salinity, turbidity and sediment accumulation in the Scheldt estuary. Elsevier Oceanography Series, 32, 319-332.

Baeyens, W., Goeyens, L., Monteny, F., & Elskens, M. (1997). Effect of organic complexation on the behaviour of dissolved Cd, Cu and Zn in the Scheldt estuary. Hydrobiologia, 366(1-3), 81-90.

Baeyens, W., Van Eck, G., Lambert, C., Wollast, R. & Goeyens, L. (1998). General description of the Scheldt estuary. Hydrobiologia, 366, 1–14.

Baldock, T. E., Tomkins, M. R., Nielsen, P., & Hughes, M. G. (2004). Settling velocity of sediments at high concentrations. Coastal engineering, 51(1), 91-100.

Bates, P. D. & Hervouet, J. M. (1999). A new method for moving–boundary hydrodynamic problems in shallow water. In Proceedings of the Royal Society of London Series A: Mathematical, Physical and Engineering Sciences (Vol. 455, No. 1988, pp. 3107-3128). The Royal Society.

Best, J., Bennett, S., Bridge, J., & Leeder, M. (1997). Turbulence modulation and particle velocities over flat sand beds at low transport rates. Journal of Hydraulic Engineering, 123(12), 1118-1129.

Bi, Q., & Toorman, E. A. (2015). Mixed-sediment transport modelling in Scheldt estuary with a physics-based bottom friction law. Ocean Dynamics, 65(4), 555-587.

Bigillon, F., Niño, Y., Garcia, M. H. (2006). Measurements of turbulence characteristics in an open-channel flow over a transitionally-rough bed using particle image. Exp. Fluids 41, 857-867.

Bollen, M., Sas, M., Vanlede, J., & De Mulder, T. (2006). Measuring high concentration benthic suspensions (HCBS): using a high resolution siltprofiler.

Bolle, A., Bing Wang, Z., Amos, C., & De Ronde, J. (2010). The influence of changes in tidal asymmetry on residual sediment transport in the Western Scheldt. Continental Shelf Research, 30(8), 871-882.

Breugem, W. A., Uijttewaal, W. S. J. (2006). A PIV/PTV experiment on sediment transport in a horizontal open channel flow. River Flow 2006, Balkema, pp. 789-798.

Breugem, W. A. (2012). Transport of suspended particles in turbulent open channel flows. TU Delft, Delft University of Technology.

Bridge, J. S. (2009). Rivers and floodplains: forms, processes, and sedimentary record. John Wiley & Sons.

Burchard, H., & Baumert, H. (1998). The formation of estuarine turbidity maxima due to density effects in the salt wedge. A hydrodynamic process study. J. Phys. Ocean., 28, 309–321.

Cancino, L., & Neves, R. (1994). 3D-numerical modelling of cohesive suspended sediment in the Western Scheldt estuary (the Netherlands). Netherland Journal of Aquatic Ecology, 28(3-4), 337-345.

Cancino, L., & Neves, R. (1999a). Hydrodynamic and sediment suspension modelling in estuarine systems: Part I: Description of the numerical models. Journal of Marine Systems, 22(2), 105-116.

Cancino, L., & Neves, R. (1999b). Hydrodynamic and sediment suspension modelling in estuarine systems: Part II: Application to the Western Scheldt and Gironde estuaries. Journal of Marine Systems, 22(2), 117-131.

Cellino, M. (1998). Experimental study of suspension flow in open channels. PhD dissertation, No. 1824, Ecole Polytechnique Fédérale de Lausanne.

Cellino, M., & Graf, W. H. (1999). Sediment-laden flow in open-channels under noncapacity and capacity conditions. Journal of hydraulic engineering, 125(5), 455-462.

Chauchat, J., & Guillou, S. (2008). On turbulence closures for two-phase sediment-laden flow models. Journal of Geophysical Research: Oceans (1978–2012), 113(C11).

Chen, C.J. and Jaw, S.Y. (1998). Fundamentals of Turbulence Modelling, Taylor and Francis, Washington D.C.

Cheng, N. S. (2004). Analysis of velocity lag in sediment-laden open channel flows. Journal of Hydraulic Engineering, 130(7), 657-666.

Chesher, T. J., & Ockenden, M. C. (1997). Numerical modelling of mud and sand mixtures. In Cohesive sediments—Proc. of INTERCOH Conf. (Wallingford, England). John Wiley & Son, Chichester (pp. 395-406).

Cleveringa, J. (2013). Grootschalige sedimentbalans van de Westerschelde. VNSC Basisrapport grootschalige ontwikkeling G-2. Report 076945827:0.4, Arcadis Nederland, Arnhem (NL), 81 pp. (in Dutch).

Coleman, N. L. (1981). Velocity profiles with suspended sediment. Journal of Hydraulic Research, 19(3), 211-229.

Corino, E. R., & Brodkey, R. S. (1969). A visual investigation of the wall region in turbulent flow. Journal of Fluid Mechanics, 37(01), 1-30.

Crowe, C. T. (2000). On models for turbulence modulation in fluid–particle flows. International Journal of Multiphase Flow, 26(5), 719-727.

Czuba, J. A., Magirl, C. S., Czuba, C. R., Grossman, E. E., Curran, C. A., Gendaszek, A. S., & Dinicola, R. S. (2011). Comparability of Suspended-Sediment Concentration and Total Suspended Solids DataSediment Load from Major Rivers into Puget Sound and its Adjacent Waters. USGS Fact Sheet 2011–3083. Tacoma, WA: US Geological Survey.

Dam, G., Bliek, A. J., Labeur, R. J., Ides, S., & Plancke, Y. (2007). Long term process-based morphological model of the Western Scheldt Estuary. In Proceedings of 5th IAHR symposium of the River, Coastal and Estuarine Morphodynamics Conference, Enschede, The Netherlans (Dohmen-Janssen CM and Hulscher SJMH (eds)), Taylor & Francis, Leiden, The Netherlands (Vol. 2, 1077-1084).

Dam, G., & Bliek, A. J. (2013). Using a sand-mud model to hindcast the morphology near Waarde, the Netherlands. In Proceedings of the

Institution of Civil Engineers–Maritime Engineering (Vol. 166, No. 2, pp. 63-75).

Dam, G. & Cleveringa, J. (2013). De rol van het slib in de sedimentbalans van de Westerschelde. VNSC Basisrapport grootschalige ontwikkeling G-3. Report G3; 1630/U12376/C/GD, Svasek Hydraulics, Rotterdam (NL), 35 pp. (in Dutch).

Da Silva, P. A., Temperville, A., & Seabra Santos, F. (2006). Sand transport under combined current and wave conditions: A semi-unsteady, practical model. Coastal Engineering, 53(11), 897-913.

De Brye, B., de Brauwere, A., Gourgue, O., Kärnä, T., Lambrechts, J., Comblen, R., & Deleersnijder, E. (2010). A finite-element, multi-scale model of the Scheldt tributaries, river, estuary and ROFI. Coastal Engineering, 57(9), 850-863.

De Ruijter, W., Huber, K., Backhaus, J. (1987). North Sea circulation. In: Report of the Ocanography Subroup. Second International Conference on the Protection of the North Sea, Scientific and Technical Working Group, pp. 19–36 (Chapter 4).

Defina, A., D'alpaos, L., & Matticchio, B. (1994). A new set of equations for very shallow water and partially dry areas suitable to 2D numerical models. In Modelling of Flood Propagation over Initially Dry Areas (pp. 72-81). ASCE.

Dyer, K. R. (1986). Coastal and Estuarine Sediment Dynamics. Chichester, New York, Brisbane, Toronto, Singapore: Wiley Interscience.

Einstein, H. A. (1950). The bed-load function for sediment transportation in open channel flows (No. 1026). US Department of Agriculture.

Elghobashi, S. E., & Abou-Arab, T. W. (1983). A two-equation turbulence model for two-phase flows. Physics of Fluids, 26(4), 931-938.

Elghobashi, S. (1994). On predicting particle-laden turbulent flows. *Applied Scientific Research*, 52:309-329.

Ellis, K. M., Binding, C. E., Bowers, D. G., Jones, S. E., & Simpson, J. H. (2008). A model of turbidity maximum maintenance in the Irish Sea. Estuarine, Coastal and Shelf Science, 76(4), 765-774.

Engelund, F., & Hansen, E. (1967). A monograph on sediment transport in alluvial streams. TEKNISKFORLAG Skelbrekgade 4 Copenhagen V, Denmark.

Fan, D., Li, C., & Wang, P. (2004). Influences of storm erosion and deposition on rhythmites of the Upper Wenchang Formation (Upper Ordovician) around Tonglu, Zhejiang Province, China. Journal of Sedimentary research, 74(4), 527-536.

Ferziger, J. H., & Peric, M. (2002). Computational methods for fluid dynamics (third, rev. edition). Springer-Verlag Berlin Heidelberg NewYork.

Fettweis, M., Sas, M., & Monbaliu, J. (1998). Seasonal, neap-spring and tidal variation of cohesive sediment concentration in the Scheldt Estuary, Belgium. Estuarine, Coastal and Shelf Science, 47(1), 21-36.

Fettweis, M., & Van den Eynde, D. (2003). The mud deposits and the high turbidity in the Belgian–Dutch coastal zone, southern bight of the North Sea. Continental Shelf Research, 23(7), 669-691.

Fettweis, M., Nechad, B., & Van den Eynde, D. (2007). An estimate of the suspended particulate matter (SPM) transport in the southern North Sea using SeaWiFS images, in situ measurements and numerical model results. Continental Shelf Research, 27(10), 1568-1583.

Fokkink, R. J. (1998). Morphodynamic network simulations of the Western Scheldt. WL| Delft Hydraulics, Report Z, 919.

Gelfenbaum, G., & Smith, J. D. (1986). Experimental evaluation of a generalized suspended-sediment transport theory.

Gore, R.A., Crowe, C.T. (1989). The effect of particle size on modulating turbulent intensity. Int. J. Multiphase Flow 15, 279-285.

Gourgue, O., Baeyens, W., Chen, M. S., de Brauwere, A., de Brye, B., Deleersnijder, E., Elskens, M. & Legat, V. (2013). A depth-averaged two-dimensional sediment transport model for environmental studies in the Scheldt Estuary and tidal river network. Journal of Marine Systems, 128, 27-39.

Greimann, B., M. Muste, and F. M. J. Holly (1999). Two-phase formulation of suspended sediment transport, J. Hydraul. Res., 37, 479 – 500.

Haecon, 2006. Actualisatie van de zandbalans van de Zee-en Westerschelde. Report 1249760008/lvp.

Hartsuiker, G. (2004) 2Dh NEVLA Scheldemodel: Bouw en afregeling stromingsmode (in Dutch). Report MOD 753. Antwerp, Belgium, Flanders Hydraulics Research.

Hetsroni, G. (1989). Particle-turbulence interaction. Int. J. Multiphase Flow 15, 735-746.

Herman, P. M. J. & C. H. R. Heip, 1999. Biochemistry of the maximum turbidity zone of estuaries (MATURE): some conclusions. Journal of Marine Systems 22: 89–104.

Hervouet, J. M., & Janin, J. M. (1994, June). Finite element algorithms for modelling flood propagation. In Modelling of Flood Propagation over Initially Dry Areas (pp. 102-113). ASCE.

Hervouet, J. M., & Bates, P. (2000). The Telemac modelling system. Hydrological Processes, 14(13), Special Issue.

Hervouet, J. M. (2007). Hydrodynamics of free surface flows: Modelling with the finite element method, John Wiley & Sons, Chichester, UK

Hoffmann, M. & P. Meire (1997). De oevers langs de Zeeschelde: inventarisatie van de huidige oeverstructuren. Water 95: 131–137.

Hoogduin, L., Stive, M. J. F., Wang, Z. B., Uijttewaal, W. S. J., Hibma, A., & Eelkema, M. (2009). Sediment transport through the Eastern Scheldt storm surge barrier. Delft University of Technology.

International Marine and Dredging Consultants *et al.* (2010). Langdurige metingen Deurganckdok: opvolging en analyse aanslibbing: deelrapport 1.23. Sedimentbalans 01/01/2009 - 31/03/2009. Versie 2.0. Waterbouwkundig Laboratorium: Antwerpen. IV, 28 + annexes (in Dutch).

Ishii, M. and Chawla, T. C. (1979). Local Drag Laws in Dispersed Two-phase Flow, Argonne National Lab. Report, ANL-79-105.

Janssens, J.; Delgado, R.; Verwaest, T.; Mostaert, F. (2012). Morfologische trends op middellange termijn van strand, vooroever en kustnabije zone langsheen de Belgische kust: Deelrapport in het kader van het Quest4D-project. Versie 1_0. WL Rapporten, 814_02. Waterbouwkundig Laboratorium: Antwerpen, België.

James, S. C., Jones, C. A., Grace, M. D., & Roberts, J. D. (2010). Advances in sediment transport modelling. Journal of Hydraulic Research, 48(6), 754-763.

Jeuken, M. C. J. L. (2000). On the morphologic behaviour of tidal channels in the Westerschelde estuary. Nederlandse geografische studies (Netherlands).

Jha, S. K., Bombardelli, F. A. (2010). Toward two-phase flow modelling of non-dilute sediment transport in open channels. Journal of Geophysical Research. Earth Surface 115 (3).

Johnson, B., Kim, K., Heath, R., Hsieh, B., Butler, H. (1993). Validation of three-dimensional hydrodynamic model of Chesapeake Bay. J. Hydraulic Res. 119(1), 2–20.

Kaftori, D., G. Hetsroni, and S. Banerjee (1995). Particle behaviour in the turbulent boundary layer. II. Velocity and distribution profiles, Phys. Fluids, 7(5), 1107 – 1121.

Kiger, K. T., and C. Pan (2002). Suspension and turbulence modification effects of solid particulates on a horizontal turbulent channel flow, J. Turbulence, 19(3), 1 – 21.

Krone, R. B. (1962). Flume Studies of the Transport of Sediment in Estuarial Shoaling Processes: Final Report. Hydraulic Engineering Laboratory and Sanitary Engineering Research Laboratory, University of California, 118 pp.

Kuijper, C., Steijn, R., Roelvink, D., van der Kaaij, T., Olijslagers, P. (2004). Report: Morphological modelling of the Western Scheldt: validation of Delft3D. Deltares (WL). Chapter 2, 1-2

Kulick, J.D., Fessler, J.R., Eaton, J.K. (1994). Particle response and turbulence modification in fully developed channel flow. J. Fluid Mech. 177, 133-166.

Lau, Y. L., and V. H. Chu (1987). Suspended sediment effect on turbulent diffusion, paper presented at 22nd IAHR Congress, Lausanne, France.

Le Louvetel-Poilly, J., Bigillon, F., & Champagne, J. Y. (2007). Experimental investigation on the turbulent structures involved in particle motion. In Geophysical Research Abstracts (Vol. 9, p. 11075).

Lee, B.J., Toorman, E. & Fettweis, M. (2014). Flocculation of fine-grained cohesive sediments developing multimodal particle size distributions: field investigation and mathematical modelling. Ocean Dynamics, 64:429-441.

Lyn, D.A. (1991). Resistance in flat-bed sediment-laden flows. J. Hydraulic Eng., ASCE 117, 94-114.

Lyn, D.A. (1992). Turbulence characteristics of sediment-laden flows in open channels. J. Hydraulic Eng., ASCE 118, 971-988.

Malherbe, B. (1991). A case study of dumping in open seas. Terra et Aqua 45, 5 – 32.

Mansour, N. N., Kim, J., & Moin, P. (1988). Reynolds-stress and dissipation-rate budgets in a turbulent channel flow. Journal of Fluid Mechanics, 194, 15-44.

Maximova, T., Ides, S., De Mulder, T. & Mostaert, F. (2009a) Verbetering 2D randvoorwaardenmodel. Deelrapport 4: Extra aanpassingen Zeeschelde (in Dutch). WL Rapporten, 753_09. Antwerp, Belgium, Flanders Hydraulics Research

Maximova, T., Ides, S., Vanlede, J., De Mulder, T. & Mostaert, F. (2009b) Verbetering 2D randvoorwaardenmodel. Deelrapport 3: Calibratie bovenlopen (in Dutch). WL Rapporten, 753_09. Antwerp, Belgium, Flanders Hydraulics Research.

McLaren (1994). Sediment transport in the Western Scheldt between Baarland and Rupelmonde. Report prepared for the Antwerp Harbour Authorities.

Medeiros, S. C., & Hagen, S. C. (2013). Review of wetting and drying algorithms for numerical tidal flow models. International Journal for Numerical Methods in Fluids, 71(4), 473-487.

Mehta, A. J., Hayter, E. J., Parker, W. R., Krone, R. B., & Teeter, A. M. (1989). Cohesive sediment transport. I: Process description. Journal of Hydraulic Engineering, 115(8), 1076-1093.

Mehta, A. J., McAnally Jr, W. H., Hayter, E. J., Teeter, A. M., Schoellhamer, D., Heltzel, S. B., & Carey, W. P. (1989). Cohesive sediment transport. II: Application. Journal of Hydraulic Engineering, 115(8), 1094-1112.

Meire, P., Ysebaert, T., Van Damme, S., Van den Bergh, E., Maris, T., & Struyf, E. (2005). The Scheldt estuary: a description of a changing ecosystem. Hydrobiologia, 540(1-3), 1-11.

Meyer-Peter, E., & Müller, R. (1948). Formulas for bed-load transport. IAHR.

Mitchener, H., & Torfs, H. (1996). Erosion of mud/sand mixtures. Coastal Engineering, 29, 1-25.

Mulder, H. P., & Udink, C. (1990). Modelling of cohesive sediment transport. A case study: the western Scheldt estuary. Coastal Engineering Proceedings, 1(22).

Muste, M., Patel, V. C. (1997). Velocity profiles for particles and liquid in open-channel flow with suspended sediment. J. Hydraulic Eng., ASCE 123, 742-751.

Muste, M., Yu, K., Fujita, I., & Ettema, R. (2005). Two-phase versus mixed-flow perspective on suspended sediment transport in turbulent channel flows. Water resources research, 41(10).

Muste, M., Yu, K., Fujita, I., Ettema, R. (2009). Two-phase flow insights into open-channel flows with suspended particles of different densities. J. Environ. Fluid Mech. 9, 161-186.

Nezu, I., Azuma, R. (2004). Turbulence characteristics and interaction between particles and fluid in particle-laden open-channel flows. J. Hydraulic Eng., ASCE 130, 988-1001.

Nguyen, K. D., Guillou, S., Chauchat, J., & Barbry, N. (2009). A two-phase numerical model for suspended-sediment transport in estuaries. Advances in Water Resources, 32(8), 1187-1196.

Nihoul, J.C.J., F. Ronday, J.J. Peters, A. Sterling (1978). Hydrodynamics of the Scheldt estuary. In: J.C.J. Nihoul (ed.), Hydrodynamics of Estuaries and Fjords, Elsevier, Amsterdam, pp. 27–53.

Nikuradse, J. (1933). Laws of flow in rough pipes. *NACA Tech. Mem.,* No.1292 (translation, 1950), Washington, 62 pp.

Niño, Y., and García, M. H. (1998). Experiments on saltation of fine sand in water, J. Hydraul. Eng., 124(10), 1014–1025.

Noguchi, K., Nezu, I., Sanjou, M. (2008). Turbulence structure and fluid-particle interaction in sediment-laden flows over developing sand dunes. J. Environ. Fluid Mech. 8, 569-578.

Noguchi, K., & Nezu, I. (2009). Particle–turbulence interaction and local particle concentration in sediment-laden open-channel flows. Journal of Hydro-environment Research, 3(2), 54-68.

Palermo, M. R., Schroeder, P. R., Estes, T. J., & Francingues, N. R. (2008). Technical Guidelines for Environmental Dredging of Contaminated Sediments. US Army Corps of Engineers: Engineer Research and Development Center, ERDC/EL TR-08-29.

Panagiotopoulos, I., Voulgaris, G., & Collins, M. B. (1997). The influence of clay on the threshold of movement of fine sandy beds. Coastal Engineering, 32(1), 19-43.

Parchure, T. M., & Mehta, A. J. (1985). Erosion of soft cohesive sediment deposits. Journal of Hydraulic Engineering, 111(10), 1308-1326.

Peters, (1975). Les mechanismes de mélange des eaux dans l'estuaire de l'Escaut. Tijdschrift der Openbare Werken van België 2, pp. 101–119.

Portela, L. I., & Neves, R. (1994). Numerical modelling of suspended sediment transport in tidal estuaries: a comparison between the Tagus (Portugal) and the Scheldt (Belgium-The Netherlands). Netherland Journal of Aquatic Ecology, 28(3-4), 329-335.

Prandtl, L. (1925). Bericht über Untersuchungen zur ausgebildeten Turbulenz. ZAMM, 5:136–139.

Rashidi, M., Hetsroni, G., & Banerjee, S. (1990). Particle-turbulence interaction in a boundary layer. International Journal of Multiphase Flow, 16(6), 935-949.

Richardson, J.F., Zaki, W.N., 1954. Sedimentation and fluidisation:part 1. Trans. Inst. Chem. Eng. 32, 35 – 53.

Righetti, M., Romano, G.P. (2004). Particle-fluid interactions in a plane nearwall turbulent flow. J. Fluid Mech. 505, 93-121.

Rodi, W. (1980). Turbulence models and their application in hydraulics, State-of-the-art Paper, IAHR, Delft.

Smagorinsky, J. (1963). General circulation experiments with the primitive equations: I. The basic experiment. Monthly Weather Review, 91(3), 99-164.

Song, T., Graf, W.H., Lemmin, U. (1994). Uniform flow in open channels with movable gravel bed. J. Hydraulic Res. IAHR 29, 387-401.

Soulsby, R. (1997). Dynamics of marine sands: a manual for practical applications. Thomas Telford.

Sumer, B. M., and R. Deigaard (1981). Particle motions near the bottom in turbulent flow in open channel: Part 2, J. Fluid Mech., 109, 311 – 337.

Toorman, E.A. (2000). Numerical simulation of turbulence damping in sediment-laden flow. Part 2. Suspension capacity of uniform turbulent shear flows. Report HYD/ET/00/COSINUS4, Hydraulics Laboratory, K.U.Leuven, 23pp.

Toorman, E.A. (2002). Modelling of turbulent flow with cohesive sediment. In: Proceedings in Marine Science, Vol.5: Fine Sediment

Dynamics in the Marine Environment (J.C. Winterwerp & C. Kranenburg), pp.155-169, Elsevier Science, Amsterdam.

Toorman, E.A. (2003). Validation of macroscopic modelling of particle-laden turbulent flows. Proceedings 6th Belgian National Congress on Theoretical and Applied Mechanics (Gent, 26-27 May 2003), CD Rom, 7 pp.

Toorman, E. A. (2008). Vertical mixing in the fully developed turbulent layer of sediment-laden open-channel flow. Journal of Hydraulic Engineering.

Toorman, E.A. (2011). Low-Reynolds modelling of high-concentrated near-bottom suspended sediment transport. IAHR Symposium on Two-phase Modelling for Sediment Dynamics in Geophysical Flows (THESIS-2011, Paris, April 26-28, 2011), Abstract, 4 pp.

Toorman, E., Bi, Q. (2011). Dealing with benthic high-concentrated layers and fluid mud in cohesive sediment transport modeling. INTERCOH'11. Book of Abstracts. Int. Conf. on Cohesive Sediment Transport Processes. Shanghai, China, 18-21 October 2011, 85-86.

Toorman, E., Bi, Q. (2013). Hybrid two-phase/mixture modelling of sediment transport. Abstracts THESIS-2013 (CDRom). Symposium on Two-phase Modelling for Sediment Dynamics. Chatou (France), 10-12 June 2013, 4 pp.

Toorman, E., Bi, Q. (2013). A practical model for drag modulation by suspended sediment, with application to the Scheldt estuary. INTERCOH2013 Book of Abstracts. Int. Conf. on Cohesive Sediment Transport. Gainesville, Florida, 20-24 October 2013, 7-8.

Toorman, E., Bi, Q. (2013). Hybrid two-phase/mixture modelling of sediment transport as a tool for large-scale morphological model development. Advances in Water Resources (SI THESIS2013).

Tsuji, Y., & Morikawa, Y. (1982). LDV measurements of an air-solid two-phase flow in a horizontal pipe. Journal of Fluid Mechanics, 120, 385-409.

Uittenbogaard, R.E., van Kester, J.A.Th. and Stelling, G. (1992). Implementation of three turbulence models in TRISULA for rectangular horizontal grids, Report Z162, Delft Hydraulics.

Vlaams-Nederlandse Scheldecommissie (2015). De Schelde: van bron tot monding. Retrieved from http://www.vnsc.eu/de-schelde/de-schelde-van-bron-tot-monding/

Van Driest, E.R. (1956). On turbulent flow near a wall. J. Aeronautical Science, 23, 1007-1011+1136.

Van den Eynde, D., Fettweis, M., Francken, F., Janssens, J., Toorman, E., Van Lancker, V., & Verwaest, T. Modeling transport of mixed sediments on the Belgian Continental Shelf.

Vanderborght, J. P., Folmer, I. M., Aguilera, D. R., Uhrenholdt, T., & Regnier, P. (2007). Reactive-transport modelling of C, N, and O_2 in a river–estuarine–coastal zone system: application to the Scheldt estuary. Marine chemistry, 106(1), 92-110.

Van Kessel, T., Vanlede, J., & Bruens, A. (2006). Development of a mud transport model for the Scheldt estuary in the framework of LTV. Report Z4210 WL| Delft Hydraulics and Flanders Hydraulics Research, Delft.

Van Kessel, T., Vanlede, J. (2010). Impact of harbour basins on mud dynamics Scheldt estuary in the framework of LTV. Deltares: Delft. 29 pp.

Van Kessel, T., J. Vanlede & J. de Kok (2011). Development of a mud transport model for the Scheldt estuary. Continental Shelf Research, 31:S165-S181.

Van Ledden, M. (2002). A process-based sand-mud model. In: Fine Sediment Dynamics in the Marine Environment, J.C. Winterwerp and C. Kranenburg, C. (eds.), Proceedings in Marine Science, 577-594.

Van Ledden, M., Wang, Z. B., Winterwerp, H., & De Vriend, H. (2004). Sand–mud morphodynamics in a short tidal basin. Ocean Dynamics, 54(3-4), 385-391.

Van Maldegem, D. C., Mulder, H. P. J. & Langerak, A. 1993 A cohesive sediment balance for the Scheldt estuary. Netherlands Journal of Aquatic Ecology 27 (2–4), 247–256

Van Rijn, L. C. (1984). Sediment transport, part I: bed load transport. Journal of hydraulic engineering, 110(10), 1431-1456.

Verbeek, H., Jansen, M. H. P., & Wouters, C. A. H. (1998). Adaptation of 2D sediment transport patterns using 3D hydrodynamic modelling. In OCEANS'98 Conference Proceedings (Vol. 1, 444-448), IEEE.

Verlaan, P. A. J., Donze, M., & Kuik, P. (1998). Marine vs Fluvial Suspended Matter in the Scheldt Estuary. Estuarine, Coastal and Shelf Science, 46(6), 873-883.

Waeles, B. (2005) Detachment and transport of slay sand gravel mixtures by channel flows. PhD thesis. University of Caen Caen, France.

Waeles, B., Le Hir, P., Lesueur, P., & Delsinne, N. (2007). Modelling sand/mud transport and morphodynamics in the Seine river mouth (France): an attempt using a process-based approach. Hydrobiologia, 588(1), 69-82.

Wartel, S. & van Eck, G.T.M. (2000). Slibhuishouding van de Schelde. Report, Koninklijk Belgisch Instituut voor Natuurwetenschappen (Brussels) & Rijksinstituut der Kust en Zee (Middelburg, NL), 66 pp. (in Dutch).

Wiberg, P. L., & Smith, J. D. (1987). Calculations of the critical shear stress for motion of uniform and heterogeneous sediments. Water resources research, 23(8), 1471-1480.

Widera, P., Toorman, E., & Lacor, C. (2009). Large eddy simulation of sediment transport in open-channel flow. Journal of hydraulic research, 47(3), 291-298.

Wilcox, D. C. (1998). Turbulence modelling for CFD. La Canada, CA. DCW Industries.

Winterwerp, J. C. (2001). Stratification effects by cohesive and noncohesive sediment. Journal of Geophysical Research, 106(C10), 22559-22574.

Winterwerp, J. C., & Van Kesteren, W. G. (2004). Introduction to the physics of cohesive sediment dynamics in the marine environment. Elsevier.

Yamamoto, Y., Potthoff, M., Tanaka, T., Kajishima, T., & Tsuji, Y. (2001). Large-eddy simulation of turbulent gas–particle flow in a vertical channel: effect of considering inter-particle collisions. Journal of Fluid Mechanics, 442, 303-334.

Yarin, L. P., & Hetsroni, G. (1994). Turbulence intensity in dilute two-phase flows—3 The particles-turbulence interaction in dilute two-phase flow. International Journal of Multiphase Flow, 20(1), 27-44.

Zaichik, L. I., Alipchenkov, V. M., & Sinaiski, E. G. (2008). Particles in turbulent flows. John Wiley & Sons.

Zaimes, G., & Emanuel, R. (2006). Stream Processes Part I: Basics. Arizona Watershed Stewardship Guide, Master Watershed Steward. https://cals.arizona.edu/watershedsteward/resources/docs/stream_processes.pdf.

Zyserman, J. A., & Fredsøe, J. (1994). Data analysis of bed concentration of suspended sediment. Journal of Hydraulic Engineering, 120(9), 1021-1042.